

Investigation of a Magnetically Enhanced Inductively Coupled Negative Ion Plasma Source

Stuart John Nulty

A thesis submitted for the degree of Doctor of Philosophy of
The Australian National University.



Supervisor: Dr. Cormac Corr

November 2018 © Copyright by Stuart John Nulty All Rights
Reserved

Declaration

This thesis presents my research undertaken between July 2013 and May 2018 at the Research School of Physics and Engineering at the Australian National University.

Except where otherwise indicated in the standard manner, all material presented in this work is original and has not been submitted in whole or in part for a degree to any other university.

A handwritten signature in black ink, appearing to read "S. Nulty".

Stuart John Nulty

5 November 2018

Acknowledgments

First and foremost i would like to thank my supervisor Dr. Cormac Corr who accepted me as a PhD candidate without a prior background in plasma physics and gave me a chance to work in his group at the Plasma Research Laboratory. I thank him for his strong scientific knowledge and guidance, his perennial availability, his patience throughout my project and for his motivating support when i needed it the most. Thank you.

I would like to thank Mr. Michael Blacksell and Mr. Mark Gwynneth for their assistance, diligence and technical insight and helping me troubleshoot laboratory issues with the ICPS equipment over the years.

To the fantastic PhD candidates in the PRL group, both past and present thank you for the hours of plasma discussions, friendship and a lot of mischief: Jesse Santoso, Sam Cousens, Tamara Babij, Alex Thorman, Romana Lester, Cameron Samuell, Juan Caneses, Roisin Boadle, Alex Bennet and Colin Campbell.

I would like to acknowledge the senior academic staff for generously sharing their extensive knowledge and guidance: Dr. Clive Michael, Dr. Boyd Blackwell, Dr. John Howard, Dr. Amy Shumak, Dr. Daniel (Danny) Cocks, Dr. Lan Fu and Dr. Matthew Hole.

Thank you to Mrs. Karen Nulty and Mrs. Uyen Nguyen and the administration staff who worked through the thicket of paperwork which is generated during a PhD program including my enrolments, scholarships, conference applications and equipment orders.

The team in the electronics unit were an invaluable source of assistance, including the cups of tea and discussions about equipment diagnostics and circuits. Thank you especially to the talented Mr. Luke Materne, Mr. Daniel Tempra and the inimitable Dennis Gibson.

I gratefully acknowledge the financial support of the Australian Government and the Research School of Physics and Engineering for my Australian Post-graduate Award and scholarships to complete my work.

Thank you to Nian Jiang and to Raiha Gardezi for your companionship and support through thick and thin.

Lastly i would like to thank my family for the years of unwavering support and encouragement for me to pursue a dream. This work is dedicated to you and i could not have done it without you. With all my heart, thank you.

Publications and Conferences

Publications

S. Nulty and C. S. Corr

Electron cooling and negative ion production in a hydrogen ICP plasma source across a magnetic filter (Submitted)

Applied Physics Letters

S. Nulty and C. S. Corr

Time resolved hydrogen negative ion dynamics in a pulsed plasma afterglow (submitted)

Plasma Sources Science and Technology

S. Nulty and C. S. Corr

Power transfer efficiency gains using a magnetically enhanced ICP system. (Final Draft)

Conference Presentations

Australian Physics Society (Brisbane, 2017)

Gaseous Electronics Conference (Hawaii, 2015)

Gaseous Electronics Meeting (Melbourne, 2015)

Australian Physics Society Conference (Canberra, 2014)

Awards

2016 John Carver award

2015 APA PhD Scholarship

2015 Student Support Travel grant (American Inst. Phys.)

Abstract

Experiments and numerical models were used to investigate an inductively coupled plasma source (ICPS) operating with a magnetic filter field. The work shows that applying magnetic filters transversely to the plasma offers several new control parameters to help enhance the properties of a plasma source. The application of these new results using magnetic enhancement is discussed with respect to both industrial plasma fabrication processes and neutral beam injection for fusion power.

Experimental measurements of the power transfer efficiency of the ICPS were undertaken comparing the effect of the magnetic field for both hydrogen and argon plasmas. The location and strength of the magnetic field was varied while measurements of the plasma resistance and power transfer efficiency were performed. The changes in forward power transfer were correlated with plasma density measurements and a numerical model of the electrical plasma circuit was used to guide the optimal choice for the power system components. The results demonstrate that the magnetic field increases the total efficiency of the plasma source and that the gains are strongly dependant on the choice of location for the magnetic field.

Plasma properties were then investigated across the plasma source 1 cm intervals. Experimental measurements comparing the effect of the magnetic filter on the plasma properties include: electron densities using a hairpin probe, electron energy probability functions using a compensated Langmuir probe, negative ion densities by laser photo detachment and rotational gas temperatures by optical emission spectroscopy. These measurements revealed interesting new properties of the plasma when a magnetic filter is applied including: the formation of a high density cold particle trap, changes in particle transport and drift motions, increased gas temperatures, and a peak in negative ion density under the magnetic filter center.

Pulsing the plasma can greatly affect the plasma dynamics, leading to electron cooling in the afterglow and increased negative ion production. A combination of a pulsed plasma with a magnetic filter was then investigated.

Measurements of the negative ion and electron populations were performed in the plasma afterglow with the magnetic filter applied. The results reveal a complex and dynamic afterglow process including strong spatial dependencies measured for diffusive transport, ambipolar breakdown and ion-ion plasma formation.

The applications for this work include offering new avenues for control over processing plasma chemistry as well as initial results toward the future viability of a caesium-free pulsed negative ion neutral beam source.

Contents

Declaration	ii
Acknowledgments	iii
Publications and Conferences	v
Abstract	vii
1 Introduction	1
1.1 Fusion Power and Negative Ion Sources	1
1.2 Plasma Processing and Pulsed Application	7
1.3 Thesis Scope	9
2 The Inductively Coupled Plasma System and Diagnostics	12
2.1 The Inductively Coupled Plasma System	13
2.1.1 Vacuum System and Plasma Source	13
2.1.2 Magnetic field Geometry	15
2.2 System Circuit and Impedance Matching Model	19
2.3 Plasma Probe Diagnostics	27
2.3.1 Langmuir Probe Theory	27
2.3.2 Langmuir Probe Construction and RF Compensation	32
2.3.3 Radio Frequency Interference	35
2.3.4 Current Depletion and Magnetization	37
2.3.5 The Hairpin Probe	40
2.3.6 Hairpin Probe Theory	41
2.3.7 Electric permittivity in magnetized conditions	42
2.3.8 Hairpin Probe Design and Operation	44
2.3.9 Limits of the Hairpin Probe	50
2.4 Optical Emission Diagnostics	51

2.4.1	Theory of the H ₂ Fulcher Band	52
2.4.1.1	Emission channels	53
2.4.2	Experimental Setup	55
2.4.3	Gas Temperature Fit Method	57
2.4.4	Assumptions	60
2.5	Laser Photodetachment Diagnostic	61
2.5.1	Theory of Laser Photodetachment	61
2.5.2	Laser Diagnostic Experiments	63
3	Power Efficiency and Magnetic Enhancement	69
3.1	Power Transfer in the ICPS	70
3.1.1	Source Dynamics	70
3.1.2	Measuring Power Efficiency	73
3.2	Hydrogen Power Transfer	75
3.2.1	Hydrogen E-mode to H-mode Power Dependency	75
3.2.2	Hydrogen Pressure Dependency	78
3.2.3	Hydrogen Magnetic Field Dependency	80
3.3	Argon Power Transfer	82
3.3.1	Argon Power Dependency	82
3.3.2	Argon Pressure Dependency	83
3.3.3	Argon Magnetic Field Dependency	85
4	Charged Particle Dynamics Across the Magnetic Filter	88
4.1	Electron Density Profiles	89
4.1.1	Hydrogen Electron Density Profiles	90
4.1.2	Hydrogen HP and LP Comparison	95
4.1.3	Magnetic Permeability and Electron Cooling	96
4.1.4	Hydrogen Magnetic Field Strength Comparison	97
4.1.5	Argon Electron Density Profiles	98
4.2	Electron Energy Distributions and Plasma Parameters	101
4.2.1	Hydrogen EEPF Profiles	103
4.2.1.1	IV Profiles	103
4.2.1.2	10 mtorr Profiles	103
4.2.1.3	50 mtorr Profiles	108
4.2.1.4	100 mtorr Profiles	111
4.2.2	Argon EEPF Profiles	111
4.2.2.1	10 mtorr	113
4.2.2.2	50 mtorr	115
4.2.3	EEPF Magnetic Field Strength Comparison	117

4.3	Optical Emission Spectroscopy	119
4.3.1	Power Dependence	119
4.3.2	Pressure Dependence and Spatial Dependence	121
4.4	1d Particle Transport Model	124
4.4.1	1d Model Theory and Solution Method	125
4.4.2	1d Electron Modelling Results	127
4.4.3	1d Modelling Concluding Remarks	133
4.5	3d Particle Modelling	133
4.5.1	3d Model Solution Method	135
4.5.2	3d Model Results	137
4.5.3	H_3^+ Visualization	138
4.5.4	Ar^+ Visualization	141
4.5.5	3d Modelling Concluding Remarks	143
5	Negative Ion Measurements	146
5.1	Spatial Variation of H^-	148
5.1.1	Modelling Negative Ion Results	151
5.2	Temporal Variation of H^-	155
5.2.1	$x = 1$ cm Afterglow Results	157
5.2.2	$x = 5$ cm Afterglow Results	159
5.2.3	$x = 8.5$ cm Afterglow Results	160
5.2.4	$x = 11.5$ cm Afterglow Results	162
5.2.5	Concluding Afterglow Remarks	164
5.3	Reaction Rate Comparisons	164
5.3.1	Ambipolar Diffusion	165
5.3.2	Total Reaction Rate Fit	167
5.3.3	Reaction Rate Results	170
5.3.3.1	$x = 1$ cm Total Rates	170
5.3.3.2	$x = 5$ cm Total Rates	171
5.3.3.3	$x = 8.5$ cm Total Rates	174
5.3.3.4	$x = 11.5$ cm Total Rates	174
5.3.3.5	Afterglow Concluding Remarks	175
6	Conclusions and Future Work	177
6.1	Power Transfer Optimization	177
6.2	Plasma Properties Across the ICPS	179
6.3	Negative Ion Dynamics into the Afterglow	181
6.4	Future Work	182

A Appendix: Magnetic Field Code	184
A.1 Python Code	185
B Appendix: The Plasma Frequency	189
B.1 Plasma Frequency Derivation	189
C Appendix: Molecular Dynamics	191
C.1 Electronic Term Symbols	191
C.2 Rotation	192
C.3 Vibration	195
C.4 Nuclear Spin	196

Introduction

This chapter introduces the motivation and historical research context with respect to the findings presented in this work.

This new research contributes primarily to two important areas of plasma science: negative ion sources for fusion heating and low temperature industrial plasma fabrication. An introduction to negative ion sources for fusion applications will be given first in Section 1.1 followed by plasma processing applications in Section 1.2. The scope of the PhD work will be outlined in Section 1.3

The work centers around the optimization and investigation of a new magnetically enhanced inductive coupled plasma (ICP) device using both experimental measurements and modelling.

1.1 Fusion Power and Negative Ion Sources

The United Nations population projections indicate that the world's population will grow from 7.6 billion to around 10 billion by 2050 [1] which will place increased demands on energy and natural resources. This growing population will require new and clean technologies to meet the growing needs for base load power. Fossil fuels currently account for 81% of the world's energy consumption with energy demand globally set to increase by a further 10% by 2050. Despite a predicted growth in fossil fuels, there is uncertainty surrounding the global energy trajectory as there is a growing demand from consumers for different forms of renewable energy. 2015 marked a year of record investment in renewable energy investment [2] as the world's appetite

for clean energy grows and the price point of renewable becomes competitive. In their 2018 report the US Energy Information Administration stated that [3]

"Energy market projections are subject to much uncertainty, as many of the events that shape energy markets and future developments in technologies... cannot be foreseen with certainty."

Nuclear fusion power sources have been researched since the 1950s and major progress towards commercial scale fusion power has been made in recent decades. Several large plasma fusion projects have been undertaken which, if successful, could reshape future developments in the renewable energy market. The large projects with long-term funding have included developments at the National Ignition Facility in the USA, JET in the United Kingdom, Wendelstein 7-X in Germany, the EAST test reactor in China, KSTAR in Korea, JT-60 in Japan and now the ITER test fusion reactor in France. Indeed such progress has been made in fusion power for some scientists to suggest that [4]:

"The last quarter of this century will see the dawn of the Age of Fusion."

Unlike nuclear fission reactors, the cleaner nuclear fusion reactor currently requires larger and more expensive facilities and has required the work of several generations to solve problems such as confinement, instabilities and importantly, plasma heating.

One of the major challenges for tokamak and stellarator fusion reactors is the optimization of the neutral beam injection system (NBI) which is the primary method of heating the plasma to achieve sustained fusion. Neutral beam systems begin by generating large numbers of negative ions in a plasma environment and then accelerate them into a reactor. NBI systems have been developed since the late 1970s and have replaced the positive ion beams as the leading candidate for large NBI systems due to their inherently higher neutralization efficiency [5]. Modern NBI sources typically are magnetically enhanced ICP sources which use a transverse array of permanent magnets to enhance the formation of negative ions within the plasma.

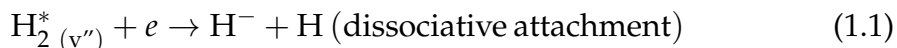
Interest in the process of negative ion formation in hydrogen began to grow around the 1950s [6] where vapour experiments were developed which could yield low levels of negative ions. In the 1960s electron scattering experiments

revealed the resonant short-lived (${}^2\Sigma_u^+$) state in spectral peaks indicating an intermediate electron capture state of H_2^- prior to decay into dissociation into H^- and H (see [7] and references therin). This process was later found to be sensitive to the initial rovibrational excitation state of the molecule where the reaction rate could be increased up to several orders of magnitude when attaching to molecules in higher rovibrational states [8]. More recently, modelling work on quantum scattering from Horacek *et al.*, [9] reveals the dynamic cross-sections and low energy ranges of these H_2 dissociative attachment resonance peaks which occur in the range of 0 eV to 5 eV for various rovibrational states. This range has been found to be ideal for negative ion sources as low electron temperature environments reduce the rate of destructive electron stripping events.

During the 1980s high density plasma devices were constructed with transverse fields to try to maximize this negative ion production inside the plasma bulk primarily for use in thermonuclear fusion NBI [10] [11] [12]. The photodetachment technique used in this work was applied to hydrogen for the first time around this period by Bacal *et al.*, to measure the negative ion densities [13] and has since become one of the standard techniques to measure negative ions in plasma sources.

Negative ion measurements for hydrogen inside magnetically enhanced plasma sources has been a growing area of research in recent decades due to the continued demand for high current density NBI sources [14] [15] [16] and more recently the ITER source [17].

There are two major methods for generating high density negative ions sources: volume production and surface production. Volume production (also called bulk production) is the production of negative ions from inside the main body of the plasma itself. For hydrogen the process mainly occurs via attachment of a slow electron to a rovibrationally excited H_2 molecule:



The first evidence of volume production occurred in 1976 and 1981 from two experiments [19] [20]. The negative ion density was measured in response to changing plasma potential and two conditions were tested. Firstly, increasing gas was shown to lead to a higher density of H^- ions. Secondly, when caesium was allowed to coat the chamber surfaces, a second population of en-

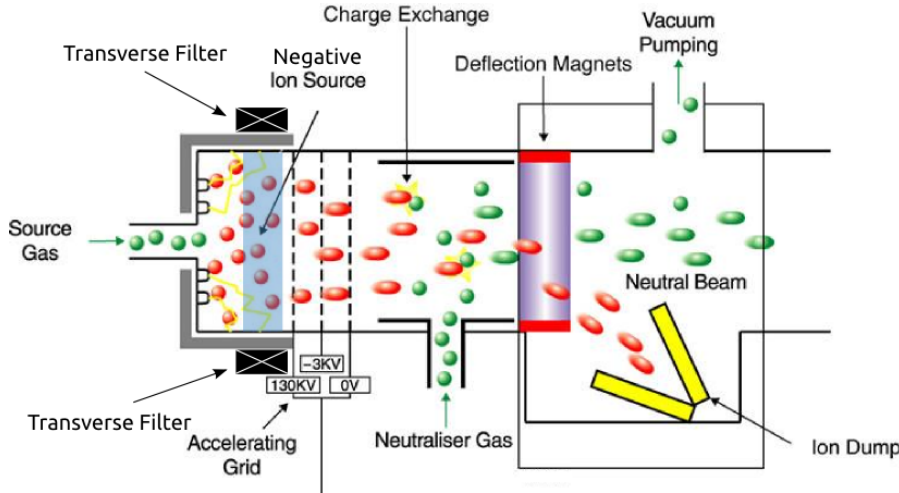


Figure 1.1: Schematic of a neutral beam injection system. The negative ion source region is on the left and includes the transverse filter region (light blue). Image adapted from [18].

energetic H^- ions appeared which increased in response to increased caesium injection. This process was reversible and showed for the first time that negative ion production, using a hydrogen plasma had two distinct generation pathways: volume and surface.

The volume production process unfortunately requires the two competing processes of high electron energies, to maintain the plasma ionization, and low electron energies to perform the attachment and negative ion formation. To solve this problem, transverse magnetic fields have been applied to the plasma source. A primary feature in the NBI designs is this transverse field where permanent magnets are arranged either side of the source to produce a North-South transverse field geometry. The filter has been shown to spatially partition the plasma into regions of fast electrons upstream of the filter and cold electrons inside the filter [21] [15] [22]. Often larger systems have only limited optical access to the source and the effect of the filter can only be correlated to a few locations. This work will present experimental measurements of the full spatial and temporal profile of the negative ion population in hydrogen along the length of the source.

The second method to create negative ions is via surface production which is used in larger neutral beam injection systems. The surface method involves electrons attaching to hydrogen atoms via quantum tunnelling events from a surface with a sufficiently high work function such as tungsten or caesium

[23] [24] [25].

Publications in the late 1980s showed evidence that surface produced negative ions were the dominant ion population during beam extraction [26] and surface production rather than volume production became the primary mechanism to generate negative ions for fusion applications. The use of pulsed plasmas for large scale negative ion production and extraction was discontinued after several works such as Hopkins *et al.*, [15] found insufficient H⁻ levels compared to continuous operation in their cusp system to continue looking into a pulsed negative ion production source.

These early works were important for initial NBI source development, however the plasma systems used during the works incorporated obsolete thermionic filaments and were undertaken with inefficient source geometries. Recent developments in source design combined with the preliminary findings in this work suggest that a competitive volume-only pulsed negative ion source may be viable into the future and warrants further investigation.

The motivation for such a source is due to the problems encountered from operating continuous mode caesiated sources such as: excessive current loads on the plasma facing surfaces [17], heat loads [27] extensive caesium sputter contamination of the source [28] [29] [30], and ion beam divergence [31]. The toxicity of caesiated sources is an ongoing concern and the constant maintenance requirements draw questions regarding the long-term viability of such sources [32] [30].

Ideally, hydrogen and deuterium negative ions could be produced in sufficient quantities (>30%) inside the volume of the plasma via a magnetic filtration system and optimized source design. For a viable NBI source which uses volume production the electron current must be removed from the plasma bulk to avoid excessive co-extracted electrons. This is extremely challenging since the electronegativity is low for a hydrogen plasma and hence there is a large fraction of electrons present. One way to deal with this is by pulsing the plasma system on and off which allows for the highly mobile electrons to first exit the system while the longer-lived negative ions remain for extraction.

This research will center around a comprehensive characterization of the new ICPS and will include initial measurements and modelling of the volume produced negative ion distribution throughout the source. The effect of pulsing

the plasma in combination with the application of magnetic fields will be quantified and the transport of plasma across the magnetic field will be investigated.

Transport of charged plasma particles across transverse magnetic fields is a complex process has been the subject of several works in the last decade motivated by improvements in NBI efficiency. The magnetic filter has been found to affect many aspects of the plasma experimentally including power transfer efficiency [33], electron cyclotron heating [34], plasma drift rates [35], and electron temperatures [22] [15]. These effects can change the localization of negative ions within the source and hence the efficiency of negative ion extraction. Since 2011, an increased focus on modelling of NBI sources using a transverse magnetic filter has revealed new complexities arising from the presence of the magnetic field such as creating plasma asymmetries [36] [37] plasma instabilities [38] and source wall effects [39]. There have been many NBI sources tested in recent decades with notable progress coming from the high power test sources developed at the Max Planck Institute such the BAT-MAN source and more recently the ELISE source [40]. These sources have been developed to asses the challenges in up-scaling the source size and optimization of the negative ion density to meet the high density requirements of the ITER NBI.

Despite this increased work on magnetically filtered sources, negative ion source efficiency remains at levels below the requirement for a continuous high density fusion environment. Fantz *et al.*, have noted recently that [35]:

"The challenges on such negative ion sources are enormous... further investigations on the modelling side as well as on the experimental side are desirable to understand the complex behaviour of the source performance on the magnetic filter field"

The inductive plasma system used in this work is ideal for investigating new plasma processes related to the transverse filter without conflation from the effects of extraction grids and caesiation. The size of the ICPS and its optical access means that a complete treatment of spatially resolved measurements can be made on a single plasma system. The lower operating power and wide range of pressures available in the ICPS means that fundamental processes relating to the magnetic filter can be investigated in detail.

1.2 Plasma Processing and Pulsed Application

Since the 1990s, motivations from the semiconductor industry have generated an increasingly strong demand for commercial plasma processing for applications such as etching, coating and doping of materials. The plasma process can catalyze reactions at lower temperatures which also creates a host of new chemical species which have industrial importance. The global plasma processing industry was recently valued at \$20.8 billion US in 2016 with a growth trajectory set to reach as high as \$48 billion US by 2025 [41].

Many of these commercial plasma systems are pulsed magnetically enhanced sources with duty cycles less than 10%. The majority of the commercial value to fabrication companies using these sources lies in the complex pulsed afterglow dynamics of the electrons, ions and recombined neutral chemical species in these sources. The characterization of the evolution of the afterglow chemistry attracts strong interest from the fabrication industry due to its complexity and importance to the quality of processed end products. Negative ion formation in the afterglow is a complex process involving both temporal and spatial variations in plasma properties. The changing conditions inside different pulsed plasmas can affect several parameters including: modifying the sheath potential and ion temperature [42], modification of plasma polymerization and the formation of functional surfaces [43] and surface contamination by-products [44]. This work will present detailed measurements of several afterglow features with an emphasis on the H^- negative ion population and provide new insight into the spatial and temporal variation of negative ions in pulsed magnetically enhanced plasmas.

There exists a large body of literature relating to afterglow chemistry of plasmas across a variety of gasses and plasma system types. Typically measurements are made using mass spectrometry, emission spectroscopy and photodetachment in the case of negative ion chemistry. Negative ion densities in plasma afterglows have been studied less completely with sporadic works across a range of plasma gasses and conditions including negative ion measurements in nitrogen plasmas [45], chlorine plasmas [45] [46] [47], oxygen plasmas [48] [49], fluorine mixtures [50] [51] and silicon hydride plasmas [43].

In low temperature plasmas, the electron population can determine much of the plasma chemistry such as density, ionization fraction, excitation states, plasma potentials and drift motions. Electron population measurements can

be made using a Langmuir probe which can produce the electron energy probability function (EEPF). Spatial variations in the temperature of the electron population from the EEPF can reveal key information about plasma process and plasma chemistry within a system. There are two important ways of controlling the electron temperature, the first is by applying external magnetic fields which can increase the plasma confinement in certain areas of the source and enhance the collisional cooling of the electrons. The second way to control the electron temperature is by pulsing the plasma on and off whereby the hot electrons exit the system first in the early plasma afterglow. Both of these methods to cool electron population will be explored in this work and EEPF results will be presented for measurements through the transverse field and correlated with changes in plasma chemistry.

The neutral gas from which plasmas are formed have both translational (elastic) motion and a complex internal (inelastic) energy structure. Collisions between particles which preserve translational motion are said to be 'elastic' while those which excite internal energy states at the cost of some kinetic energy after collision are said to be 'inelastic'. Information of the internal energetic state of the background feedstock gas is an important diagnostic in both low temperature, low ionization industrial plasmas and also for high power NBI beam plasma sources. Collisions between electrons which heat the neutral molecules not only form the major energy sink for low power plasma chemical processes but importantly, they excite higher rovibrational states and increase the collisional cross section of the molecule. Since dissociative attachment process which creates negative ions is highly sensitive to the H₂ cross section, measuring the inelastic energy state of neutrals becomes a key factor in determining conditions which optimize the formation of negative ions. Spatial results will be presented in this work measuring the effect of the magnetic field on H₂ rotational temperatures across the source to help correlate negative ion formation to the inelastic neutral gas temperature.

In commercial plasma systems the forward power is one of the important control parameters to adjust the plasma product properties including: ion flux, reaction energies, material chemistry, deposition layer size and etch consistency. In recent decades, dry plasma etching has revolutionized the semiconductor fabrication industry allowing for nanometer scale circuits and surfaces with thin film layers to be produced. Hydrogen plasmas have been used widely in the semiconductor industry since the 1980s due to their ability to uniformly etch semiconductor substrates, remove oxides and create electronically neutral surfaces [53]. New pulsed magnetized plasma sources

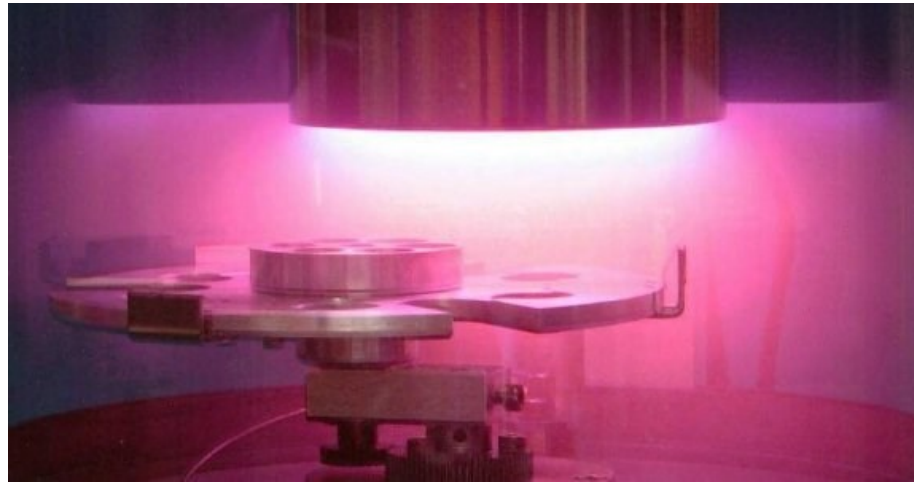


Figure 1.2: A typical commercial pulsed DC magnetron sputtering system used for thin films and coatings. Photograph adapted from [52].

operated at low power have been applied widely for fabrication of thin films and custom nano-layers using techniques such as plasma enhanced chemical vapour deposition (PECVD) high power impulse magnetron sputtering (HiP-IMS), ion implantation doping and direct current RF magnetron sputtering (DCMS/RFMS) [54]. This work will present extensive measurements of the power transfer efficiency of the source using magnetic enhancement for both hydrogen and argon plasmas. These results will help to provide new avenues for optimization of plasma sources used in commercial fabrication.

Hydrogen plays a key role in plasma processing when used with a mixture of other gasses as it can offer several controls on the desired chemistry. Hydrogen plasmas specifically can be used for applications such as: acting as a carrier for a target material [55], semiconductor material passivation (eg. silane) [56] and it can also be used to catalyze targeted plasma chemistry reactions [57]. Argon has been used extensively for ion implantation, as a metastable buffer gas and has also been found to affect surface nucleation in processing plasmas [43].

1.3 Thesis Scope

Results will be presented across four chapters which aim to help contribute to both experimentally and through modelling to the knowledge of mag-

netically enhanced inductive plasma systems. The contributions to plasma science which arise from the results in this work are:

- 1) Development of a new inductive plasma system including diagnostic techniques and probe construction to study low temperature plasma phenomena.
- 2) Quantifying the interaction between the transverse magnetic filter and the power transfer efficiency in hydrogen and argon.
- 3) Increasing the knowledge of the transverse magnetic filter in plasmas including interesting new effects and transport properties.
- 4) Advancing the knowledge of negative ion formation and afterglow dynamics within a magnetically filtered plasma source.

This thesis is set out in four chapters with all experimental results conducted on a single inductive system.

Chapter 2 will introduce the inductive source and discuss all of the diagnostics, equipment and methodologies used throughout the work. The chapter also includes a model and measurements of the power transfer circuit.

Chapter 3 provides detailed measurements of power transfer efficiency of the source and correlates it with plasma density results. The effect of the magnetic filter is compared between hydrogen and argon while changing several plasma parameters such as forward power, pressure and location of the magnetic filter.

Chapter 4 presents key results of axial measurements along the length of the source and magnetic filter region both experimentally and theoretically. The results include plasma density measurements, electron energy distributions, rotational gas temperatures and two custom plasma transport models written for the new system. This complete treatment of the source will show new effects to emerge from the physics of the magnetic filter.

Lastly, Chapter 5 will show the spatial and temporal evolution of the negative ions along the source and into the afterglow. Rate coefficients of the

production and loss of the negative ions will show interesting new information about the afterglow dynamics of negative ions including the formation of ion-ion plasmas.

The Inductively Coupled Plasma System and Diagnostics

The new plasma system developed during this PhD is a magnetically enhanced inductively coupled plasma source (the ICPS) located within the Materials Diagnostic Facility at the Plasma Research Laboratory (PRL) at the Australian National University (ANU). The system is a newly constructed inductive source designed for studying low temperature plasma physics phenomenon and the development of plasma diagnostics. This work presents the first characterization of the ICPS and so this chapter will include measurements of the power transfer circuit, RF plasma oscillations, the external magnetic field and power system grounding.

This chapter presents all of the experimental diagnostics and methodology used in the subsequent results chapters. The term 'ICPS' will be used exclusively throughout this work to describe the apparatus used for this PhD whereas terms such as 'ICP devices' or 'ICP sources' will be used to refer more generally to other inductive systems in the literature.

Section 2.1 describes the source apparatus and operating conditions. Section 2.2 details the power transfer circuit including the impedance matching network and presents a model designed to predict power transfer efficiency. Section 2.3 provides details for the two probe diagnostics used on the system: Langmuir probe and hairpin probe. Section 2.4 describes the optical emission spectroscopy diagnostic and Section 2.5 presents the methodology for the laser photodetachment measurements.

2.1 The Inductively Coupled Plasma System

2.1.1 Vacuum System and Plasma Source

A schematic of the the ICPS is shown in Figure 2.1 showing the matching unit, source tube and gas inlet, the location of the magnetic filter and the diffusion chamber downstream. The ICPS consists of a 30 cm long, 6 cm diameter, cylindrical borosilicate source tube connected to a stainless steel diffusion chamber. The borosilicate tube allows for both physical and optical access throughout the source as well as resistance to heat expansion under vacuum.

A 7-turn copper solenoid antenna surrounds the outside of the source tube and is driven by a 13.56 MHz 1000 W ENI power supply through a variable L-type matching network (details given in Sec. 2.2). The matching network is adjusted for each measurement to achieve a minimum in reflected power determined by standing wave ratio (SWR) readings from a Diamond SX-100 power meter. Due to the performance of the impedance matching system and the relatively low forward power (<1 kW) used across the experimental parameter space, SWR ratios were able to be kept within 5% of the ideal SWR ratio of 1 in this work.

The coordinate system used throughout the thesis begins at the 'front' edge of the antenna at $x = 0$ cm and proceeds in the positive x-direction downstream of the antenna through the filter toward the diffusion chamber (Figure 2.1). The y-axis is defined laterally across the side of the 6 cm diameter tube from $y = -3$ cm to $y = 3$ cm and similarly with the z-axis for $x = 3$ cm at the top of the tube and $z = -3$ cm at the bottom of the tube.

Negative x-axis values indicate positions under the antenna upstream toward the gas cap inlet. All experimental measurements were performed within a 20 cm region of the source tube ranging from $x = -10$ cm to $x = 10$ cm as this region corresponds to the full range of densities and areas used in most plasma sources. Diagnostic probes were inserted along the center of the tube ($y = 0$ cm, $z = 0$ cm) from the diffusion chamber side and into the source region (see Fig. 2.1 g) and e)).

Gas enters the system through one end of the source tube upstream of the

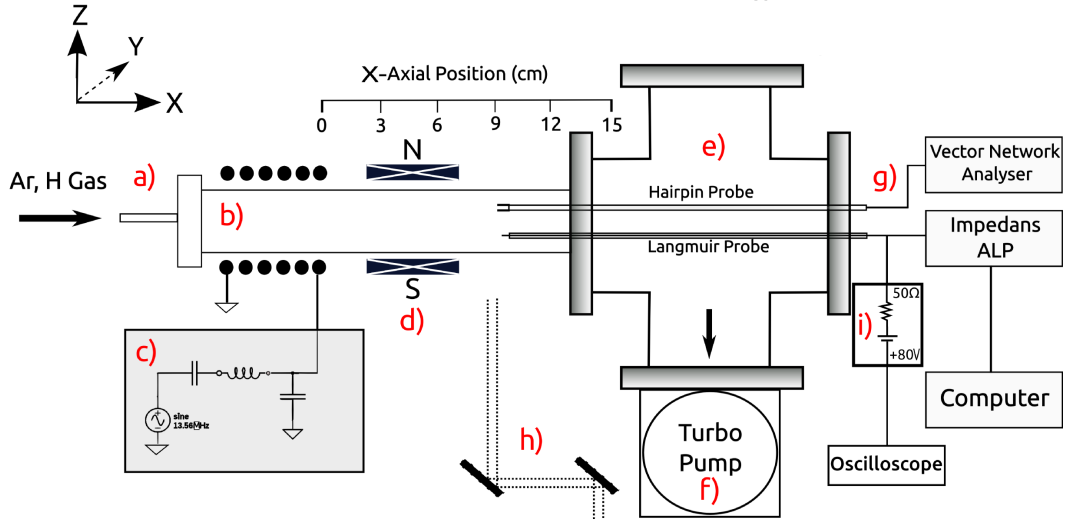


Figure 2.1: The ICPS device showing (from left): a) the gas inlet and conductive gas end-tap b) the Pyrex source tube and coil antenna c) the impedance matching network, d) magnetic field location e) diffusion chamber, f) turbo-molecular pump, g) Langmuir probe / hairpin probe h) mirrors and infra-red laser path i) Photodetachment circuit.

antenna via an inlet valve attached to a stainless steel end cap and is pumped out through the bottom of the diffusion chamber downstream of the source. The operating gas is let into the chamber with a gate valve and flow is then controlled by adjusting the gas inlet via a fine-scale needle valve.

The vacuum chamber operates over a wide range of pressures from high vacuum to atmospheric pressure and so the ICPS is equipped with two pressure gauges: a Pirani style MKS Granville Phillips 275 convectron gauge to measure typical plasma pressures from atmospheric pressure down to 10^{-4} Torr and a Pfeiffer cold cathode ion gauge which covers the higher vacuum conditions from 10^{-3} Torr down to 10^{-7} Torr. For this work, experimental operating gas/plasma pressures were used up to 150 mtorr. The ICPS is not able to generate an inductive discharge for hydrogen below 10 mtorr and so this was the lowest operating pressure available in this work.

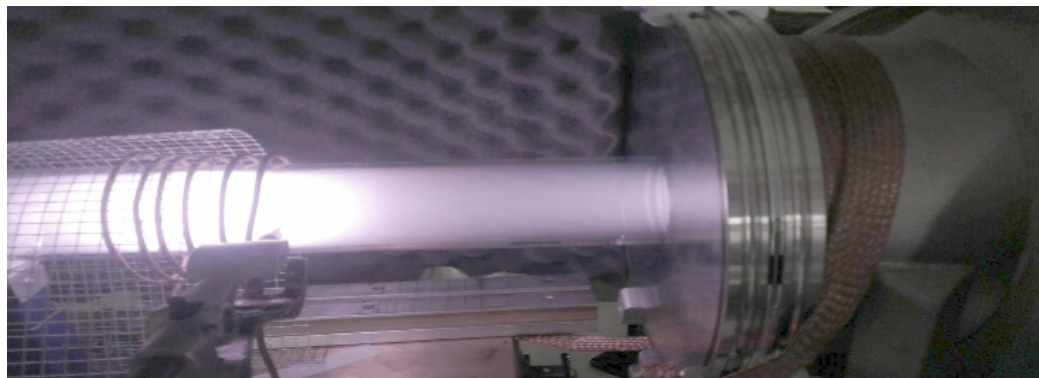
Initially there were electrical grounding issues with the ICPS which were found to affect several plasma parameters. Due to the high frequency RF, troubleshooting grounding issues can be difficult as the RF currents can propagate along the skin layer of both conductive and dielectric surfaces. Insufficient return paths for wall currents from the plasma in some cases caused DC

potentials to build up on surfaces and were seen to also affect sheath sizes, plasma potentials, RF noise and power transfer stability. Several grounding configurations were tried, including the commonly used 'star' configuration. The entire system was moved from a conductive bench top to a wooden table to assist in troubleshooting. The optimal termination point for grounding the ICPS was eventually determined to be via the copper impedance matching unit chassis where the neutral return of the antenna was also terminated in series (Fig. 2.1 c). The RF current exits via the neutral return path shielding of the UHF power cable which is attached to the matching unit. RF conductive braiding was used to connect both the diffusion chamber and the gas feed inlet caps (the two plasma exposed surfaces) to the impedance matching box chassis to provide the same return path for the wall currents as the path of the antenna driving current. A single grounding braid was attached to the system and connected to a local earth terminal (building ground) in case of an electrical accident. The success of this setup was seen in reliable and repeatable plasma operation and the absence of DC potential build-ups on surfaces.

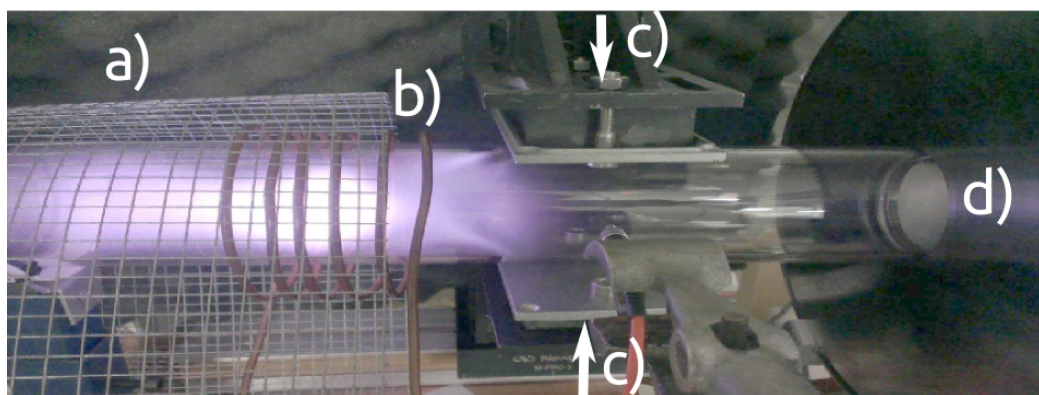
2.1.2 Magnetic field Geometry

The main magnetic field configuration used throughout the experiments was the transverse magnetic filter. The configuration consisted of two ferrite block magnets measuring 5 cm x 5 cm x 1 cm which were externally clamped to a variable sliding stage and were positioned either side of the source tube. Figure 2.2 shows two photographs of the source tube, one without the magnetic filter applied (Fig. 2.2(a)) (top) and the other with the magnetic blocks clamped either side of the filter (Fig. 2.2(b)) (bottom). The magnetic blocks could be separated in the z-direction above and below the tube and could also be moved in the x-direction along the length of the source tube to measure the effect of the filter location on the plasma. This region shown in the photographs between the front of the antenna and the entrance to the diffusion chamber is the area in which all of the plasma experiments were conducted for this work.

At first glance, the unfiltered plasma is seen to generate a uniform plasma which extends downstream of the antenna and into the diffusion chamber. However with the application of the magnetic filter, the discharge is seen to create a 'dark' region between the magnets which continues downstream toward the chamber entry. This dark region is due to the magnetic filter cooling



(a) A typical ICPS H-mode hydrogen discharge without a magnetic filter.



(b) A typical ICPS H-mode hydrogen discharge with a magnetic filter attached at $x = 5$ cm. Note the 'dark' region under the filter field.

Figure 2.2: The ICPS source discharge comparison showing: a) Faraday cage, b) front of antenna, c) transverse magnetic field magnets, d) diffusion chamber.

electrons to energies below the ionization potential of the gas but this dark region will be shown to contain significant plasma density despite the lack of light emission. The particle dynamics and chemistry surrounding this dark region will be a major focus throughout this work as interesting properties and new results will emerge when magnetically enhancing an inductive system in this way.

Since the magnetic field forms a key aspect to this work, a model was created of the transverse filter's 3d magnetic field profile (See Appendix A for the code). The domain of the field calculation was made at a 1:1 scale size to the 1000 cm^{-3} surrounding the magnets. A 3d gridded finite element method was developed whereby the Biot-Savart Law was integrated with respect to each point on a 3d spatial grid with the permanent magnet blocks modelled as layers of permanent dipole vectors. This process yields the 3d magnetic vector potential field $\vec{A}(\vec{r}_a)$ which is calculated at each point in the spatial domain \vec{r}_a :

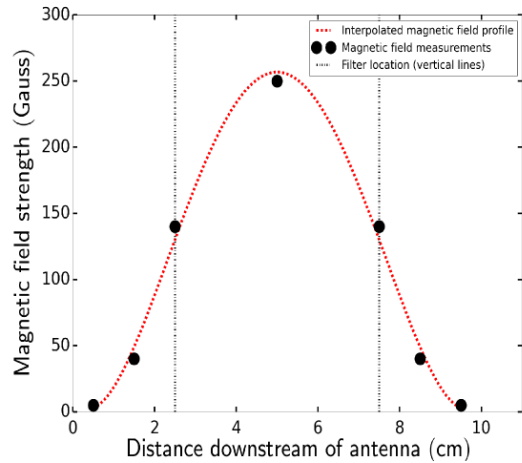
$$\vec{A}(x, y, z) = \sum_m \vec{A}(\vec{r}_a) = \sum_m \frac{\vec{M}(\vec{r}_m) \times (\vec{r}_m - \vec{r}_a)}{|\vec{r}_{m-a}|^3} \quad (2.1)$$

where \vec{A} is the magnetic vector potential field, a is each location of 3d grid to iterate over, m is the position of each permanent magnetic pole, $\vec{M}(\vec{r}_m)$ is the magnetic moment of each magnetic pole. After performing the calculation for each point in space a for each magnetic moment, the vector field \vec{A} is produced. The curl of this magnetic vector potential field yields the magnetic field vector at each point in space:

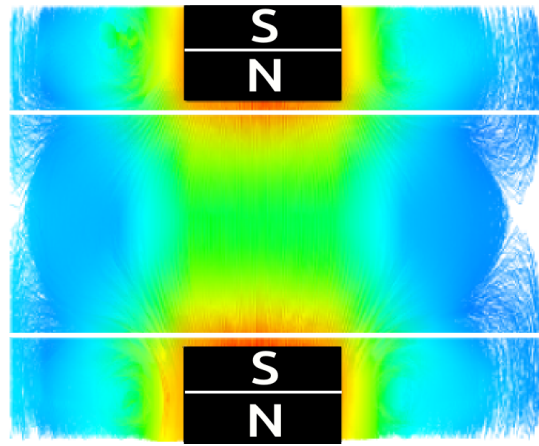
$$\vec{B}(x, y, z) = \vec{\nabla} \times \vec{A}(x, y, z) \quad (2.2)$$

The motivation behind this modelling is to visualize the field and to apply the 3d field to a particle transport model which will be presented in Chapter 4.

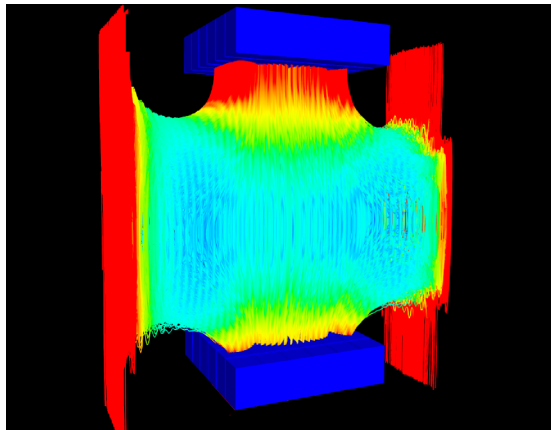
The magnetic field strength was measured experimentally along the center x-axis of the tube at 1 cm intervals using a Bell 640 Incremental Gaussmeter attached to a three-axis Hall probe. The Gaussmeter probe was oriented in the $-\hat{z}$ direction and the measurements showed a Gaussian field profile which are shown in Figure 2.3(a). The magnetic field through the center axis from the source ranges from 0 to 250 Gauss with the surface field of the magnets



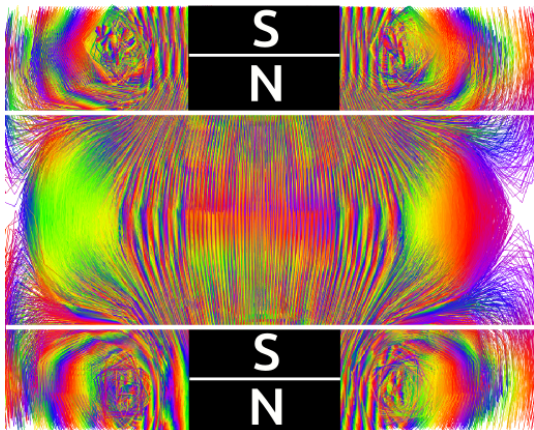
(a) Measurements of the ($-\hat{z}$) transverse magnetic field strength (black dots) and an interpolated Gaussian field profile (red).



(b) X/Z transverse slice of the filter region showing the magnetic field strength profile.



(c) 3d contour of the magnetic field strength (coloured contours) between the transverse filter magnets (blue blocks). The red far edges of the field are an artefact of the domain boundary conditions.



(d) X/Z transverse slice of the filter region in false colour showing the rounded 3d field geometry at the edges of the filter region.

Figure 2.3: Measurements and simulations of the transverse magnetic field configuration used for the experiments from $x = 0$ cm on the left, to $x = 10$ cm downstream on the right. The white lines in the contour plots indicate the location of the source tube edges along its length.

measured at 1000 Gauss. Except where otherwise stated, the magnetic field configuration used is in the attracting transverse North-South position which is center d at $x = 5$ cm downstream of the antenna edge as shown in Figure 2.2(b).

The magnetic field strength profile is shown as a transverse slice in Figure 2.3(b) and as a 3d rendering in Figure 2.3(c) with the permanent magnets shown as blue blocks. Figure 2.3(d) shows a transverse slice of the magnetic field profile in false colour to highlight the field contour lines. The rounded edges seen in the false colour image are seen to follow the rounded shape of the plasma light emission seen in Figure 2.2(b) indicating that the ionization profile of the plasma follows the 3d magnetic filter field geometry.

The field applied to the transport code was run at 1 mm per grid. The reason for such a resolution was necessary to capture the smallest scale transport and drift behaviour including conservation of Larmor forces and the ∇B drift motion of electrons. At higher resolution grid sizes, the number of magnetic dipoles from the permanent magnets must also increase to maintain a smooth field and so a field of 10^6 grid locations was used with 5×10^4 magnetic dipoles.

2.2 System Circuit and Impedance Matching Model

The power circuit of the ICPS will be presented here with both experimental and modelling results of the impedance matching circuit.

To provide an efficient transfer of power in driven AC circuits and in order for an electrical standing wave to develop, the impedance of the voltage source must match the total load of the circuit. Most RF amplifiers which drive plasma systems have an in-series $50\ \Omega$ internal source resistance (R_s) with a purely real component which must be matched to an equivalent real load. The plasma resistance of common laboratory discharges range from approximately $1\ \Omega$ to $20\ \Omega$ depending on the gas type and gas pressure. This means that the difference between the plasma resistance and the source resistance must be added to the circuit to match the impedance of the system thereby preventing reflected power losses and possible damage to the source

amplifier. A variable resistor could be used to solve this problem however, such a resistor would require excessive cooling at higher power. The solution for many AC driven plasma devices is the use of an impedance matching network consisting of inductors and variable capacitors to augment the real component of the load. The core circuit design and choice of component specifications is crucial in order to ensure an efficient discharge which can be generated across the desired range of operational parameters such as different pressures and powers for a variety of gasses.

The ICPS uses a matching circuit made in-house, at ANU's PRL, which features: two variable vacuum capacitors, a small copper inductor, a copper antenna and a ceramic core capacitor at the end of the circuit. For a matching unit to be able to change the resistance of a load, at least one of the reactance components must be in parallel with the load. The variable components should be resistant to high voltages and heat.

There was a wide experimental parameter space used for the project, covering pressures ranging from 2 mtorr to 150 mtorr, and powers from 1 W to 450 W in both argon and hydrogen with the use of magnetic enhancement. This meant that a wide range of impedances were required to achieve a good resistance match across the plasma parameters. In order to satisfy the experimental requirements, a custom impedance matching circuit model was developed to help inform which designs and circuit components were suitable for the ICPS. The motivation behind the model came from capacitor component failures and electrical issues early in the project which required a redesign and reconstruction of the matching network and new choices of components. Incorrect matching network components can cause early component failure and also dangerous arc discharges inside the matching circuit due to high kV potentials.

A model was designed to incorporate arbitrary circuit designs and components to assess the properties of any type of load matching system prior to redesigning the ICPS matching unit. The model consisted of a simplified matching circuit where the components are complex valued resistors (Fig. 2.4(b)). The model was benchmarked against measurements of the physical network using a vector network analyser which was found to be a reliable device to test the operational range of matching circuits. The network analyzer is a frequency sweeping diagnostic tool used for investigating circuits and will be described in more detail in Section 2.3.8.

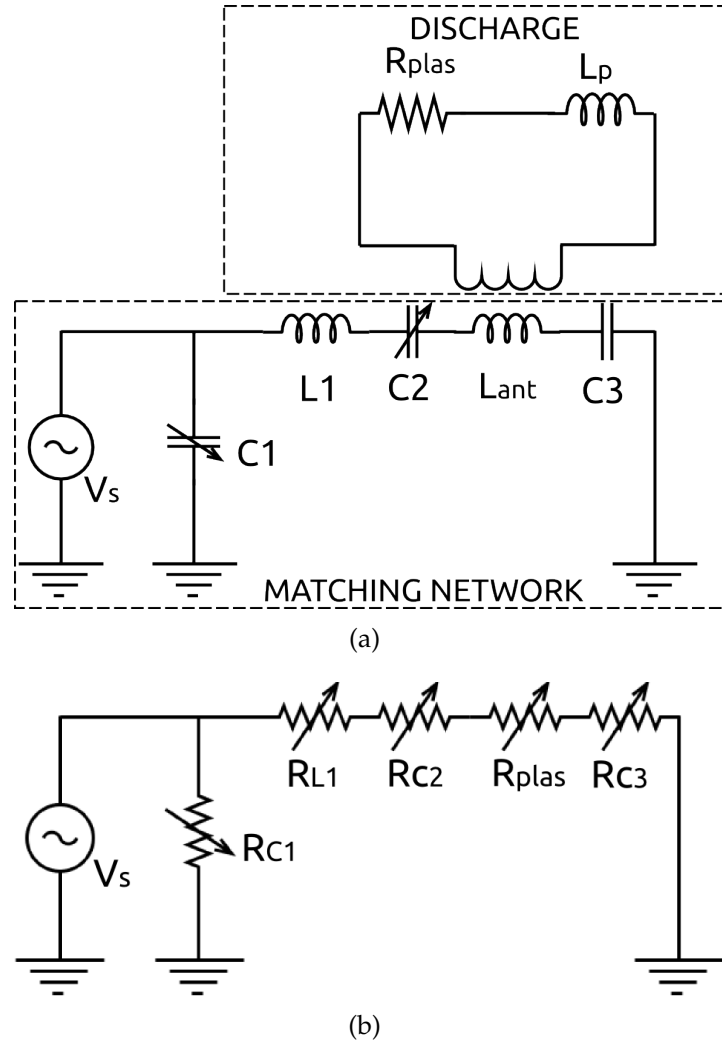


Figure 2.4: Two ways to model the ICPS matching circuit: a) Circuit diagram of the ICPS L-type network representing the discharge as a transformer coupling. V_s is the source voltage, C_1 and C_2 are the variable capacitors, L_{ant} is the antenna inductance, L_p is the plasma self inductance and R_{plas} is the plasma resistance. b) The simplified plasma circuit used to create a model of the impedance matching network using variable complex value resistors.

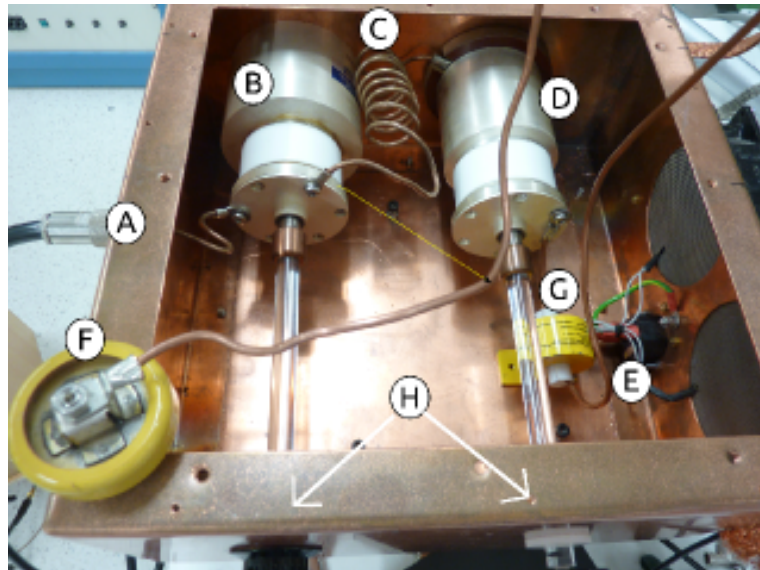


Figure 2.5: Reconstructed L-type Impedance matching network showing: a) power I/O, b) 0-2500 pf variable capacitor, c) 3.94 μ H inductor, d) 0-500 pf variable capacitor, e) antenna, f) 100 pf grounding capacitor, g) current monitor, h) capacitor control knobs.



Figure 2.6: The 1000 W ENI 13.56 MHz amplifier, turbo molecular pump controller and pressure gauge

The vector network analyser can be operated in 'reflective' mode whereby AC signals of different frequency are generated by the VNA and sent through a single coaxial cable into a circuit such that the total impedance frequency response of the circuit can be measured. This single cable measurement is ideal for testing the matching circuit as the matching unit has a single input port and the return current from the source is via the matching units chassis. During the reflection measurement, the variable capacitors in the matching circuit can be changed while the VNA can be used then to measure changes in several parameters including: the total impedance, impedance phase, complex resistance and real resistance.

The impedance matching network was modelled as a series of variable resistors with complex reactances. The reactance of each component was determined as a function of frequency for a wide range of components and architectures and the total impedance of each circuit type was determined using the usual additive circuit rules for resistors with imaginary components:

$$\chi_C(f) = \frac{1}{j\omega C} \quad , \quad \chi_L(f) = j\omega L \quad (2.3)$$

where ω is the driven angular frequency of the source and j denotes the imaginary unit. The capacitive reactance can be considered a 'negative' resistor and the inductive reactance considered a 'positive' resistor for the calculation of the total impedance of the system. Unlike voltage and current, the impedance vector of each circuit component is not time varying and so the impedance phase angle in the complex plane can be simply summed across all components using Kirchhoff's laws and the rules for complex numbers. From this the voltage and current phase and amplitudes can be determined across each component but these are not required for determining just the impedance response of the system. The impedance response of the system as a function of frequency is precisely what a vector network analyser is designed to measure and so this kind of model can be benchmarked against a VNA output for validation.

Figure 2.7 shows the comparison between the model (red) and the experimental output from the network analyser (black) for four impedance properties of the matching unit. The component values used in the model for these results were the component values from the ICPS matching unit. The model amplitudes were normalized by a factor of 0.5 and the frequency shifted higher by approximately 1 MHz to achieve the overlay with the experimental measure-

ments of the matching unit.

The model is seen to accurately predict the major features of the matching circuit when tuned to match a 50 Ohm real load at 13.56 MHz. Figure 2.7(a) shows that both the matching unit and the model produce a single resonance peak with a maximum match of anywhere up to a 1900 Ohm load. This peak can be shifted left or right using the two variable tuning capacitors which are components b) and d) from Figure 2.5. In the case of a 50 Ohm load at 13.56 MHz the matching units peak is not needed as its impedance is too high. Instead the match is achieved by moving the peak sideways using the variable capacitors to match to the 'shoulder'. The total real impedance is shown in Figure 2.7(d) and shows a 50 Ohm impedance at 13.56 MHz on the shoulder of the peak. If the tuning range of the capacitors is wide enough to move the peak across to the other shoulder, then two optimal matching points would be possible on the system.

The impedance phase and complex impedance is shown in Figures 2.7(b) and 2.7(c) as are both seen to cross the zero line at 13.56 MHz which means that the forward power is being delivered to a purely real load. This is desirable for optimizing plasma power efficiency and also matching unit safety as off-phase impedances can cause voltage arcs from the matching unit components to surrounding surfaces. Good agreement was found between the properties except for the higher frequency part of the impedance phase in Fig. 2.7(c); this discrepancy is due to the additional periodic 1/4 wavelength resonance of the power cable which was not included in the model.

While inputting values from a known matching unit can provide validation of existing matching ranges and expected impedances, a model such as this can be used instead to solve for unknown component values for optimization of power transfer prior to the purchasing of expensive components. Various matching unit circuit configurations can be fed to the model without specifying their value and the model can scan a range of driving frequencies, capacitances and inductances for the optimal component choice. This allows for better choices of components with superior matching ranges and power factors, (ratios of real power to apparent power). Not only can the frequency response of forward and reflected power be determined quickly, but also extra information can be found such as the frequency span of the power factor for a given combination of components.

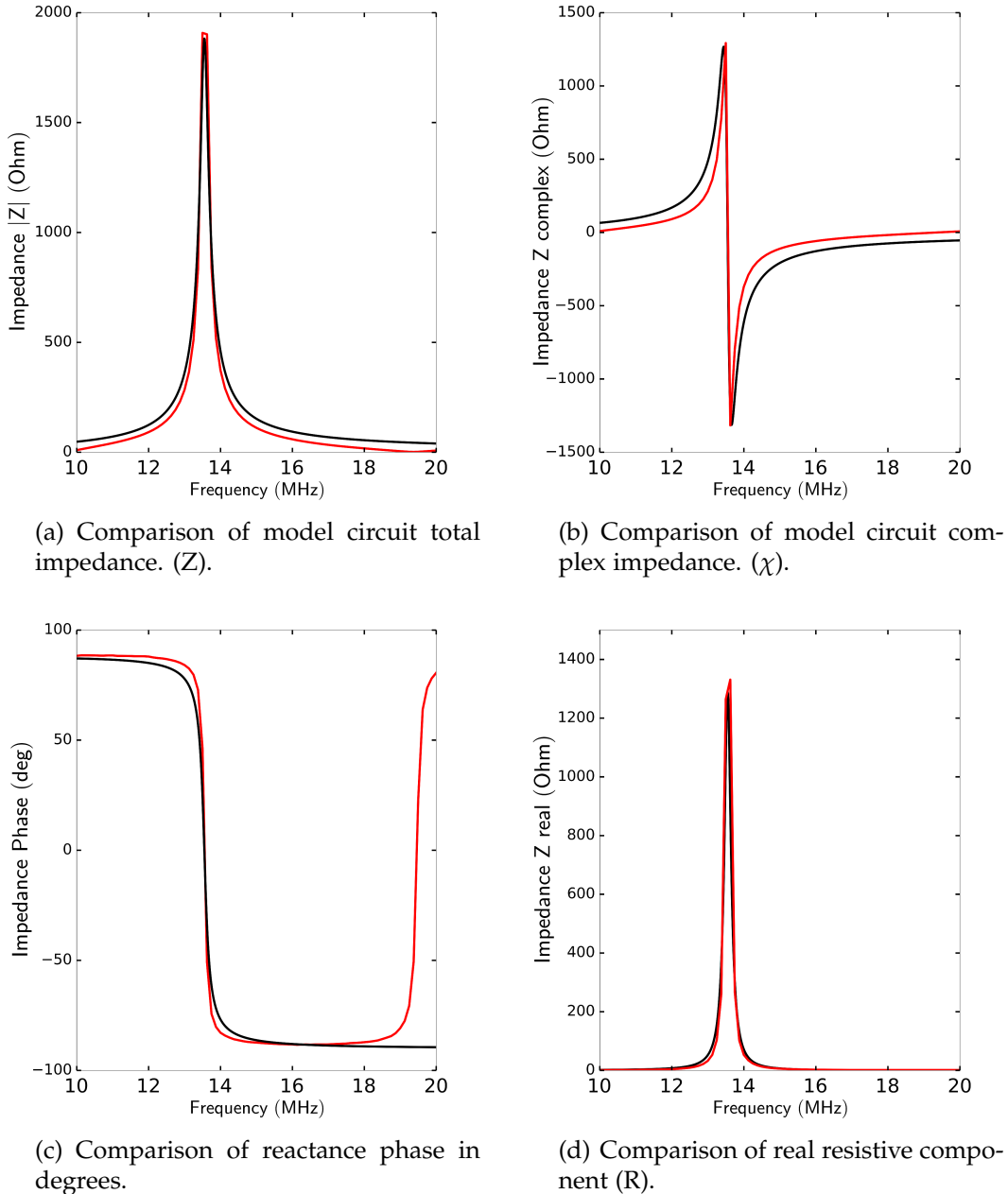


Figure 2.7: Comparison of matching circuit model (black) and network analyser output (red) for various circuit parameters.

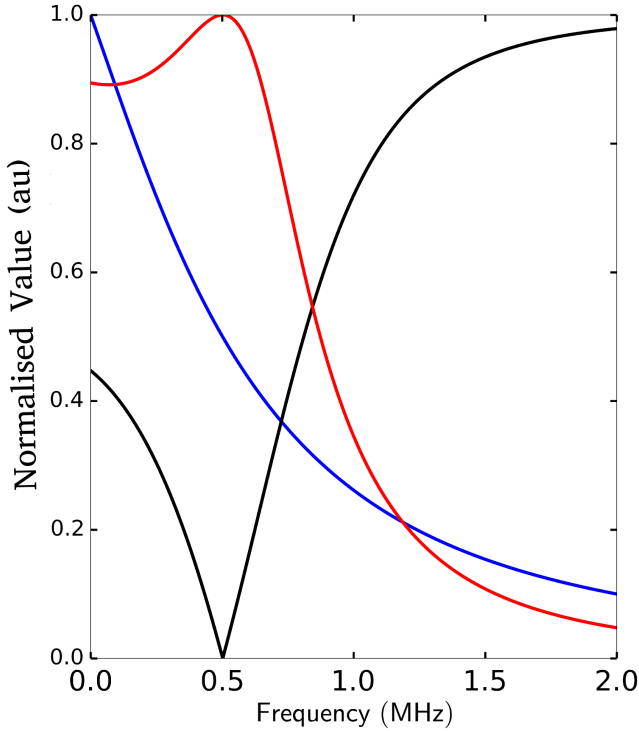


Figure 2.8: Matching circuit parameters search-matched to an arbitrary 500 kHz driven 50 Ohm plasma circuit: reflected power fraction (black), power factor (red), total normalized impedance (blue).

The model was tested for a hypothetical case where a new 500 kHz amplifier was used instead of the 13.56 MHz amplifier. Figure 2.8 shows an output from the model with initial conditions requiring an L-type 50 Ω , 500 kHz AC source, with one of the capacitors between 0 and 1000 pf capacitance and the other chosen by the models frequency search.

The model provided new values for suggested circuit components and showed the resultant range of reflected power fraction (black), power factor (red) and normalized impedance (blue) should those components be chosen. The figure shows the frequency response of the reflected power (black) is relatively narrow around 500 kHz but the power factor (red) remains above 90 % from 0 kHz to 500 kHz. The shoulder of the normalized impedance (blue) is equivalent here to 50 Ohms at 500 kHz. This means that while the optimal circuit design was for 500 kHz here, a lower efficiency match could also occur at lower frequencies using these suggested components.

Using this model it can quickly determined whether or not a circuit can achieve a zero reflected power frequency for a given set of initial components and how wide the power factor can be made. These results can be informative prior to purchasing expensive components or quantify equipment already in use if an expensive network analyser is not available.

2.3 Plasma Probe Diagnostics

This section introduces first the theory and then measurement methodologies for the Langmuir probe and the hairpin probe plasma diagnostics. The physics for both diagnostics will be introduce briefly in turn and calibration results which establish the validity of each technique will be shown.

2.3.1 Langmuir Probe Theory

While the use of electrodes inside a plasma discharge had been around since the early 20th century from early pioneering works from Stark and others [58], it was Irving Langmuir and Harold Mott-Smith who were the first to develop a theory of measuring particle populations using a 'sweep' of voltages applied to an electrode from positive to negative bias [59]. A Langmuir probe is the term used simply for a plasma exposed electrode which draws a small amount of current from the plasma; when it is biased positively it will mostly draw negative charges, when biased negatively it will mostly draw (neutralize) positive charges. The probe can still draw same-polarity charges if the energy of the particle is enough to overcome the retarding electric field of the probe i.e if $E_{particle} > e(V_p - V_{probe})$ where V_p is the plasma potential and V_{probe} is the voltage applied to the Langmuir probe electrode. The symbol for the voltage difference at this minimum particle energy is often written as ϵ in Langmuir probe literature and it changes as the probe is swept from negative to positive voltages.

The total current draw on an exposed electrode for electrons and ions in a

plasma can be given by [60]:

$$I_{probe} = eA \left(\frac{-n_0 \bar{v}_e}{4} \exp \left(\frac{e(V_{probe} - V_p)}{kT_e} \right) + n_s u_B \right) \quad (2.4)$$

where A is the probe tip area, n_0 is the plasma density in the bulk, \bar{v}_e is the average electron speed, V_{probe} is the bias voltage applied to the probe tip, n_s is the sheath plasma density and u_B is the Böhm velocity. The current draw to the probe is primarily a function of the electron density, bias voltage and electron velocity.

In inductive systems such as the ICPS, the use of an AC amplifier creates a RF oscillation in the plasma potential amplitude (V_{RF}) at the driving frequency (13.56 MHz) and its harmonics. This RF oscillation modifies the V_p term in Equation 2.4 with a non-linear time varying contribution in the exponential term by the addition of $V_{RF} \cos(\omega t)$. Since the sweep rate of the probe is generally lower than the driving frequency of the generator, the RF interference can distort the shape of the IV curve throughout the Langmuir probe sweep. This 'RF noise' is visible on an oscilloscope and can be measured using fast Fourier transforms. The RF contribution in the ICPS and the use of passive compensation to reduce it will be discussed in the next section (Sec. 2.3.2).

Many plasma properties may be calculated from the IV curve such as electron density (n_e), ion density (n_i), electron temperature (T_e) and the electron energy distribution function (EEDF). The versatility of plasma parameters which the Langmuir probe can measure is why it is still the most common plasma diagnostic tool.

Conductive and dielectric surfaces which are plasma exposed and not connected to any other potentials are said to be at an equilibrium 'floating' potential with respect to ground where no net current is drawn. The floating arises due to a conservation of flux between positive and negative charges and the floating potential of a conductor is always negative with respect to the plasma potential in an electron-ion plasma since $T_e > T_i$ and $m_e < m_i$. The electron and ion flux to plasma exposed surface can be given by [60]:

$$\Gamma_e = \frac{-n_s \bar{v}_e}{4} \exp \left(\frac{e(V_f - V_p)}{kT_e} \right) , \quad \Gamma_i = n_s u_B \quad (2.5)$$

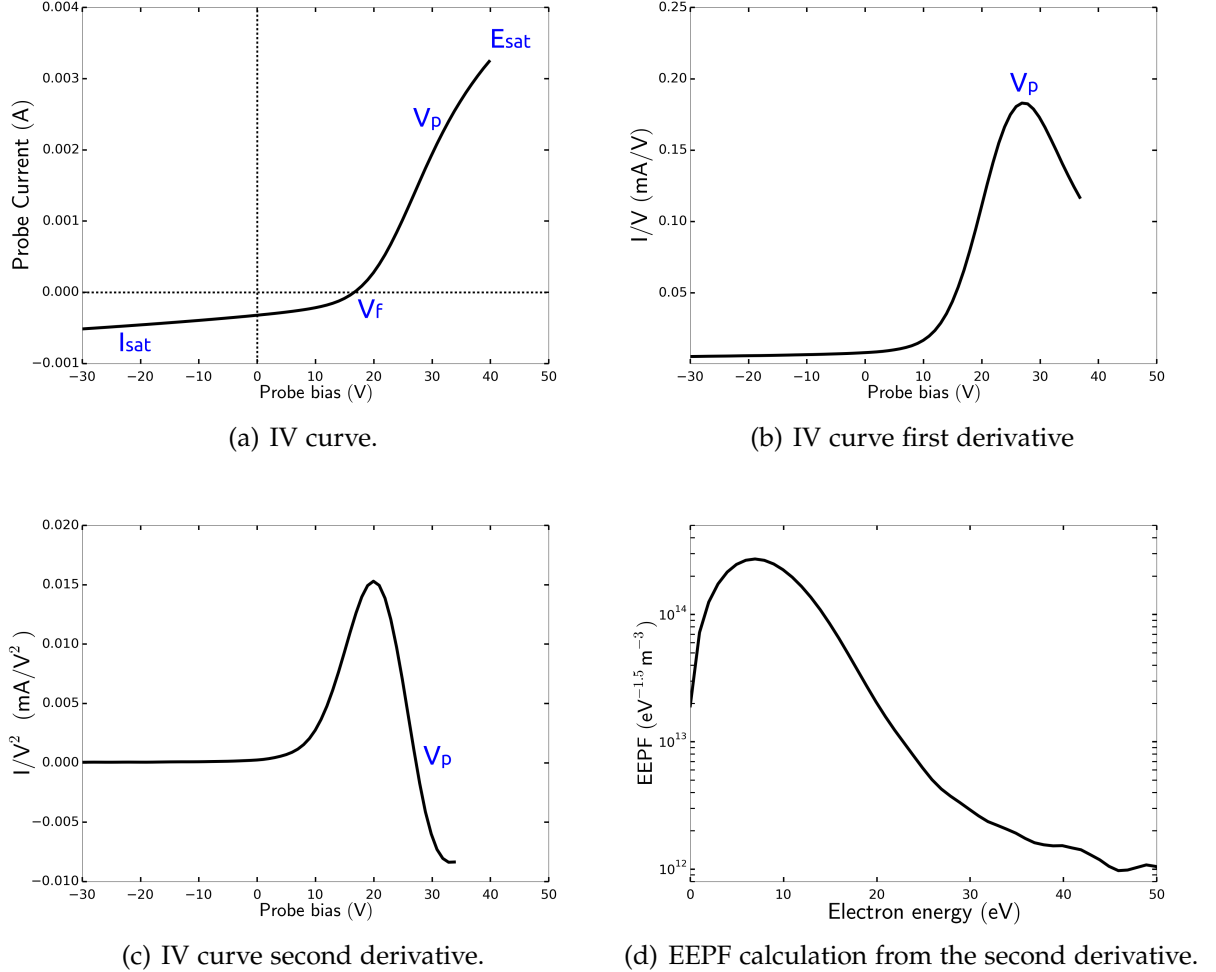


Figure 2.9: Compensated Langmuir probe measurements in the ICPS without a filter in hydrogen at 50 mtorr 200 W.

where V_f is the floating potential. Since the ion and electron fluxes at the wall must balance we can equate the terms in Equation 2.5 and substitute in the Böhm velocity and solve for this floating potential:

$$V_f = \frac{-k_B T_e}{2e} \cdot \ln \left(\frac{2\pi m_e}{m_i} \right) \quad (2.6)$$

The floating potential of a surface is then simply a constant factor multiplied by the electron temperature. For plasmas with multiple ion species the floating potential becomes a function of the average ion mass in the vicinity of the surface.

Figure 2.9 shows examples of Langmuir probe data from the ICPS taken at $x = 2$ cm downstream of the antenna. The first figure (Fig. 2.9(a)) shows a typical Langmuir probe sweep from inside the plasma where the voltage axis shows the applied bias to the probe tip and the y-axis shows current drawn from the plasma at that voltage. At large negative biases the probe draws positive ion current in the so called ion saturation regime (I_{sat}). At higher voltages the current draw is zero on the probe indicating the floating potential of the plasma (V_f) has been reached. The 'knee' of the IV curve occurs when the exponential current draw above the floating potential changes indicating the plasma potential (V_p). At higher positive biases the electron current to the probe saturates in the so called electron saturation regime (E_{sat}). Depending on plasma conditions, the collection radius of the probe may not fully saturate and increasing biases continue to draw more current in the I_{sat} or E_{sat} regime as the sheath around the probe expands with increasing voltage. This can be problematic if these regions of the profile are being used to calculate the ion densities and electron densities and other techniques are not employed to verify the results.

Figure 2.9(b) shows the first derivative of the IV curve where the 'knee' of the plasma potential is obvious as a peak. Figure 2.9(c) shows the second derivative of the IV curve where the zero crossing represents the plasma potential and the distance from the peak and the zero crossing can be used to assess the RF effect on the profile. RF interference of the probe broadens the knee area of the IV characteristic more prominently than other areas of the profile as measurements near the plasma potential represent the current draw primarily from low energy particles. Figure 2.9(d) shows the resultant EEPF from an integration of the second derivative from the plasma potential to the ion saturation region. The rounding of the low energy region is indicative of RF interference.

The method used to calculate the electron energy distributions (Fig. 2.9(d)) using the Langmuir probe is the Druyvesteyn method. In 1930 a seminal paper from Dutch plasma physicist Mari Johan Druyvesteyn first demonstrated the ability to obtain a map of the electron population inside a plasma using a Langmuir probe [61] although preceding work from Mott-Smith and Langmuir was arguably the catalyst. The Druyvesteyn method is still the most common way of measuring electron populations inside plasmas. Measurements of electron populations are important as fast moving electrons exhibit increased ionization and atomic excitations processes within the plasma while populations of slow moving electrons instead favour recombination and elec-

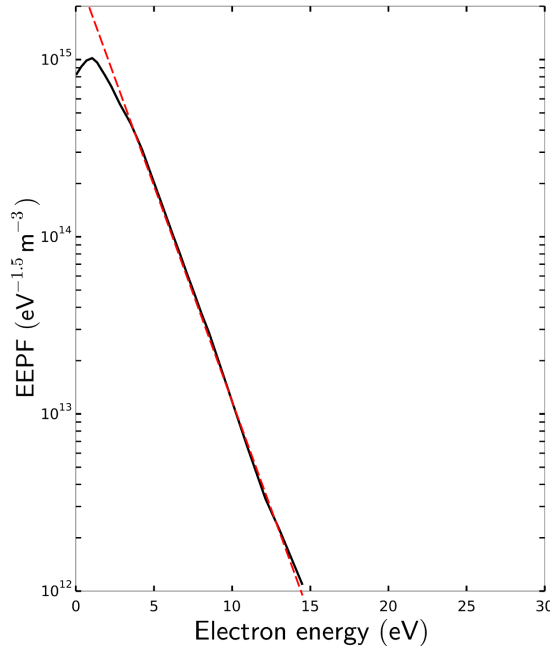


Figure 2.10: Example EEPF with an 2.17 eV effective electron temperature fit. The low energy resolution here is indicative of successful RF compensation.

tron attachment events [62] [63]. The EEPF can highlight both high and low energy populations of electrons and this is of particular interest when using magnetic filters and investigating negative ion formation.

The electron energy distribution function (EEDF) was measured along the axis of the ICPS tube at 1 cm intervals for both argon and hydrogen using the Druyvesteyn method (Eqn. 2.7). The resulting function was then normalized by the energy at each voltage step $\epsilon = e(V - V_p)$ to produce an electron energy probability function (EEPF) for each measurement (Figure 2.9(d)). The EEPF is used throughout this work as the effective electron temperature of the population can be calculated from these profiles.

The number of particles N with energy ϵ in the vicinity of the probe was calculated from the IV characteristic using the Druyvesteyn equation:

$$N(\epsilon) = \frac{2d^2 I(V)}{dV^2} \cdot \frac{1}{eA} \cdot \sqrt{\frac{2m_e(V_p - V)}{e}} \quad (2.7)$$

Equation 2.7 was used to produce the EEDF where the function $I(V)$ is the current drawn at each voltage (V) on the IV characteristic. The EEPF is constructed the same way as above but removing the electron energy term ($V_p - V$) for each step. If the plasma is sufficiently collisional, these EEPF profiles will yield Maxwell-Boltzman distributions of the form:

$$f(\epsilon) = \frac{2}{\sqrt{\pi}} \sqrt{\frac{\epsilon}{kT_e}} \cdot \exp\left(-\frac{\epsilon}{kT_e}\right) \quad (2.8)$$

Taking the inverse slope on a log plot of these distributions yields the effective electron temperature $T_e(\text{eff})$ for the population (Fig. 2.10). This method of the inverse slope was used for all electron temperature measurements and was found to have an error of around $\pm 5\%$ due to the choice of slope interval taken on the EEPF.

2.3.2 Langmuir Probe Construction and RF Compensation

The Langmuir probe used in the ICPS consisted of a custom hollow stainless steel rod housing measuring 1 m long and 7 mm in diameter. The rod was inserted from the diffusion chamber side of the apparatus and into the source tube along the central axis. The probe shaft was vacuum sealed and movable in the x-direction while maintaining the vacuum to make axial measurements of the plasma along the length of the source. Inside the housing a LMR-100A shielded coaxial cable was used as the primary conductor. At the rear of the probe a vacuum sealed BNC connector was installed to connect the probe to measurement equipment such as the Impedans ALP sweeper or oscilloscope or the photodetachment circuit. The coax shielding was soldered onto the grounded end of the probe at the rear BNC connector to prevent static build up. At the front end of the Langmuir probe on the plasma exposed side, the core of the cable was soldered to a custom made tunable compensation circuit (Fig. 2.11). The plasma exposed probe tip on the end of the probe was a 0.05 mm radius, 7 mm in length tungsten wire.

An Impedans ALP unit was used as a remote controlled voltage sweeper for the Langmuir probe measurements. The sweep parameters such as sweep rate and number of averages was controlled via software and the output of each set of IV measurements was saved to CSV files for post analysis.

During a typical voltage sweep, the current drawn at a given voltage was

recorded and a current (I) to voltage (V) characteristic curve (IV curve) was constructed from averaging multiple sweeps from negative bias voltages to positive bias voltages.

The passive compensation was a small hand-made tuned circuit to mitigate the effect of RF on the probe measurements at 13.56 MHz and the first harmonic of 27.12 MHz. A series of tunable capacitors and inductors in parallel were incorporated just behind the probe tip which resonate at the driving frequency of the source and its first harmonic (Fig. 2.11(b)). A compensation electrode was placed in the vicinity of the probe tip and was AC coupled to the components via a capacitor. The ‘notch filter’ circuit produces up to 100 dB attenuation at the two frequencies primarily responsible for the RF interference (Fig. 2.11(c)), however this value represents only the bench top rather than the *in situ* attenuation of the chokes. When the choke circuit was attached in series inside the probe shaft and the probe was inserted into an operating plasma environment several issues can still cause signal quality degradation such as: the choke tuning range being temperature shifted off-frequency, parasitic capacitances between the choke, the shaft and grounded surfaces, as well as interference from displacement currents.

In addition to the previously mentioned criteria of the probe tip radius ($r_p/r_L \ll 1$) it has been shown that for EEDF measurements that the main criteria for producing reliable measurements is that the RMS value of RF interference on the probe should not exceed three times the electron temperature [64].

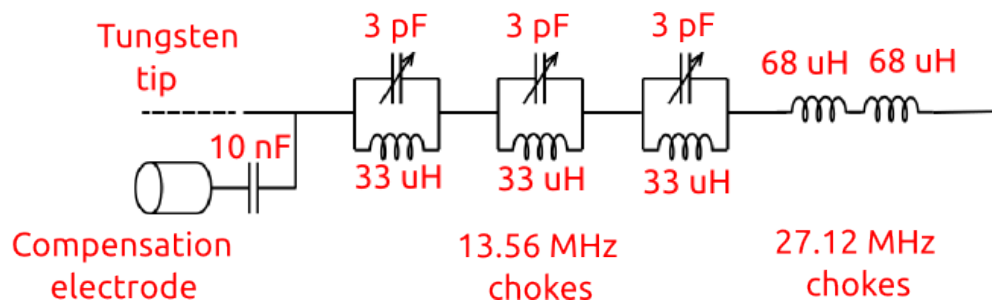
The plasma collisionality of the sheath surrounding the Langmuir probe tip can also affect current draw at higher densities. The sheath collisionality term Ψ_s is a measure of the collisional sheath effect on the EEDF given by:

$$\Psi_s = \frac{4r_p}{3\lambda_e} \cdot \frac{r_l}{2r_p} \quad (2.9)$$

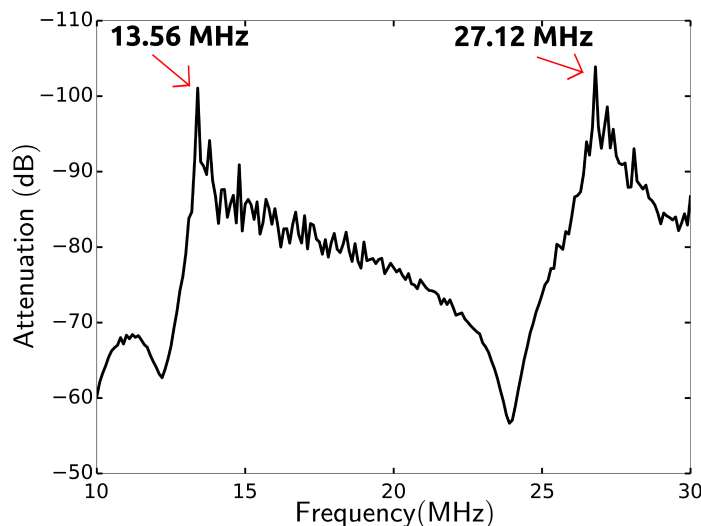
where λ_e is the electron mean free path and r_p and r_l and the probe tip radius and length respectively. Across the operating range, the effects of sheath collisionality were calculated to be insignificant with Ψ_s values of at most only 0.014 were found across the parameter space [65]. Additionally other probe considerations summarized by Godyak & Demidov for reliable EEDF measurement were also satisfied [66].



(a) The front of the compensated Langmuir probe showing the three driving frequency chokes and the two first harmonic self-resonant inductors.



(b) Choke circuit diagram of a).



(c) Network analyzer attenuation spectrum for the chokes (not *in situ*).

Figure 2.11: Compensated Langmuir probe photograph, circuit diagram and network analyser measurement of choke attenuation.

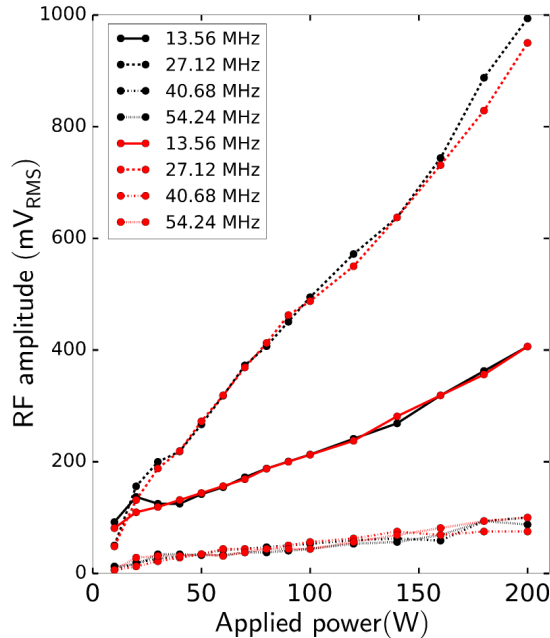
2.3.3 Radio Frequency Interference

Prior to adding the compensation circuit to the Langmuir probe, measurements were made with a floating uncompensated probe to characterize the degree of RF interference in the ICPS.

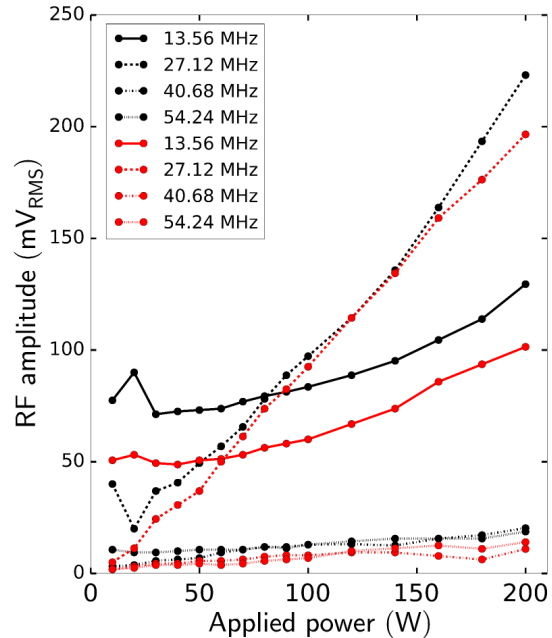
Several centimeters from the antenna the IV measurement sweeps taken in the ICPS show that each sweep is highly repeatable and time invariant on the order of microamps (μA) meaning that averaging the sweeps was not distorting the overall characteristic. However probe measurements taken close to the antenna, the RF oscillations in the plasma potential cause a voltage displacement in the characteristic which is seen to widen the knee of the IV curve and affects subsequent analysis of the low energy electron profile. The RF 'noise' is mediated via capacitative coupling through the probe sheath and standing waves form within the sheath generating harmonics in the current draw. The RF currents can flow to other capacitive paths before being captured on the oscilloscope and change non-linearly when a bias is applied to the probe. This means that using a floating probe to take RF noise measurements represents a minimum level in the RF experienced by the probe when compared to operating it with a bias sweep.

Figure 2.12 shows the results from Fourier transforms of the floating potential oscillations as a function of power and pressure. Figure 2.12(a) shows the RF amplitude as a function of power near the antenna at $x = 1 \text{ cm}$ using argon. The RF amplitudes for the fundamental (13.56 MHz) and harmonics are seen to vary in the ICPS with the first harmonic at 27.12 MHz seen to dominate across all applied powers and it accounts for more than double the RF noise generated by the fundamental mode at this location. At this location there is no effect of the magnetic filter on the RF. The transition from the capacitive E-mode to the inductive H-mode occurs in argon at very low powers ($< 25 \text{ W}$) and this transition is seen to not strongly affect the RF.

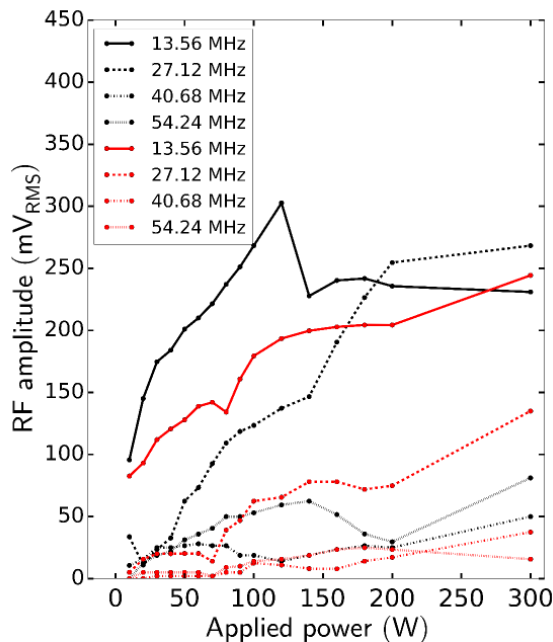
Figure 2.12(b) shows the RF amplitudes to the probe for argon downstream at $x = 5 \text{ cm}$ which is directly underneath the magnetic filter. The fundamental mode dominates at lower powers before the first harmonic begins to take over as the dominant RF noise source above 50 W. The effect of the magnetic filter on the RF in argon is seen to be limited, although interestingly the magnetic filter is seen to affect only the fundamental RF mode at this $x = 5 \text{ cm}$ location and is seen to reduce its amplitude by around 35%. Note the reduction in



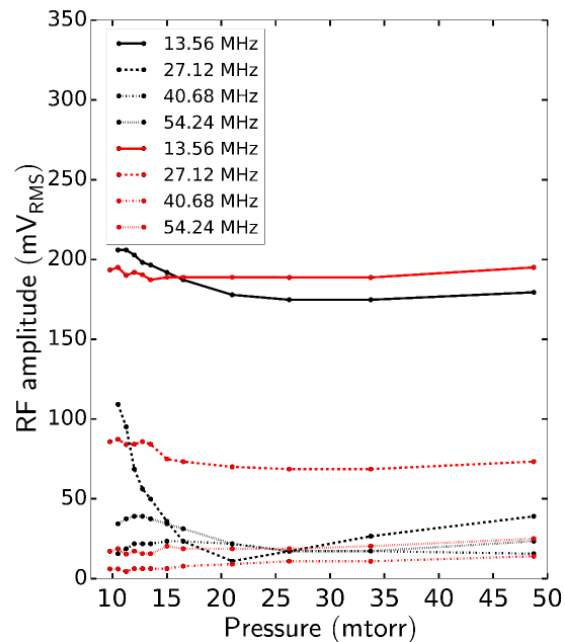
(a) Argon RF oscillation amplitudes and three harmonics at $x = 1$ cm downstream of the antenna. With the filter (red), without the filter (black).



(b) Argon RF oscillation amplitudes and three harmonics at $x = 5$ cm downstream of the antenna. With the filter (red), without the filter (black).



(c) Hydrogen power dependence RF at $x = 5$ cm downstream of the antenna. With the filter (red), without the filter (black).



(d) Hydrogen pressure dependence of RF at $x = 5$ cm downstream of the antenna. With the filter (red), without the filter (black).

Figure 2.12: Power and pressure dependence of the RF at two positions in the source. Fast Fourier transform measurements of the amplitude of RF plasma oscillations comparing the magnetic filter in argon at 10 mtorr, 200 W.

overall RF amplitudes here at $x = 5$ cm compared to the $x = 1$ cm profiles. This is the reason why even with RF compensation circuitry, measurements near the antenna in the ICPS using a Langmuir probe were difficult, especially for sensitive measurements such as the EEPF.

The two figures (Fig. 2.12(c) and Fig. 2.12(d)) show the results for hydrogen. the first figure (bottom left) shows the pressure dependence of the RF under the filter region at $x = 5$ cm, and the second (bottom right) shows the pressure dependence for hydrogen at the same location.

The RF power sweep under the filter for hydrogen shown in Figure 2.12(c) shows far more complexity in the RF amplitudes than in argon. Importantly, the magnetic field is seen to reduce the RF more strongly in hydrogen than argon and the reduction occurs for both the fundamental mode (13.56 MHz solid lines) and first harmonic (27.12 MHz). This result shows that Langmuir probe measurements which are sensitive to the RF noise such as the EEPF can be improved by the presence of the magnetic filter.

Figure 2.12(d) shows the pressure dependence of the RF at $x = 5$ cm downstream for hydrogen. With the exception of the first harmonic without the magnetic filter in place (27.12 MHz, black) increasing the pressure is not seen to affect the RF generally.

2.3.4 Current Depletion and Magnetization

When operating a Langmuir probe in the presence of a magnetic field, the ratio of the probe tip radius to the Larmor radius must be less than 1:1 to prevent localized electron depletion near the probe tip [67]. For the strongest applied magnetic field in these experiments (250 Gauss at $x = 5$ cm) and at the lowest electron energy (0.2 eV) the Larmor radius is approximately 0.07 mm. With a probe tip radius of 0.05 mm the so called 'thin probe criteria' of $r_{probe} / r_L < 1$ is satisfied.

To determine the effect of probe tip orientation on the Langmuir probes current draw, a 'dogleg' L-shaped probe tip was used attached to an uncompensated Langmuir probe. Measurements were taken at 1 cm intervals along the x-axis of the source tube and the probe was biased at a set voltage using

batteries to bias the probe in either the ion saturation or the electron saturation region (Fig. 2.13). The current was compared at 10 mtorr and 50 mtorr pressure with and without the filter in place.

The electron saturation profiles are shown in Figure 2.13 at 10 mtorr and 50 mtorr (top left and top right). The unfiltered profiles (black) show no dependence of current draw on tip orientation with the profiles lying directly on top of each other and not able to be distinguished. This is indicative of electron behaviour in an unmagnetized isotropic plasma. With the filter attached (red profiles), the current draw shows a dependency on probe tip orientation with a depletion in the current draw seen in the parallel orientation. This is indicative of magnetized electrons which are tightly bound to the transverse field lines at both 10 mtorr and 50 mtorr. The electrons are seen to be magnetized from $x = 3$ cm onwards and continues downstream of the filter.

The ion saturation profiles at 10 mtorr and 50 mtorr are shown in Figure 2.13 (bottom left and bottom right). While the ions can become magnetized at lower pressures near the magnetic filter, the ion saturation profiles show no dependency on probe tip orientation as their Larmor radii across all the magnetic field strengths is always greater than 1.5 mm allowing the thin probe tip to collect them in either parallel or perpendicular probe tip orientation with respect to the magnetic field lines.

The higher upstream electron saturation current at 10 mtorr compared to 50 mtorr is not due to higher electron densities but rather due to higher upstream electron temperatures altering the current draw. This will be shown in Chapter 4 with the measurements of electron densities and electron energy populations. From this data, the Langmuir probe orientation was chosen to be perpendicular to the field lines for all following measurements to ensure current depletion was not an issue when measuring through the center of the magnetic filter.

A comparison of the Larmor radii for both hydrogen and argon is shown in Figure 2.14 for the range of temperatures seen in the ICPS for hydrogen (left) and argon (right) plasmas. The ions for both species are above the thin probe limit for all magnetic fields and the Larmor orbits for argon are higher than hydrogen ions due to the higher mass nucleus. The ion mass will be shown to play a role in the cross field transport of plasma through the filter which will be discussed in Chapter 4.

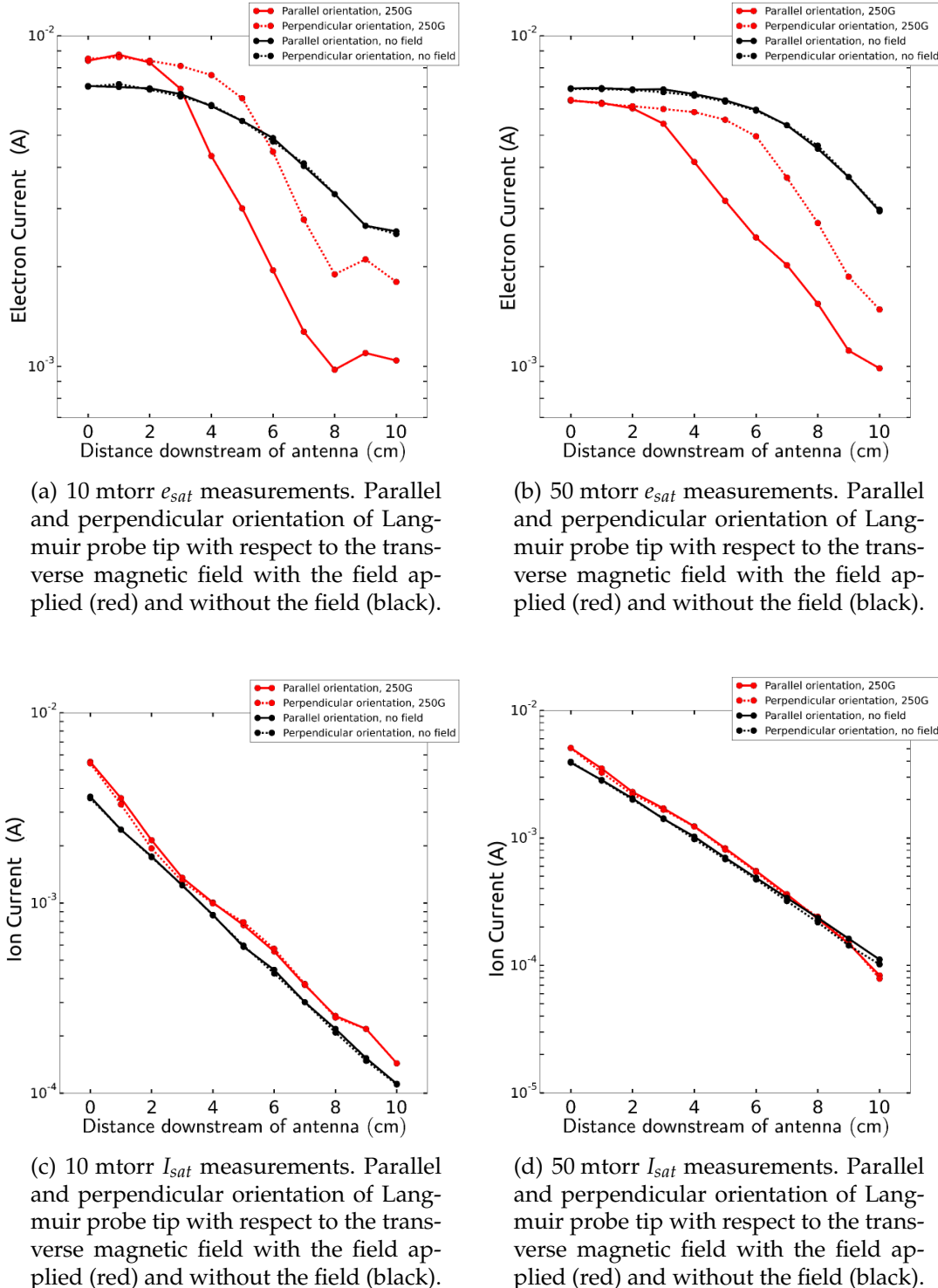


Figure 2.13: Dependence of the probe tip orientation for the electron saturation current and the ion saturation current at 10 mtorr and 50 mtorr in hydrogen.

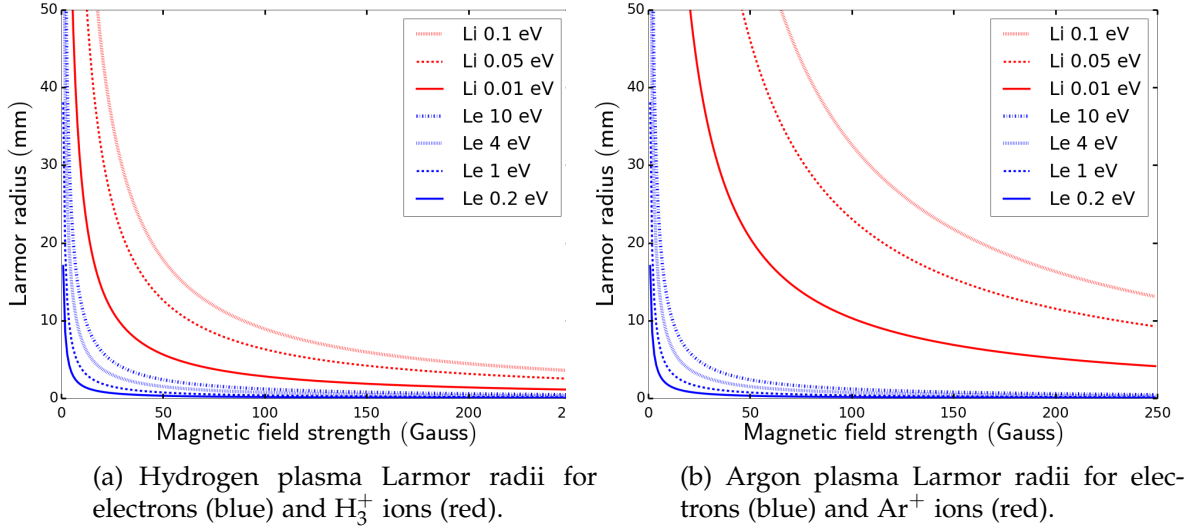


Figure 2.14: Hydrogen and argon cyclotron orbital radii across the range of magnetic fields found in the ICPS.

2.3.5 The Hairpin Probe

The measurement results of electron density profiles using the hairpin probe will be shown later in Chapter 4 with the theory and background for the technique to be presented here first.

The basic plasma physics properties and background related to the hairpin probe measurement will be shown in Sections 2.3.6 and 2.3.7. The methodology and operation will be covered in Section 2.3.8 and the limits of the hairpin probe technique will be covered in Section 2.3.9.

In a landmark paper from 1976, Stenzel showed that a simple inductive probe could be built for a direct measurement of the electron density inside a plasma [68]. The hairpin probe measures the relative electric permittivity of a material surrounding two ends of 'U' shaped wire pin. When a high frequency AC signal is sent through a loop positioned near the pin parallel to its surface, a varying AC current of the same frequency is magnetically induced within the pin perpendicular to the changing magnetic flux lines from the loop. If the AC frequency matches the resonant frequency of the hairpin, an electrical standing wave is formed along the pin and a noticeable drop in resistance to the AC coupling is seen. The frequency at which this occurs corresponds to the resonant frequency of the pin which can change depending on the electric

permittivity of the medium surrounding it. This change in electric permittivity can then be related to an electron density within the plasma giving the ability of the probe to sense plasma densities. The hairpin probe is considered one of the most direct and reliable methods of measuring plasma density.

2.3.6 Hairpin Probe Theory

The electric permittivity ϵ which also called the dielectric constant (κ) is a dimensionless measure of the opposition of a material to an externally applied electric field. It is related to the polarizability of any substance whether it be neutral atoms, a solid material or free charges and it originates from the formation of dipole moments which counter the external field. In the case of the hairpin probe, the electrostatic wave (eg. the signal through the floating pin) is immersed in a dielectric medium (the plasma) and the speed of signal propagation is attenuated from c to c/ϵ_r where ϵ_r is the relative permittivity of the dielectric medium surrounding the pin.

The hairpin measurement can be related to a plasma density without any knowledge usually required for the density measurement such as electron temperature, ion saturation current, or ion flux at the sheath edge. In this respect the hairpin measurement can make a reliable indirect measurement of electron density within a plasma [69]. The quarter-length resonant frequency (f_r) of an AC signal travelling at the speed of light c along a wire of length L is:

$$f_r = \frac{c}{4L\sqrt{\epsilon}} \quad (2.10)$$

The way the hairpin probe can sense the plasma density is through changes in this dielectric permittivity. The experimental relationship between the hairpin f_{res} and the plasma density can be derived from first considering the electric dipole moments \vec{P} from n gas atoms induced by an electric field \vec{E} :

$$\vec{P} = n \cdot \frac{e^2}{m_e(\omega_0^2 - \omega^2)} \vec{E} \quad (2.11)$$

where ω_0 is a an excitation frequency and ω is the variable driving frequency of the external electric field \vec{E} . Noting that the ne^2/m_e here looks similar to

the square of the plasma frequency (see Appendix B for a plasma frequency derivation) but is missing the ϵ_0 . Since the the dipole moment per unit volume can be represented in terms of permittivity as:

$$\tilde{P} = \epsilon_0(\epsilon_r - 1) \vec{E} \quad (2.12)$$

Combining Equations 2.11 and 2.12 and setting $\omega_0 = 0$ gets us close. Now imagining the varying electric field from equation 2.11 originates from a resonant standing wave frequency at the end of the hairpin tips, then $\omega \rightarrow f_{res}$. Solving for ϵ_r yields the relative permittivity of a plasma:

$$\epsilon_r = 1 - \frac{f_{plas}^2}{f_{res}^2} \quad (2.13)$$

where f_{res} is the resonant frequency of the hairpin surrounded by a plasma of relative permittivity ϵ_r . Substituting Equation 2.13 into Equation 2.10 shows the relationship between the plasma frequency, resonant pin frequency and vacuum frequency as:

$$f_{res}^2 = f_{plas}^2 + f_{vac}^2 \quad (2.14)$$

Finally this allows us to solve for the number density (n) of particles by expanding the plasma frequency f_{plas} term. Typically these numbers lie within the GHz band and so an electron plasma density (n_e) can be quickly calculated during a measurement from:

$$n_e = \frac{(f_{res})^2 + (f_{vac})^2}{0.81} \cdot 10^{16} \quad (2.15)$$

where f_{res} and f_{vac} resonance frequencies are in units of GHz.

2.3.7 Electric permittivity in magnetized conditions

It is important to consider the effect of magnetized plasmas have on the electric permittivity as the hairpin probe is sensitive to changes in the electric permittivity of the plasma rather than the density directly. Changes in the electric permittivity of the plasma can occur without changes in density and this can lead to errors when making the density calculation using the hairpin

probe.

If a medium resists an electric field more strongly in one direction than another, the electric permittivity can no longer be described simply by one number ϵ_r and must be split into tensor components in three directions with respect to an external magnetic field. These components are parallel (ϵ_{\parallel}), perpendicular (ϵ_{\perp}) and co-perpendicular (ϵ_{\times}) [70] and can be expressed as:

$$\epsilon_r = \epsilon_0 \begin{pmatrix} \epsilon_{\perp} & -j\epsilon_{\times} & 0 \\ j\epsilon_{\times} & -j\epsilon_{\perp} & 0 \\ 0 & 0 & \epsilon_{\parallel} \end{pmatrix} \quad (2.16)$$

In a plasma this usually occurs in the presence of a magnetic field where the electrons gyrate in circular orbits perpendicular to the applied \vec{B} field with angular cyclotron frequency ω_{ce} such that the permittivity components in collisionless conditions can be given by:

$$\epsilon_{\perp} = 1 - \frac{\omega_{pe}^2}{\omega_{res}^2 - \omega_{ce}^2}, \quad \epsilon_{\times} = \frac{\omega_{ce}}{\omega_{res}} \cdot \frac{\omega_{pe}^2}{\omega_{res}^2 - \omega_{ce}^2}, \quad \epsilon_{\parallel} = 1 - \frac{\omega_{pe}^2}{\omega_{res}^2} \quad (2.17)$$

In the absence of a \vec{B} field in Equation 2.17, $\omega_{ce} \rightarrow 0$ and the dielectric tensor in equation 2.16 reduces to the unit matrix. From Equation 2.17 and Equation 2.16, the cold plasma dispersion relation for the relative permittivity can be calculated as [71]:

$$\epsilon_r = \sqrt{1 - \frac{\omega_{pe}^2}{\omega_{res}^2} \cdot \frac{\omega_{res}^2 - \omega_{pe}^2}{\omega_{res}^2 - (\omega_{pe}^2 + \omega_{ce}^2)}} \quad (2.18)$$

This new electric permittivity reduces to being a multiplicative correction factor of $1 - \frac{f_{ce}^2}{f_{res}^2}$ in front of Equation 2.15 when calculating the electron density. For the ICPS, the maximum magnetic field strength the hairpin probe experienced was 250 Gauss and the change in electric permittivity due to magnetization of the electrons equates to, at most, a 3% underestimate of electron density by the hairpin probe. This is supported by the parallel and perpendicular density measurements taken through the magnetic field which will be shown and discussed in the following section (see Fig. 2.18).

2.3.8 Hairpin Probe Design and Operation

A custom hairpin was constructed for use in the ICPS for electron density measurements. Several designs were tried which included trying multiple loops, different loop geometries, different types of coaxial cables and various pin positions and lengths before a final design was settled upon. Several coupling techniques were also developed to maximize the signal to noise ratio of the hairpin measurement and the new coupling result will be shown.

Figure 2.15(a) shows a schematic of the hairpin probe, Figure 2.15(b) shows a photograph of the tip and Figure 2.15(c) shows a photograph of the network analyzer used for the measurements. The Rohde & Shwarz ZVB 20 network analyser was used to capture the resonant hairpin probe data for measuring electron densities. A single LMR-100 coaxial cable was used for the measurement which was connected to the vector network analyser. One cable end was cut and the exposed cable core was looped onto the shielding forming the inductive loop at one end. Frequency sweeps of microwave signals were sent through the coaxial cable using the VNA. The signal was returned via the coaxial shielding with the VNA operating in S1-1 'reflection' mode. The loop and cable were inserted inside a thin glass tube before being inserted into the plasma chamber, thereby preventing any plasma contact to the cable and limiting RF coupling to the probe (Fig. 2.15(a)). The inside of the glass tube was at atmospheric pressure so the cable can be inserted and adjusted during the plasma discharge without breaking the vacuum. A tungsten 'U' shaped hairpin was adhered to the outside of the glass adjacent to the coupling loop and was plasma exposed. This type of hairpin probe is called a 'floating' probe as the resonant pin has no ground reference and is 'floating' with respect to the plasma. The design was chosen following the paper of Piejak *et al.*, [72] who compared many hairpin probe designs in RF discharges such as biased probes, AC/DC coupled probes where the floating probe design was shown to be superior for density measurements especially in RF driven discharges.

In the absence of plasma surrounding the hairpin wire, the signal can propagate freely along the wire and the relative permittivity is equal to 1 giving the 'vacuum' resonance frequency as simply $f_{vac} = c/4L$. When a plasma surrounds the hairpin wire, the electric permittivity decreases, and is measured as an upward shift in the resonance frequency of the hairpin resonance and is seen on the network analyzer. The difference between the vacuum frequency peak and the 'shifted' plasma-on frequency peak (f_{res}) gives the density measurement. This technique is not suitable for measuring changes in neutral

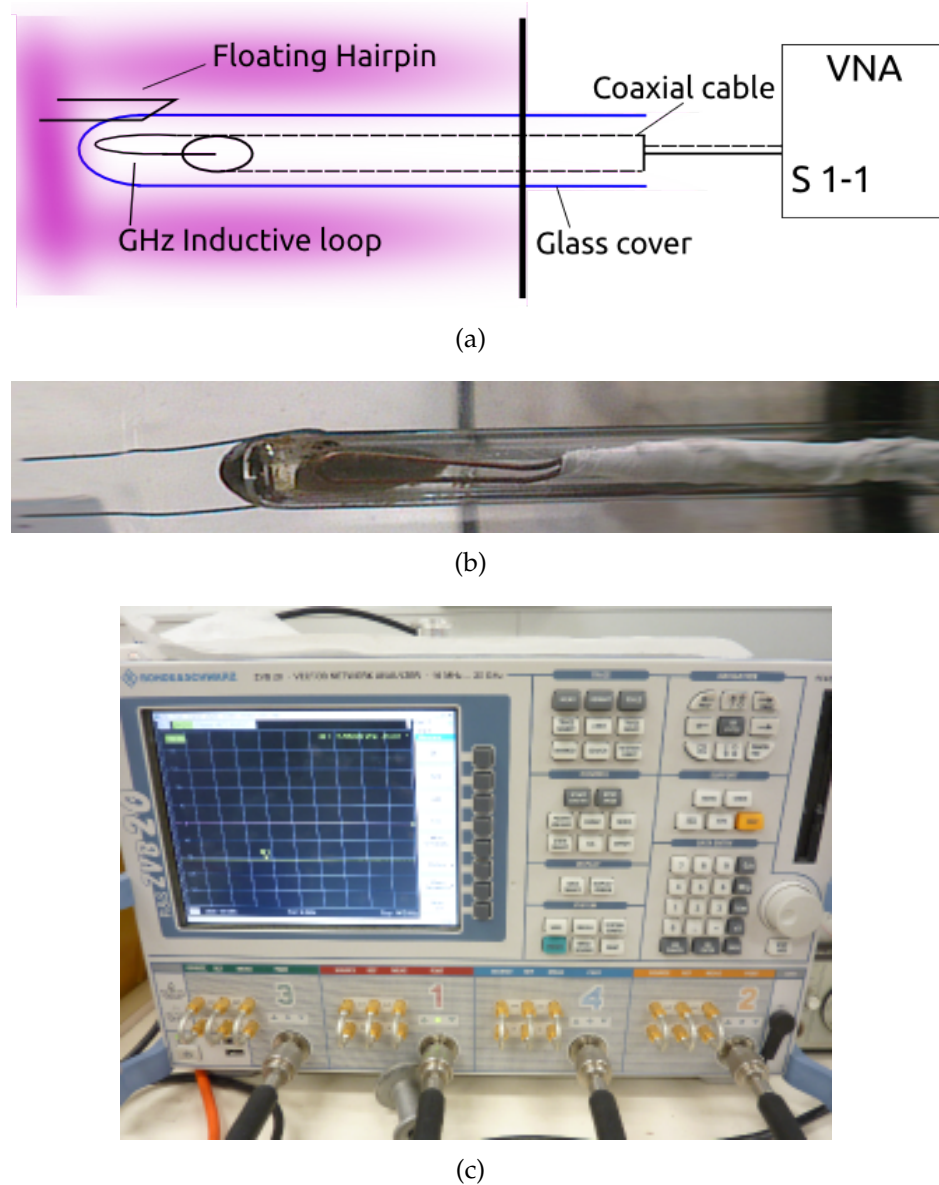


Figure 2.15: a) Schematic of the hairpin setup showing the plasma exposed hairpin, coaxial cable, pickup loop and connection to the VNA S1 port measurement. b) Photograph of the hairpin probe. Coaxial loop inside a glass tube with the floating hairpin adhered to the outside. c) Rohde & Shwarz ZVB 20 network analyser used for the hairpin probe measurements.

gas densities as the relative permittivity of gasses at lower pressures is approximately equal to 1 and there is no discernible shift in the signal from the reference vacuum resonance when increasing the gas pressure.

The pin length during these experiments was 2.11 cm giving a vacuum pin resonance frequency of 3.55 GHz and this corresponds to a theoretical maximum maximum measurable plasma density of approximately 10^{17} m^{-3} from the plasma frequency limit, however reliable measurements were found to be possible at higher densities outside of plasma frequency limit via evanescent coupling of the hairpin signal while operating below the plasma frequency. The option to use the hairpin probe in the evanescent regime is generally not mentioned in the literature and it was found produce reliable results and allowed for extended ranges of pin lengths to be used. The evanescent regime will be discussed further in Section 2.3.9.

The proximity of the loop to the hairpin was found to be important as the signal could vary an order of magnitude when moving the loop only a few millimeters from the pin. A single long loop design was finally used which was bent so it ran flush against the inside of the glass tube was used to place the loop as close to the plasma exposed pin as possible.

Due to the background noise associated with microwave band measurements, a subtraction of 'background' noise from signals was developed. In order to obtain a visible 'peak' in the hairpin resonance signal, the noise from the 1/4 wavelength self-resonant cable mode was the first subtraction. Typically the cable noise is saved as a background during the plasma 'off' period where only the vacuum resonance peak is present in the absence of a discharge [73] [74]. While this method works at low power and with short probes, the non-linear interactions between the cable and the plasma during the 'on' period is not taken into consideration and can result in wide resonance peaks at low resolution which were found to cause miscalculations of the plasma density.

To mitigate these common effects, a method was developed whereby the background subtraction was done while the pick-up loop was turned 90 degrees away from the hairpin which decoupled the cable and plasma noise from the hairpin measurement. The decoupled 90 degrees signal was saved in-situ with the plasma running and then the loop was re-coupled near the pin to be saved again. The comparison of this signal subtraction method are shown in Figure 2.16 during a high density argon discharge. Figure 2.16(a) shows

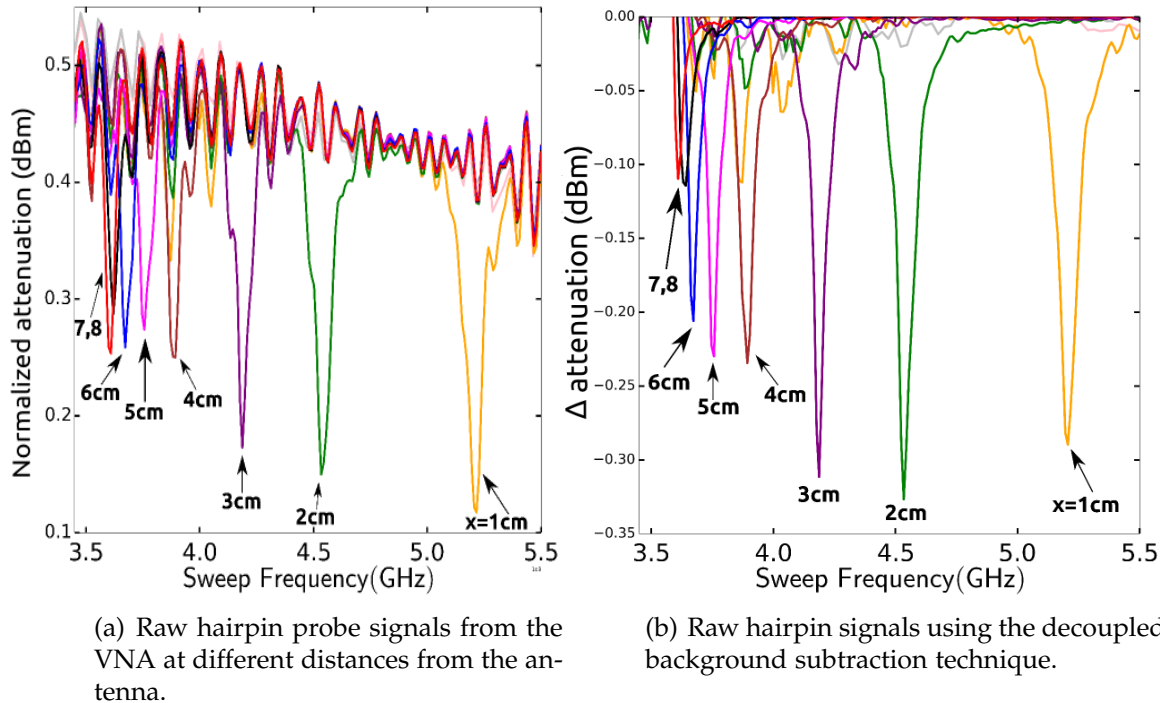


Figure 2.16: Comparison of raw signals from the hairpin probe without background subtraction to the 90 degree decoupling subtraction technique. a) raw signals b) signals with decoupled background subtraction. Argon at 5 mt, 200 W.

8 hairpin measurements without any subtraction at different locations along the source and Figure 2.16(b) shows the same positions with the 90 degree decoupling subtraction, note this method is best used to increase the signal to noise ratio in the low density (10^{15} m^{-3}) measurements from $x = 4 \text{ cm}$ through to $x = 8 \text{ cm}$.

The final probe design performed well under a wide range of pressures, powers and magnetic field conditions and showed high signal fidelity relative to other hairpin measurements [73].

A general criteria was developed for the minimum signal resolution for a hairpin measurement. To achieve reliable peak resolution each frequency step on the network analyzer sweep must be equal to, at most, a 1% change in the plasma density. Ideally there should be at least 10 steps per 1% change to resolve the full features of the density change. This minimum step size is dependant on the hairpin length and is summarized in Figure 2.17. The

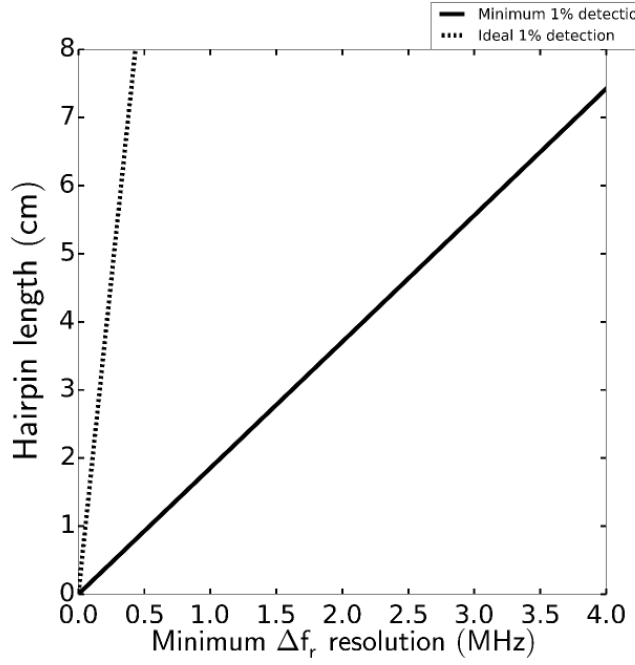


Figure 2.17: Step sizes of the VNA frequency sweep required to resolve 1% density changes. Solid line shows a single step size per 1% density change and the dotted line shows the ideal frequency step required for 10 steps per 1% change.

resolution steps used in this work were always within the ideal range of approximately 0.1 MHz per 0.1% density shift for a 2.5 cm pin.

Previous modelling of the hairpins resonant electric and magnetic field structure have shown that the fields are generally isotropic and peak at the end of the pin where the anti-nodes of the standing wave occur [75] [76]. The ability of the hairpin probe to operate well under anisotropic field conditions was found to be due to the shape of the electric field structure which forms between the end tips of the hairpin during resonance [76]. This modelling by Gogna showed that the open end of the hairpin is the most sensitive to changes in the dielectric permittivity and so the tip of the hairpin was considered the 'center' coordinate for all hairpin measurements in this work.

This indicates two desirable properties of the hairpin: the hairpin measurement is spatially sensitive at open ends of the tip and that the measurement should be robust to axial rotation of the pin within anisotropic conditions such as low pressure magnetized plasmas.

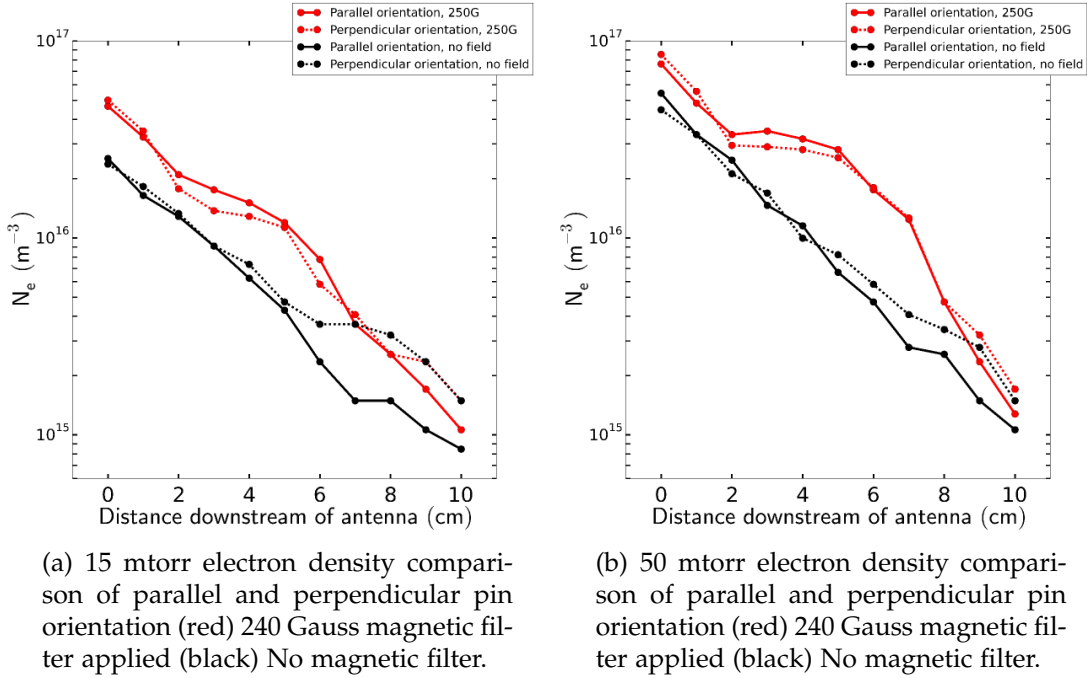


Figure 2.18: Axial electron density profiles through the source comparing pin orientation parallel and perpendicular to the magnetic field orientation. Hydrogen at 200 W.

To test the probes response to axial rotation under magnetized conditions in the ICPS (see Equation 2.18) axial profiles of the electron density was taken at 15 mtorr and 50 mtorr both parallel and perpendicular relative to the transverse magnetic field direction (Fig. 2.18). The hairpin density measurement was found to be largely unaffected by parallel or perpendicular measurement meaning that the probe is able to capture the value of the dielectric tensor regardless of orientation.

The figures show good agreement between density measurements through the filter under different orientations for both magnetized low-collisional pressures (10 mtorr) and higher collisional magnetized conditions (50 mtorr). Gogna & Karkari [73] performed similar experiments and showed that the hairpin probe is resistant to anisotropic permittivities through transverse fields up to 600 Gauss. This highlights one of the strengths of the hairpin probe; its robustness under magnetized \vec{B} field conditions. The increase in the downstream unfiltered profile density in Figure 2.18(a) was an accidental measurement due to an unstable capacitive coupling of the antenna to the chamber faceplate.

2.3.9 Limits of the Hairpin Probe

If the resonant frequency of the hairpin f_{res} is below the plasma frequency, then the signal energy is absorbed locally into the plasma and the pin should be unable to form a standing wave necessary for the measurement. However, this work shows that the pin resonant frequency f_{res} can remain below the plasma frequency and still make reliable measurements as the signal is only attenuated over the plasma skin depth δ which ranges between 2 cm to 10 cm for the densities seen in most ICP systems. This distance is far greater than the separation between the hairpin tip and so hairpin measurements below the plasma frequency can be made comfortable via this 'evanescent coupling' regime. Importantly this evanescent coupling was not found to shift the resonant peak but only degrade the quality of the peak with increasing density. At densities above 10^{18} m^{-3} this degradation becomes apparent as the skin depth for GHz microwaves becomes small with respect to typical hairpin separation distances. This is the primary drawback of the hairpin probe technique; that it is unsuitable for high density applications.

If the resonant frequency of the probe is above the plasma frequency, the probe can radiate electromagnetic waves and the electric permittivity between the pins can be sensed without the electric field being attenuated. If the pins are too far apart the pin will radiate but will not form a standing wave. If the pins are too close, the pin will be sensing the dielectric permittivity of the ion rich floating sheath around the pins rather than the permittivity of the bulk plasma and this results in an underestimate of the plasma density [69]. The sheaths surrounding the pins used in these experiments range from approximately 0.3 mm at high pressure to 1.8 mm at low pressure which equates to a pin-to-sheath separation ratio of 20:1 to 3:1 respectively across the pressure and power range of the experiments. Theoretical modelling and experiments show that at the separation ratio of 3:1, which occurs at low densities of approximately 10^{15} m^{-3} indicates that the density from the hairpin probe may be underestimated by up to a factor of two [72] at $x = 10 \text{ cm}$ downstream. This effect may be mitigated by a slight increase in densities seen just outside the diffusion chamber downstream possibly due to capacitive coupling of the antenna to the chambers faceplate.

2.4 Optical Emission Diagnostics

Measurements of the H₂ gas rotational temperature will be shown later in Chapter 4 Section 4.3 to correlate internal energy structure of the hydrogen gas to negative ion formation. The experimental setup, emission theory and spectral temperature fit methodology for these optical measurements will be presented here first.

Measurements were made using optical emission spectroscopy (OES) of the Fulcher- α emission band of H₂ to quantify the effect of the magnetic filter on the rotational energy of the background gas population and to determine the spatial distribution of energetic neutrals axially along the ICPS.

Optical emission spectroscopy of the Fulcher band is as well established technique and has been used across a variety of applications. including: planar ICP [77], electrodeless lamps [78], linear helicon [79], hollow cathode devices [80] and in NBI neutralizers [81]. Previous work using Fulcher band measurements for inductive plasma devices similar to the ICPS include: RF cycle heating [82] [77], plasma food sterilization [83] and afterglow sheaths [84].

Despite these wide applications, the number of measurements in ICP devices investigating the spatial effect of transverse magnetic fields on hydrogen gas temperatures are limited. Work in this area includes Takama & Suzuki [85] who measured gas temperatures through axial magnetic fields along the length of the discharge showing a decrease in gas temperature. Tsankov *et al.*, [86] used a pseudo-axial cusp field using a North-North magnetic configuration which showed no change in gas temperature. Fulcher measurements were also taken through a cusp magnetic field in the caesiated prototype Linac4 negative ion source which showed no major changes to rotational or vibrational temperatures [87]. Fantz *et al.*, [88] in 2006 measured a power and pressure sweep of hydrogen gas temperatures at a single position within the transverse filter region in their NBI test BATMAN source at high powers and showed that molecular vibrational temperatures were up to three times higher than the translational gas temperature. In this work, rotational temperatures will be measured along the source tube to determine the effect of the magnetic filter.

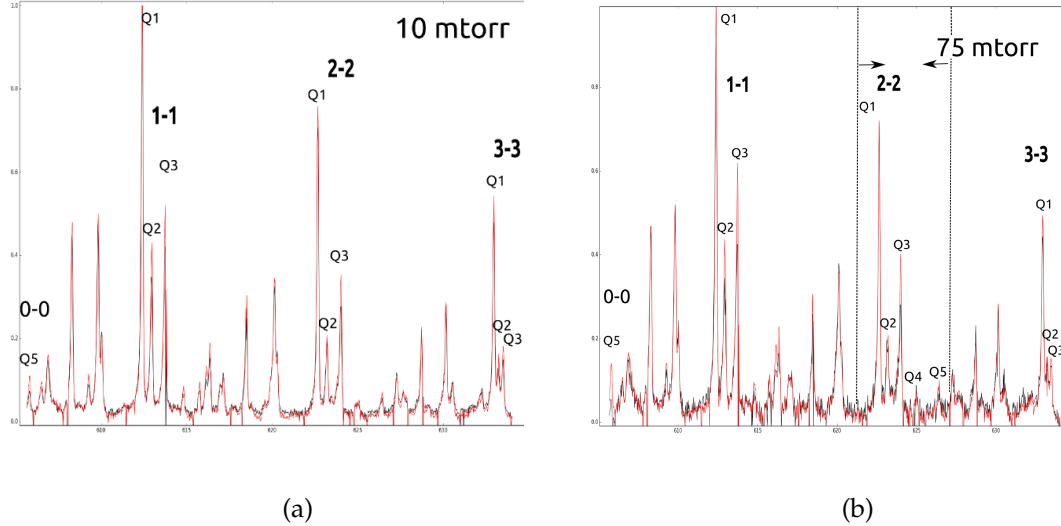


Figure 2.19: Experimental H_2 emission spectrum taken in the ICPS from 606 nm to 636 nm showing the rotational Q-bands for the $v = 0,1,2,3$ vibrational states. Note the alternating intensity due to nuclear spin degeneracy. Figures show magnetic filter applied (red) and without the magnetic filter (black) superimposed for each showing changes in emission intensity. a) is at 10 mtorr, b) at 75 mtorr. Measurements are determined from the relatively unperturbed $v = 2-2$ band.

2.4.1 Theory of the H_2 Fulcher Band

Neutral gas species temperature plays an important role in determining the plasma chemistry for many applications as the rate coefficient for chemical reactions is often a function of neutral gas temperature. For plasma enhanced chemical vapour deposition, the neutral gas temperature is a critical parameter in the fabrication process as the neutral gas temperature gradient within the chamber determines the relative chemical species densities produced [89]. Importantly for negative ion production, rotational gas temperatures are also closely associated with increased vibrational modes [90]. This is due to rovibrational coupling of angular momentum which requires that each change in vibrational state is accompanied by a change in rotational quantum number. However, in gas systems where vibrational changes from surface recombination effects dominate over bulk processes, the vibrational states can be measured as being independent of the discharge conditions [85] [86]. Generally however, vibrational temperatures of H_2 have been shown experimentally to linearly track the rotational/translation temperature for changes in both power and pressure in ICP NBI sources [91], Tokamaks [90] and low power

ICP systems similar to that in this work [84].

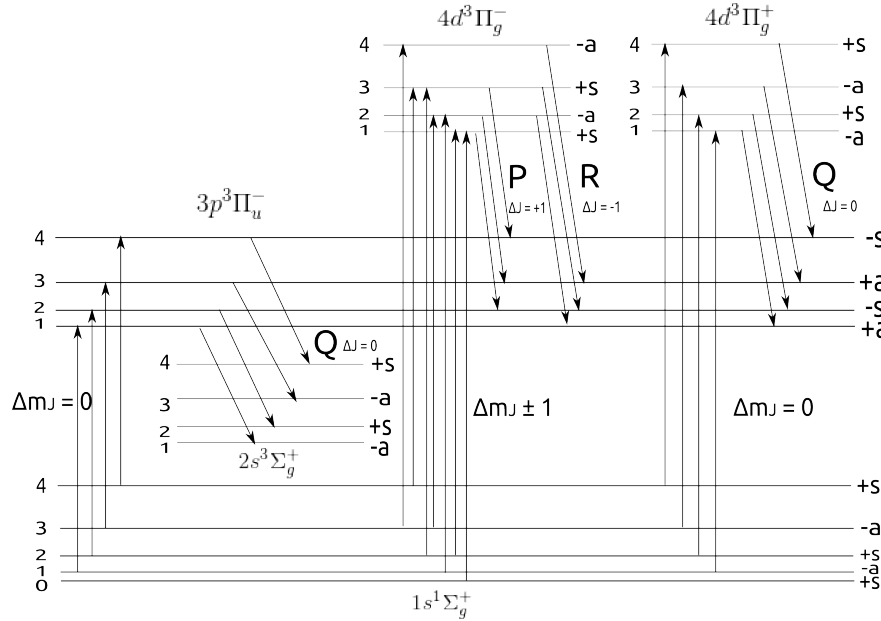
Trends in rotational temperatures can be extended to trends in vibrational temperatures and increased rovibrational states have been shown to strongly enhance negative ion formation both experimentally [12][63][92] and in model simulations [93][94].

2.4.1.1 Emission channels

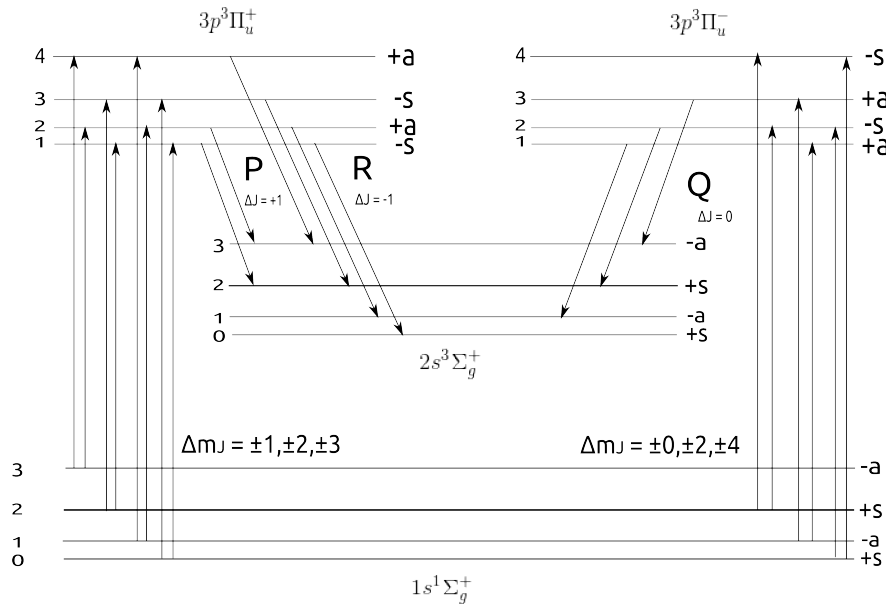
Appendix C defines the molecular term symbols used here and includes an introduction to molecular bonding, rotation, vibration and nuclear spin states with respect to H₂ and the Fulcher band. The theory for the emission channels here relates to the temperature fit application in Section 2.4.3

The Fulcher- α Q-branch lines can originate from several excitation levels in a spontaneous emission decay down to the 2s³ Σ_g^+ state, which occurs via the intermediate triplet state 3p³ Π_u^- . The intermediate state can either be populated from below via direct excitations from the ground 1s¹ Σ_g^+ state or from above via spontaneous decay from the higher state 4d³ Π_g^- through P and R channels and from the 4d³ Π_g^+ state via the Q channel (See Fig. 2.20(a)).

Figure 2.20(b) shows alternative channels for Fulcher- α emissions from the 3p level where 3p³ Π_u^+ decays into the 2s³ Σ_g^+ via P and R branches and 3p³ Π_u^- decays into the Q branch. Note the Δm_J changes which populate these states compared to those in Figure 2.20(a). The assumptions outlined in Section 2.4.4 requires that the primary population channel for the Fulcher emissions is from below via the $\Delta m_J = 0$ ground excitations shown in Figure 2.20(a). These transitions preserve the rovibrational ground state numbers through both the excitation and then decay to the final 2s³ Σ_g^+ state which is a key detail in determining the ground state rotational population. The assumption of the dominance of ground excitations rather than cascading emissions from above levels is part of the so called 'Coronal' equilibrium condition and it is generally fulfilled for most low density Maxwellian plasmas. This important assumption in emission channels for this diagnostic is discussed in detail in Section 2.4.4 with respect to the operating conditions of the ICPS measurements.



(a) Excitation pathways for the Fulcher- α emission. Each electronic state is split into rotational quantum numbers $m_J = 0, 1, 2, 3, 4$. Nuclear spin states s,a and +/- parity states are shown. Figure adapted from [82].



(b) Secondary pathways for the Fulcher- α emission for Δm_J transitions. Each electronic state is split into rotational quantum numbers $m_J = 0, 1, 2, 3, 4$. Nuclear spin states s,a and +/- parity states are shown. The Q-branch direct transition from $3p^3\Pi_u^-$ to $2s^3\Sigma_g^+$ emits Fulcher- α wavelengths while the $3p^3\Pi_u^-$ to $1s^1\Sigma_g^+$ produces P and R side bands. Figure adapted from [95].

Figure 2.20: .

While Figure 2.20(a) and Figure 2.20(b) show the primary channels for the Fulcher- α band emission, higher excitation states can also cascade downward to populate the Fulcher band as high as $4d\Sigma$, $4d\Pi$ and even $4d\Delta$ levels [82]. These levels are considered rare emission pathways and their influence on the overall Fulcher population is thought to be negligible at low densities and temperatures.

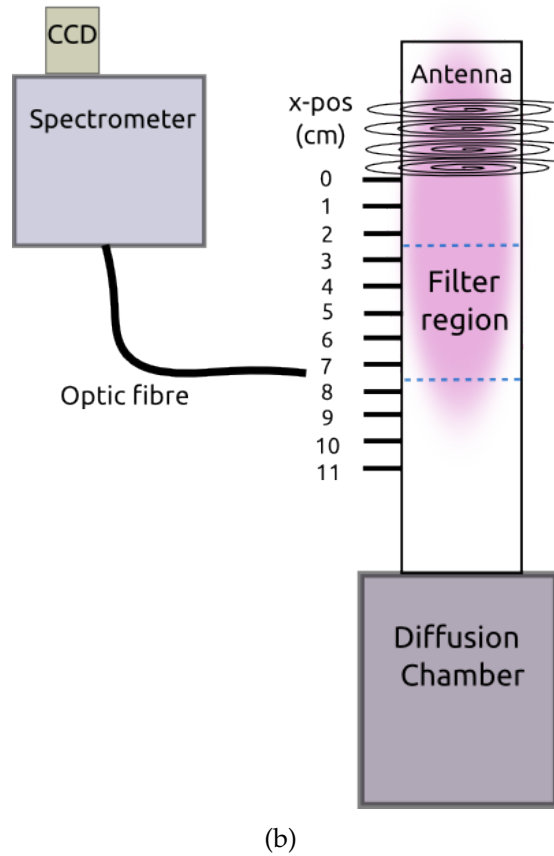
2.4.2 Experimental Setup

Measurements of the optical emission were taken along the length of the source at 1 cm intervals using a movable optic fibre connected to a Princeton Instruments SCT-320 spectrometer and a PI-MAX 4 ICCD camera (Fig. 2.21(a)). The spectrometer is a Schmidt-Czerny-Turner style with adjustable diffraction grating and blazing and a 320 mm focal length. For these experiments a diffraction grating of 1200 grooves per mm was used with a 500 nm blazing. The PI-MAX 4 ICCD camera connected to the spectrometer is an internally cooled 1024×1024 pixel array with a variable intensifier. For dark regions of the plasma downstream of the source and under the magnetic filter, the intensifier was required for long time-integrated exposures to achieve desirable spectra.

Axial profiles were taken of the source with and without the magnetic filter via a narrow optical fibre which was clamped in a fixed position on a sliding stage next to the source. The optical fibre was positioned 1 mm from the source tube surface, limiting any lateral light collection, and then the sliding stage was moved along the length of the source for each x-position measurement. The PI-MAX 4 ICCD was controlled using the PI LightField software which outputs raw intensity 2D CSV files from the integrated CCD data. The raw files were then analysed to produce spectra and to calculate gas temperatures. Generally 10 to 50 CCD images were summed per 'frame' and 10 to 100 frames were averaged to produce a final spectrum depending on light levels at each location. The diffraction slit width was optimized for the strongest fidelity.



(a)



(b)

Figure 2.21: a) The Princeton Instruments IsoPlane SCT-320 spectrometer connected to the PI-MAX 4 ICCD used for the OES measurements. b) Schematic view from above of the plasma source tube showing axial measurement locations using an optic fibre.

2.4.3 Gas Temperature Fit Method

The process to convert Fulcher- α line emissions into rotational temperatures begins with an expression from Herzberg [96] relating the measured line intensity to the emission frequency and transition probability:

$$I_{n''}^{n'} = \frac{64\pi^4 f^3}{3h} \cdot \frac{1}{(2J' + 1)} \cdot N_{n',v',m'_J} A_{n''}^{n'} \quad (2.19)$$

where $I_{n''}^{n'}$ is the intensity for the transition from a lower n' state to an upper n'' state where the n state is a function of the electronic, vibrational and rotational quantum numbers $n'(e', v', m'_J)$, f is the emission frequency for a particular line, N_{n',v',m'_J} is the number density of each of the lower states and $A_{n''}^{n'}$ is the state transition probabilities (Einstein coefficients). The number density N_{n',v',m'_J} can be related to the rotational temperature of the ground state [97]:

$$N_{n',v',m'_J} = C_{n',v'} \cdot g_{a,s} \cdot (2J' + 1) \cdot \exp\left(\frac{-hcE_{n',v',m'_J}}{k_B T_{rot}(n', v')}\right) \quad (2.20)$$

where $C_{n',v'}$ is a normalization constant, $g_{a,s}$ is the $2I + 1$ nuclear spin degeneracy, and $T_{rot}(n', v')$ is the effective rotational temperature in the lower state. The transition probabilities $A_{n''}^{n'}$ can be separated into the probabilities for electronic, vibrational and spin respectively [98]:

$$A_{n''}^{n'} = A_{e',e''} \cdot q_{v',v''} \cdot S_{J',J''} \quad (2.21)$$

where $q_{v',v''}$ is the Frank-Condon factor and $S_{J',J''}$ is the Hönl-London factor. Finally, substituting Eqns. 2.21 and 2.20 into Eqn. 2.19 eliminates the number density, and noting that transition constants now include: the FC factor, the HL factor, $C_{n',v'}$, and $S_{J',J''} = \frac{1}{2}(2J + 1)$, an experimentally useful relationship to get at the rotational temperature T_{rot} is then found:

$$\ln\left(\frac{I_{n''}^{n'}}{g_{a,s} \cdot (2J' + 1) \cdot f^3}\right) \propto \frac{E_{n',v',m'_J}}{T_{rot}(n', v')} \quad (2.22)$$

The left hand side can be plotted on a log scale from experimental measurements of the intensity and frequency of each line emission. Inserting the spin degeneracies $g_{a,s}$ and the rotational numbers $(2J' + 1)$ for each line is straightforward. The LHS can be plotted against a linear scale of the energy

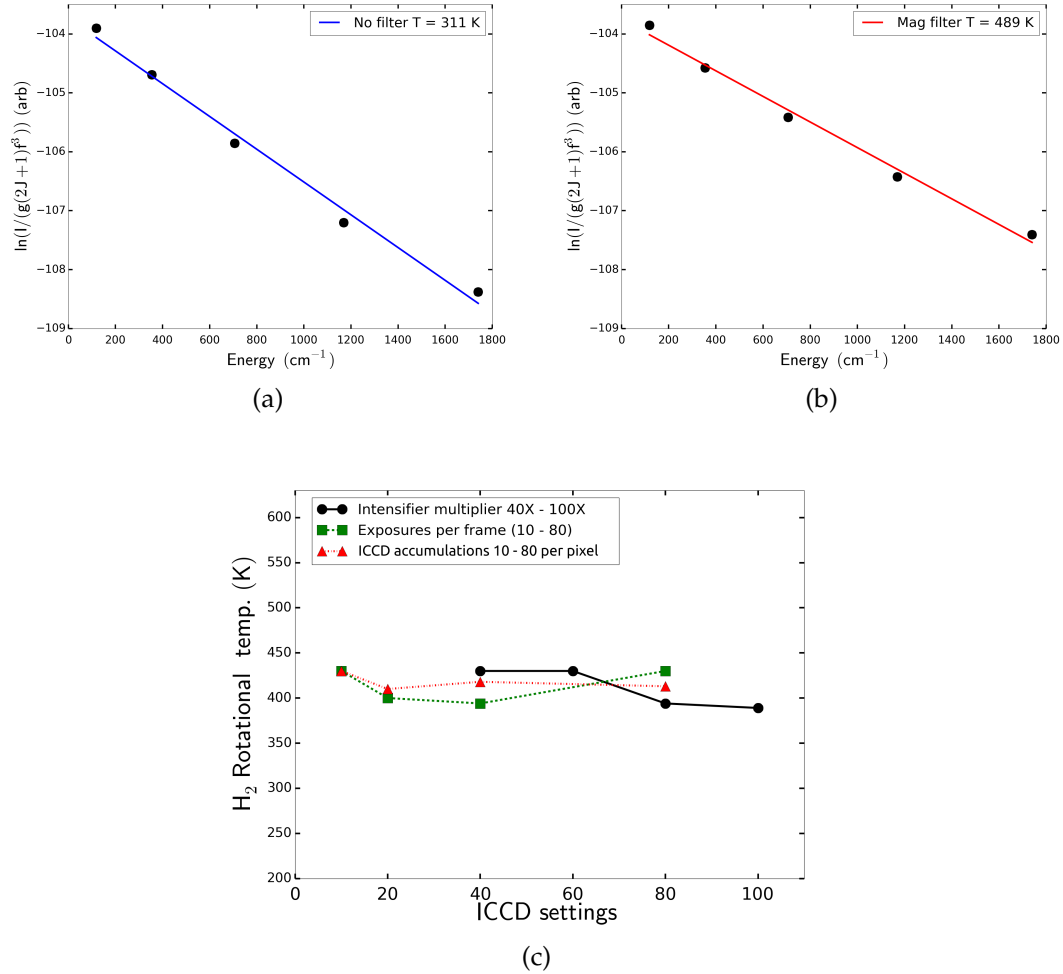


Figure 2.22: Processed Fulcher peaks Q1 through Q5 and the fitted temperature gradients. Measurements taken downstream at $x = 5 \text{ cm}$ and at 10 mtorr. The gas temperature fit shown in a) without the magnetic filter is compared to b) at the same location under the center of the field. The y-axis of the temperature fits are the LHS of Equation 2.22. Changes in ICCD camera settings are shown in c) and were taken at intermediate conditions of $x = 2 \text{ cm}$, 160 W, 10 mtorr.

levels $E_{n',v',m'}$ for each rotational level where the values for these levels can be taken from the reliable works of Dieke [99], Astashkevich *et al.*, [97] or Fantz & Wunderlich [100]. A correction for overestimating temperatures due to overpopulation of upper states was provided by a calculation in the thesis of de Graaf [101] and has been implemented for the measurements presented in this work.

Raw emission spectra showing the $\Delta v = 0$ Fulcher bands are shown in Figure 2.19 for 10 mtorr and 75 mtorr. The Q1 through Q5 peaks were processed following Equation 2.22 and fitted to a temperature gradients. The results of this fitting procedure are shown in Figures 2.22(a) and 2.22(b) with typical R^2 values for the temperature fits ranged between .96 and .99 which indicate good agreement with Boltzmann-like distributions across the emission peaks. Despite some authors stating that this fitting procedure can be performed for subsets of the Q1 through Q5 lines [97] [101], the temperature gradient fits were found to be sensitive to the low intensity Q4 and Q5 peaks and exclusion of these peaks from the fit resulted in underestimates of gas temperatures relative to the expected room temperature minimum at low powers and therefore all temperatures shown in this work include Q4 and Q5 peak fits.

For the experimental OES plasma measurements, the shot-to-shot variability of the ICCD was determined as well as the effect of changing three different camera settings (See Figure 2.22(c)). The ICCD control software allowed for three primary changes to the frame capture: intensifier multiplier, exposures per frame and on-pixel accumulations. Measurements were taken to investigate the effect on the gas temperature fits of changing the control settings.

Measurements were taken at a single position and power ($x = 2$ cm at 160 W) as the ICCD settings were changed capturing the variability between different ICCD settings. The maximum change to the temperature fits was found to be 40 K and therefore this was the maximum error assigned to each of the gas measurements shown later in Chapter 4 Section 4.3. Measurements downstream of the filter in the 'dark' region required long exposures of approximately 45 minutes for each position. A comparison of these profiles was performed with a temperature difference of only 50 K highlighting the robustness of these temperature estimates between multiple long exposures in the plasma.

2.4.4 Assumptions

To relate rotational gas temperatures to translational gas speeds from the Fulcher band, several assumptions must be made regarding the population channels and excitation states that are contributing to the measured emission.

1) Firstly, the majority of the emission is assumed to arise from collisional excitation from the ground state followed by radiative decay to the $2s^3\Sigma_g^+$ rather than the majority of the emissions occurring from cascades from higher states. When a plasma is this equilibrium state it is referred to the 'Corona' regime and is one of the core assumptions in certain radiative transition models [102]. A rule of thumb value to determine if a plasma is in the Corona regime depends on the electron density:

$$p_{cr} = \sqrt[9]{\frac{9 \times 10^{23} \text{ m}^{-3}}{n_e}} \quad \text{where} \quad p = Z \sqrt{\frac{R_y \cdot h \cdot c}{|E_{pi}|}} \quad (2.23)$$

where R_y is the Rydberg constant, $R_yhc = 13.6 \text{ eV}$, $E_{n'}$ is the energy level for the transition, the $d^3\Pi$ state is 1.6 eV and Z is the nuclear weight number. If the value of the critical threshold p_{cr} is below the p value for the transition then the plasma is said to be in the Corona regime. For the ICPS the electron density ranges from 10^{14} m^{-3} to 10^{18} m^{-3} , well below the $5 \times 10^{19} \text{ m}^{-3}$ required to exceed the corona regime.

2) If the excitation/relaxation time for rotational states is fast compared to the radiative decay time of the electronic state, the rotational states will exhibit a Boltzmann distribution between the levels and this will be captured during the emission event [97]. When this occurs for the ground state $1s^1\Sigma_g^+$, the rotational and translational energy of the molecule is in equilibrium and can then be assumed to be equal. Typical radiative lifetimes for rovibrational states of H₂ have been measured since the 1970s and generally range from 10 ns to 70 ns depending on the transition and the initial state [97]. Electronic decay lifetimes for the electronic transition from the Fulcher $d^3\Pi_u$ state has been shown to range from 30 ns to 70 ns [103] and so this assumption is only partially fulfilled.

3) The rate coefficients for the Fulcher- α transitions under varying collisional regimes and electron populations are assumed to be reliable and unchanging. This assumption is related to the final part of 2) but extended for all vibra-

tional and spin processes involved in the rate coefficients and 'constants' from Equation 2.22.

4) The line emission is dominated by $\Delta J = 0$ channels for both excitation and de-excitation processes rather than the emission being populated from mixed $\Delta J = \pm 1, \pm 2$, etc states. This assumption essentially states that the upper P, Q and R branches (see Figs. 2.20(a) and 2.20(b)) are not the primary population channels for the final transition. This is generally the case as the transitional probabilities are dominated by the $\Delta v = 0$ Q-branches for the Fulcher- α transitions (see Spindler [104] and Tables 6.3 and 6.4 and 6.5 in [101]). The Frank-Condon radiative decay factors heavily favor preservation of the 'diagonal' transitions which include the $\Delta v = 0$ (2-2) Fulcher band as presented in this work.

2.5 Laser Photodetachment Diagnostic

In order to measure the effect of the magnetic field for enhancing negative ion densities inside the hydrogen plasma, the laser photodetachment technique was used along the axial length of the tube with the results to be presented later in Chapter 5. The theory and methodology of the diagnostic will first be described here.

2.5.1 Theory of Laser Photodetachment

The basic principle of laser photodetachment is summarized in Figure 2.23(b) where a laser beam is sent into the plasma to detach H^- ions and a Langmuir probe is positioned inside the beam to collect the detached ions to measure the abundance of negative ions within that region.

The core electron of a hydrogen atom is bound to the nucleus with a ground state energy of 13.6 eV however, when the negative hydrogen ion is formed (H^-) the binding energy of the extra electron is only weak with a ground state energy of 0.75 eV. At this energy, a 1064 nm infra-red laser has the energy to photo-ionize (photodetach) the 0.75 eV electron without ionizing other bonds present in a pure hydrogen plasma. A Langmuir probe can be placed inside

the laser beam column to capture the detached electrons and the current can be read using an oscilloscope where an increase in electron current is seen at the time of the laser shot. If the Langmuir probes positive bias is set above the plasma potential in the electron saturation part of the IV characteristic and the laser is at a sufficient energy to saturate the detachment process, then the increase in electron current from the negative ions can be compared to the background current draw. The signal spike seen on the oscilloscope during the laser shot is called the photodetachment current (I_{PD}) and the background direct current draw from the bulk plasma electrons is the electron direct current (I_{DC}). During these experiments both I_{PD} and I_{DC} were measured simultaneously and averaged over approximately 100 laser shots. A negative ion fraction was then calculated from the ratio I_{PD}/I_{DC} also called the alpha (α) of an electronegative plasma.

To ascertain what power is required to photodetach all H^- ions within the laser column, a sweep of the laser power can be performed and compared against the theoretical detachment limit from the known photodetachment cross section. The theoretical curve is characterized by [13]:

$$\frac{\Delta I_{PD}^-}{I_{PD}^-} = 1 - \exp\left(\frac{\text{Laser Energy/beam area}}{\sigma_{PD}/hf}\right) \quad (2.24)$$

where σ_{PD} is the photodetachment cross section and h is Planck's constant in units of Joule seconds. This theoretical curve was compared to the normalized I_{PD} signal data as the laser energy was increased to verify that the experimental photodetachment signal is valid (Fig. 2.24(b)).

For the Langmuir probe to collect an accurate ratio of negative ions to electrons the particle collection radius of a biased Langmuir probe must be less than or equal to width of the laser column. Typically a Langmuir probe collects particles in a radius from one to three sheath widths. The Child-Langmuir law estimates sheath size for a biased probe and is given by:

$$s = \frac{2}{3}V_0^{3/4} \cdot \sqrt{\frac{J_i}{\epsilon_0}}^{-1} \cdot \left(\frac{2e}{M_i}\right)^{1/4} \quad (2.25)$$

where J_i is the ion current density given by:

$$J_i = n_e \cdot e \cdot u_B \quad (2.26)$$

The collection area here is dependant on electron density, bias voltage, electron temperature and ion mass. The law gives sheath size approximations between 0.4 mm and 4 mm for the Langmuir probe across the range of operating conditions within the ICPS. The laser beam diameter was 1 cm^2 for these experiments so the Langmuir probe and so the probe was collecting a representative fraction of charged particles inside the laser column.

Diagnostic experiments were undertaken to confirm that the collection regime was consistent with Equation 2.25 and that the laser energy and voltage bias were properly calibrated for this laser technique. The results are shown in the following section which discusses the diagnostics.

2.5.2 Laser Diagnostic Experiments

The laser used for the photodetachment measurements was a Quantel Brilliant B Nd:YAG laser operating at 1064 nm (Figure 2.24(a)). The laser beam formed a circular 10 mm diameter laser shape and the intensity could be varied using the internal Q-switch delay which ranged between 475 μs (low power) and 225 μs (high power) yielding beam energies of 50 mJ per cm^2 to 700 mJ per cm^2 respectively (Fig. 2.24(c)).

Measurements were unable to be made during continuous mode operation due to the prohibitively high RF noise in the ICPS and so measurements were taken in pulsed mode as close as possible to the discharge on time at around 2 μs into the afterglow. During this afterglow period the negative ions are only able to diffuse at most 4 mm which is less than the radius of the laser beam and so this can be considered a 'snapshot' of the continuous discharge. Additionally, the most destructive process for the negative ions during this afterglow period is associative detachment from atomic hydrogen. The atomic hydrogen density is approximately 10% for the ICPS [105] [106] and with a rate coefficient for associative detachment of approximately $K_{AD} = 2 \times 10^{-15} \text{ m}^3 \text{ s}^{-1}$ and estimate for the loss of negative ions in 2 μs at 100 mtorr can be made using the product of the reactants multiplied by the rate coefficient of the reaction and the time period given by $n_H \cdot n^- \cdot K_{AD} \cdot 10^{-6}$

$\approx 1 \times 10^{14} \text{ m}^{-3}$ negative ions lost. This number assumes no production of negative ions occurs in the afterglow and represents a density loss fraction of at most 1/10 of the negative ions compared to when the discharge is on (see Chapter 5 Fig. 5.1). For the negative ion laser photodetachment at 2μ are considered a measurement of 90% of the density of the negative ion population.

The laser was positioned on an optics bench 2 m from the ICPS and the beam was deflected using three hand aligned mirrors to be perpendicular to the source tube allowing for axial measurements of the negative ions along the source tube (Figure 2.23(a)). A simple custom-made series circuit of batteries and a 50 Ohm resistor were connected to an uncompensated Langmuir probe and the oscilloscope. An oscilloscope was used to acquire the photodetachment signal from the probe. The uncompensated Langmuir probe tip was a 'dogleg' L-shape and set perpendicular to the central axis of the tube. This orientation allowed for the beam to be coincident with the Langmuir probe tip axis while also allowing the tip to be perpendicular to the field lines of the magnetic filter to prevent electron current depletion.

For the pulsed afterglow measurements, a double trigger setup was implemented using two function generators to create a variable delay between the plasma off cycle and the timing of the laser shot. The pulses were 5 V TTL offset square waves which provided reliable temporal control between the laser and the ENI power supply.

Figure 2.23(b) shows a diagram of the atomic detachment process for H^- and the positioning of the positively biased Langmuir probe to collect the detached electron. A diagram of a typical resultant oscilloscope signal is shown below with the size of the downward voltage spike corresponding to the negative ion density. The raw detachment signals from the oscilloscope are shown in Figure 2.25.

The Q-switch delay which controls the power level on the laser was first investigated to map the delay to an energy density. The laser energy density of the laser was measured using a beam calorimeter as the laser Q-switch delay was changed. By limiting the beam size to 1 cm^2 using an adjustable iris, the beam energy density as a function of the laser Q-switch delay was determined. Figure 2.24(c) shows that the response of the laser energy to changes in the Q-switch delay is non-linear. The borosilicate source tube itself was

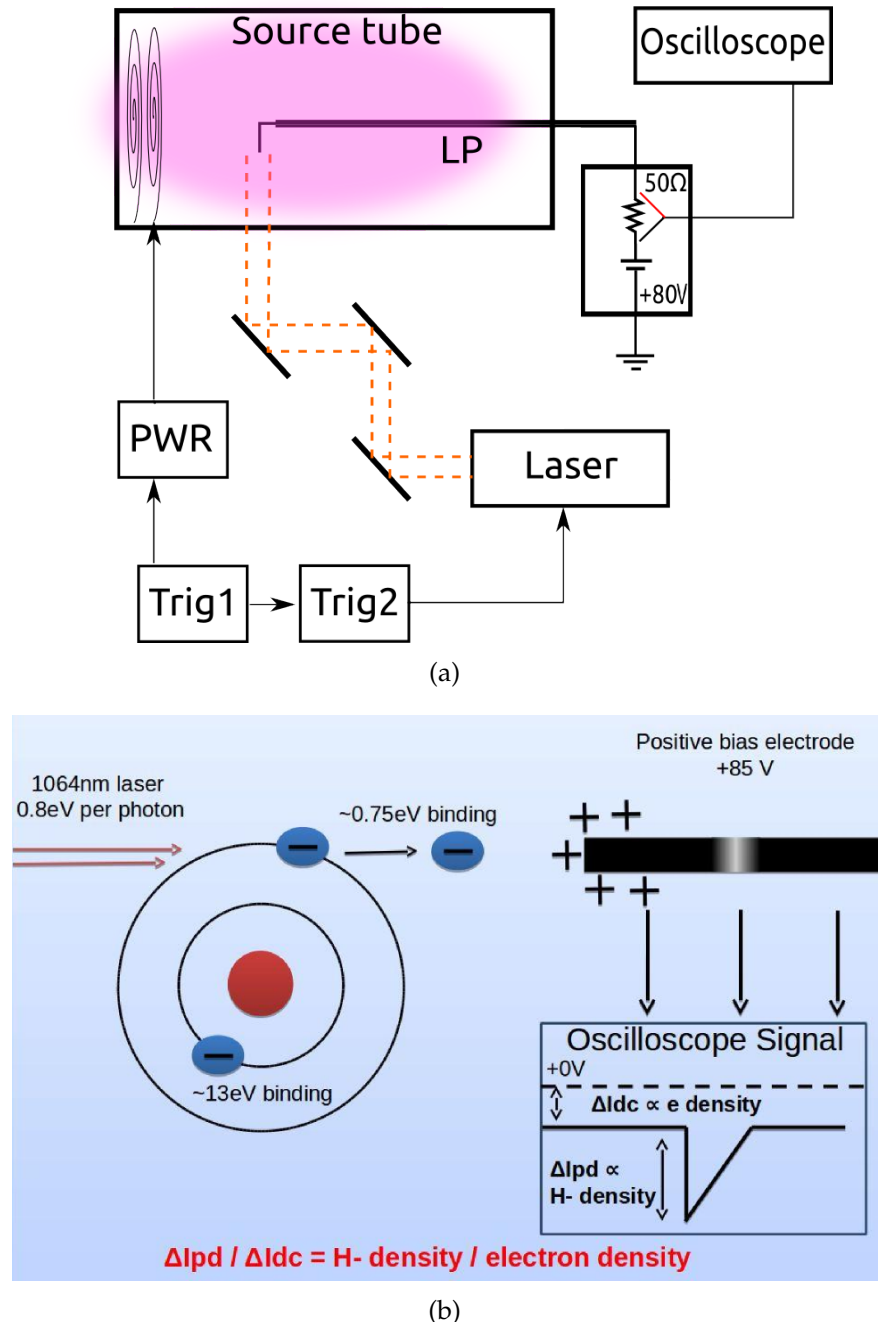


Figure 2.23: a) The photodetachment setup using a double trigger with 'Trig2' used as delay line for afterglow measurements. b) Diagram of the photodetachment process showing the laser beam incident on a H^- ion inside the plasma, the positively biased Langmuir probe (black) to collect the detached electrons and the resulting signal as seen on an oscilloscope.

also found to attenuate the beam energy by up to 15% due to scattering compared to the open air beam power.

The optimal laser power was then investigated. The laser energy was assessed during photodetachment measurements using the Langmuir probe. The detachment signal was compared to the theoretical energy cross section from Equation 2.24 and the result is shown in Figure 2.24(b). The detachment is seen to increase as a function of laser power until the signal plateaus as all negative ions within the collection radius are being photoionized. Above this laser energy the laser becomes high enough to ablate the probe tip material which liberates extra electrons and ions causing an undesirable spurious signal. The diagnostic was found to have saturation energy from 100 mJ cm^2 to 150 mJ cm^2 which is consistent with established literature and known cross sections from both Langmuir probe photodetachment [13] [107] [108] and also hairpin probe photodetachment [109].

The dependency of the detachment signal to the voltage bias was then investigated to ensure the electron collection was maximized. Figure 2.24(d) shows the bias voltage as a function of the negative ion to electron ratio with and without the filter in place at $x = 5 \text{ cm}$. The signal is seen to saturate without the filter (black) and when using a radial magnetic filter (blue) which will be discussed later. While the signal with the transverse filter was not able to fully saturate up to the maximum voltage of $+100 \text{ V}$, this diagnostic was performed in the strongest negative ion producing region of the ICPS and subsequent measurements at different locations showed saturation at $+60 \text{ V}$. A voltage of $+80 \text{ V}$ was chosen as the general operating voltage for the technique due to electrical safety reasons and for probe survivability.

Finally the sheath collection radius was compared to the previous estimates using the Child-Langmuir Law of 0.4 mm to 4 mm in Equation 2.25. A laser iris was used to attenuate the beam width from 1.5 mm to 9 mm in order to measure the response of the Langmuir probes H^- collection radius to the laser radius and to estimate the sheath width. Figure 2.25 shows an example of the photodetachment signal spike on the oscilloscope in a high density region at $x = 1 \text{ cm}$ downstream of the antenna. The depth of the spike indicates the number of negative ions being collected by the probe and this experiment showed that even at a laser beam width of only 1.5 mm , the negative ion collection from the probe remained the same at around 20 mV . This validates the sheath size estimate made previously and fulfils the requirement that the laser width is always greater than the collection width of the probe. The angle

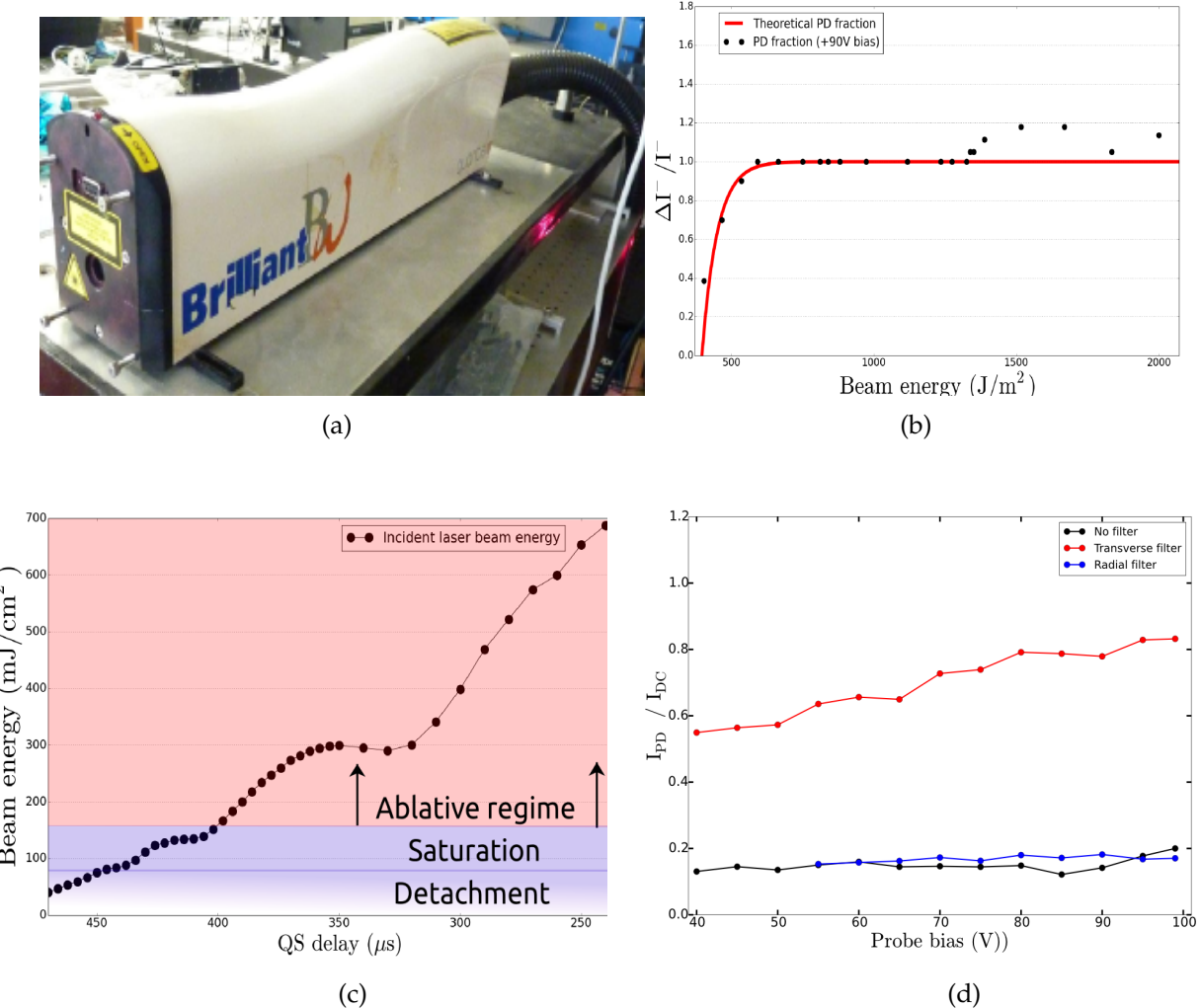


Figure 2.24: Laser photodetachment diagnostics including a) Brilliant B 1064nm Nd YAG. b) the laser energy function. c) laser energies and ablative limits. d) negative ion fractions. Hydrogen, 100 mtorr at 200 W.

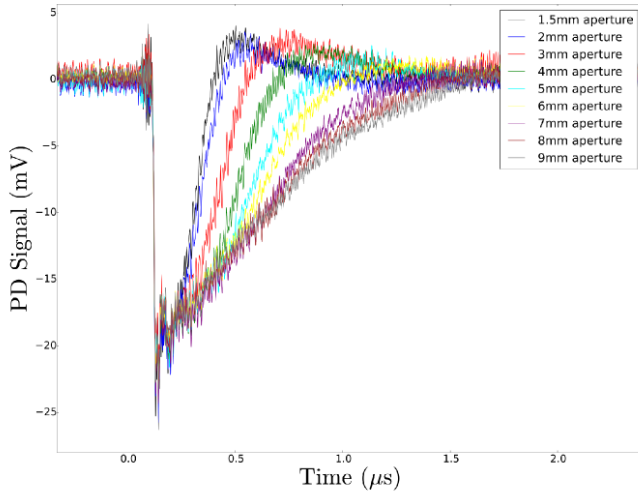


Figure 2.25: Change in raw photodetachment signal when changing the laser beam diameter.

of the slope after the photodetachment peak is related to the re-population of the negative ions after being depleted in the laser column [107], Figure 2.25 also shows that when the iris diameter is increased the recovery time of the negative ions also increases. This is consistent with the re-population of negative ions on microsecond time scales after the photodetachment process.

Power Efficiency and Magnetic Enhancement

This chapter discusses the optimization of the ICPS discharge and presents measurements of the efficiency gains when using magnetic enhancement of the plasma source. An increase in the plasma source efficiency is important to many plasma applications ranging from low power commercial systems to larger industrial and laboratory plasma systems. For the larger systems increasing the system efficiency can be important in reducing the power requirements, component costs and cost of system cooling. For smaller commercial processing plasmas, which typically use low power at low densities, limitations exist in maintaining uniform H-mode discharges across a range of low power levels and different operating pressures. Magnetic enhancement can help solve these issues by increasing ionization efficiency and allowing for increased control over plasma uniformity and particle fluxes.

While power transfer studies have been performed on ICP systems previously (eg. [33] [65] [110]) to the authors knowledge this chapter presents the most comprehensive study of power transfer optimization of an ICP for both hydrogen and argon and includes the effect of magnetic enhancement.

The power transfer efficiency was investigated for both argon and hydrogen plasmas while the operating power, gas pressure and the spatial position of the magnetic filter was changed. A brief introduction will be given to inductive power coupling in Section 3.1.1 and then the power transfer results will be presented.

The key findings from this chapter include:

- 1) The magnetic filter increases the plasma resistance up to a factor of two in argon and up to a factor of three in hydrogen.
- 2) The increase in plasma resistance translates to a system efficiency gain of up to 6% in argon and up to 25% in hydrogen and the increased efficiency is shown to correlate with increased ionization rates inside the plasma.
- 3) The increases to system efficiency is sensitive to both the positioning of the magnetic field with respect to the antenna and the strength of the magnetic field.
- 4) The magnetic field is shown to be able to initiate the H-mode at lower powers.

3.1 Power Transfer in the ICPS

Initially Section 3.1.1 will introduce the basics of inductive power transfer and then Section 3.1.2 will provide the methodology of measuring power transfer. Section 3.2 presents the power optimization results for hydrogen and Section 3.3 presents the power optimization results for argon.

3.1.1 Source Dynamics

Typically, in a plasma source, energy for the discharge is provided by a power amplifier which couples power to the plasma either capacitively, inductively or via microwaves. For inductively coupled plasma sources such as the ICPS, both the capacitive and inductive paths are employed. Initially an alternating current is passed through the antenna which creates a near-field time varying magnetic field through the solenoid. If the AC frequency driving the antenna current is below the plasma frequency, (which is often the case), then the near-field emission from the antenna is evanescent and diminishes within the plasma at a characteristic length scale (the plasma skin depth). When the momentum transfer collisional frequency of the electrons (ν_m) is greater than the driven near-field frequency (ω), the 'collisional' skin depth δ_c is used,

when $\nu_m \ll \omega$ the 'collisionless' skin depth δ_p is used [60]:

$$\delta_p = \frac{c}{\omega_{pe}} , \quad \delta_c = \sqrt{\frac{m_e}{e^2 \mu_0 n_s}} \quad (3.1)$$

where c is the speed of light, ν_m is the collisional frequency given by $(\bar{\sigma}_{el} n_g \bar{v}_e)$, n_s is the sheath density and ω_{pe} is the electron plasma frequency.

The electron plasma frequencies in hydrogen in the ICPS range from 17.8 GHz in the high density region near the antenna to 1.8 GHz in the low density areas downstream at $x = 10$ cm. The plasma frequencies in argon are higher than hydrogen due to the increased power coupling yielding increased densities at a given power. They range between 56.3 GHz under the antenna and 5.6 GHz in the downstream region.

The skin depth of the hydrogen plasma discharge in the ICPS ranges between 20 cm at low plasma densities to 1.6 cm at higher densities. This means the H-mode plasma power coupling is able to penetrate across the diameter of the source tube for hydrogen. However for argon, the skin depth ranges between 5.3 cm at low density and as low as 5 mm at the higher operating power. This means the H-mode argon plasma power coupling is not able to penetrate the source tube at higher powers and the power deposition profile is instead confined to a thin layer near the antenna.

The ratio of the collision frequency to the driving frequency gives an indication of the collisionality within the skin depth during one RF cycle. For the ICPS, this ratio ranges from approximately 1 to 50 for hydrogen in the pressure range from 10 mtorr to 100 mtorr respectively. This places the ICPS measurements in an intermediate collisional skin regime.

In addition to the time varying magnetic field, there is also a capacitive coupling of the antenna arising from the time varying applied voltage. At low power, this capacitive potential field is the dominant mode of power coupling to the plasma despite its low efficiency. This coupling results in a low density diffuse plasma throughout the source called the E-mode typically present from 0 W up to 80 W depending on the plasma resistance. As the power is increased, the primary power coupling switches to the inductive mode whereby the time varying magnetic field of the antenna gives rise to induced closed-

loop azimuthal electric fields perpendicular to the magnetic field lines [111]:

$$\vec{E}_{ind} = -\frac{\delta \vec{A}}{\delta t} \quad (3.2)$$

With \vec{A} as the magnetic vector potential where $\vec{B} = \nabla \times \vec{A}$. The low mass electrons responding to these high frequency induced electric fields are accelerated and undergo collisions dissipating the power from the source. Collisional energy transfer of this kind is called ohmic heating and is the primary channel for power deposition in ICP devices operating at higher powers. When the azimuthal currents are the primary sink for the electrons the coupling mode is called H-mode operation and it is highly power efficient. The H-mode also typically exhibits a uniform plasma discharge profile with Maxwellian particle distributions making inductively coupled systems ideal for plasma processing applications. The power absorbed by a volume of plasma is related to the azimuthal current density and the effective plasma conductivity by [70]:

$$P_{abs} = \frac{J_\theta^2}{2\sigma_{eff}} \pi V_{vol} \delta_c \quad (3.3)$$

where J_θ is the current density, V_{vol} is a plasma volume and σ_{eff} is the effective plasma conductivity:

$$\sigma_{eff} = \frac{\epsilon_0 \omega_{pe}^2}{\nu_m + j\omega} \quad (3.4)$$

where ϵ_0 is the electric permittivity of free space. The azimuthal electron flow induced in the plasma skin layer creates its own magnetic field and along with the inertial electron induction, the total plasma inductance is defined L_p . It is clear from Eq. 3.4 that increasing the collisional frequency of the electrons decreases the conductivity, (equivalent to an increase in the resistivity), of the plasma. Higher resistivity increases the ability of the plasma to absorb power. The plasma resistance R_p (in ohms) is described as the inverse of the plasma conductivity containing no imaginary part and can be considered as an in-series resistive component of the plasma:

$$R_p = \nu_m L_p \quad (3.5)$$

The plasma resistivity can be increased by increasing the collisional frequency or increasing the plasma inductance. Increasing the plasma resistance is the primary way in which the efficiency of the source can be increased however, increased plasma resistance does not always imply increased ionization. Power may be deposited via inelastic collisions such as atomic orbital excitation or power may also be deposited by pumping of rovibrational atomic bond modes if the feedstock gas is molecular.

3.1.2 Measuring Power Efficiency

Initial calibration of the current measurements were made by comparing an Ion Physics CM-10 current monitor ring with a Tectronix TCPA300 current probe. The two devices were found to closely agree across a power range of 2 W to 200 W within an offset of 7% between them (Fig. 3.1(a)). Due to its simplicity and size, the CM-10 ring was permanently installed in the ICPS matching box and then used for all subsequent power measurements in this chapter. The CM-10 current monitor was terminated at $50\ \Omega$ into an oscilloscope and the AC current waveform amplitude was converted to RMS to obtain the current measurement.

Power efficiency measurements were made using knowledge of the antenna current, forward power, plasma resistance and the contact resistance of the system (eg. matching unit and antenna). The contact resistance was first determined by taking antenna current measurements in the absence of a plasma load under vacuum (R_{vac}). Power was run through the system circuit (matching unit and antenna) and was impedance matched for near zero reflective power using a Diamond SX-100 power meter. With knowledge of the applied power and the current through the antenna, the relationship $P_{forward} = I_{ant}^2 R_{vac}$ was used to find the contact resistance and shown in Figure 3.1(b). This measurement must be performed at low powers to avoid contact solder melting and component damage to the matching unit or antenna. Typically in inductive plasma systems the vacuum resistance of the matching unit (R_{vac}) is approximately 1 Ohm, and > 1 Ohm in CCP systems.

The plasma was then turned on and the plasma resistance was calculated from $R_p = R_{total} - R_{vac}$ where R_{total} is the resistance calculated with the plasma running. The total resistance (R_{total}) of the circuit was determined by converting the 'plasma on' current at a known power into a resistance by using the power relation $R_{total} = \frac{P_{forward}}{I_{ant}^2}$. Once the vacuum resistance

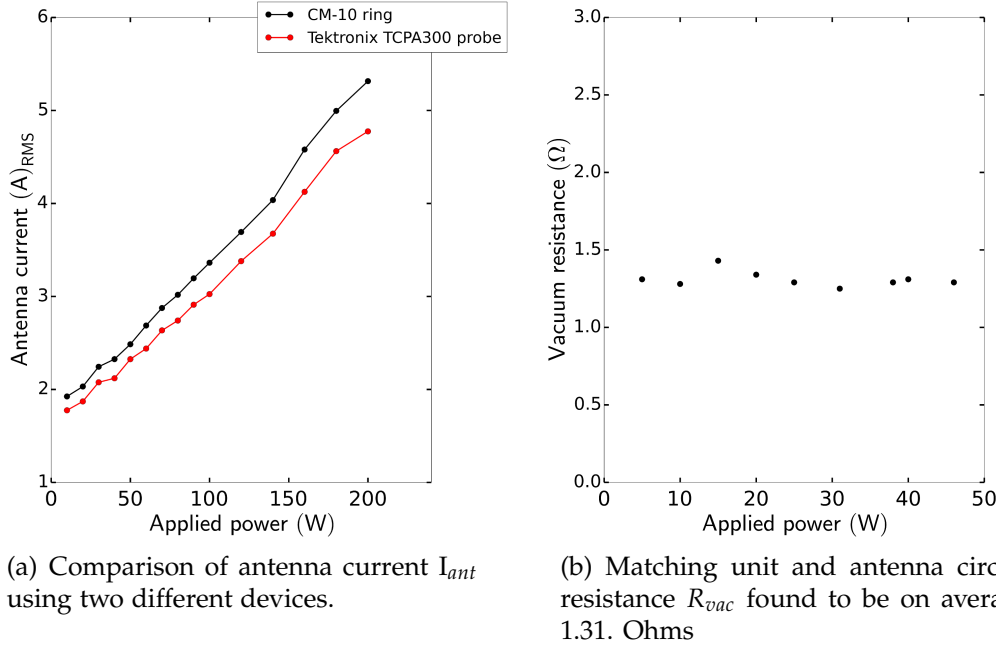


Figure 3.1: Calibration of antenna current measurements (I_{ant} and assessing the vacuum resistance (R_{vac}) of the impedance matching network.

and plasma resistance have been found, the overall power deposition (η) of the system can be determined as the ratio of the plasma resistance to the resistance of the plasma driving circuit:

$$\eta = \frac{R_p}{R_p + R_{vac}} \quad (3.6)$$

This is a measure of the fraction of power being deposited into the plasma and is the method used to measure the overall efficiency of the plasma source in this chapter. The power fraction of the system can be increased by either increasing the plasma resistance or decreasing the vacuum resistance of the system circuit. Since the vacuum resistance is set by the physical components, the plasma resistance is the key factor for determining source efficiency.

3.2 Hydrogen Power Transfer

The following three sections will describe the power transfer for hydrogen: the E to H mode transition, pressure changes and changes to magnetic field. The efficiency of a plasma source is a key property

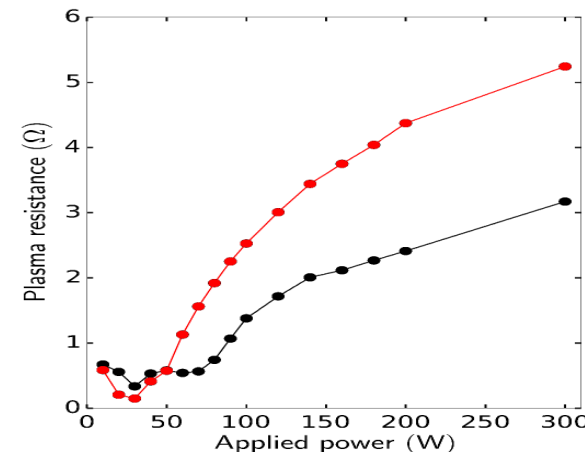
3.2.1 Hydrogen E-mode to H-mode Power Dependency

Figures 3.2(a) and 3.2(b) shows the how the plasma resistance and power deposition change with increasing power. The red profiles show data for when the transverse field is applied to the plasma. The filter is centered at $x = 5$ cm downstream of the antenna for these results. The black profiles show data without the transverse field applied. The low power range from 0 W to 50 W represents the low efficiency E-mode coupling state of the plasma where the power is not coupled to the inductive fields but rather capacitive coupling to the plasma via the antenna voltage.

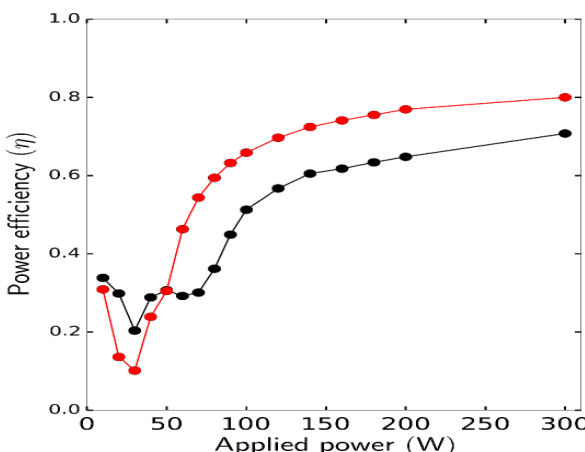
Figure 3.2(a) shows that the downstream magnetic filter increases the plasma resistance in hydrogen up to 70% (roughly 2 Ohms) during the H-mode. The magnetic field also increases the plasma resistance per Watt faster than without the filter. Figure 3.2(b) shows that this increase in plasma resistance translates into a power efficiency increase by up to 20% in the H-mode. The figure importantly shows that the magnetic filter allows access to H-mode transition by up to 40 W lower than without magnetic filtration. This effect is important for pulsed applications and will be discussed further with respect to the argon results in Section 3.3.

The magnetic field in Figure 3.2(b) shows increasing gains in plasma resistance with increasing power up to 300 W here which means that the gains from the magnetic field range can apply to a wide range of system powers. While there is a paucity of detailed literature on hydrogen ICP power deposition, these trends show similarities in the available literature for both ICP systems [33] [112] [113] [114].

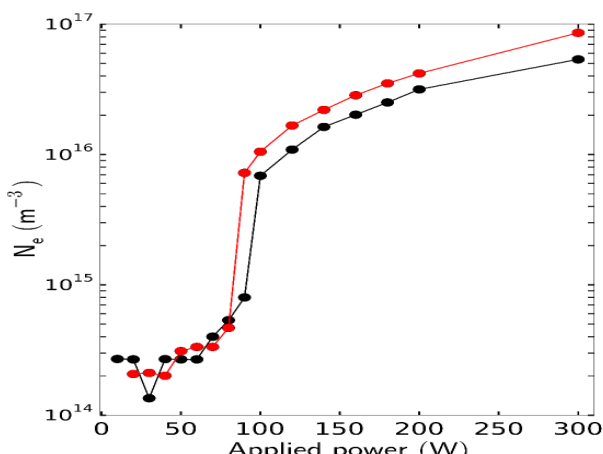
Interestingly, Figure 3.2(b) shows that the efficiency of the source decreases through the capacitive mode from around 0 W to 60 W. This drop in power efficiency is due to increasing screening of the electric field with increasing charged particle density. The measurement of this effect closely matches the



(a)



(b)



(c)

Figure 3.2: Hydrogen plasma power deposition and densities at 10 mT pressure. (Black) no field, (Red) 250 G field centered at $x = 5$ cm. a) Hydrogen plasma resistance as a function of power. b) Hydrogen plasma power efficiency as a function of power. c) Hydrogen electron density (n_e) as a function of power.

analytical model of ICP power transfer from the E-mode to H-mode developed by Chabert [60] when capacitive coupling was included.

To determine whether or not the increased efficiency translates into increased ionization, electron density measurements were taken inside the center of the discharge under the antenna at $x = -2.5$ cm upstream of the front of the coil. Figure 3.2(c) shows the electron density as a function of power from hairpin probe measurements. The E-mode to H-mode transition is well-defined for the electron density measurements occurring around 80 W forward power (Fig. 3.2(c)) and increasing the electron density by an order of magnitude. The trend in electron density (ionization) is seen to follow the trend in power transfer efficiency. The effect of magnetic filter increases in electron density by a factor of 2 to 3 in the H-mode compared to the unfiltered case which corresponded to a 10% increase in power deposition. Note that the magnetic filter is located 5 cm downstream of the antenna and this density measurement was taken in the center of the discharge at $x = -2.5$ cm and so the increase in ionization efficiency from the magnetic filter can be non-local. The onset of the H-mode with the magnetic field applied is seen to be delayed compared to the power transfer measurements due to the presence of the probe inside the discharge. When the probe was removed the H-mode was seen to trigger at a lower power with the application of the magnetic filter consistent with Figure 3.2(b) when the density probe was not inserted.

It is unclear exactly what the mechanism is which produces the increased power transfer efficiency when using the magnetic field, however several explanations can be offered. Firstly power transfer gains may be driven by increases in the plasma resistivity from increased particle confinement whereby longer particle residence times allow for greater numbers of ohmic collisional events. Secondly the plasma inductance L_p could be being modified by the coincidence of magnetic field line geometry of the nearby filter with the antenna. Thirdly any effects which increase in the effective plasma conductivity σ_{eff} will lower the required antenna current for a given power setting [110].

3.2.2 Hydrogen Pressure Dependency

The power transfer efficiency as a function of pressure was investigated. Measurements were taken during an H-mode discharge at a constant forward power of 100 W. The hairpin probe was again used to measure electron density changes in the central discharge.

Figure 3.3(a) shows the hydrogen plasma resistance measurements as a function of pressure. The plasma resistance is seen to increase from 10 mtorr up to around 35 mtorr where it then begins to decline. The magnetic field is seen to enhance the plasma resistance by around 60% compared to the unfiltered case at low pressure but at high pressure increases the plasma resistance by only 6%. This indicates that the efficiency gains from the magnetic field are strongest for low pressure hydrogen plasmas and make little difference to transfer efficiency on high pressure systems.

Figure 3.3(b) shows the power transfer efficiency profile. At low pressure, the plasma resistance gain of approximately 1 Ohm from the magnetic filter is seen here to translate into enhancing the system efficiency by around 13%. At higher pressures of 50 mtorr however the system shows little increase in the power efficiency with both filtered and unfiltered profiles at around 70% efficiency. The saturation of the power efficiency at higher pressure stems from the inability of the azimuthal inductive current to couple energy into highly collisional electrons who have short mean free paths and are subjected to high frequency scattering.

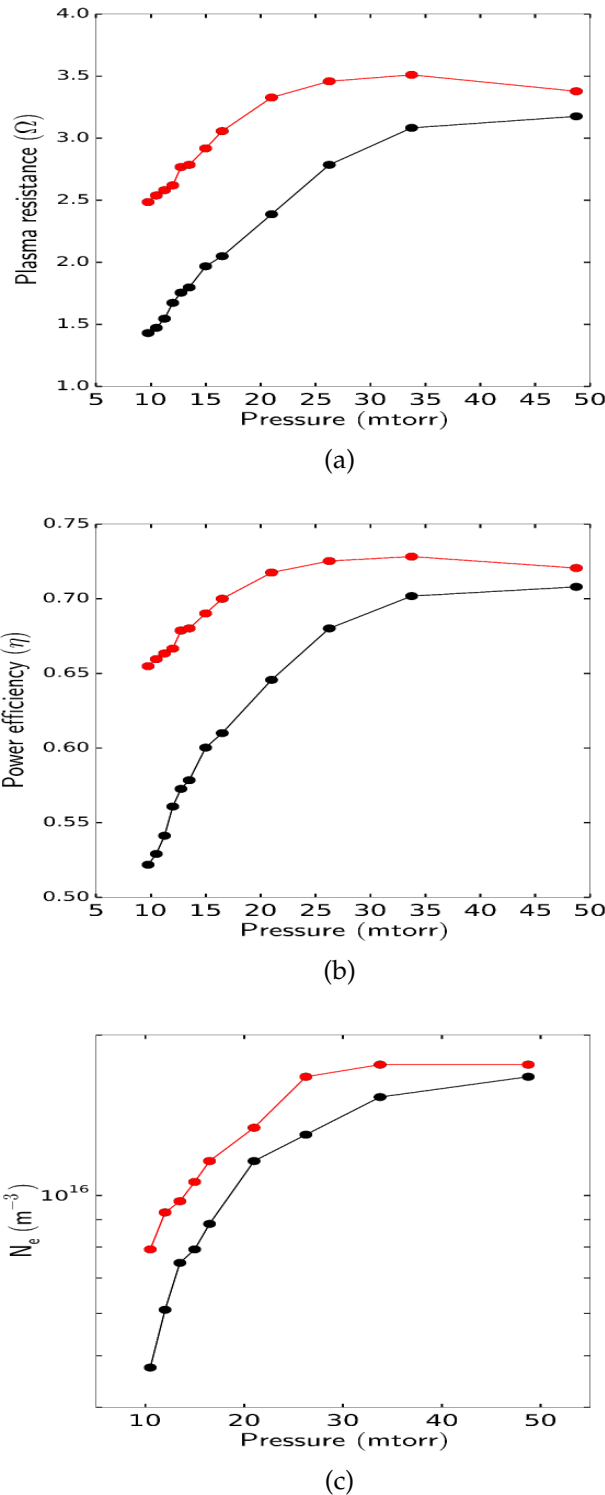


Figure 3.3: Hydrogen plasma pressure dependencies and densities. H-mode operation at 200 W power. (Black) no field, (Red) 250 G field centered at $x = 5$ cm. a) Hydrogen plasma resistance a function of pressure. b) Hydrogen plasma power efficiency as a function of pressure. c) Hydrogen electron density as a function of pressure.

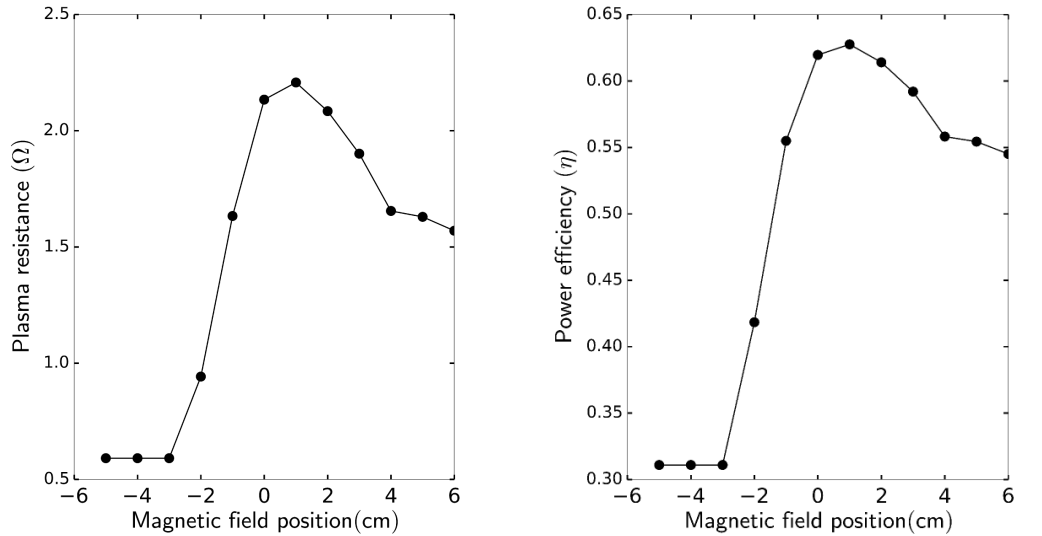
3.2.3 Hydrogen Magnetic Field Dependency

Two sets of experiments were conducted to ascertain the spatial effect of the magnetic filter on the power efficiency by moving it along the x-axis and separating it in the z-direction. In the first experiment the filter field was moved along a sliding stage so the magnetic filter could be moved to different positions along the length of the source as well as vertically separated above and below the source including over the antenna.

Figures 3.4(a) and 3.4(b) (top figures) show the resistance and efficiency changes when the magnetic filter is moved along the length of the source in the x-direction. The maximum efficiency gains are made for hydrogen when the center of the magnets were placed just downstream of the front of the antenna at $x = 1$ cm. When the magnets were centered above the antenna from $x = -5$ cm to $x = -1$ cm the H-mode discharge was abruptly suppressed and only a diffuse E-mode plasma was able to be made. When moving the magnets further downstream the H-mode reappeared. The plasma resistances range from 0.5 Ohms up to 2.25 Ohms when moving the magnets. The power transfer efficiency ranged from 30% up to 62% when the magnets were moved along the length of the source. These results show the optimal efficiency gains for the hydrogen source is when the transverse magnetic field is positioned close to the front of the antenna.

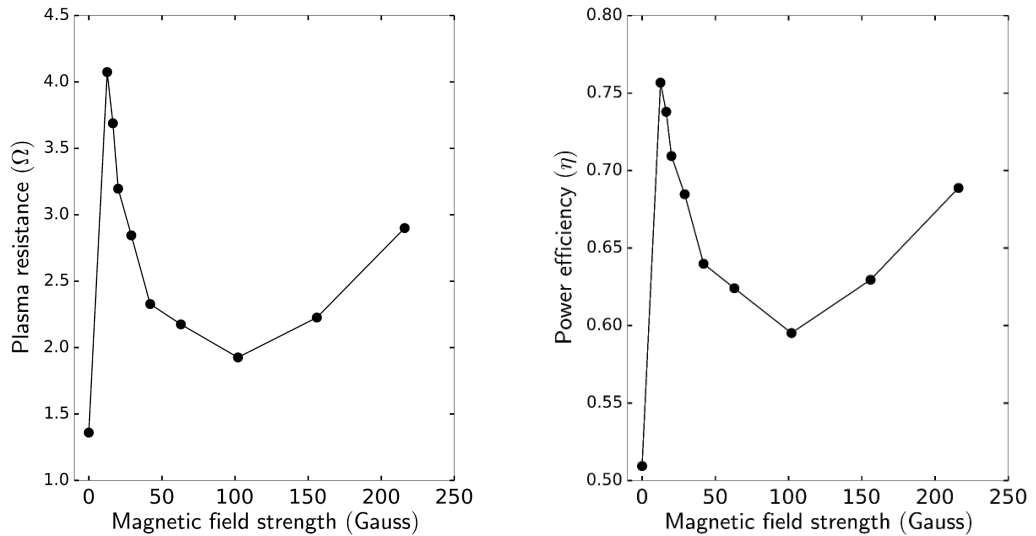
This suppression of the discharge may be due to the superposition of the time varying axial field inductive with a permanent transverse field disrupting the formation of azimuthal electric fields and currents. The peak in the source efficiency which occurred when the magnetic filter was positioned directly adjacent to the front of the antenna at ($x = 0$ cm). As mentioned, this effect may be a result of the lateral field lines of the filter edge improving the upstream inductance of the plasma or improving collisional confinement of the discharge.

The second set of experiments involved placing the field at $x = 5$ cm and changing the magnetic field strength by separating the magnets shown (Figures 3.4(c) and 3.4(d)). The plasma resistance measurements shown in Figure 3.4(c) shows a strong 4Ω peak in plasma resistance at low magnetic field strengths at around 10 G. The plasma resistance then declines toward 2Ω at a field strength of 100 G before increasing back up to 3Ω at around 225 G. This low field peak corresponds to a strong jump in efficiency from the



(a) Hydrogen plasma resistance as a function of the center magnetic filter distance from antenna.

(b) Hydrogen plasma power efficiency as a function of the center magnetic filter distance from antenna.



(c) Hydrogen plasma resistance as a function of field strength.

(d) Hydrogen plasma power efficiency as a function of field strength.

Figure 3.4: Hydrogen plasma resistances and power deposition fractions changing transverse field position in a) and b) and changing the field strength in c) and d). The magnetic field was centered at $x = 5$ cm for Figures c) and d). Operating power was 200 W, H-mode discharge at 10 mtorr pressure.

H-mode coupling up to a high power transfer efficiency of 75%. This low field peak may be related to a resonance matching between the 13.56 MHz driving frequency of the plasma and the electron cyclotron frequency at 5 Gauss. This effect from transverse filters has been seen recently by Kim *et al.*, [34] and also by Lee *et al.*, [110] and has been shown to be related electron cyclotron resonance heating. Electron energy probability functions (EEPFs) near the antenna will be shown in Chapter 4 which will support this hypothesis.

It is noted that changing the magnets in the z-direction changes two parameters simultaneously: the strength of the filter field and the geometry of the magnetic field with respect to the source.

3.3 Argon Power Transfer

Comparative power deposition experiments were then performed with argon for the plasma resistance, source efficiency and magnetic field position. The experiments show much higher plasma resistances for argon than those measured in hydrogen due to the wider range of available electric excitation states and the ability of argon to absorb energy into metastable states. Detailed electron density measurements of the central discharge were attempted to match the hydrogen data but the probe was not able to withstand long periods inside the discharge due to the high plasma densities and temperatures.

3.3.1 Argon Power Dependency

In argon the higher plasma resistance allows for H-mode coupling activation at powers as low as 10 W forward power and so the E to H mode transitions were not able to be characterized. Figures 3.5(a) and 3.5(b) show the power dependency of argon. The plasma resistance when the magnetic filter is applied is seen to increase strongly from around 3 Ohms to 15 Ohms when the power is increased from 0 W to 50 W. The plasma resistance then steadily decreases with increasing power down to around 10 Ohms. Without the magnetic filter the plasma resistance trend is similar but peaks around 11 Ohms before declining to 8 Ohms.

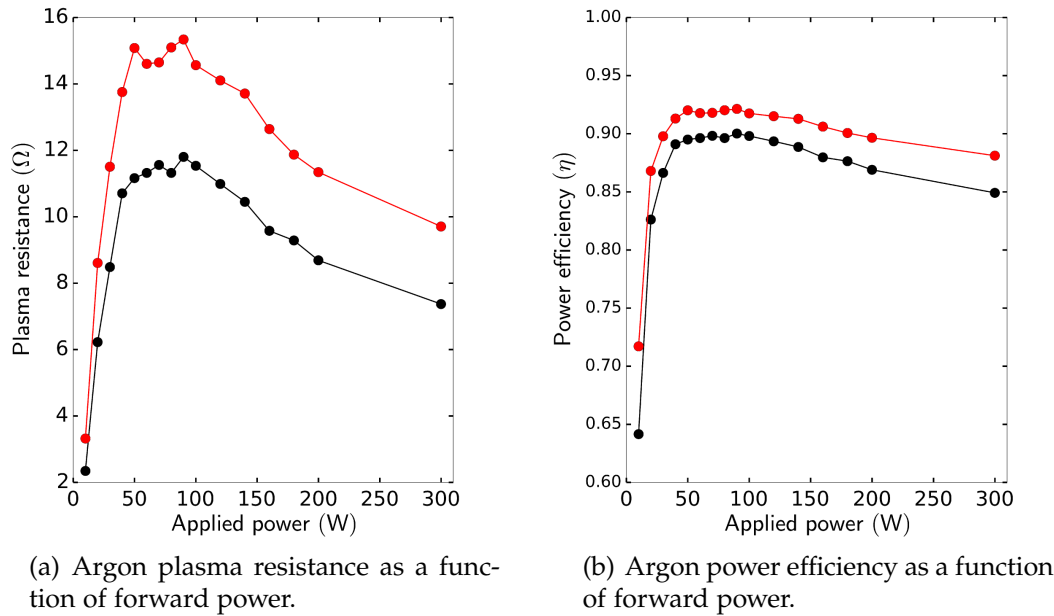


Figure 3.5: Argon power dependencies at 10 mtorr. (Red) magnetic field applied, (black) no field applied. The field was centered at $x = 5$ cm.

These high argon plasma resistances translate into high power transfer efficiencies. Argon efficiencies range between 64% at 10 W and 92% at 50 W before slowly decreasing in efficiency by 4% as the power is increased to 300 W. The greatest gain in efficiency for argon is seen at the lowest power range of 10 W where the difference between the filtered and unfiltered efficiency is around 8%. To emphasize the high plasma resistance of argon, at 10 W argon already has the same plasma resistance of hydrogen at 200 W.

3.3.2 Argon Pressure Dependency

Figures 3.6(a) and 3.6(b) show the pressure dependency for argon. The pressure profile for argon looks similar to that of hydrogen with increasing plasma resistance and efficiency from low pressure up to 15 mtorr before plateauing up to 25 mtorr. The plasma resistance changes by around 4 Ohms over the pressure range and the power transfer efficiency increases by around 8 Ohms with increasing pressure. A maximum gain from magnetic enhancement of only 4% is seen at the lowest pressure of 2.5 mtorr. Argon displays plasma resistances ranging from 2Ω to 15Ω , which is three times higher than those measured in hydrogen.

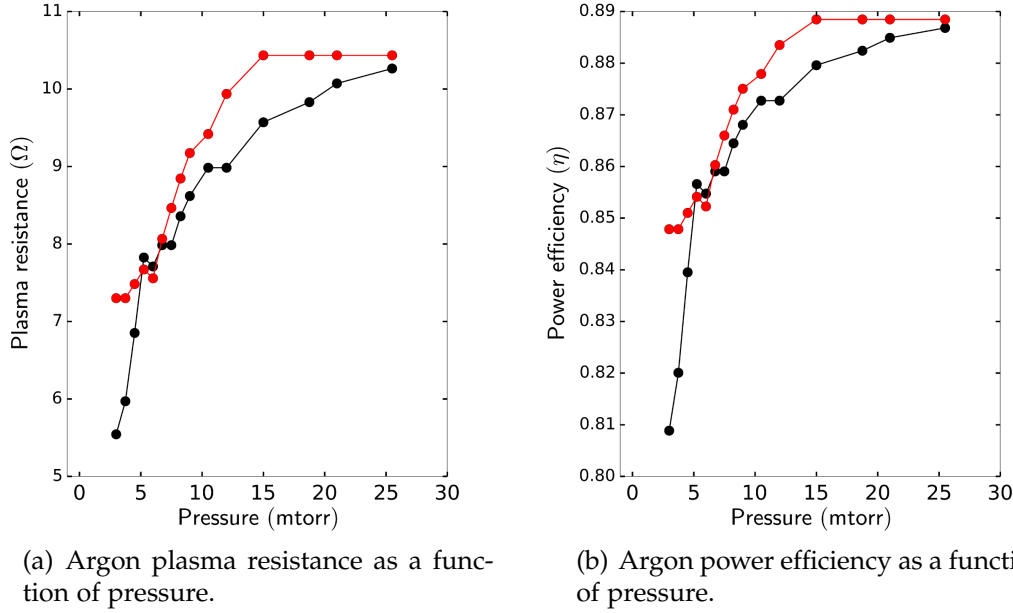


Figure 3.6: Argon pressure dependencies at 100 W power. (Red) magnetic field applied, (black) no field applied. The field was centered at $x = 5$ cm.

The argon pressure sweeps show that the magnetic filter increases the plasma resistance more strongly at low pressure by around 2 Ω at 3 mtorr and around 1 Ohm at 10 to 15 mtorr. There was a noticeable saturation of the plasma resistance at around 10.5 Ohms for increasing pressure at 15 mtorr for the field on case, and at around 25 mtorr for the field off case (Figs. 3.6(a) and 3.6(b)). The pressure range of this saturation effect closely supports the findings of Arancibia *et al.*, [33] who used a novel ICP coupling system to perform power efficiency measurements in argon.

Since the power efficiency is a ratio of plasma resistance to the contact resistance of the system (Eqn. 3.6), increasing the plasma resistance higher provides depreciating returns for system efficiency. For this reason, the largest gains in power efficiency are found when improving the plasma resistance from low levels especially if the plasma resistance is comparable to the contact resistance of the system. In the case of hydrogen which has low plasma resistance, the increases in plasma resistivity of only a few Ohms from the magnetic filter can equate to a 20% increase in the power transfer efficiency. Whereas in argon the plasma resistance can be increased by 12 Ohms with only a gain of only a few percent in transfer efficiency. This result suggests

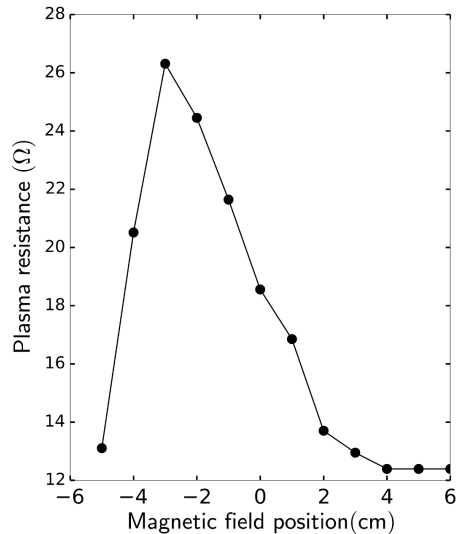
that the best improvements in power transfer efficiency from the magnetic filter is for low resistance plasma gas species. The finding also suggests that the best efficiency gains are made when operating at low gas pressures.

3.3.3 Argon Magnetic Field Dependency

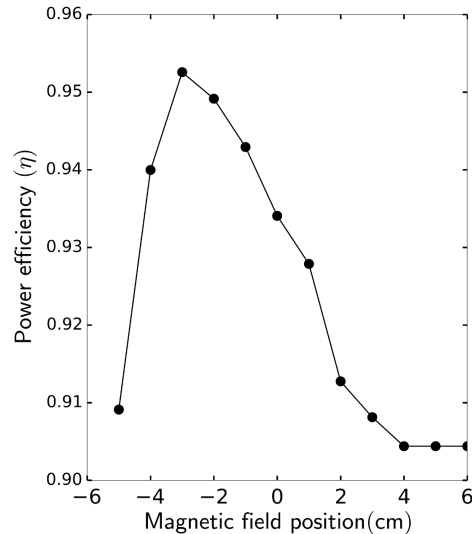
Similar to the previous experiments in hydrogen the position of the filter along the source tube was moved along the x -direction and then separated in the z -direction. Figures 3.7(a) and 3.7(b) show the results for moving the filter in the x -direction along the length of the source. The plasma resistance again shows a strong local effect from the position of the magnetic filter with plasma resistances ranging from 13 Ohms to 26 Ohms. Interestingly the H-mode discharge was not able to be suppressed at any position of the magnetic filter in argon. In fact the maximum plasma resistance is seen when the transverse field is centered behind the antenna at $x = -3$ cm.

In hydrogen placing the filter in this position transitioned the plasma from the H-mode to E-mode but in argon this was actually the optimal position for the filter. This could be due to the plasma skin depth in argon being around only 5 mm compared to several centimeters in hydrogen. The DC magnetic field of the permanent magnets has no skin depth and can penetrate the plasma volume, this means that the transverse field has an increased ability to suppress the formation of the inductive mode in hydrogen but not in argon.

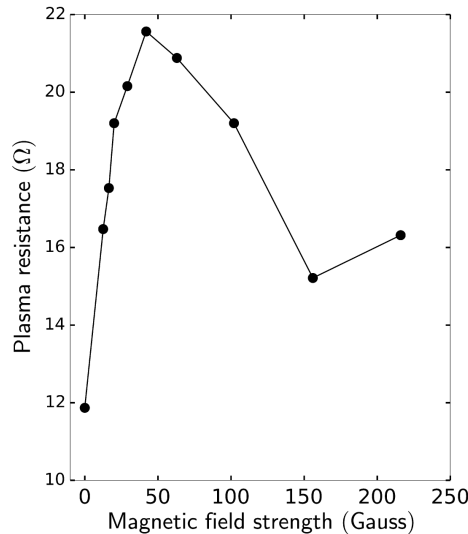
Figures 3.7(c) and 3.7(d) show the effect of separating the magnets in the z -direction when they are stationed at $x = 5$ cm downstream. The gain in plasma resistance is seen to increase from 12 Ohms to 22 Ohms at a field strength of approximately 40 Gauss. The field strength profile trend is similar to hydrogen with an early increase in the resistance followed by a dip, then a recovery. However, this peak is higher than that seen in hydrogen where the peak coincided with the electron cyclotron frequency possibly due to a slight positioning error in the field during this run. Despite a drop in plasma resistance of 14 Ohms when moving the filter from $x = -3$ cm to 4 cm downstream, the plasma transfer efficiency only changes by 4% due to the already high ratio of plasma resistance to contact resistance. These relatively high argon power efficiency measurements agree closely with recent publication of power measurements in argon [33].



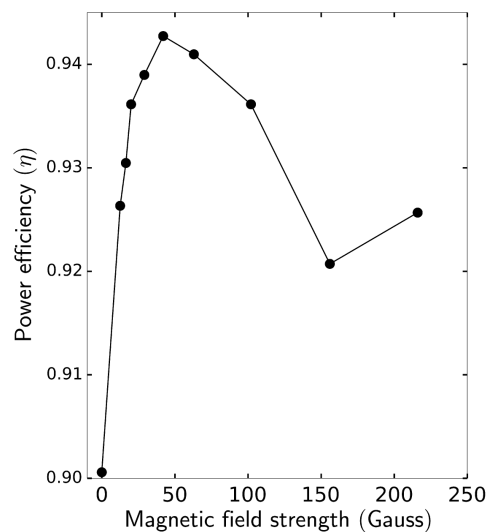
(a) Argon plasma resistance as a function of the center magnetic filter distance from antenna (100 G separated field)



(b) Argon power deposition as a function of the center magnetic filter distance from antenna (100 G separated field)



(c) Argon plasma resistance as a function of the magnetic field strength



(d) Argon power deposition as a function of the magnetic field strength

Figure 3.7: Argon plasma resistances and power deposition fractions changing transverse field position a) and b) and changing the field strength c) and d). The magnetic field was centered at $x = 5$ cm for Figures c) and d). All plots at 100 W at 10 mtorr pressure.

The results in this chapter suggest that the magnetic field geometry strongly affects the power transfer efficiency of the source and so several mechanisms were proposed to explain this effect including increased inductance, conductance and confinement of the plasma. However to fully ascertain the mechanism for the efficiency gains from the magnetic field, a model would need to be developed which takes into account not only the magnetic fields spatial geometry, but also its interaction with the inductive coupling and plasma chemistry.

Modelling this effect analytically is difficult as the spatial sensitivity of the power enhancement presented in this work suggest that at least a 2d axisymmetric B-field solution is required. Since a 2d+ filter field is highly non-linear, adding such a field into analytical models is not straightforward and has been explicitly avoided historically for this reason [115] [47]. Recently a circuit based power transfer model designed to optimize the efficiency of the ITER NBI source was developed [116] which also excluded external magnetic field effects. Basic monte-carlo modelling approaches have shown that the external field can increase the plasma conductance [117] and hence power transfer.

To the authors knowledge, no model has yet had the ability to both quantify dynamic changes in inductive power coupling and changes to plasma chemistry under external magnetic fields. A comprehensive model such as this would be required to compare the dataset presented in this chapter. A leading candidate to achieve the required modelling results of this type would be a hybrid fluid/global model approach similar to that of Yang *et al.*, [118] with the additional inclusion of a 2d+ magnetic field. The development of such a model here lies outside the scope of this work but could be an important choice for future work.

Charged Particle Dynamics Across the Magnetic Filter

This Chapter presents the results of the effect of the magnetic filter on important plasma properties along the length of the source at various pressures. These results are discussed with respect to conditions which are conducive to increased negative ion formation. Section 4.1 presents the electron density profiles, Section 4.2 presents the axial EEPF measurements, Section 4.3 presents results of H₂ rotational temperatures and Section 4.4 presents two models of plasma transport to help explain the results.

Interesting new results emerge in this chapter from the magnetic filter experiments including:

- 1) The formation of a particle 'trap' occurring only at certain pressure ranges and magnetic field strengths.**
- 2) A strong increase in the density of low energy electrons inside the trap downstream of the source.**
- 3) Unexpectedly high electron temperatures near the source antenna at low pressure due to electron cyclotron resonance heating from the edge magnetic field geometry of the transverse filter.**
- 4) Increased gas heating of H₂ rotational temperatures seen with the addition of the magnetic field.**

5) 1d and 3d modelling suggesting a mechanism for the formation of the particle trap inside the magnetic filter and suggesting the parameter range under which it can form.

4.1 Electron Density Profiles

This section presents the electron density measurements from both hydrogen and argon at a variety of pressures for a 200 W H-mode discharge. Measurements were taken using the hairpin probe at 1 cm intervals from the front of the antenna from $x = 0$ cm to $x = 10$ cm. The effect of the transverse filter on electron density was compared.

The first experiments investigating the effect of transverse magnetic filters on plasmas were made in the 1920s [119]. Theoretical treatments in the 1940s indicated that the filter caused decreasing electron temperatures and increases in axial electric field strengths [120]. The Lorentz force from electrons travelling in a cathodic arc through a filter was seen to affect the radial particle distributions and transport in the 1970s [121] [122] and electron transport through a filter was able to be halted creating a negative ion positive ion plasma downstream of the filter [123]. The 1970s and 1980s saw renewed interest in magnetic filtration for both plasma industrial processing [124], the rise of Monte Carlo collisional simulations and the creation of negative ion beam candidates for fusion power heating [125] [126].

Despite the publication history of magnetic filtration in plasmas, the precise mechanism behind particle transport across a transverse magnetic field is still contentious. Classical transport theory at low collisional regimes (1 mtorr to 10 mtorr pressure) disallows electrons from crossing from the source discharge across strong transverse fields as the electrons should be tightly confined in cyclotron orbits to the transverse field lines they encounter and are unable to transport via collisions before being lost to the walls or recombining. Despite this, appreciable electron densities through magnetic fields can still be measured in most plasma sources [127] [128] [129] [21]. Overwhelmingly, plasma sources that use transverse magnetic fields report declines in electron density along the positive gradient of the magnetic field downstream of the filter consistent with the known ability of the magnetic field to inhibit plasma diffusion and mobility. This decline in plasma density is also associ-

ated with the characteristic lowering of electron energy [130] [21] which make the filter desirable for negative ion formation. A recent review was conducted by Aanesland *et al.*, of ion-ion plasmas and provide a brief outline of the contention surrounding the question of filter transport [22] and suggested that models of the electron cooling and negative ion transport are incomplete. Ideally, it would be useful for the filter to lower electron temperatures without a decline in plasma density.

Since 2012, theoretical modelling of new transport mechanisms through transverse filter has been an active research topic which has been inspired partly by problems encountered for optimization of ITER neutral beam prototype sources [91] [35]. Several works covering particle transport across the filter have since been produced including: 1d flux particle in cell (PIC) modelling [38], 2d modelling of flux asymmetries from $E \times B$ drift currents [37], wall-induced pre-sheath transport [39] [131] [36] and experimental external bias control [132]. Despite these recent theoretical developments, there is a strong lack of experimental evidence of obvious non-classical transport through the filter to support it.

In 2016 Cho *et al.*, [133] provided the first experimental evidence of their 'unexpected' increased hydrogen plasma electron density inside their transverse filter. They investigated the role of electron cooling and H^- production in their tandem cusp negative ion system and showed the formation of a peak in electron density which increased with gas pressure and magnetic field strength. The explanation for this increase was suggested as particle trapping due to decreasing perpendicular diffusion with the increasing magnetic field strength. This paper will be discussed further with respect to the results presented in the following section.

4.1.1 Hydrogen Electron Density Profiles

During the first set of axial measurements with the hairpin probe, an increase in the electron density through the magnetic filter in the ICPS was immediately noticed for hydrogen. The operating pressure of 50 mtorr was the first pressure used during initial testing which is higher than that used some applications including NBI sources, however it will be shown that the may be formed at lower pressures which are applicable to NBI relevant conditions.

The electron density profiles were found to be repeatable over several days of testing and so a series of profiles were taken at different pressures to quantify the pressure dependence of the density peak. Six pressure ranges were then chosen from 10 mtorr to 150 mtorr to investigate if the increase in density through the filter occurred only at 50 mtorr. The forward power for the experiments was 200 W and the applied magnetic field used was the standard 250 Gauss filter.

Note that in inductive hydrogen plasmas with less than 1 kW power, the dominant ion present in the plasma is H_3^+ which increases also with higher gas pressures. This has been shown theoretically in ICP modelling [105] [106] [93] and also through early experimental verification using a mass spectrometer which was installed on the ICPS.

Figure 4.1 shows the results for the axial electron density profiles at a variety of pressures in the ICPS with the red profiles taken with the magnetic filter applied and the black profiles show the results without the filter. The electron density profiles taken without the filter show the common exponential decline in density with distance from the driving antenna (linear in the log-scale shown here). With the application of the filter however the formation of a peak in the electron density profile can be seen. The peak forms initially at a pressure range between 10 mtorr and 25 mtorr and reaches a maximum between 50 mtorr and 75 mtorr. At 150 mtorr the density profile looks to be transitioning away from the trapping regime. The density peak appears localized around the center of the filter and is predominantly bound to the area between physical edges of the permanent magnet blocks. The largest difference between magnetically filtered and unfiltered densities occurs in the center of the filter at $x = 5 \text{ cm}$ and is more than three times higher for the 50 mtorr and 75 mtorr peaks. Electron densities for hydrogen at this power are seen to range from $2 \times 10^{15} \text{ m}^{-3}$ up to $7 \times 10^{16} \text{ m}^{-3}$.

To test whether or not the density peak was an artefact from anisotropic electric permittivities arising from an effect of the magnetic filter, density profiles were measured using both parallel and perpendicular orientations of the hairpin probe with respect to the magnetic field lines. The results were shown previously in the diagnostics chapter (Figure 2.18 in Chapter 2) and show the density peaks are not a measurement error from anisotropy in the plasma permittivity.

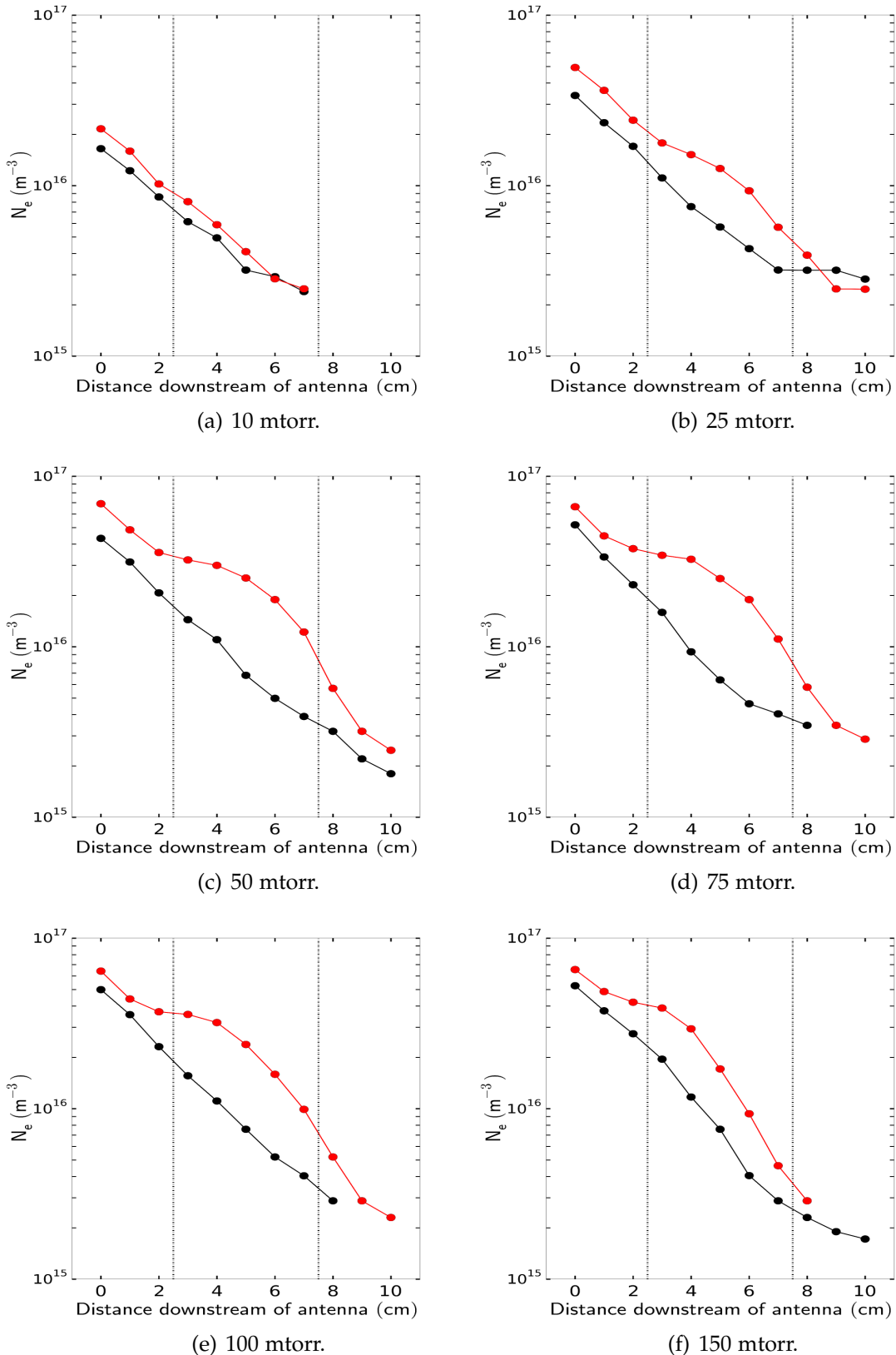


Figure 4.1: Hydrogen plasma electron densities measured using the hairpin probe. (Black) no field, (red) 250 G field center d at $x = 5$ cm.

This same density increase seen in Figure 4.1 was also seen by Cho *et al.*, [133] in their negative ion source showing a similar width and increase inside the peak. While the magnetic field strength here of 250 G is similar to their peak field of 220 G, the peak seen here is centered on the peak magnetic field position rather than a few centimeters upstream of the peak. This may be due to the presence of a bias electrode near the filter in their work. The pressure of the peak formed in this work begins above 10 mtorr and has a maximum around 50 mtorr to 75 mtorr which is above the pressures used in NBI devices. However, in the work of Cho *et al.*, [133] the peak forms at a lower pressure of 3 mtorr (0.4 Pa) and so this feature is reproducible at NBI relevant pressures.

The ability to produce the density peak and tailor its creation at different gas pressures is due to a number of factors including collisional frequency, ion mass, magnetic field strength, and the presence of a tandem cusp field. These factors will be discussed later with transport modelling in Section 4.4 and the criteria for generating this trapping effect in a source will be presented. It will be also be shown in Chapter 5 that optimization of this density peak may be exploitable for use in fusion relevant plasma sources using different magnetic field combinations.

While electron-driven processes are usually used to explain cross filter transport, these results for hydrogen can instead be explained by considering ion-driven plasma transport initiating the cross filter diffusion followed by particle trapping occurring over microsecond time scales for ion diffusion.

Due to the low ionization fraction in the ICPS the dominant collisional transport processes in the plasma are the elastic collisions between charged particles and neutrals [92] [134]. At pressure ranges between 1 mtorr and 100 mtorr, the light-weight H_3^+ ion dynamics of hydrogen plasmas have several different properties which can contribute to this trapping behaviour. Modelling of the filter dynamics in Section 4.4 of this trapping effect will show that the filter particle transport is dominated by the ion transport properties and ∇B drift fields but a qualitative explanation of the process will be explained briefly here.

At the lower measurement pressures here of around 10 mtorr the H_3^+ ions exhibit weakly collisional magnetized kinetics characterized by long mean free paths and with wall loss lifetimes on the scale of roughly 30 μs to 70 μs .

At intermediate pressures between 25 mtorr and 75 mtorr the combination of moderate mean free paths and Larmor radii on the order of the source tube width allows for strong cross field transport from upstream near the antenna into the central region of the magnetic filter where they become magnetized and trapped.

At higher pressures of 100 mtorr to 150 mtorr, the ions are highly collisional and freely diffuse throughout the source across field lines at long timescales of 100 μ s to 500 μ s. Table 4.1 summarizes the ion properties of H_3^+ through the filter region. At the trapping pressure of 50 mtorr the Table 4.1 shows that the momentum exchange collisions per cyclotron orbit ($v_m \cdot \omega_{ci}^{-1}$) is approximately 1.91 meaning that collisions occur at each half cycle which allows for the maximum cross field displacement per collision. This idea is qualitatively supported by Hayashi *et al.*, [135] who used different ion mass plasmas to show an indirect relationship between ion mass and filter transport. Their work reasoned that the ion Larmor radius is related to filter transport, but they provided no density measurements or transport theory.

Table 4.1: Leading collision parameters for dominant hydrogen ions (H_3^+) in the ICPS. 0.05 eV ion energy at (10 Gauss / 250 Gauss) respectively in the brackets

Parameter	1 mtorr	10 mtorr	50 mtorr	100 mtorr
Mean free path λ_{mfp} (cm)	41	4.1	.83	0.04
Cyclotron frequency ω_{ci} (kHz)	(5 / 126.9)	(5 / 126.9)	(5 / 126.9)	(5 / 126.9)
Collision frequency v_m (kHz)	4.85	48.5	242.8	485
Larmor radius r_L (cm)	(6.3 / 0.25)	(6.3 / 0.25)	(6.3 / 0.25)	(6.3 / 0.25)
Collisions per cyclotron orbit $v_m \cdot \omega_{ci}^{-1}$	(0.97/0.38)	(1.7/0.38)	(48.56/1.91)	(97/3.82)

These initial experimental results for hydrogen on the ICPS show that the transverse filter can cause particle traps to occur which increase the local plasma density by several factors. This trap has been previously shown to form at NBI relevant pressures [133] and so this chapter will provide a suite of measurements and modelling of the source to elucidate the mechanisms which lead to its formation. This work could help inform a future set of ex-

periments which could specifically target this phenomena and optimize the process on an up-scaled negative ion device at lower pressure.

It should be noted that when the magnetic field is in place, a 'dark' region occurs in the vicinity of where this peak in plasma density occurs (See Figure 2.2(b) from Chapter 2 for a photograph of the dark region). Previously shown ion saturation and electron current data (Figs. 2.13) support these density measurements which indicate that this region is certainly not devoid of plasma. Further supporting evidence of the density peak using EEPF measurements will be shown in Section 4.2. The lack of light emission under the magnets implies low levels of electronic de-excitation are taking place within the filter region. Recombination events are rare within the plasma bulk due to the low cross section for radiative recombination [136] and the majority of recombination occurs due to charged particle flux to the walls with an emission in the invisible ultraviolet region. Despite this, successful measurements of the optical emission through the dark region were made and will be shown in Section 4.3.

4.1.2 Hydrogen HP and LP Comparison

The hairpin probe electron densities from Figure 4.1 were compared to the Langmuir probe measurements using an integration of the EEDF (see Eqn. 2.7). It should be noted that while the EEDF and EEPF look similar, the EEDF is used for the density integration and the EEPF is used for the effective electron temperature fits. Using the EEDF for the electron temperature fits result in incorrect temperature fits.

Figure 4.2 shows the hairpin electron density profiles overlain with the densities calculated from the Langmuir probe EEDFs. The Langmuir probe densities are seen to generally follow the hairpin probe profiles.

The flattening of the densities toward the antenna for the LP measurements result from the RF fluctuations near causing rounding of the EEPF near the plasma potential which degrades the resolution of the low energy electrons arriving at the probe tip. In this case, increases in RF close to the antenna are balanced by increasing electron density resulting in a roughly flat density profile toward the source.

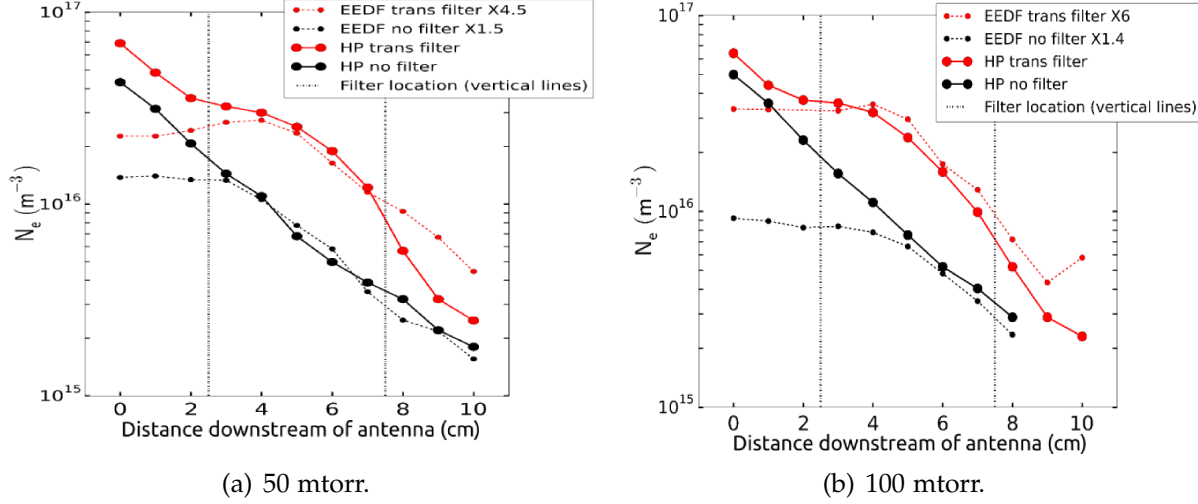


Figure 4.2: Comparison of hairpin probe electron densities with EEDF integration densities. (black) no field, (red) 250 G field center d at x = 5 cm. Vertical lines show the physical edge of the filter magnets.

The EEPF profiles shown in this chapter show data trends and EEPF electron temperatures consistent with other ICP sources [21] [130]. This rounding effect can be unavoidable in some ICP systems and can be seen even when using high quality commercial probes [33].

4.1.3 Magnetic Permeability and Electron Cooling

It should be stated briefly about how far into the plasma the magnetic field penetrates. Under the effect of a magnetic field, a plasma can be considered to be a diamagnetic material whereby free charges in cyclotron orbits create discrete magnetic moments in opposition to an external magnetic field. This process is analogous to the formation of electric dipole moments which arise from external electric fields to create the electric permittivity of a material. The magnetic dipoles can be described by the magnetization moment:

$$\vec{M} = -\hat{z} n(\vec{r}, \vec{v}) \mu_{mag} \quad (4.1)$$

where μ_{mag} is the magnetic permeability of the plasma, n is the number of particles at position \vec{r} with velocity \vec{v} , and $-\hat{z}$ is the unit vector opposite the direction of the external magnetic field. For low density plasmas less than

10^{17} m^{-3} , the plasma is essentially transparent to DC magnetic fields and the field is able to permeate throughout the source. The magnetic field penetration from the filter is not strongly attenuated in either hydrogen or argon discharges in the ICPS and so the axial measurements taken in the center of the tube are under the same magnetic field conditions for both gasses.

4.1.4 Hydrogen Magnetic Field Strength Comparison

A set of experiments were performed to examine the formation of the density peak as a function of transverse filter strength. Figure 4.3 shows the results for increasing magnetic field strength at two pressures. Three types of filter were used with the same physical dimensions as the standard 250 Gauss filter presented in the majority of this work. A smaller set of 120 Gauss transverse field strength (Fe) magnets were used (blue profiles) along with a pair of strong neodymium 800 Gauss magnets (green profiles). The electron density profiles were measured at two pressures of 10 mtorr and 50 mtorr with the three filter strengths.

At 10 mtorr the formation of a peak did not occur at any of the field strengths and indeed the 800 Gauss field was shown to inhibit electron densities into the filter immediately from the front end of the antenna at $x = 0 \text{ cm}$. However at the higher pressure of 50 mtorr a small peak is seen to form under the magnetic filter around 120 Gauss and grows in size at 250 Gauss. The trapping effect of the filter therefore is seen to be a maximum at magnetic field strengths around 250 G and intermediate pressure ranges of around 50 mtorr.

At the higher pressure of 50 mtorr here (Fig. 4.3(b)) the 800 Gauss filter is seen to increase the upstream density by up to a factor of 4 near the antenna. This increase in upstream electron density is due to the strong suppression of perpendicular diffusion of the plasma and the magnetic filter acts to reduce the effective plasma size (d_{eff}). At higher gas pressures d_{eff} has been shown to become shorter [137] [70] and so the plasma 'sees' a smaller chamber size for a given RF power yielding higher local plasma densities. This result shows that the transverse magnetic filter can also be used to control the effective system size and increase densities inside the discharge by up to a factor of 6 under certain collisional regimes.

These two experiments show that transport and trapping property of the filter in hydrogen is a function of not only pressure (collisionality) but also mag-

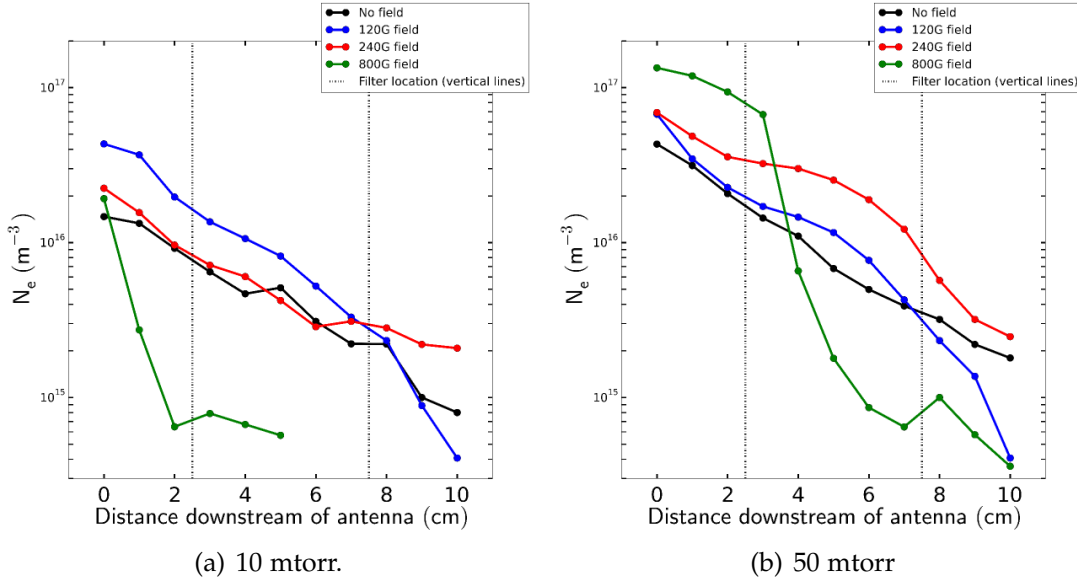


Figure 4.3: Investigation of the density peak as a function of magnetic filter strength at 200 W.

netic field strength and both of these are required to create the density peak. This finding shows that the origin of the increased filter transport is related to an interplay between collisionality and cyclotron orbits. An argon plasma was next measured to investigate the dependence of ion mass and collisionality on the trap formation.

4.1.5 Argon Electron Density Profiles

Figure 4.4 shows the axial electron density measurements in argon across a range of pressures. Electron densities in argon were measured between $3 \times 10^{15} \text{ m}^{-3}$ to $3 \times 10^{17} \text{ m}^{-3}$ which were higher than for the same 200 W forward power in hydrogen due to the higher plasma resistance in argon (see power transfer results in Chapter 3). Near the antenna the electron density approached 10^{18} m^{-3} and exceeded the density limit of the hairpin design used for these experiments (see Section 2.3.9).

In contrast to the hydrogen measurements, no development of a density peak was seen in argon across the pressure range of 2 mtorr to 75 mtorr for the 250 Gauss filter. The filtered and unfiltered density profiles show similar den-

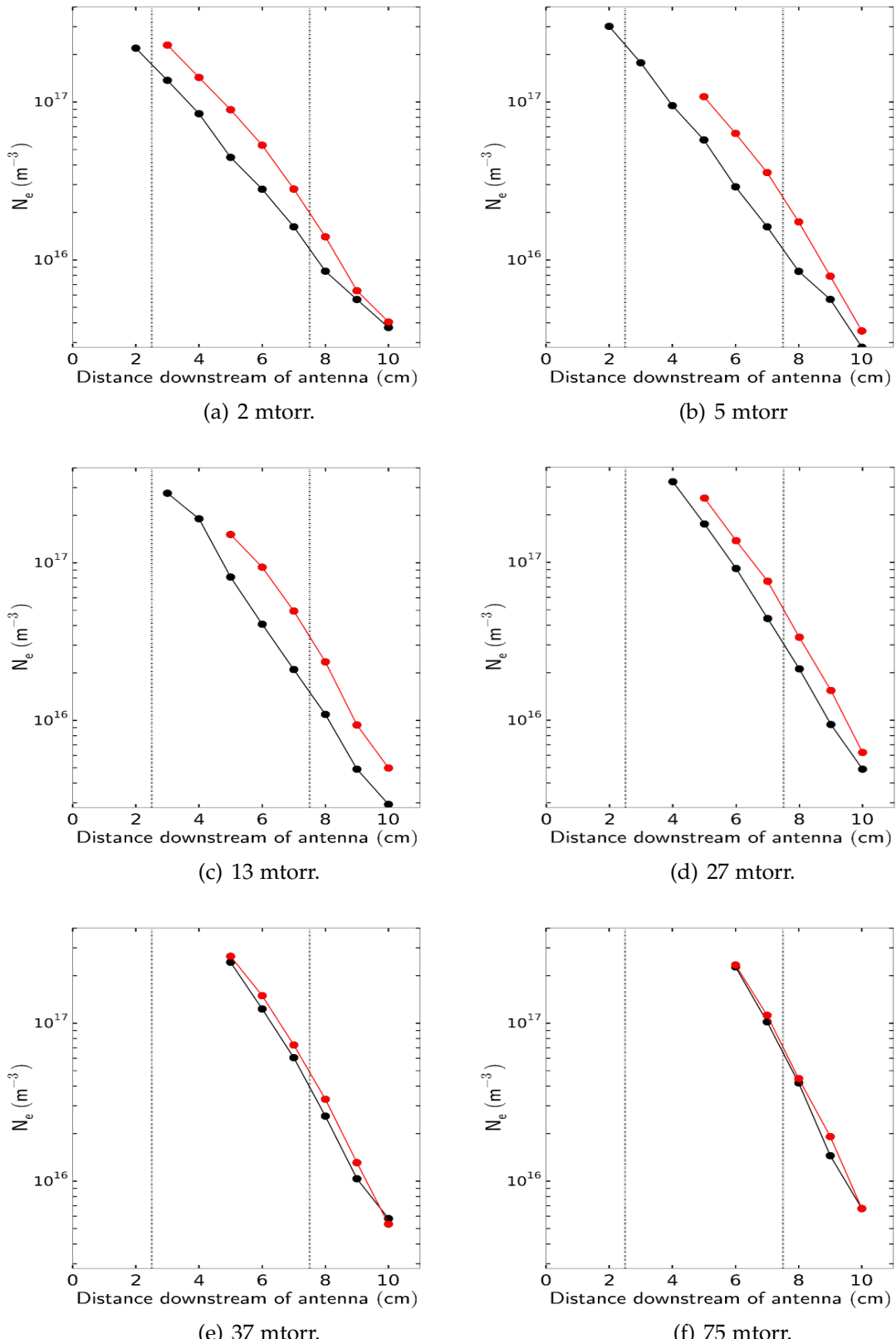


Figure 4.4: Argon plasma electron densities measured using the hairpin probe at 200 W. (black) no field, (red) 250 G field center d at $x = 5$ cm. Vertical lines show the physical edge of the filter magnets.

sities throughout the source. This finding implies that the ion mass or ion collisional frequency may be a key variable governing the formation of the trap.

Argon plasmas have similar frequencies for electron-neutral collisions to hydrogen but have an order of magnitude higher collision frequency for ion-neutral collisions than hydrogen. The higher argon ion-neutral collision cross section means that the argon ions have five times the collisional frequency as hydrogen for a given gas pressure and so the cyclotron orbits are frequently disrupted and the ions can diffuse via collisions through the filter more easily.

Compared to hydrogen, argon's heavier ion mass means that the Ar^+ ions also have larger Larmor radii and so are unable to become magnetized even at the center of the magnetic filter at 250 G. Modelling in Section 4.4 will show the argon ions also exhibit long residence times, between 100 μs and 1000 μs , and are free to collisionally diffuse throughout the filter and the source.

The argon electron density measurements support this as they show no local effect of the magnetic filter across a wide range of pressures (Fig. 4.4). The negligible effect of the filter on argon density profiles was also seen by Aanesland *et al.*, [21] at 10 mtorr using a similar magnetic filter in a conductive walled source.

The magnetic field is seen to produce higher electron densities in argon by around 2 factors at pressures up to 75 mtorr. These power efficiency gains from the magnetic field become lower as the pressure is increased.

Since the magnetic field penetration and collisional frequencies are similar between argon and hydrogen, the strength of the electron cooling effect is instead determined by the ion mass. The amount of energy loss per background gas collision is two orders higher in hydrogen and so electrons require less collisions to dissipate their energy. Inelastic collision pathways also play a role as argon also exhibits a relatively high threshold for electronic excitations of 12.38 eV, whereas hydrogen has rovibrational molecular channels which can be accessed from as low as 0.1 eV to 10 eV [92].

4.2 Electron Energy Distributions and Plasma Parameters

This section shows spatial measurements through the ICPS including: electron energy distributions, floating potentials and effective electron temperatures for both hydrogen (Sec. 4.2.1) and argon (Sec. 4.2.2). The effect of the magnetic field strength on electron cooling will also be shown (Sec. 4.2.3).

This section characterizes the effect of the magnetic filter on the electron populations at 10 mtorr, 50 mtorr, and 100 mtorr pressure and demonstrates that the peak in electron densities seen in the previous section consists of a high density of low energy electrons. The formation of the trap is accompanied by a slight 'dome' shaped potential profile which is seen to develop at higher pressures centered around the filter.

The evolution of the EEPF as the electron population is the main parameter for assessing the plasma chemistry of the source as many of the key plasma chemistry processes are related to the electron speed via minimum threshold energies or collisional cross sections. The EEPF profiles provide a snapshot of the temperature of the electron population and can highlight regions where differing chemistry is taking place within the source including negative ion formation.

Many publications have been made showing EEPF measurements in both ICP and CCP systems including detailed measurements of the dependencies of electron temperatures to pressure and power levels for noble gasses [138] [66], spatial profiles of electron temperatures through transverse filtered systems [130] [21], novel ICP coupling regimes [33] and pulsed afterglow plasmas [15]. Hopkins and Graham [139] performed spatially resolved EEPF measurements through their magnetic filter systems back in the late 1980s however they were using a hot cathode system at very low pressure with a high central magnetic field strength of around 1000 G. They showed a strong suppression in electrons at the filter region and they created a situation similar to the conditions seen in Figure 4.3(a) where a strong magnetic filter at low pressures reduces the effective size of the system along with the opportunities for optimization and customization of the plasma.

While taking EEPFs measurements inside a magnetic filter is not new, often

the measurements are taken at either a single position or for a single gas pressure condition. This dataset presents comprehensive measurements of the spatial cooling effect of the filter in both hydrogen and argon at 1 cm intervals and reveals the spatial evolution of the electron population using the 250 G filter. Detailed comparisons between filtered and unfiltered cases will be shown including comparisons to the same conditions in argon.

The electron populations shown in the following sections were measured using a custom made compensated Langmuir probe (see Section 2.3.1) inserted from the chamber side of the system through the central tube axis at 1 cm intervals from $x = 0$ cm to $x = 10$ cm downstream. The profiles were measured under continuous power operation (no pulsing) at 200 W and the IV curves were generated by sweeping the Langmuir probe at kHz frequencies using an Impedans ALP unit. Each IV curve was an average of 100 profiles which were exported as CSV files for post-processing to calculate the EEPF, electron temperature and floating potentials. The effective electron temperature was calculated from the inverse slope of the EEPFs as described in Chapter 2 Section 2.3.2. The dynamic range of the EEPFs is around 3 orders of magnitude which is a good indicator for resolving the high energy electron 'tails'. All profiles were taken while operating the inductive H-mode.

Measurements to obtain the EEPF inside the ICPS proved to be difficult and required many probe construction iterations. The difficulties encountered while measuring the EEPF in the ICPS included:

- 1) The chamber geometry required long Langmuir probe poles which attracted larger parasitic capacitances and required the custom made RF chokes to be located near the tip of the Langmuir probe rather than externally.
- 2) High plasma temperatures near the antenna destroyed RF choke circuitry and casings several times before a more robust design was made.
- 3) The combination of both dielectric and conducting surfaces surrounding the source generated different capacitive field coupling environments.

Despite these issues, a probe design was eventually made such that the EEPF could be reliably resolved with a reliable low energy electron resolution under most conditions and a long dynamic range of 3 orders of magnitude.

4.2.1 Hydrogen EEPF Profiles

4.2.1.1 IV Profiles

Figure 4.5 shows an example of the raw IV profiles and their second derivative for hydrogen used to calculate the EEPFs, electron temperatures and floating potentials. For a general description of the IV profile and its features, see Section 2.3.1.

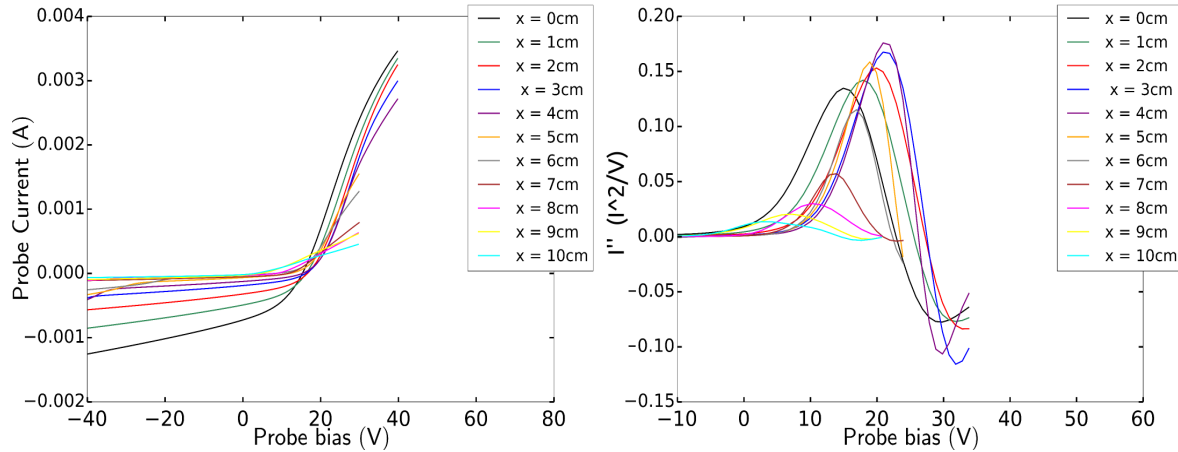
Without the magnetic filter applied, the IV profiles and their second derivative are shown in Figures 4.5(a) and 4.5(b) (top figures), and with the application of the filter are shown in Figures 4.5(c) and 4.5(d) (bottom figures).

Both filtered and unfiltered raw IV profiles (Figs. 4.5(a) and 4.5(c)) show increasing ion saturation current with increasing negative bias. This is a common Langmuir probe effect due to the increasing Debye sheath as a function of voltage. The expansion only affects I_{sat} region and does not affect the results as the plasma density is not measured using the ion saturation current. The IV profiles with the magnetic filter applied (Fig. 4.5(c)) show a reduction in the electron saturation currents. This effect is not due to lower electron densities but rather a reduction in the electron temperature when the magnetic filter is applied which reduces the current to the probe.

Figure 4.5(d) shows the second derivatives of the IV when the magnetic filter is applied. The shorter distance between the first peak and the zero crossing of the profile means that the 'knee' of the IV is better defined and allows for better resolution of the low energy electrons compared to the unfiltered profiles shown in Figure 4.5(b). This better resolution of the second derivative is due to the property of the magnetic filter which was shown to lower the RF noise inside the plasma (see Section 2.3.3).

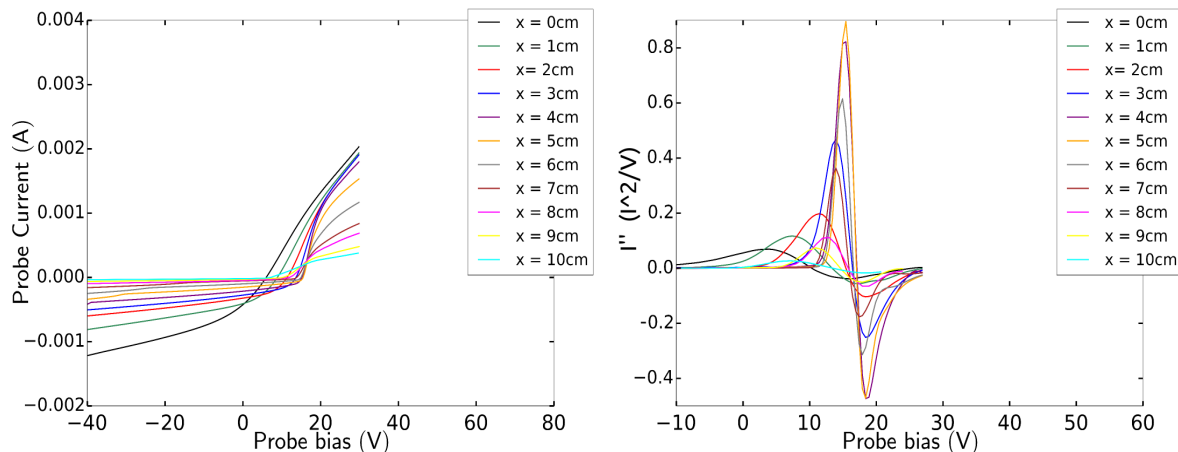
4.2.1.2 10 mtorr Profiles

Figure 4.6 shows EEPF measurements, T_e and V_f made at 10 mtorr in hydrogen for both filtered and unfiltered source conditions. Without the magnetic



(a) Axial profiles of IV characteristic profiles without a filter in hydrogen at 50 mtorr 200 W.

(b) Axial profiles of 2nd derivative IV characteristic profiles without filter in hydrogen at 50 mtorr 200 W.



(c) Axial profiles of IV characteristic profiles with the filter in hydrogen at 50 mtorr 200 W.

(d) Axial profiles of 2nd derivative IV characteristic profiles with the filter in hydrogen at 50 mtorr 200 W.

Figure 4.5: Compensated Langmuir probe, first and second derivatives, with and without the magnetic filter. Profiles in 50 mtorr hydrogen at 200 W.

filter in place (Fig. 4.6(a)), the EEPFs show similar Maxwellian populations of electrons throughout the length of the ICPS and a steady reduction in density with distance from the source is seen. This shows that the electron populations in the ICPS are Maxwellian and can be considered collisionally thermalized even at 10 mtorr.

However, with the application of the magnetic field, the electron populations exhibit strong localized spatial dependency. Figure 4.6(b) shows the EEPFs with the magnetic filter applied where a clear change in the electron population is evident with a hot population of electrons at the front of the antenna at $x = 0$ cm (black profile). The increasing slope of the EEPF profiles toward center the filter (orange profile) indicate a cooling of the general population with the lowest electron temperatures occurring around the center of the filter. The change in EEPFs with the application of the filter is well known effect and has been characterized for electronegative plasmas previously including hydrogen [130] and SF₆ [128]. The shift from non-local kinetics to local kinetics with the application of the magnetic field is due to the electrons becoming magnetized and confined to field lines. This forces them to collisionally dissipate their energy locally. At pressures below 10 mtorr, a cooling effect can also be seen as a result of the faster electrons being preferentially lost to the walls along transverse field lines before they can lose their energy collisionally.

Figure 4.6(c) shows the effective electron temperature, with the unfiltered profile (black) and the filtered profile (red) calculated from the slopes of the EEPFs. The unfiltered profile remains similar throughout the source with electron temperatures ranging from 4 eV to 5 eV. These flat temperature profiles are indicative of semi non-local electron kinetics whereby the mean free path for momentum transfer for the electrons is approaching the size of the plasma system. Under these conditions the mean free paths for the electrons in the ICPS is around 3 cm with residence times in the system of between 100 ns and 300 ns at 10 mtorr. These conditions are typical for low pressure discharges in inductive systems [140] [60].

With the application of the filter (red profile) the electron temperature is seen to reach as high as 12 eV near the antenna and as low as 1 eV inside the filter region. This electron temperature is very high for a low power inductive source. The high electron temperature occurs only when the filter field is applied at this pressure of 10 mtorr. This high electron temperature effect is likely due to a resonance between the frequency of the driven inductive

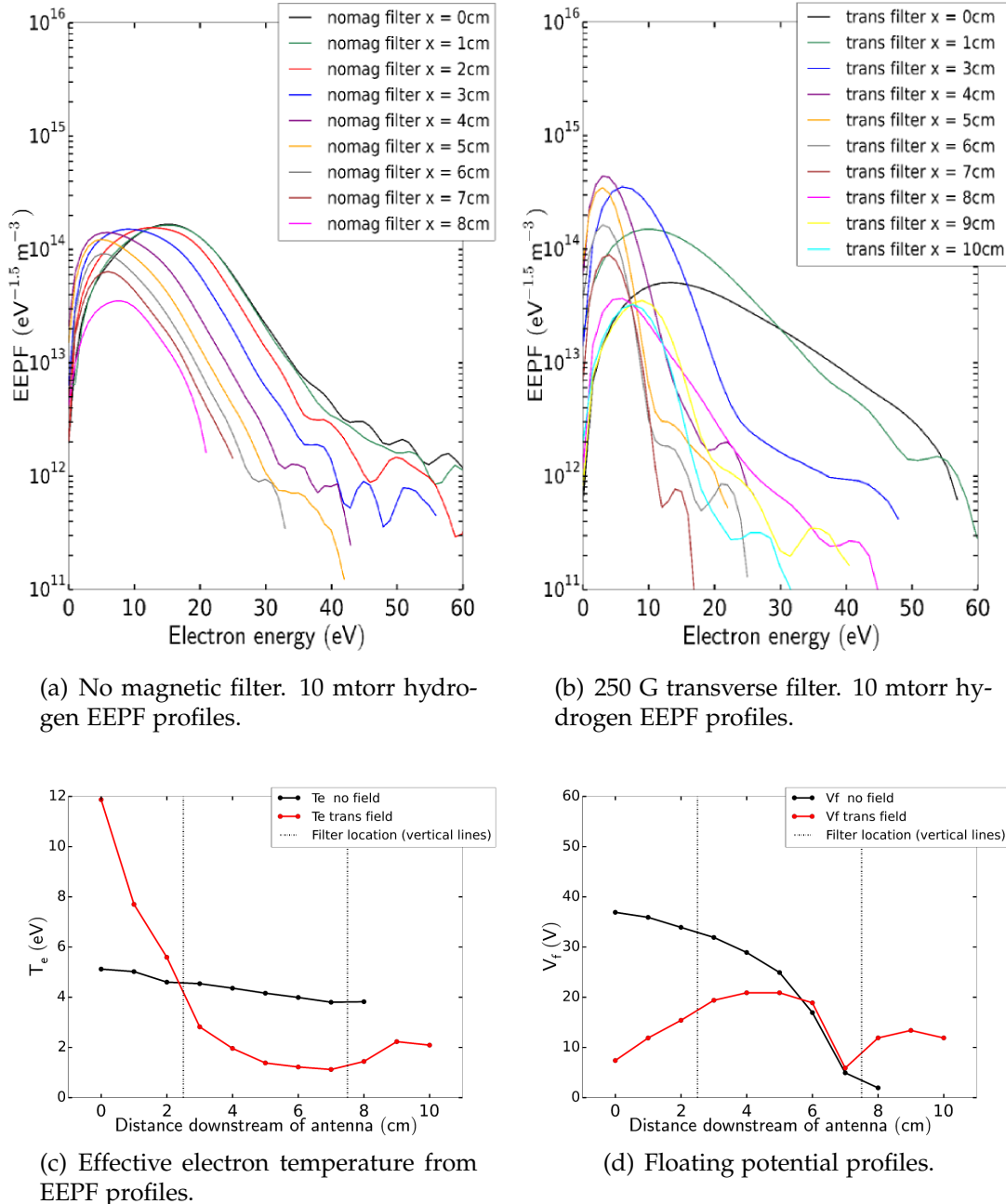


Figure 4.6: Hydrogen EEPF profiles, T_e , and V_f at 10 mtorr, spatial evolution of plasma properties downstream of the antenna. The filter is centered at $x=5$ cm. Measurements taken at 200 W forward power and at 10 mtorr pressure.

electric fields (ω) of 13.56 MHz and the cyclotron orbits of the electrons (ω_{ce}). Near the front of the antenna, the edge of the magnetic filter has a weak x-directed magnetic field component of around 5 G to 9 G which corresponds to an electron cyclotron frequency of 13.56 MHz and 27.12 MHz for the fundamental and first harmonic cyclotron frequencies respectively. This effect of electron cyclotron resonance (ECR) heating has been seen in other magnetically enhanced ICP systems such as in Lee *et al.*, [110] and more recently in the work of Kim *et al.*, [34]. The effect here is seen to produce far higher electron temperatures than in those works which indicates that the heating effect may be quite sensitive to the position of the filter with respect to the antenna. The high electron temperatures here correlate with the strong increase in forward power transfer seen in Chapter 3 which supports the hypothesis that the power is being transferred to the electron population via ECR heating.

This unexpectedly high resonance heating from the filter offers another control option possibly for processing applications. Electron cyclotron resonance enhancement has been used to create hot localized plasma conditions previously in industrial fabrication etching but this often requires the careful use of external microwave sources (eg. [141]). These results suggest that specific placement of permanent magnets could be used to tailor location-specific ECR for a variety of future uses in plasma processing which require localized hot electron populations or high temperature gradients.

Inside the filter the electron temperature is as low as 1 eV however, these EEPF profiles can also exhibit hot population 'tails' (Figure 4.6(b)) (blue profile)). These hot tails are typically in the range of 10 eV to 20 eV and are at a lower density compared to the bulk electrons. These tails can be important not only for maintaining excitation and ionization processes but also for undesirable destruction processes such as in the case of negative ions due to electron detachment: $e + H^- \rightarrow 2e + H$ [62]. The other primary destruction process for negative ions is mutual neutralization and electrons need to be kept below 2 eV to maintain electron stripping rates below those of mutual neutralization [142].

The floating potential profile in the unfiltered case (Fig. 4.6(d)) (black profile) ranges between 38 V near the antenna to almost 0 V at $x = 8$ cm downstream. The application of the magnetic filter showed a marked change in the overall potential structure with potentials ranging from around 8 V inside the wave coupled region, to a peak of around 20 V inside the filter.

4.2.1.3 50 mtorr Profiles

These EEPF profiles taken at 50 mtorr (Fig. 4.7) represent measurements of the electron population though the ideal conditions for the density peak formation was seen previously in Section 4.1.1). The 50 mtorr profiles show again Maxwellian profiles for both filtered and unfiltered cases and exhibit lower overall electron populations compared with the 10 mtorr case.

The filtered EEPFs show strong cooling toward the center of the filter and importantly, the filter shows not only a cooling population of electrons but also an increased density of the low energy electrons at the center of the filter (Fig. 4.7(b) orange profile). This is an important result as these measurements are taken though the maximum of the density peak and they show that the filter is trapping a high density of low energy electrons which is ideal to assist dissociative attachment that can increase negative ion formation. Furthermore, EEPF results showing an increase in low energy electrons through a magnetic filter in hydrogen are rare and the only other case the author is aware of in the recent work by Cho *et al.*, [133] using a low power prototype NBI source.

These results represent a new effect of the transverse filter and can help answer broader questions related to plasma transport across magnetic fields by presenting some of the first reproducible experiments showing filter transport and trapping. Historically electron temperatures and electron densities are seen to go down together which is undesirable as a lower density of electrons produces less opportunities for negative ion formation. This result shows that electron densities in hydrogen can be increased at locations far from the initial plasma discharge and together with the findings of Cho *et al.*, show that this density peak can be created over a wide range of pressures.

Figure 4.7(c) shows the effective electron temperatures at 50 mtorr which range from around 4.5 eV to 2.5 eV for the unfiltered case and from 6.5 eV down to 0.5 eV for the filtered case. The higher pressure reduces the overall electron temperature due to increased collisional losses. Interestingly the 50 mtorr T_e profiles show a reduction in the high energy upstream electrons seen in the 10 mtorr filtered plasma. This can be explained by the increased electron collisionality at the higher pressure either disrupts the efficiency of the ECR power coupling inside the discharge or the electrons have more opportunity to collisionally cool by the time they reach the center of the tube and are measured on the Langmuir probe.

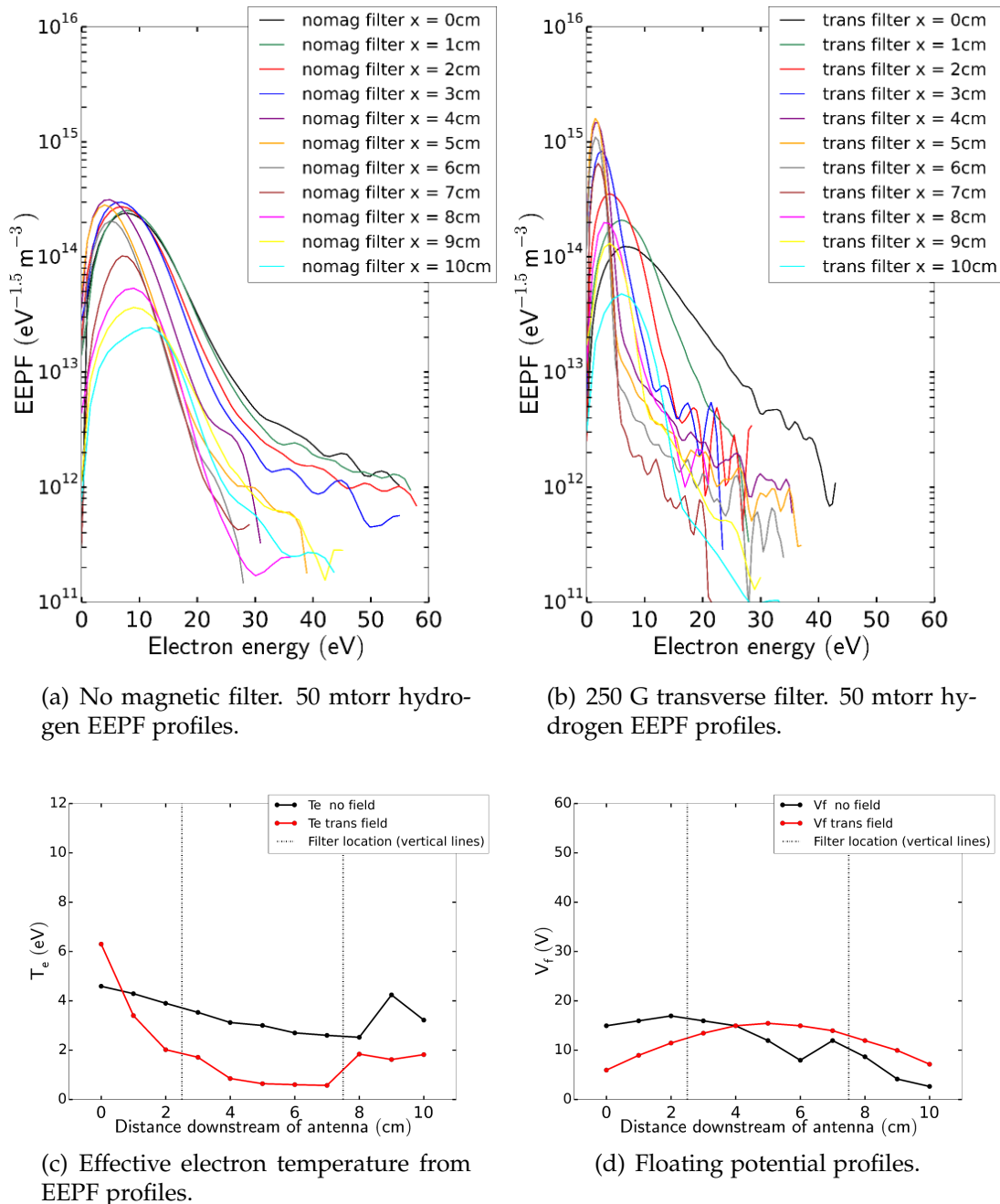


Figure 4.7: Hydrogen EEPF profiles, T_e , and V_f at 50 mtorr, spatial evolution of plasma properties downstream of the antenna. The filter is centered at $x=5$ cm. Measurements taken at 200 W forward power at 50 mtorr.

At 50 mtorr (Fig. 4.7(c)), the electrons are still strongly magnetized within the filter region but undergo more collisions prior to being lost to the walls. The collisional cooling mechanism is more efficient under these conditions and is seen here to generate lower overall electron temperatures than at the 10 mtorr pressure range. The effective electron temperature inside the filter region is very low at around 0.5 eV. A hot tail of 5 eV electrons also exists in the filter center which comprises approximately 1% of the total population. For electrons over the ionization threshold for H₂ of 15.43 eV, only 0.01 % of the population exhibit the energy required for this ionization reaction: $e + H_2 \rightarrow H_2^+ + e$. This finding suggests that the high electron densities seen inside the filter region cannot be generated locally from ionization but are instead being transported from elsewhere in the source. Since these electrons downstream of the antenna are no longer within the vicinity of the azimuthal inductive current, there is no way to recouple energy to the electrons and the population is collisionally cooled over time during transport into the filter region.

These EEPF measurements explain the 'dark region' observed in the source tube where the electronic de-excitation emissions from higher energy states of H₂ are not occurring. The EEPFs in Figure 4.7(b) show a strong reduction in the electron energies above 10 eV which means that the optical emission channels responsible for the visible discharge (primarily from H₂) are not able to be pumped by sufficiently energetic electron impact inside the filter region and this indicates that a majority of the gas population is in the electronic ground-state inside the dark region of the filter. While the electronic state is mostly in the ground state, the H₂ rovibrational energy of H₂ may not be in the ground state as the cross section for pumping rovibrational modes occurs at a much lower energy range < 1 eV range [92].

The EEPF profiles inside the dark region are not only below the standard ionization threshold but are also below the energy threshold for destruction of vibrational states via dissociation $H(v)_2 + e \rightarrow H_2^+ + 2e$ and $H(v)_2 + e \rightarrow H_2^+ + 2e \rightarrow H^+ + H + 2e$ [136]. This implies that rovibrational states from upstream are also not destroyed through the filter region. The following Section 4.3 will present optical emission results to ascertain the rovibrational population along the source.

Finally at 50 mtorr, a 'dome' shape potential profile begins to form around

the magnetic field center (Figure 4.7(d)) with V_f potentials ranging between 5 V and 15 V. This dome potential appears at the pressures consistent with the formation of the density peak (Chap. 4.1, Fig. 4.1(c)) and could indicate that the trap is slightly rich in positive ions which lends support to the theory of ion-driven processes leading to its formation.

4.2.1.4 100 mtorr Profiles

The 100 mtorr EEPF profiles in Figures. 4.8(a) and 4.8(b) show an increased overall cooling effect and exhibiting similar properties to the 50 mtorr case including an increase in the low energy electrons (< 4 eV) and also show a further reduction of the hot population tails.

The effective electron temperatures from the EEPFs at 100 mtorr are shown in Figure 4.8(c) showing electron temperatures ranging between 4.5 eV and 2 eV for the unfiltered case and between 4 eV and 0.3 eV for the filtered case. The upstream electron heating is seen to be completely suppressed at the higher collisional regime with lower electron temperatures than the unfiltered case across the entire length of the source.

The domed floating potential profile is seen to persist at this pressure when the filter is applied (Fig. 4.8(d)) with floating potentials ranging between 0 V and 10 V. This is consistent with the continuation of the density peak from the trap seen previously in the electron density profiles at this pressure (Fig. 4.1(e)).

4.2.2 Argon EEPF Profiles

Comparative axial measurements of the EEPF profiles were conducted in argon. Data is presented for two pressure regimes, 10 mtorr and 50 mtorr. The magnetic field shows less localized effects in argon, less electron cooling and negligible changes to the floating potential profiles which are findings consistent with the reduced effect of the filter on the electron population in argon.

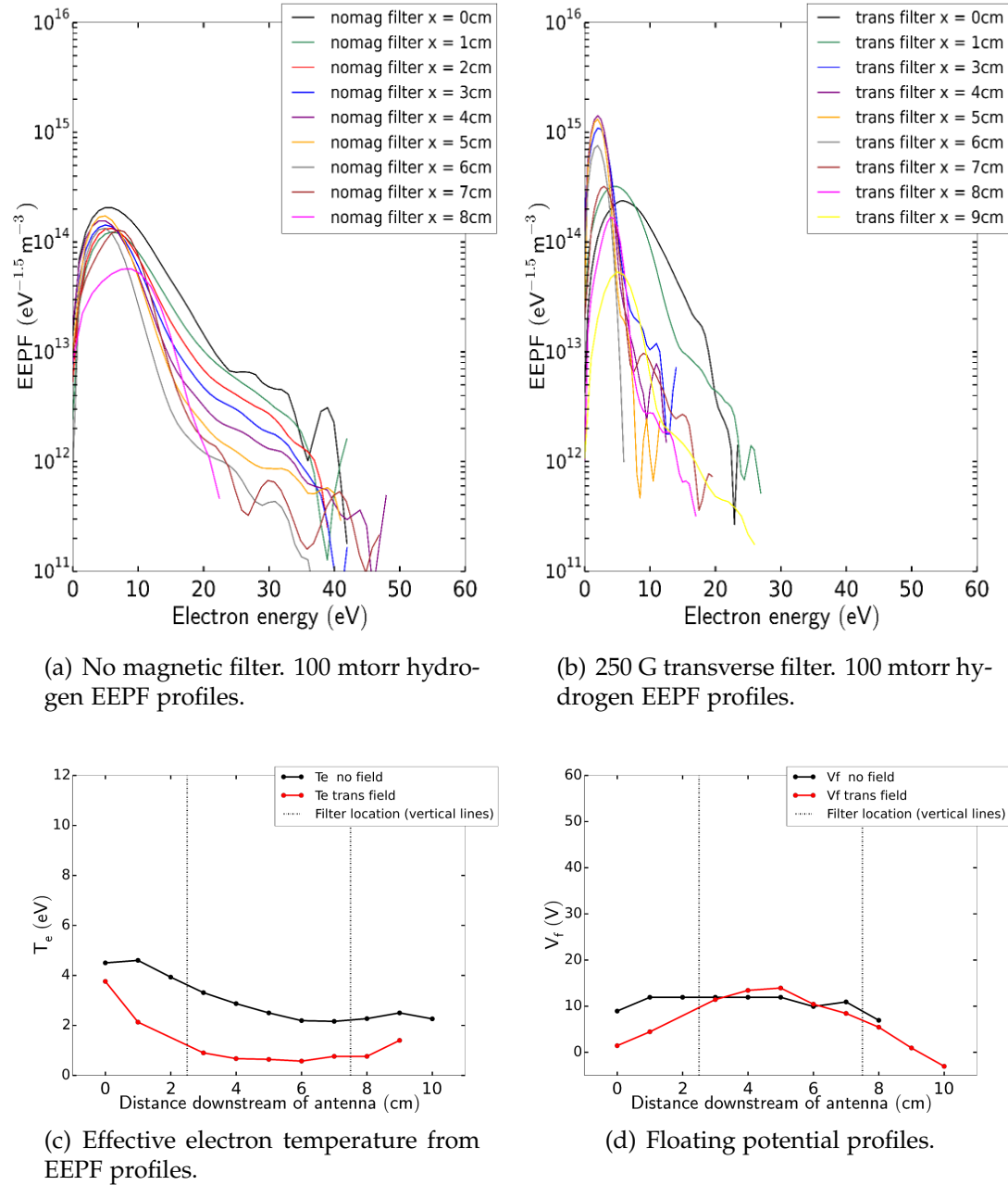


Figure 4.8: Hydrogen EEPF profiles, T_e , and V_f at 100 mtorr, spatial evolution of plasma properties downstream of the antenna. The filter is center d at $x=5$ cm. Measurements taken at 200 W forward power and at 100 mtorr pressure.

4.2.2.1 10 mtorr

The EEPF profiles along the source at 10 mtorr are shown in Figure 4.9. The results show that similarly to hydrogen, the argon discharge in the ICPS also exhibits thermalized Maxwellian EEPF profiles along the length of the source. This result is commonly found in argon discharges for ICP systems [65]. The unfiltered profiles in Figure 4.9(a) exhibit high energy tails which are seen to reduce in temperature with distance from the antenna. The tails range in temperature from 14.5 eV at $x = 2$ cm to around 5.4 eV at $x = 10$ cm downstream of the source. The EEPFs with the magnetic filter applied show a slight increase in low energy electrons (Fig. 4.9(a)). This effect does not occur inside the filter region like in hydrogen and instead occurs several centimeters downstream. The effect of increased density of low energy electrons is also much less than seen in hydrogen.

The magnetically filtered profiles for argon at 10 mtorr are shown in 4.9(b). Immediately noticeable for these EEPF profiles is that they show a much weaker spatial dependence to the magnetic filter than the EEPFs seen in hydrogen exhibiting only a slight cooling effect seen from their slopes. This is reflected in the calculated effective electron temperatures shown in Figure 4.9(c). The localized effect of the magnetic filter on electron temperature is negligible in argon at 10 mtorr with electron temperatures ranging between 2.2 eV and 1.5 eV without the filter and between 2.5 and 0.75 eV with the filter.

It is interesting to note that the electron heating effects on the electron temperature seen in hydrogen at 10 mtorr do not appear in the argon data for effective electron temperatures in Figure 4.9(c). This is despite the increases seen in the power efficiency at low magnetic field strengths shown in Chapter 3 Figure 3.7(d). This is likely due to the much shorter mean free path for electron collisional momentum transfer in argon (ν_m) resulting from the much higher plasma densities in argon near the antenna. Additionally the collisional skin depth of the plasma for power deposition is much shallower in argon. In hydrogen at discharge densities of around $2 \times 10^{16} \text{ m}^{-3}$ the collisional skin depth for power deposition is around 5 cm, and so the inductive field coupling can penetrate the source tube completely to deposit power. In argon however, the higher source densities of up to densities of around $1 \times 10^{18} \text{ m}^{-3}$ mean that the collisional skin depth for the inductive field is only 0.5 cm and so the electrons have time to re-thermalize before reaching the central axis of the plasma and being measured on the probe. This means that if ECR heating is occurring in the argon discharge, it is occurring only in

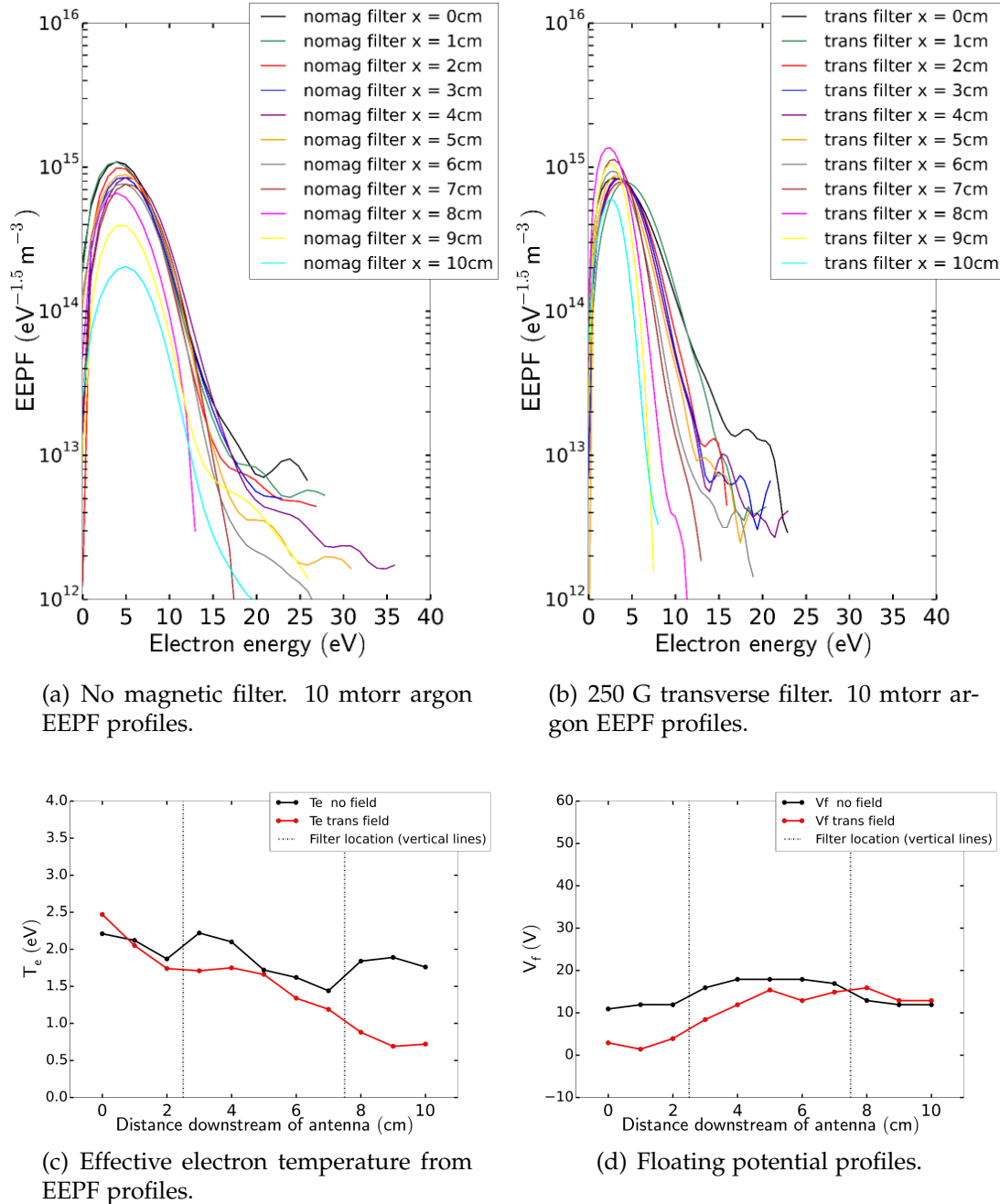


Figure 4.9: Argon EEPF profiles, T_e and V_f at 10 mtorr, spatial evolution of plasma properties downstream of the antenna. The filter is centered at $x=5$ cm. 200 W forward power at 10 mtorr.

the outer layer of the plasma unlike in hydrogen and so measurements of the electron temperature in the skin depth would be required to see ECR heating in argon.

The floating potentials for argon at 10 mtorr is shown in Figure 4.10(d) and exhibits similar floating potential profiles for both filtered and unfiltered cases. The potentials range between 0 V and 10 V with no indication of a dome shape with the application of the filter at this pressure.

4.2.2.2 50 mtorr

The argon profiles at 50 mtorr again show only a weak effect of the magnetic filter across the source with no major localized effects in electron temperature. The transverse filters EEPFs shown in Figure 4.10(b) also do not show the increase in low energy electrons downstream of the filter as seen at 10 mtorr.

The effective electron temperatures at 50 mtorr (Fig. 4.10(c)) show electron temperatures similar to those at 10 mtorr ranging between 2.2 eV near the antenna down to 1.5 eV for the downstream unfiltered case and 0.7 eV for the filtered case. These temperature gradients are similar to those for argon in other magnetically filtered ICP systems at this pressure [21] [22].

The floating potentials shown in Figure 4.10(d) are very similar for unfiltered and the filtered case indicating that the plasma fluxes across the source are unaffected by the magnetic filter for argon at this pressure consistent with the dominance of collisional diffusion for argon. The floating potentials range between 0 V upstream near the antenna and 20 V downstream at $x = 10$ cm.

In contrast to hydrogen, the effect of the magnetic field is seen to be negligible in argon for both electron cooling and localized changes in plasma floating potential for both pressures of 10 mtorr and 50 mtorr. These comparative argon measurements are supported by Arancibia *et al.*, [33] who found that applying magnetic enhancement to an argon plasma at pressures of 50 mtorr had no effect on the electron temperatures, electron densities and EEPF due to the plasma collisionality.

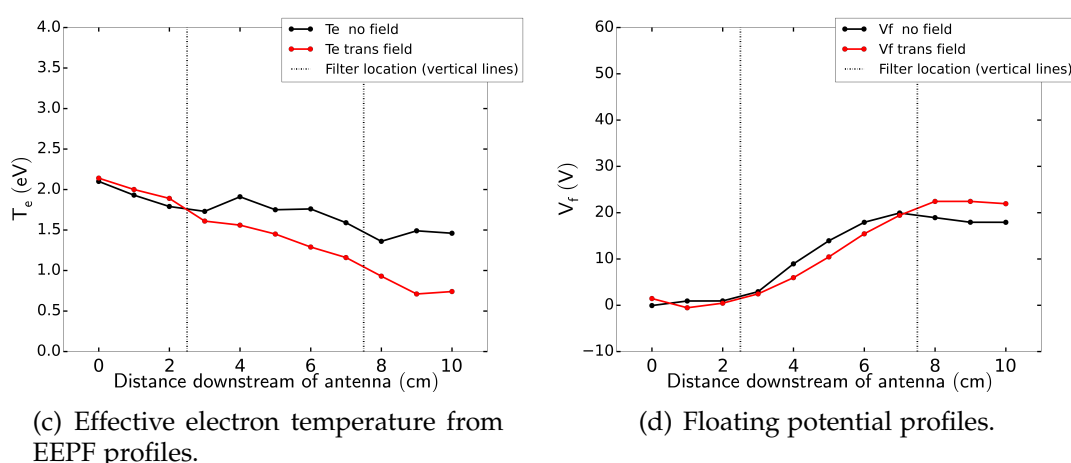
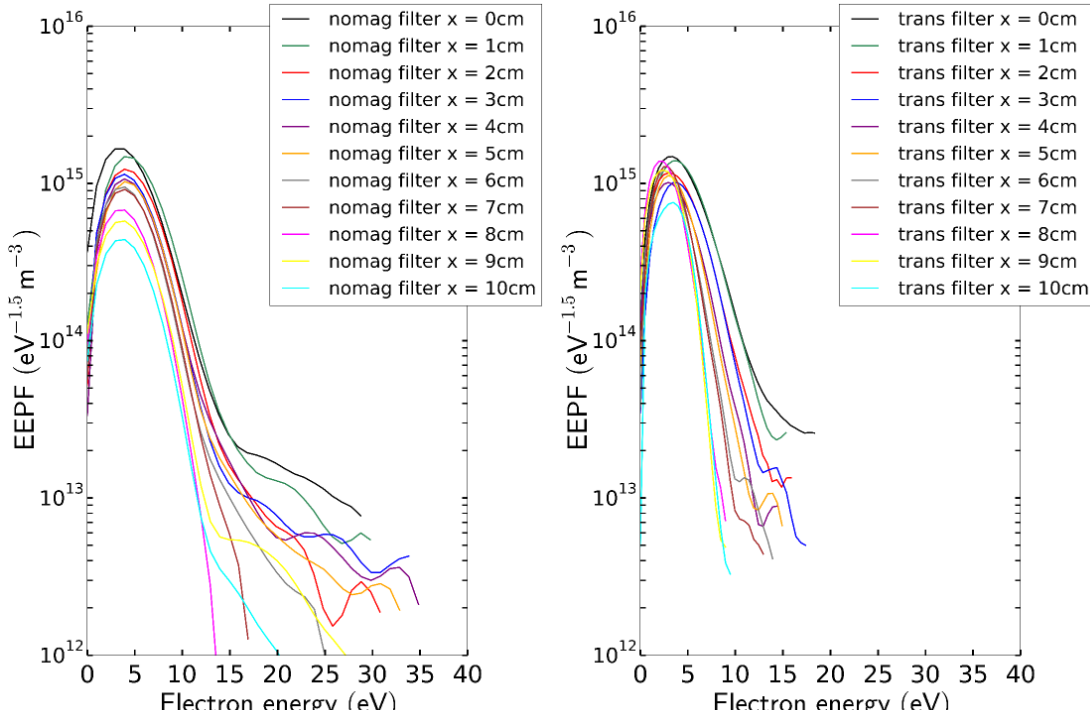


Figure 4.10: Argon EEPF profiles, Te and Vf at 50 mtorr, spatial evolution of plasma properties downstream of the antenna. The filter is centered at $x=5$ cm. 200 W forward power at 50 mtorr.

Results from Aanesland *et al.*, [22] have suggested that the magnetic field can indeed begin to show localized effects from the magnetic field for argon at very low collisional regimes for pressures of around 1 mtorr. However, these non-local results in argon may also be related to the characteristic length of the system and the magnetic field strength via its modification of the effective system length d_{eff} as discussed in Section 4.1.4.

4.2.3 EEPF Magnetic Field Strength Comparison

To ascertain the effect of magnetic field strength on the cooling of the EEPF, measurements were made at a single position ($x = 5$ cm) at 50 mtorr pressure under the magnetic filter for both hydrogen and argon (Fig. 4.11). The magnetic filter field strength was decreased from 250 Gauss to 0 Gauss by separating the magnets around the source tube while EEPF measurements were taken at the filter center.

The results in Figure 4.11(a) shows that the majority of the cooling effect at 50 mtorr in hydrogen occurs with the application of only 40 Gauss. This result shows that the electron cooling effect from increased confinement has a saturation limit. At this field strength the electrons are already magnetized with a Larmor radius of around 0.1 mm while the ions are not yet magnetized with a Larmor radius of approximately 6 cm. It is noted that the density of low energy electrons increases with increased field strength up to 250 Gauss (orange profile) due to the effect of trap formation. Interestingly the hot tails on the profiles with the application of the filter remains at a constant temperature from 43 G up to 250 G at an effective temperature of 23 eV.

In contrast the argon results in Figure 4.11(b) show the weak effect of the magnetic filter at this pressure on the electron population under the filter. The temperature remains largely unchanged ranging from 2 eV to 1.64 eV and the temperature fits are summarized in Figure 4.11(c). The reason for this is that the cooling effect in argon occurs at much lower pressures than in hydrogen [21] due to momentum transfer mean free path and the higher ion mass. The 10 mtorr data in this work shows the beginnings of cooling (Figure 4.9) but pressure comparison here at 50 mtorr are well above the cooling pressure limit seen in argon.

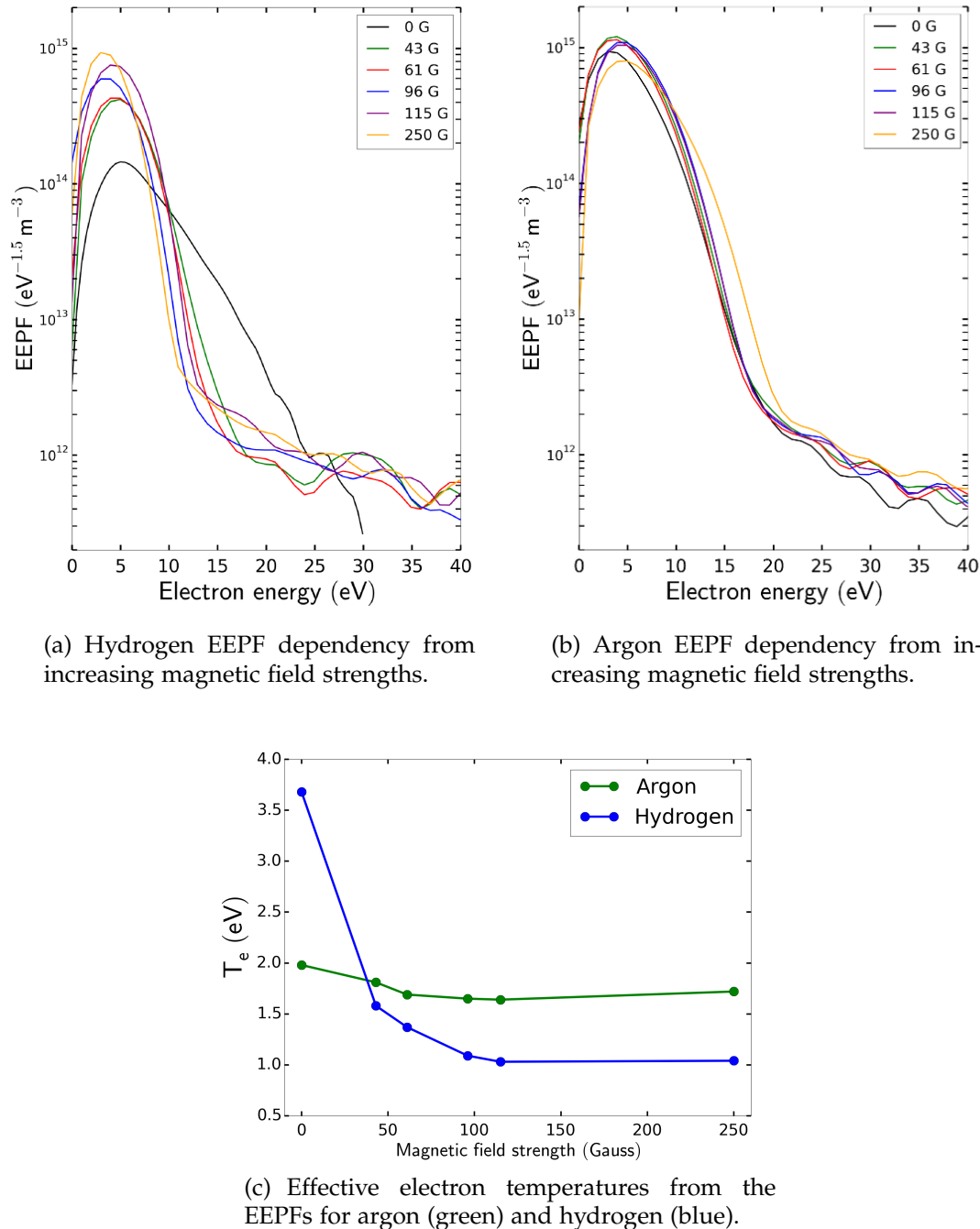


Figure 4.11: Hydrogen and argon EEDF profiles showing the effect of magnetic filter strength. The filter is center d at $x=5$ cm. 200 W forward power at 50 mtorr pressure. Effective electron temperatures shown in c).

4.3 Optical Emission Spectroscopy

This section compares the temperature of the H₂ feedstock gas in the presence of the magnetic field to ascertain the effect of the magnetic filter in generating rovibrational excited states which can promote the formation of negative ions. Optical wavelengths of the Q-branch emission from the Fulcher- α band are investigated to determine the molecular temperatures through the source.

The Fulcher band is a high intensity and historically well-characterized band in the optical region with generally unperturbed electronic transition channels making it an ideal candidate for determining molecular hydrogen temperatures in the ICPS.

These experiments were conducted both with and without the magnetic filter in place and include measurements through the 'dark' region of low H₂ electronic excitation at 10 mtorr and 75 mtorr where the particle trap forms.

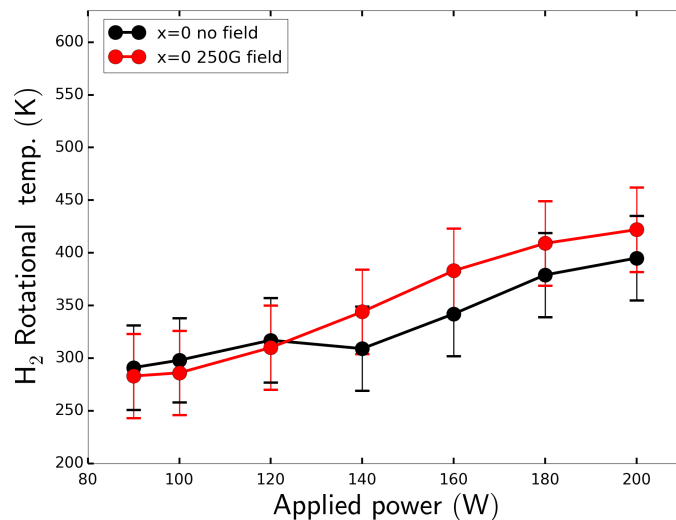
4.3.1 Power Dependence

Rotational gas temperatures was first measured up to 200 W at two positions in the source at 10 mtorr pressure to measure the dependence of the gas temperature on the forward power.

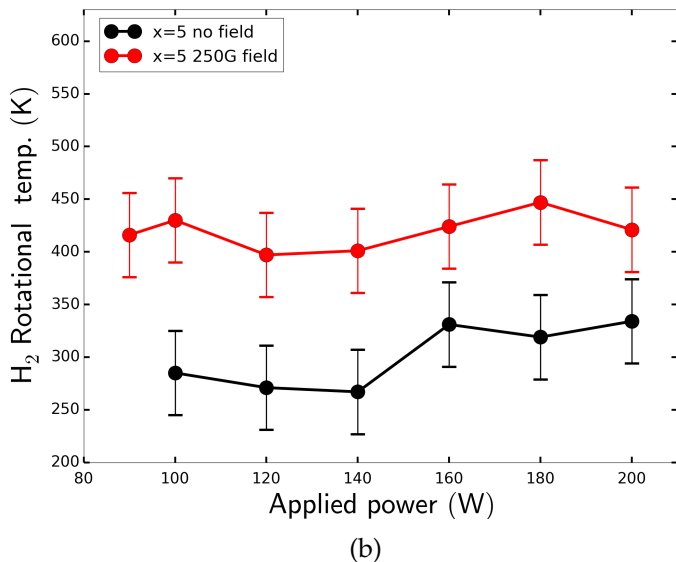
The first position measured for the power sweep was at the front of the antenna at $x = 0$ cm shown in Figure 4.12(a). The gas temperatures for both filtered and unfiltered conditions near the antenna are similar and range from around 300 K at low power to 400 K at 200 W. The reason for this similarity is the proximity of the measurement at $x = 0$ cm to the gas flow inlet and the measurement is of cold 'fresh' H₂ gas entering the system.

The temperature trends and temperature range shown here closely match the power measurements from similar ICP systems [77]. The similarity of conditions between systems in the Coronal regime implies that the rovibrational and translational energy is in equilibrium at these powers and that assumption 2) is satisfied from Chapter 2 Section 2.4.4.

The same power dependence measurements were then made at $x = 5$ cm



(a)



(b)

Figure 4.12: Power dependence of the H_2 rotational temperature at two positions, a) at $x=0$ cm in front of the antenna, and b) under the filter region at $x=5$ cm.

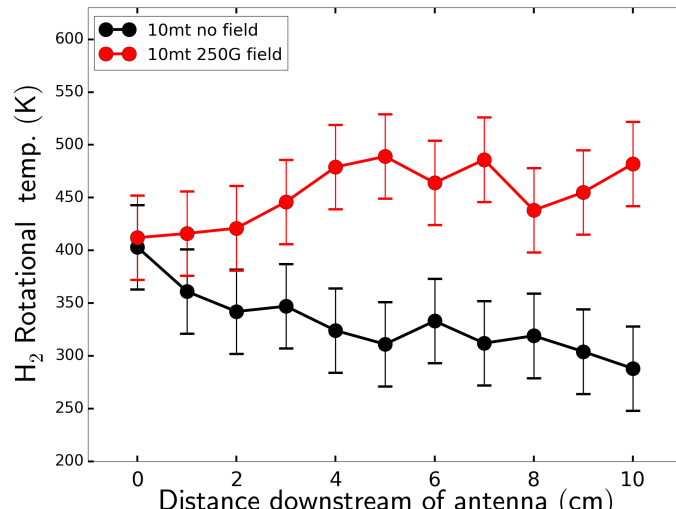
inside the filter region and are shown in Figure 4.12(b) which showed a separation in the temperatures downstream of the source. Inside the filter region the gas temperatures show a temperature increase of approximately 100 K compared to the unfiltered case and relative uniformity across the power sweep for both profiles. The unfiltered ICPS shows temperatures close to room temperature around 300 K to 350 K while the magnetically filtered condition shows gas temperatures around 400 K to 450 K. This separation is due to the filter affecting the power deposition from electrons into the gas as it flows from the upstream gas inlet. Assuming the ions are thermalized with the background gas this result gives an estimate for ion temperatures between 0.03 eV and 0.04 eV in the ICPS.

4.3.2 Pressure Dependence and Spatial Dependence

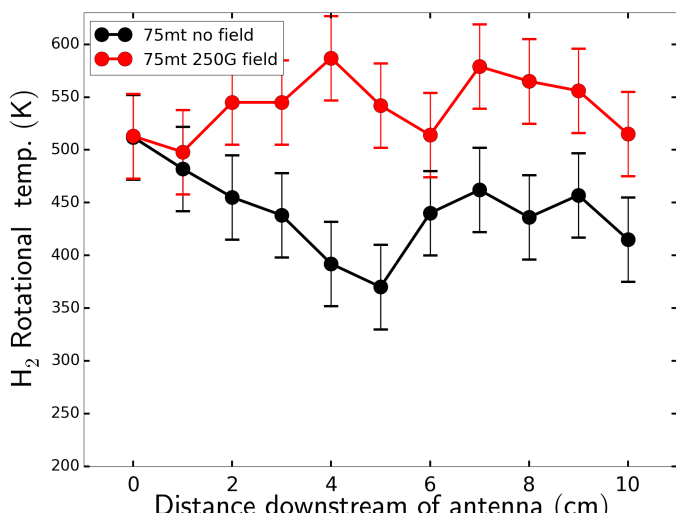
The spatial effect from the power sweep data was investigated by measuring the temperature profile along the length of the source at both 10 mtorr and 75 mtorr. Figure 4.13(a) shows the 10 mtorr profiles having a marked divergence of temperatures from the discharge with a temperature gradient of -10 K per centimeter for the unfiltered case and approximately +10 K per centimeter for the filtered case with a noticeable increase toward the center of the filter. This divergent temperature profile, where gas temperatures increase toward the center of the filter, correlate well with the reduction in electron temperature through the same region shown previously in Section 4.2 Figure 4.6. Temperatures here at 10 mtorr range from 300 K to 400 K for the unfiltered case and between 400 K and 480 K with the filter applied.

The gas temperature result here suggests that even at low pressures, the mechanism for localized electron cooling is from increased collisional energy losses to the neutral gas due to the magnetic field increasing electron confinement and hence electron power deposition within the source. The increased neutral gas temperatures freely diffuse downstream of the filter region with the majority of the gas heating occurring along the positive gradient of the magnetic filter consistent with the location of the strongest gradients of electron cooling. The temperatures shown are consistent with the gas temperature ranges seen in similar inductive plasma sources [143] [144] [82].

An increase of 100 K in gas temperature from electron collisional cooling is certainly energetically possible. The EEPF profiles from Section 4.2 show that electrons lose almost all of their energy during their migration through the



(a)



(b)

Figure 4.13: H₂ Rotational temperature profiles along the length of the ICPS comparing the effect of the magnetic filter (red) to background (black). The 10 mtorr profiles are shown in a) compared to 75 mtorr profiles in b).

filter region. If we assume an electron population loses its energy only via collisions with the gas, then the energy from a population of electrons at 7 eV (Fig. 4.6(c)) at a density of 10^{17} m^{-3} with a background gas pressure of 10 mtorr, provides enough energy to increase the total gas temperature by 80 K. Considering that the residence time of the gas is far greater than the electrons [145], (approx. 500 ms compared to 10 μs), then each gas molecule could be heated by successive groups of electrons passing through the filter.

At 75 mtorr (Fig. 4.13(b)) the profiles follow a similar divergent trend to those at 10 mtorr. The 75 mtorr case shows an overall increase in gas temperatures across the source of around 100 K compared to the 10 mtorr case. This is likely due to the increased collisional coupling of electrons to the neutral gas at the higher pressure.

The increase in gas temperature for the unfiltered case in Figure 4.13(b) from $x = 5 \text{ cm}$ to $x = 9 \text{ cm}$ may be related to a capacitive coupling mode between the antenna and the diffusion chamber faceplate downstream. It is a coupling which occasionally occurs during a run within the ICPS when no magnetic field is present and manifests as an increased glow near the chamber opening. It also results in increased plasma densities which can be seen in other measurements in this work (eg. Figure 2.18). It was present by accident during this run and manifested as a dull glow near the diffusion chamber. Interestingly it was found to increase the local gas temperature by up to 100 K from the upstream minimum at $x = 5 \text{ cm}$.

The gas temperature at $x = 0 \text{ cm}$ at the front of the antenna again shows no change in gas temperature despite the electron temperatures showing marked differences at this location especially in the 10 mtorr case (Chapter 4.2 Figures 4.6 and 4.6). This indicates that the heating of the cold neutral gas from the inlet upstream is not driven directly by the electron temperature but rather the electron confinement which occurs further downstream where the number of electron collisions is far greater in the filter due to the increased particle residence time.

A question arises as to whether or not these higher temperature H_2 molecules are able to form negative ions within their system residence time. The rovibrational mean free path for dissociative attachment of H_2 in the ICPS can be

estimated using this gas temperature data [24]:

$$\lambda_{H_2}(v'') = \frac{v_g}{n_e \cdot \langle \sigma v_{DA} \rangle} \quad (4.2)$$

where v_g is the gas velocity and $\langle \sigma v_{DA} \rangle$ is the averaged rate coefficient for dissociative attachment. Assuming higher rovibrational states for the cross section [9] and using the gas temperature of 0.05 eV (580 K) (Fig. 4.13(b)) the estimate gives a dissociative attachment mean free path of between 2 m and 20 m for an excited H₂ molecule. Since the residence time for gasses in the system is of the order of milliseconds, each gas molecule should be able to undergo at least one dissociative attachment event before exiting the system at these temperatures.

These results show that the magnetic filter enhances the rovibrational state of the H₂ by up to 150 K. This effect increases with distance from the source antenna meaning that the benefit to negative ion formation applies to locations across the source and is not localized to the main discharge near the antenna.

4.4 1d Particle Transport Model

A 1d fluid model is presented which highlights the initial considerations for plasma transport through a Gaussian magnetic field profile. The section presents the drift model and concludes with a possible explanation for the processes responsible for increased plasma transport perpendicular to the magnetic field. While the spatial axis of the model is 1d, the model resolves the x, y and z components of the drift velocity equation to produce a 1d vector field.

The model uses a 1d numerical fluid approach where the plasma drift equation is solved using the axial experimental data from the ICPS as the input parameters. The parallel and perpendicular drift velocities are calculated for both electrons and H₃⁺ ions under different system conditions.

In the case of a magnetic field applied to a plasma, the diffusion and mobility coefficients are each split into the two vector components parallel and perpendicular to the direction of the magnetic field. For a magnetic filter this

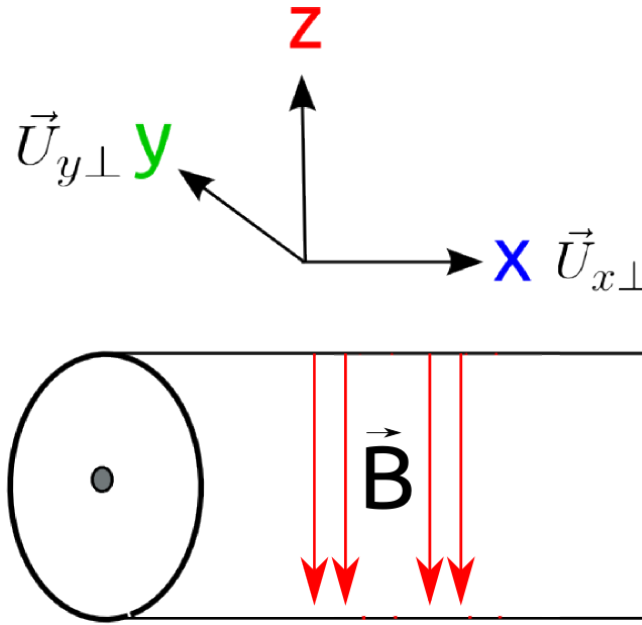


Figure 4.14: Source tube axis orientation and the two components of the total drift velocity vector. The B-field orientation is in $-\hat{z}$ due to the North-South orientation.

is important as the perpendicular components of $\mu_{x\perp}$, $\mu_{y\perp}$ and $D_{x\perp}$, $D_{y\perp}$ give indications of the rate of classical transport through the filter field and laterally across it respectively.

Figure 4.14 shows the orientation of the ICPS source tube used for the 1d modelling with the two drift vector components to be examined $U_{x\perp}$ and $U_{y\perp}$ which are both perpendicular to the transverse B-field.

4.4.1 1d Model Theory and Solution Method

Diffusion and mobility are macroscopic descriptions of plasma transport which can be used to help describe the plasma drift velocity. Mobility and diffusion in the absence of a magnetic field can be found from first considering the force balance equation:

$$m_e q \vec{E} - \nabla p - m_e n_e \nu_m \vec{u} = 0 \quad (4.3)$$

The equation describes the forces on a particle being factors of the electric field and the pressure gradient and collisions respectively where \vec{u} is the elec-

tron drift velocity and ν_m is the average collision frequency for electron momentum transfer. Substituting in now the pressure gradient to the electron density gradient at constant temperature $\nabla p = k_B T_e \nabla n_e$ and rearranging Eqn. 4.3 for the electron drift velocity:

$$\vec{u} = \frac{q}{m_e \nu_m} \cdot n_e \vec{E} - \frac{k_B T_e}{m_e \nu_m} \cdot \frac{\nabla n_e}{n_e} \quad (4.4)$$

The pair of constants on the left hand side are referred to the mobility (μ) and diffusion (D) respectively such that:

$$\mu_e = \frac{|q|}{m_e \nu_m} \text{ (m}^2 \cdot \text{s}^{-1} \cdot \text{V}^{-1}\text{)} \quad , \quad D_e = \frac{k_B T_e}{m_e \nu_m} \text{ (m}^2 \cdot \text{s}^{-1}\text{)} \quad (4.5)$$

where ν_m is the collision frequency for momentum transfer. Equation 4.5 shows that in low ionization plasmas, the electron mobility and diffusion can be enhanced by increasing the electron temperature and decreasing the gas pressure. This equation can be applied to any particle species present in the plasma.

To add the magnetic field effect on the drift velocity, the Lorentz force can be substituted into the force balance equation for \vec{E} . The mobility and diffusion terms are then each modified by the presence of the magnetic field by a factor of $1 + \frac{\omega_{+,-}^2}{\nu_m^2}$ such that the mobility and diffusion become:

$$\mu_{\perp} = \frac{|q|}{m_{(+,-)} \nu_m} \cdot \left(1 + \frac{\omega_{+,-}^2}{\nu_m^2}\right) \quad , \quad D_{\perp} = \frac{k_B T_{+,-}}{m_{(+,-)} \nu_m} \cdot \left(1 + \frac{\omega_{+,-}^2}{\nu_m^2}\right) \quad (4.6)$$

where the subscript (+,-) are for the respective value for each charged species. With the addition of the magnetic field (z-directed), the force balance Eqn. 4.3 is expanded to two equations:

$$qn_e(\vec{E}_x + \vec{u}_{y\perp} \times \vec{B}) - k_B T_e \nabla_x n_e - m_e \nu_m \vec{u}_{x\perp} = 0 \quad (4.7)$$

$$qn_e(\vec{E}_y + \vec{u}_{x\perp} \times \vec{B}) - k_B T_e \nabla_y n_e - m_e \nu_m \vec{u}_{y\perp} = 0 \quad (4.8)$$

The two perpendicular components here in the x and y directions appear in the same equation. The x-component of the velocity contributes to the Lorentz force in the y-component and visa versa. This produces two equations which can be solved simultaneously and combined to solve for \vec{u}_{\perp} [70]. The x and y final drift velocity can then be found from combining Eqns. 4.7 and 4.8:

$$\vec{u}_{x,y,\perp} = \pm \mu_{\perp} \vec{E} - D_{\perp} \frac{\nabla n_e}{n_e} + \frac{\vec{u}_{E \times B} + \vec{u}_{Dia}}{1 + (\omega_e \tau_m)^{-2}} \quad (4.9)$$

Where τ_m is the mean time between momentum transfer collisions, $\vec{u}_{E \times B}$ is the E cross B drift velocity, and \vec{u}_{Dia} is the diamagnetic drift velocity:

$$\vec{u}_{E \times B} = \frac{\vec{E} \times \vec{B}}{B_0^2} \quad , \quad \vec{u}_{Dia} = \frac{\nabla n_e \times \vec{B}}{n_e} \cdot \frac{k_B T_e}{q B_0^2} \quad (4.10)$$

Equation 4.9 is used here for the basis to develop a simple numerical classical drift-diffusion model. The model uses experimental data of the electron density n_e profile and its gradient ∇n_e and the electron temperature profile T_e .

The four leading terms from Eqn. 4.9 are largely responsible for classical transport through a magnetic filter: mobility, diffusion, $E \times B$ drifts and diamagnetic drifts. The streamwise drift velocity can occur via several ways: increased perpendicular mobility (μ_{\perp}), increased perpendicular diffusion (D_{\perp}), positive $E \times B$ drift velocities ($\vec{u}_{E \times B}$) and diamagnetic drifts (u_{Dia}). Each of these components from Eqn. 4.9 will be looked at both separately and then together to try to ascertain the leading candidates for cross-filter diffusion in the ICPS.

4.4.2 1d Electron Modelling Results

This section shows the model results for electron and H_3^+ ion transport along the ICPS. The mean collision times used in the model ν_m were calculated from the cross section for the dominant charged particle collisions within the ICPS which are the electron-neutral and ion-neutral elastic collisions. The cross section of Tawara *et al.*, [92] was used for the (electron- H_2) collision and the cross section from Phelps [146] was used for the dominant ion collision ($H_3^+ - H_2$).

The average gradient of the plasma potential measured in the ICPS is used for the electric field strength \vec{E}_x which was measured at approximately 3 V/cm along the x-direction and 10% of this value was used for the unknown y-directed plasma potential variation as per the modelling of Boeuf *et al.*, [37]. The 1d magnetic field profile used in the model was from interpolated Gauss probe measurements of the magnetic filter (see Fig. 2.3(a)) and from this the cyclotron frequency is calculated from the magnetic field strength at each point along the source.

Before considering the full drift equation, each of the leading terms in Equation 4.9 will be looked at separately. Figure 4.15 shows the modelling results for the electron diffusion and mobility along the length of the source the filter at 10 mtorr (top figures) and 50 mtorr (bottom figures). The magnetic field strength is overlain on the figures for reference (red curve).

Figure 4.15(a) shows the modelling results for the parallel and perpendicular diffusion coefficients at 10 mtorr in the ICPS. Without the magnetic filter applied (blue profile) the electron diffusion is seen to be fairly uniform across the length of the source due to the non-local electron temperature profile with an average diffusion coefficient of $10^4 \text{ m}^2 \text{ s}^{-1}$.

With the filter applied, the perpendicular diffusion coefficient (D_{\perp}) is strongly suppressed due to the magnetic field by several orders of magnitude to less than $10 \text{ m}^2 \text{ s}^{-1}$. The suppression begins around 2 cm and continues though to 9 cm downstream of the antenna. However, the electrons can still diffuse parallel to the magnetic field lines in the z-direction and so the parallel diffusion (D_{\parallel}) is seen to be of the same order of magnitude as the unfiltered case and the strength of the diffusion across the field is seen to follow the trend in the electron temperature.

The electron mobility at 10 mtorr is shown in Figure 4.15(b). Without the filter the electron mobility is equal to the parallel field mobility (μ_{\parallel}) and was calculated at a value of $2.25 \times 10^3 \text{ m}^2 \text{ s}^{-1} \text{ V}^{-1}$. With the filter added, the mobility is suppressed from the $x = 2 \text{ cm}$ position to the $x = 9 \text{ cm}$ position similar to the diffusion coefficient. This suppression is seen to occur fully at a magnetic field strength of only 25 G. This suppression of electron mobility and diffusion is the cause of a reduction in plasma density widely reported downstream of transverse filters at low pressure.

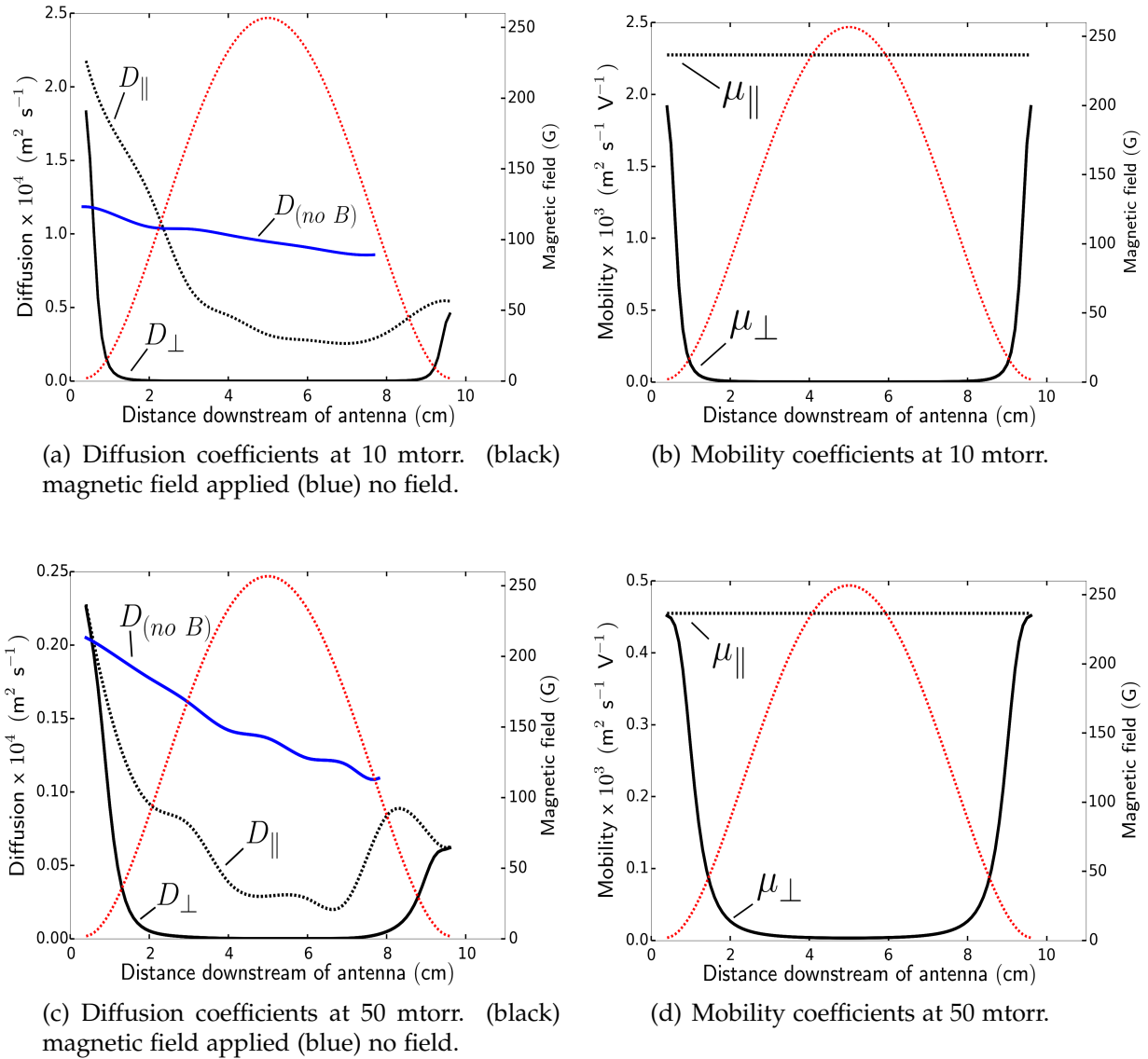


Figure 4.15: 1d model results showing the electron Diffusion, mobility through the ICPS at two pressures.

Figure 4.15(c) shows the parallel and perpendicular diffusion coefficients at a higher pressure of 50 mtorr. The higher collisional frequency at 50 mtorr along with lower electron temperatures produces an order of magnitude lower diffusion coefficients than the 10 mtorr case (note the axis scale difference). The diffusion with the filter applied shows a similar level of suppression to the 10 mtorr case except at the edges of the filter region at $x = 2$ cm and $x = 9$ cm which show higher diffusion rates and so the electrons are seen to be able to penetrate further into the filter at higher pressures. In this case a filter strength of 115 G is required to fully suppress the electron diffusion coefficient at 50 mtorr.

The individual contributions to the total drift velocity from both the $E \times B$ and diamagnetic drifts (Eqn. 4.10) were then investigated from only those components in Equation 4.9. Figure 4.16(a) shows the electron drift velocities along the ICPS. Since the diamagnetic drift occurs perpendicular to density gradients and the lateral variations in the electron density are unknown, only the y-component of the diamagnetic drift (\vec{U}_{yD}) in the ICPS is shown. The lateral plasma density gradient in ICP discharges have been found to be small compared to the axial x-directed density gradients [147] [60] and so they are not considered drifts which directly contribute to x-directed drift velocities. Instead the lateral diamagnetic drifts are suggested to create lateral (y-directed) drifts which cause charge separation and lateral electric fields. This finding has been supported by particle-in-cell modelling for NBI systems by Boeuf *et al.*, [37].

These lateral diamagnetic drifts have been shown to create charge separated electric fields and have been recently proposed to be the instigator for $E \times B$ cross filter transport [37] [38]. While these electric fields are not known in this case, the values from particle-in-cell modelling by Boeuf *et al.*, [37] were used to guide the choice of electric field at an upper bound of 0.7 V/cm.

The electron diamagnetic drift velocities calculated from this 1d model (Fig. 4.16(a)) and are shown to range up to 15 km s^{-1} either side of the filter region and are reduced to approximately 1 km s^{-1} inside the filter region due to the low electron temperatures. Assuming these electrons create a weak 0.3 V/cm electric field, the resultant $E \times B$ drift velocities ($\vec{U}_{x E \times B}$) produce relatively strong streamwise velocities either side of the filter with a constant drift inside the filter of approximately 1.5 km s^{-1} .

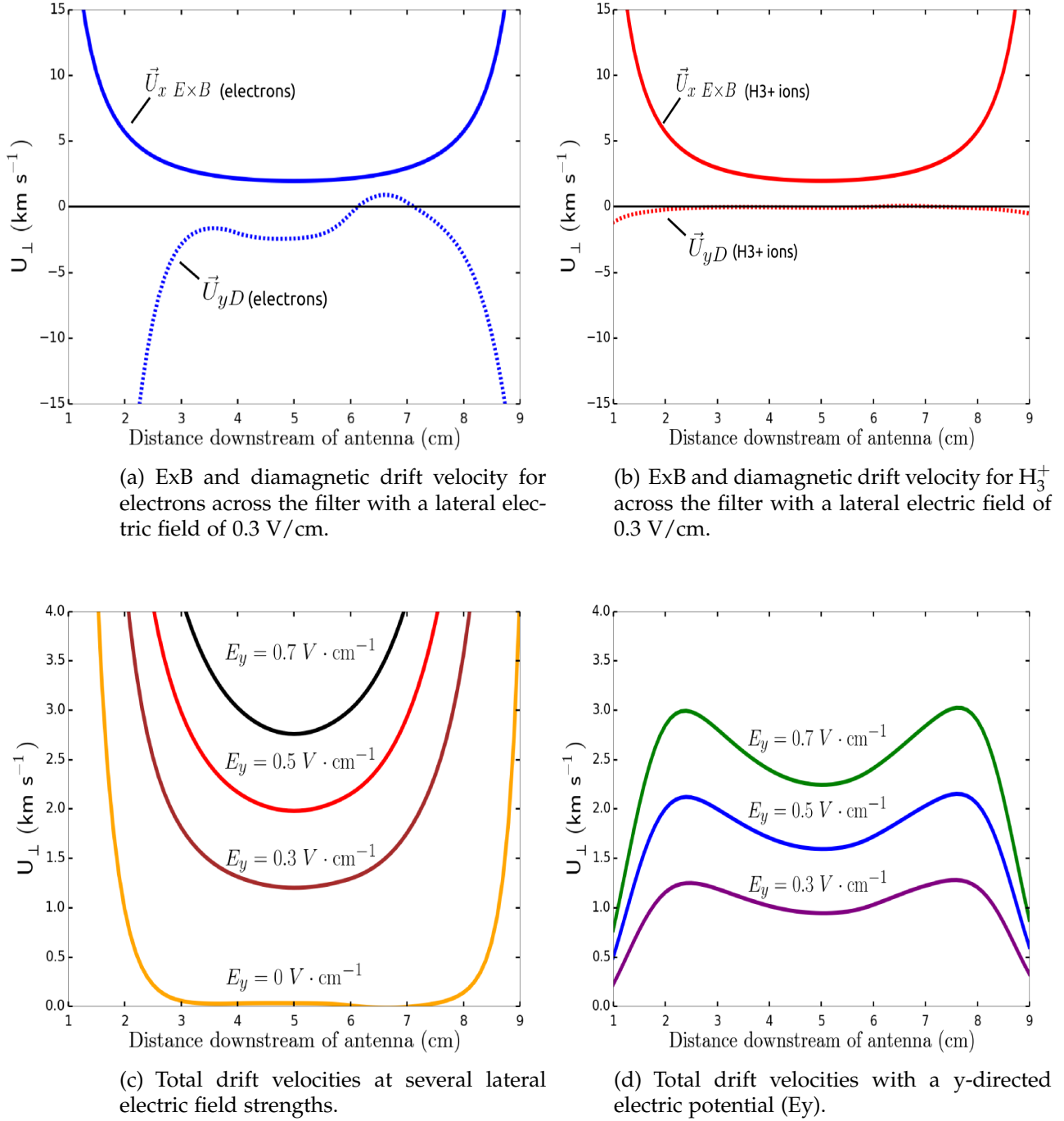


Figure 4.16: Model results for the $E \times B$ drift, diamagnetic drift and total drift velocities for both H_3^+ ions and electrons at a 50 mtorr collisional regime.

Figure 4.16(b) shows the results for the equivalent diamagnetic drift and $E \times B$ drifts for H_3^+ ion. The ion diamagnetic drift velocities are seen to be suppressed across the length of the source at low diamagnetic drift velocities of $\approx 3 \text{ m s}^{-1}$. This is primarily due to the low ion temperature rather than from the ion density gradients. This shows that any lateral electric fields are produced from charge separations driven by electron diamagnetic drifts and not lateral ion drifts. Since the $E \times B$ drift is independent of particle mass and charge, the ion $E \times B$ drift is the same as the electron drift and is in the same direction.

After looking at each part of the drift individually, the total drift velocity was then calculated for electrons and ions accounting for diffusion, mobility, electric and magnetic fields and the drifts. It has already been determined from Figures 4.16(a) and 4.16(b) that one of the major contributors to the streamwise drift velocity is the $E \times B$ force via small lateral electric fields and so the drift as a function of several electric field strengths was calculated. The total streamwise drift velocities at 50 mtorr are shown for electrons in Figure 4.16(c) and ions in Figure 4.16(d) with each different profile representing the response of the drift to different lateral y -directed electric field strengths.

Figure 4.16(c) shows the electron drift velocity using the total drift equation. It can be seen that in the absence electric fields, the streamwise electron drift velocity is strongly suppressed by the presence of the magnetic field (orange profile). At the filter edges where there is a low magnetic field the streamwise velocity approaches the 'free diffusion' limit. By simulating weak electric fields across the source, the central drift velocity becomes non-negligible with drifts between 1.25 km s^{-1} at a field strength of 0.3 V cm^{-1} up to 2.75 km s^{-1} at a field strength of 0.7 V cm^{-1} .

Figure 4.16(d) shows the total velocity for the H_3^+ ions when using the total drift equation. The ion drift profiles are seen to be quite different to the electron profiles with peak ion drifts occurring either side of the filter at $x = 2.5 \text{ cm}$ downstream and $x = 7.5 \text{ cm}$ downstream. A minima in the total ion drift is seen at the center of the filter which becomes more prominent with increasing electric field strength. Peaks in the total ion drift are seen either side of the central filter region which result from a combination of magnetic field strength, ion mass and collisional frequency. This results shows that under suitable conditions, the streamwise ion transport can be strongly enhanced either side of the filter which lends support to the theory of ion-driven processes leading to the formation of the trap seen in the hydrogen plasma

density results.

4.4.3 1d Modelling Concluding Remarks

These 1d modelling results show that electron diffusion and mobility through a magnetic filter is almost completely suppressed above fields of 60 G without the effect of lateral electric fields. The diamagnetic drift laterally across the source is driven by electrons rather than ions due to their higher temperature. If these drifts are able to create even weak electric fields, then sizeable streamwise $E \times B$ drifts emerge for electrons and ions. The total drift velocity for electrons through the filter can be enhanced with these electric fields up to several km s^{-1} . The total drift velocity for ions increases compared to the free-diffusion velocity and is seen to peak in velocity either side of the filter due a combination of magnetic field strength, electric field and collisional frequency and may be responsible for ion initiated entrainment of particles into the central filter region.

To extend these findings, a 3d model was developed to help visualize the process using some of the results from the 1d model to guide the choice of parameters.

4.5 3d Particle Modelling

A simple 3d particle tracking code was developed to try to simulate the trapping and transport within the filter using the results from the 1d model. The model process will be first described followed by the model results. While 3d analytical solutions exist for particles moving through external electric and magnetic fields, the solutions can become highly non-linear and are not solvable in complex E-field and B-field geometries. For this work, a numerical approach was required to model the complex field geometry of transport through the transverse filter.

The model domain is a 1:1 scale of the ICPS source tube from $x = 0$ cm to $x = 10$ cm and includes the 3d magnetic field profile of the transverse filter shown earlier (see Appendix A and Sec. 2.1.2). The model is a time-step

particle pushing kinetic code which tracks individual seed particles as they travel through the source to help visualize possible transport avenues. The model tracks particle properties including position, acceleration, velocity and net force. Since the dominant charged particle collisions are elastic scattering from neutrals, the model includes the collisions as randomized elastic scattering events which has been shown to be a reasonable approximation for scattering collisions under these plasma conditions [148] [149]. Generally PIC codes or fluid codes have been used for plasma transport studies through magnetic filters but this single particle approach is simpler and allows for readily available 3d particle tracking visualizations under a variety of conditions. A similar particle tracking approach was used to visualize transport and estimate negative ion extraction probabilities for individual H⁻ ions created in an NBI source by Gutser *et al.*, [17].

The background gas was simulated assuming an isotropic distribution whereby individual charged particle collisions were made to occur when the time-step reached the mean collision time interval (τ_m). This interval was varied to simulate variations in gas pressure. The elastic collisional process exchanges momentum relative to the difference in mass between the particles. Momentum exchange was considered assuming a thermalized background gas temperature of 0.05 eV (See Fig. 4.13). The velocity change for the tracked particle (v'_1) after each collision is calculated as:

$$v'_1 = \frac{v_1(m_1 - m_2) + 2m_2 v_2}{m_1 + m_2} \quad (4.11)$$

where m_2 and v_2 are the mass and velocity of the background gas. Collisional energy exchange is important when the electric field is added as the E-field can do work on the particle accelerating it between collisions. The benefits of using this type of code is that the net forces, energy and particle drifts are not externally imposed and are instead an emergent property of the model.

Energy conservation is automatic when the code is run at a sufficiently high time resolution and is a useful benchmark to test the required time-step. For particles with low mass such as electrons, the computation time is higher in order for the Lorentz force to conserve energy and requires several minutes to calculate the particle path 500 ns in the ICPS. The high ion mass means that single particle runs require shorter computation times and can simulate single ion paths for longer periods of time up to hundreds of microseconds.

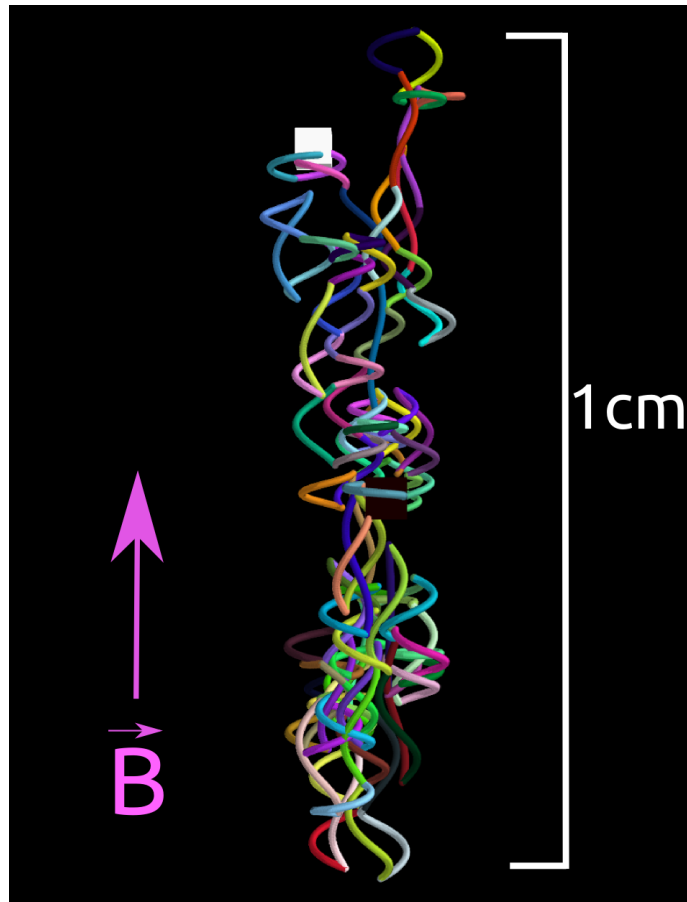


Figure 4.17: Zoomed in example of the model output for a single electron path over 110 nanoseconds at 50 mtorr inside 250 G magnetic field. The electron path begins at the white cube.

Figure 4.17 shows the result of a typical magnetized electron path in the center of the filter region. The model is able to resolve the complex path of the electron as it is confined to the field lines of the strong 250 G filter. The figure highlights the increased confinement of the electrons here by travelling only 1 cm along the field like direction but with an overall path length of 12 cm in this example.

4.5.1 3d Model Solution Method

The solution code for the 3d particle displacement used a kinematic method at each time-step (Δt) with a calculation of the Lorentz force to account for the instantaneous velocity and acceleration during each step. The only inputs to

the model are the initial conditions for velocity (\vec{v}), position (\vec{r}) and collision interval (τ_m) particle mass (m) and charge (q).

The solution procedure was iterative with each step beginning by using the previous time-step value at ($t - 1$) for acceleration, velocity and position to calculate a new set of values at at the current time-step (t). The magnetic field $\vec{B}(\vec{r})$ and electric field $\vec{E}(\vec{r})$ was assigned via a lookup table using the current position of the particle at each time-step. The solution procedure has the following form:

$$1) \quad \vec{v}(t) = \vec{v}(t - 1) + \vec{a}(t - 1) \Delta t \quad * \text{velocity calculation}$$

$$2) \quad \vec{a}(t) = q[\vec{E}(\vec{r}) + \vec{v}(t) \times \vec{B}(\vec{r})] / m \quad * \text{Lorentz force acceleration}$$

$$3) \quad \Delta\vec{r} = \vec{v}(t - 1) \Delta t + \frac{1}{2} \vec{a}(t - 1) \Delta t^2 \quad * \text{new displacement calculation}$$

$$4) \quad \vec{r}(t) = \vec{r}(t - 1) + \Delta\vec{r} \quad * \text{new position vector}$$

where the time-steps (Δt) are chosen as required for particles to conserve energy and range between 0.1 pico seconds for electrons and 0.1 nano seconds for ions. The model runs individual particles from the initial conditions until either a time limit is reached or more commonly, the particle strikes a wall and is considered lost. The number of iterations per particle lifetime is typically several million iteration steps.

The positive aspects of using this approach is that single particle drift motion is an emergent property of the model and requires no *a priori* inputs into the model. The 3d aspect of the model requires little extra computation than lower dimensional modelling and the model is naturally time resolved not time averaged.

The negative aspects of this approach is that collective particle motions can not be solved for such as changes in plasma potential or instabilities. These can be externally imposed on the model but are not emergent properties of the single particle approach.

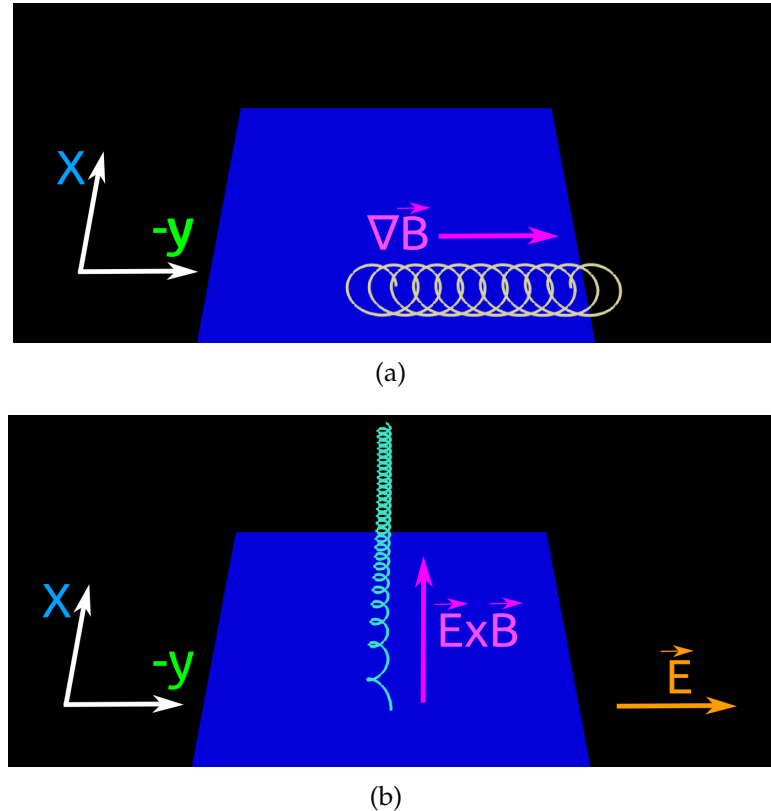


Figure 4.18: Comparison of H_3^+ ion collisionless transport after $81 \mu\text{s}$. a) without a y -directed electric field $\vec{E} = 0$ b) with a y -directed electric field $\vec{E} = 0.1 \text{ V/cm}$. The camera perspective is from inside the tube facing downstream from the antenna.

4.5.2 3d Model Results

To investigate the findings from the 1d model that y -directed fields can increase cross filter transport, the 3d model was run using single H_3^+ and Ar^+ ions to attempt to recreate the trapping effect. The ions were created in the center of the tube at $x = 2 \text{ cm}$ downstream and provided an initial velocity of 0.05 eV in the downstream direction.

Initially the non-collisional case was looked at for the H_3^+ ion to help visualize the ∇B and $E \times B$ drifts through the filter and to measure their velocity. Figure 4.18 shows the particle path over $81 \mu\text{s}$ comparing the effect of adding a lateral electric field. The model here is run under collisionless conditions to highlight the drift motion only.

Figure 4.18(a) shows the 3d particle path without the filter in place. The blue

block is the bottom magnetic block of the filter located under the source tube with the top magnetic block above the line-of-sight for the figure and not visible here. To simulate a lateral electric field from the upstream diamagnetic drifts, the electric field in Figure 4.18(b) was made to be a weak 0.1 V/cm field directed in the $-\hat{y}$ direction. The 3d perspective is from inside the tube, looking downstream into the filter region.

The model result in Figure 4.18(a) (top) shows that in the absence of collisions and electric fields, the ions are unable to transport into the filter region and instead are directed toward the side wall via a ∇B drift. The particle guiding center here travelled 1.4 cm from the initial position with a total distance covered of 16.4 cm in 81 μ s. This result gives the collisionless guiding center ∇B drift velocity for H_3^+ located at the edge of the filter as 172 m/s.

With the addition of a weak electric field of 0.1 V/cm under the same conditions the behaviour of the ion changes markedly as shown in Figure 4.18(b) (bottom). The ion is seen to easily cross the filter via the $E \times B$ drift and shows decreasing Larmor radii with increasing distance into the filter. The guiding center of the particle travels further than the field-free case with a travel distance of 3.9 cm from the starting position with a total displacement of 12.6 cm. This equates to an $E \times B$ drift velocity of 358 m/s for the ions. This result is consistent with the results from the 1d drift model when operated using the 0.1 V/cm field which is a good benchmark for results between the two different models.

The next set of simulations investigated the ion transport visualizations for H_3^+ and Ar^+ ions at a variety of collisional frequencies (pressures) with the filter applied both with and without lateral y -directed electric fields.

4.5.3 H_3^+ Visualization

Figure 4.19 shows single particle paths for H_3^+ ions at 10 mtorr (top figures) and 50 mtorr (bottom figures) comparing the effect of a weak 0.1 V/cm electric field. In all cases the 3d magnetic field is applied. The lateral electric field is not applied across the source but only in the area showing the highest diamagnetic drift between $x = 2$ cm to $x = 5$ cm as seen in the 1d model Fig. 4.16(a)).

Figure 4.19(a) shows a typical path for the H_3^+ ion at 10 mtorr without an electric field applied. At low pressure, the ion is seen to be partially magnetized and seen to follow the rounded contours of the B-field (white dotted line) outside the center of the field and is not able to easily penetrate further into the center. Interestingly, near to the top and bottom of the tube where the magnetic field lines converge, the ion is seen to reflect back into the bulk from the walls. This effect is due to the model being able to simulate the adiabatic invariance of the gyrating magnetic moment (magnetic mirror effect). The ion is seen to not easily transport into the filter region at this low pressure in the absence of an electric field.

With the application of an electric field (Fig. 4.19(b)) the H_3^+ ion is seen to easily transport across field lines and becomes entrained into the central filter region over a time scale of approximately 20 μs before it is lost to the bottom wall. While the entrainment into the filter can occur at this low density, the particles are seen to be easily lost to the walls and are unable to be trapped. This explains why at 10 mtorr the trap does not form in the ICPS (Fig. 4.1(a)). This can also help to explain why Cho *et al.*, [133] saw the trapping effect occurring at this lower pressure; the ring of alternating magnets making up the cusp field helps prevent ion losses to the walls and supports the formation of ion trapping after this entrainment process begins at low pressure.

Figure 4.19(c) shows the H_3^+ ion transport at the higher collisional regime of 50 mtorr without the electric field. The ions are seen to collide outside the filter but are prevented from penetrating into the filter due to a combination of the intermediate Larmor radius of H_3^+ and the ∇B effect (see Table 4.1). Without the electric field, the ions are invariably either lost to the walls or redirected back upstream away from the filter center.

However, with the application of the electric field at 50 mtorr, the model shows the formation of the trap (Fig. 4.19(d)). The figure shows the initial entrainment similar to the 10 mtorr case but here at 50 mtorr it is seen that the higher collisional frequency allows the ion to become trapped in a semi-magnetized state and remain within the filter region for longer ($> 80 \mu\text{s}$ here). This figure is important because it supports the combined findings of the peak in electron density experiments from Figure 4.1 with the 1d modelling results suggesting lateral electric fields and the collision frequency are key aspects to the ion mediated cross-filter transport. This finding also shows how the Larmor radius and ion mass are important in this process. The trapping effect seen in Figure 4.19(d) is found to be highly repeatable in the model

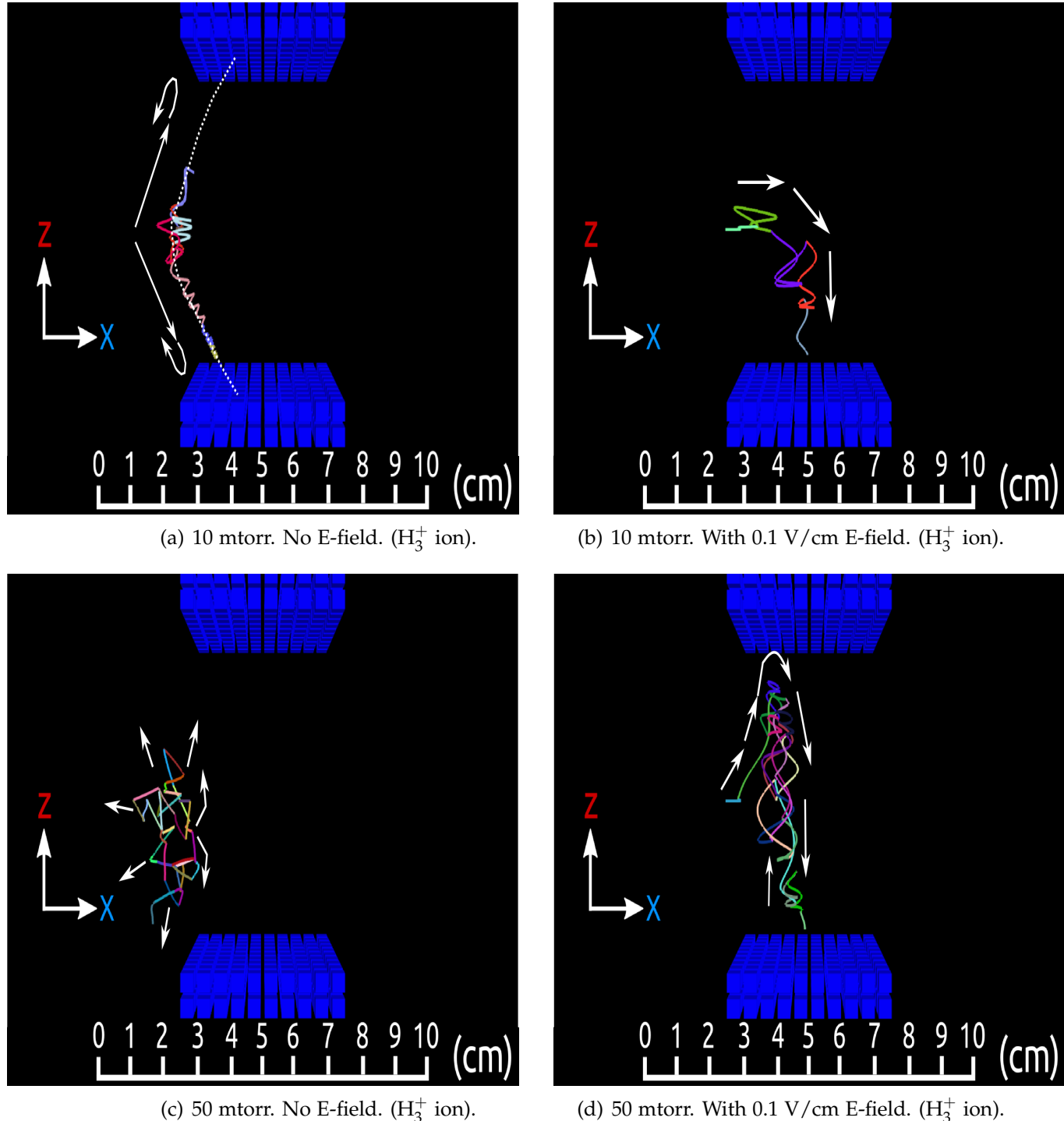


Figure 4.19: Model results for H_3^+ ions at 10 mtorr and 50 mtorr comparing the effect of a lateral electric field in 3d. Duration of model up to 80 μs . Note the entrainment and trapping process in d)

as the weak electric field ‘pushes’ the ions across field lines to become semi-magnetized and then trapped.

4.5.4 Ar⁺ Visualization

Comparative simulations were made for the argon ion Ar⁺ under the same conditions of 10 mtorr and 50 mtorr with and without a lateral electric field. The main difference between the H₃⁺ ion and Ar⁺ is that the neutral collisional frequency Ar – Ar⁺ is higher in for argon due to the larger collisional cross section. Additionally the Larmor radius is larger due to the higher ion mass in argon.

The 10 mtorr simulations for argon are shown in Figure 4.20 (top figures). Figure 4.20(a) shows the 10 mtorr case for argon without the electric field and shows a typical particle path over 80 μ s beginning outside the filter region at x = 2 cm. The ion is seen to have relatively straight paths between collisions due to its high mass which largely ignores the 250 G magnetic field. The ion does not become magnetized or to follow field lines as in the case for H₃⁺.

With addition of the electric field at 10 mtorr, the argon ion path looks similar to the case without a field. This simulation allowed a longer time of 160 μ s to give the heavier ion more time to entrain however, even up to several hundred microseconds the argon ion would not entrain and largely ignored the effect of both the magnetic field and electric field.

Figure 4.20(c) shows the argon ion at 50 mtorr without an electric field. The ion at this pressure is highly collisional and is seen to diffuse outwardly at a very slow rate. The simulation was run at to 220 μ s with the ion free to cross the magnetic field lines.

With the application of the electric field, the ion path remains unchanged Fig. 4.20(d). The high collision frequency with respect to the mean free path and the high ion mass mean that the Ar⁺ ion behaves as if it were in a field-free diffusion regime. This is supported by the plasma density measurements from Figure 4.4 which show no localized change in the plasma density when applying the magnetic filter. These simulations also show that the trap does not form at in argon above 10 mtorr under these magnetic field strengths

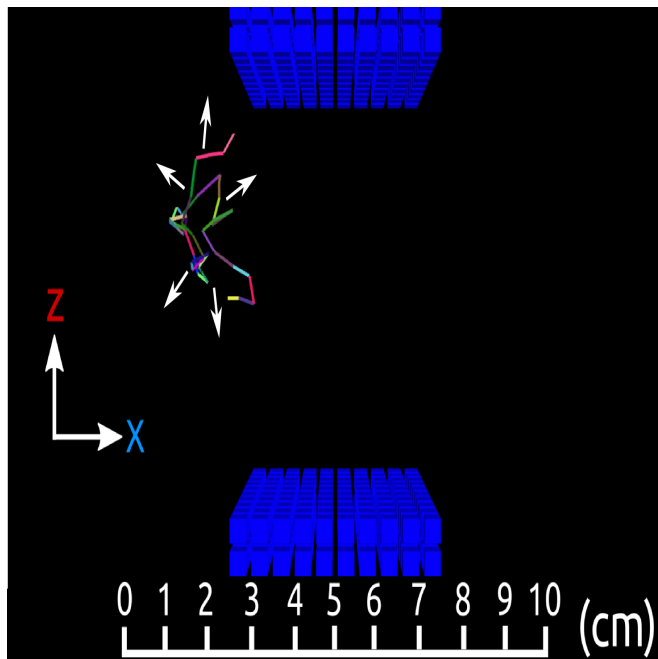
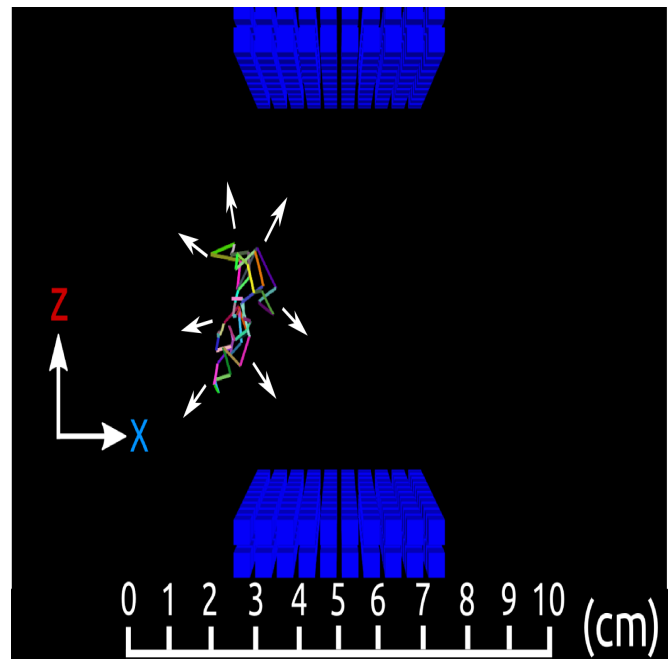
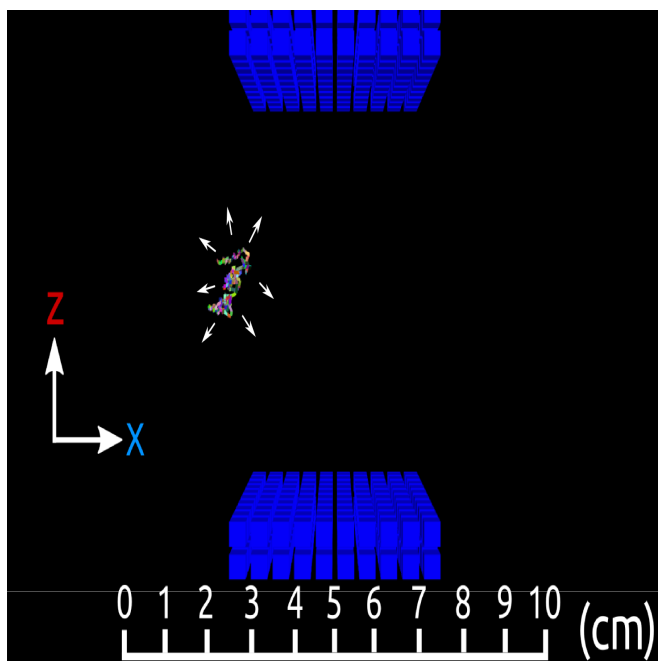
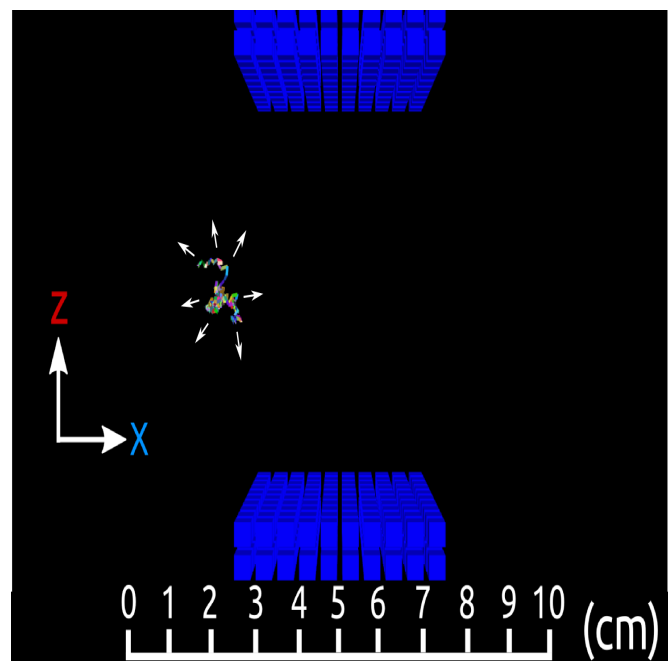
(a) 10 mtorr. No E-field. (Ar^+ ion).(b) 10 mtorr. With 0.1 V/cm E-field. (Ar^+ ion)(c) 50 mtorr. No E-field. (Ar^+ ion)(d) 50 mtorr. With 0.1 V/cm E-field. (Ar^+ ion)

Figure 4.20: Model results for Ar^+ ions at 10 mtorr and 50 mtorr comparing the effect of a lateral electric field in 3d. Duration of model up to 220 μs . The entrainment and trapping is not seen to occur here in argon.

due to a combination of high collisionality ions and large Larmor radii. The simulation does however suggest that the trap may form in argon at lower pressure and higher field strengths where the ion can become entrained and trapped but are not too collisional as to disrupt the formation of the trap.

4.5.5 3d Modelling Concluding Remarks

The 3d simulations were initially benchmarked against the 1d model rates for $E \times B$ drifts and showed that collisionless transport for charged particles into the central filter region is not possible due to ∇B drifts. The model showed a two-stage ion transport mechanism for the formation of the trap. The first stage involved an entrainment process upstream of the filter where electric fields direct the ion toward the center of the filter where the ion undergoes unmagnetized collisional transport. The second stage involves the capture and magnetization of the ion within the central filter region where it becomes collisionally confined.

The ion entrainment and trapping using the results from the 1d model and provided the time scale for the process in hydrogen of between 20 μs and 80 μs .

The argon simulations supported the density measurements in Figure 4.4 that the trap could not occur in argon above 10 mtorr with a magnetic field strength of only 250 G due to the large Larmor radius and the higher collisional frequency of the Ar^+ ion. However, the model suggests that it may form with low pressure and at a higher magnetic field strength provided the lateral electric field can form.

It should be noted here that these results together allow for the application of the trapping effect to occur across a wide range of gas pressures using different gas species if the transverse magnetic field strength and dimensions are correctly tailored. This includes creating the trap at low pressures of 3 mtorr for hydrogen for use in NBI sources. Although the trapping pressures are presented here for 25-50 mtorr which are too high for NBI applications, the results from Cho *et al.*, showing the effect at 4 mtorr are explained by the results here showing the 3d visualizations of H_3^+ entrainment at 10 mtorr whereby the entrainment process can occur but would require an appropriate

radial cusp filter to prevent wall losses of the ions at low pressure.

These results together suggest that a particle trap using the transverse filter may be achievable across a wide variety of plasma gasses and pressures provided that certain conditions are met:

1) The pressure needs to be set such that the primary collision frequency produces a mean free path which is small with respect to the radius of the source (r_S) and the width of the central transverse filter region. The mean free path however cannot be so small as to inhibit the ability of the ion to enter the filter region and become magnetized. The 'ideal' ratio of the source tube radius to the mean free paths for particles to become entrained and trapped ranges between approximately 3:1 and 11:1 such that:

$$3 \leq \frac{r_S}{\lambda_i} \leq 11$$

This requirement could perhaps be circumvented by 'simulating' a higher collisional plasma via a set of pulsed solenoids surrounding the source to mimic particle collisions and limit the mean free path for the purposes of trapping.

2) The Larmor radius of the ion must be less than both the characteristic length of the source (Λ) and the central transverse filter region (r_{filter}). The Larmor radius however cannot be so small as to be confined to magnetized outside of the central filter region. The width of the central transverse field region is typically the physical edges of the permanent magnets. Under these conditions the trapping can then occur when the ion Larmor radius is smaller than the tube at a ratio between approximately 1:4 to 1:8 such that:

$$\lambda_{Li} < r_S \quad , \quad \lambda_{Li} < r_{filter}$$

And,

$$\frac{1}{8} \leq \frac{\lambda_{Li}}{r_S} \leq \frac{1}{4}$$

3) The transverse filter width itself should be less than the characteristic

length of the system $r_{filter} < \Lambda$ and it should also posses a magnetic field gradient either side the central transverse region. This requirement is to allow for the entrainment upstream of the filter without magnetizing the ion outside of the central filter but offering a semi-magnetized or magnetized environment once the particle is entrained to form the trap.

- 4) The electron diamagnetic drifts inside the plasma which cause the lateral electric fields must be able to form. These fields do not need to be strong but are found to be necessary for the initial entrainment process to occur.

These parameters are presented here in the context of elastically dominated collisions and the range of these conditions may be modified by the addition of a cusp filter which alters the particle trajectories near the walls and increases residence time of particles.

Negative Ion Measurements

This chapter presents the spatial and temporal evolution of the negative ion population in the ICPS using the photodetachment technique (see Section 2.5). Detailed negative ion fractions (n^-/n_e) and total negative ion densities will be presented. The afterglow measurements will be compared under two different magnetic field geometries at four locations along the source.

To the authors knowledge, this is the first time such detailed spatio-temporal results have been presented for negative ions in an inductive system for a hydrogen plasma using the transverse magnetic filter. Several key results arise from these measurements including:

- 1) Unexpected evidence of strong localization of negative ion formation inside the magnetic filter.**
- 2) High negative ion fractions inside the filter center up to 1:3 during the discharge and as high as 14:1 at 40 μ s into the afterglow.**
- 3) Spatial inhomogeneities in the afterglow for negative ion production and destruction indicating the dominance of a diffusive transport regime.**
- 4) Evidence of ion-ion plasma formation throughout the source in the afterglow.**

Spatially resolved measurements of the negative ions along the x-axis are presented first before a model is shown to support the spatial measurements in Section 5.1.1. The afterglow temporally resolved measurements are presented

in Section 5.2 and the rate coefficient calculations and further discussion of the afterglow dynamics are shown in Section 5.3.

The findings for negative ions shown in this chapter could be applied to help increase the NBI extraction efficiency using a high frequency pulsed power source by taking advantage of both the increased volume production in the early afterglow and also the ambipolar removal of the problematic electron current. While measurements of pulsed negative ions in hydrogen sources have been made since the 1990s, the works which established the literature on the possibility of NBI pulsed source optimization were DC arc hot cathode systems with limited spatial measurements [150] [151] [15].

This chapter extends these works by showing contemporary measurements of negative ion densities using a combination of the transverse filter and a pulsed plasma at a high temporal measurement resolution using a modern ICP source. The higher operating pressure is also utilized of 100 mtorr where a novel cold particle trap has been seen (see Chapter 4). The results of this chapter showing low electron residence times into the afterglow and the early development of the ion-ion afterglow plasma helps develop the groundwork for the possibility of a future suite of measurements inside a pulsed prototype NBI source.

The results also contribute to the science for industry ICP semiconductor fabrication. Commercial processes such as semiconductor etching and surface coatings rely primarily on the afterglow plasma physics to tailor the chemistry inside the fabricator in order to create reliable and reproducible products. The results in this chapter show the formation of ion-ion plasmas, and provide spatial measurements of particle diffusion rates for both electrons and negative ions in the afterglow. The results will highlight the spatial and temporal sensitivity of these factors inside inductive plasma sources which can be controlled using the magnetic filter. These findings could be used to help understand etch uniformity and changes in pulsed afterglow chemistry in fabricator environments.

5.1 Spatial Variation of H⁻

A spatial scan of the negative ion particles as made in the ICPS along the length of the source at 1 cm intervals using the transverse filter. The measurements provided spatial trends for the negative ion distribution across the source and compared them to unfiltered conditions. The negative ion fraction was also measured at each location for the spatial measurements and the total negative ion density was calculated from this fraction using the known density measurements in Chapter 4 Section 4.1.1. Negative ion measurements were attempted for continuous mode operation however the RF oscillations on the probe were too high to resolve the mA signal from the RF potential of several Volts and so the first measurement was made as close as possible ($2\mu\text{s}$) to the discharge 'on' time. The changes to the negative ions in the 2 microsecond time period amounts to at most a 10% reduction in the negative ion signal through destruction and a diffusive transport of at most only 4 millimeters and so these spatial measurements can be considered a 'snapshot' of the H⁻ distribution during the discharge 'on' time (see Section 2.5.2 for details of this consideration).

Figure 5.1 presents four figures showing the spatial variation of H⁻ ions along the length of the source at the trapping pressure of 100 mtorr correlated with the electron temperature profile. To correlate the negative ion results, the top figure (Fig. 5.1(a)) shows the low electron temperature profile at this pressure (data from Chapter 4) which can help promote negative ion formation.

Figure 5.1(b) shows the raw I_{PD} signal from photodetachment along the length of the source, this signal is directly proportional to the negative ion density. The unfiltered measurements (black profile) indicate a negative ion profile with a maximum of 1.3 mA near the antenna at x = 1 cm and exhibits a declining negative ion current with distance from the source down to around 0.1 mA at x = 11 cm. This result is consistent with fluid modelling by Paunská *et al.*, [147] of a low temperature ICP source which showed that the negative ion density in unfiltered inductive systems closely follows the overall plasma density profile and that the H⁻ density maximum occurs in the discharge center before steadily decreasing with distance from the antenna.

With the application of the filter (Fig. 5.1(b)) (red profile), the negative ion profile is markedly different and shows a strong localization to the center of the filter with a peak current draw of 2 mA. The profile shows a reduction

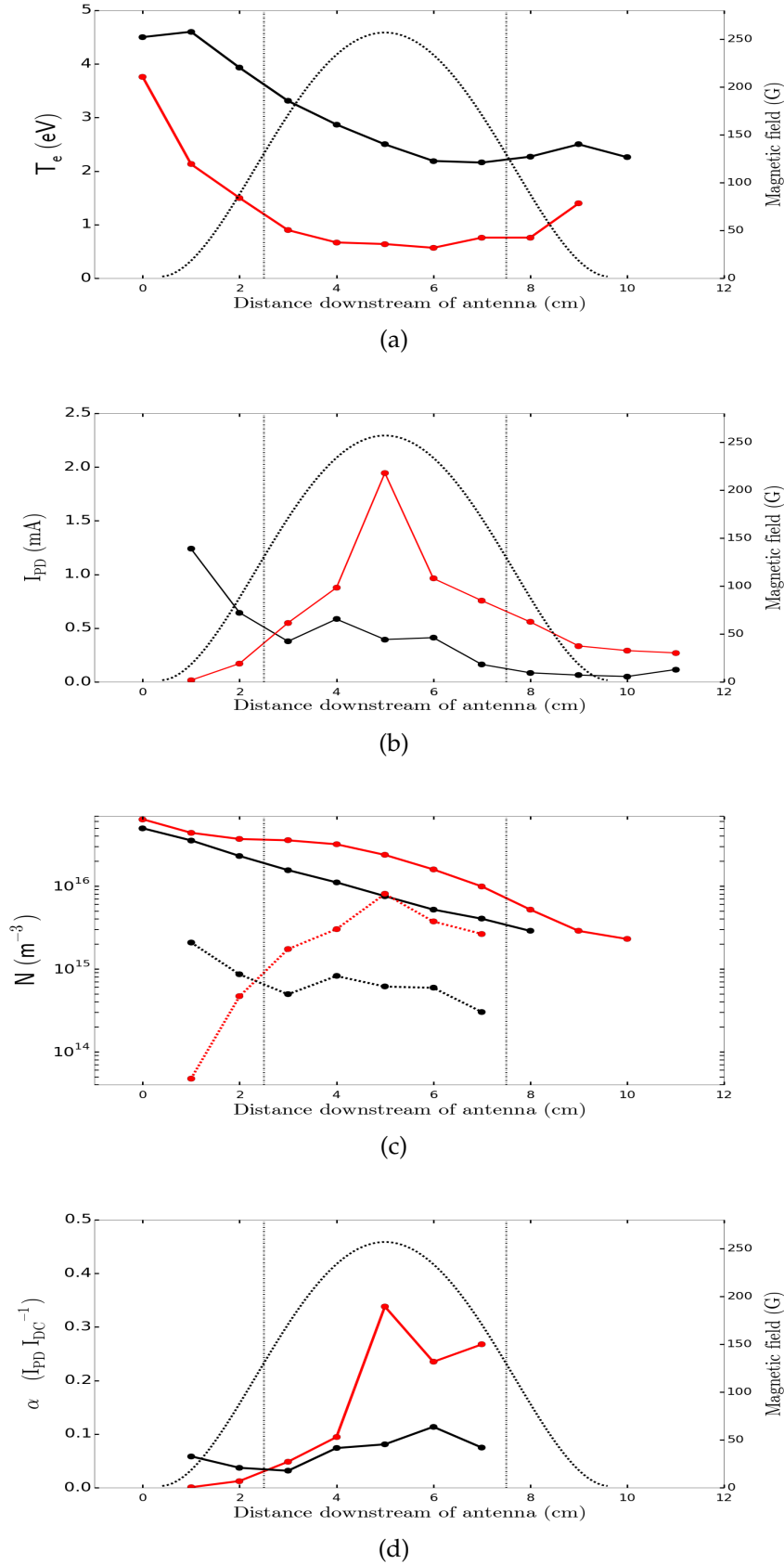


Figure 5.1: Spatial variation of negative ions across the ICPS at 100 mtorr, 250 W.

in negative ion signal near the antenna. The peak was verified under repeat measurements across the source.

Figure 5.1(c) shows an overlay of the electron densities (solid lines) with the negative ion densities (dotted lines). The negative ion densities are seen to range between $3 \times 10^{14} \text{ m}^{-3}$ and $2 \times 10^{15} \text{ m}^{-3}$ for the unfiltered profiles and between $5 \times 10^{13} \text{ m}^{-3}$ and $1 \times 10^{16} \text{ m}^{-3}$ for the filtered profiles. The density increase with the filter applied is an order of magnitude higher than without the filter at $x = 5 \text{ cm}$. The location of the negative ion peak is seen to coincide with the peak in plasma density inside the filter trap. While the plasma density increases inside the trap by several factors, the negative ion density increases by over an order of magnitude. The suppression in upstream negative ions near the filter is due to increased destructive processes from both the high electron temperature and increased collisional electron confinement. The peak in negative ion density inside the filter is due to a combination of factors which will be shown in the following modelling section (Sec. 5.1.1).

Figure 5.1(d) shows the ratio of negative ions to electrons (α) along the ICPS with and without the filter. Without the filter the negative ion fraction is negligible and ranges between 4% and 11% consistent with modelling of standard ICP systems [147] [105]. With the addition of the filter, the negative ion fraction is seen to peak in the center of the filter as high as 34%.

Since the number of publications showing spatially resolved negative ion signals across a transverse filter in hydrogen is limited, this centrally peaked negative ion signal is a new and surprising result. This increased density correlates well with the increased electron cooling, increased rovibrational states and electron density peaks through the same region.

It should be noted here that the negative ion density with the filter applied of $1 \times 10^{16} \text{ m}^{-3}$ at a fraction of 34% represents a relatively high density fraction comparable to the downstream extraction regions in larger caesium-free sources [107] [152] and is run here at a modest forward power of only 250 Watts. Recently, Cho *et al.*, [133] has shown that the trap can be formed at lower pressures and higher powers so the results from this work could have applications to NBI systems which operate at a lower density. To the authors knowledge, this is the only other work which has reported this similar plasma behaviour. In their work, Cho *et al.*, a tandem cusp system was operated at low pressure in hydrogen and similarly peaked electron density profiles were

seen in the vicinity of the transverse filter. However negative ion measurements were only taken at two spatial locations upstream of their magnetic field peak and so they were unable to confirm the negative ion peak seen in this work (Fig. 5.1(b)). This effect could offer an avenue for improved volume production and may be exploitable in larger negative ion sources to increase their negative ion densities away from the source discharge.

The effect of a high fraction of negative ions can have an effect on the Langmuir probes IV characteristic whereby the positive current and the negative currents are similar and an 'S' shaped profile develops due to the equal masses and velocities for both of the measured charged species. This effect is only expected to be seen in the plasma bulk for highly electronegative gasses such as SF₆ but can occur in hydrogen at the gridded extraction region of an NBI due to the deliberate exclusion of co-extracted electrons. Chabert *et al.*, [153] have shown that this effect on the Langmuir current draw to be present only for negative ion ratios $n^-/n_e > 100$ and this finding was supported by Corr *et al.*, [154] who showed that this effect can be seen at the edges of helicon plasmas at negative ion ratios of $n^-/n_e > 50:1$.

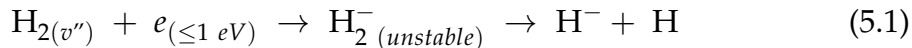
These values are much higher than the ratios of 0.3:1 seen under the filter. Figure 4.5(c) (orange profile) shows the probe IV profile measures at the center of the negative ion density peak at $x = 5$ cm and indicates that no distorted 'S' shaped profile occurs. The contribution of the the high negative ion density on the IV profile from the floating potential to the 'knee' section containing plasma potential can therefore be considered negligible. While the measured negative ion fraction here of 30% is high for a hydrogen plasma, it is insufficient to have affected the measurements of the EEPF and electron temperature Chapter 4.

5.1.1 Modelling Negative Ion Results

To help understand the negative ion results shown in Figure 5.1, modelling of the negative ion formation process is introduced which uses a combination of experimental measurements from the ICPS and the known rate coefficients from the literature. A brief mention of the main reaction processes will be given and the model results shown.

Negative ions form in electronegative plasmas in a variety of ways depend-

ing on their state and composition. For molecular hydrogen (H_2) the ground state of the electronic bond is covalent and non-polar with a relatively high electronegativity of 2.2 on the Pauling scale. The extra electron forming the H^- ion is weakly bound with a ground state binding energy of 0.75 eV. There are various pathways for negative ion formation inside the plasma [63], however in the ICPS the most common is via the dissociative attachment reaction to the background H_2 gas:



Where v'' is the molecular vibrational quantum level. Negative ions are produced in the plasma volume primarily via dissociative attachment (DA) of a slow electron to a rovibrationally excited hydrogen molecule. Other channels for negative ion formation in hydrogen can also occur via dissociative attachment to the H_3^+ ion:



An initial estimate of the negative ion density for a given system can be made by equating the primary production and loss terms for the equilibrium plasma state. Multiplying the absolute densities of the two reactants with the reaction rate coefficient of the process (k) yields the production or loss rate for the reaction where the units of density are m^{-3} and the second order reaction rate units are given in units of $m^3 s^{-1}$. Since the dissociative attachment reactions from H_3^+ are found to be negligible, the *Production = Destruction* equilibrium state of H^- can be expressed as:

$$n_g n_e k_{DA} = n_{H^-} n_{H_3^+} k_{MN} + n_{H^-} n_{H_2} k_{H_2} + n_{H^-} n_H k_H \quad (5.3)$$

Where k_{DA} , k_{MN} , k_{H_2} and k_H are the reaction rate coefficients for the processes of dissociative attachment, H_3^+ mutual neutralization and neutral gas stripping respectively. Equation 5.3 can then be rearranged and calculated for the negative ion term:

$$n_{H^-} = \frac{n_{H_2} n_e k_{DA}}{n_{H_3^+} k_{MN} + n_{H_2} k_{H_2} + n_H k_H} \quad (5.4)$$

By substituting in the approximate values for n_i and n_e (approx $1 \times 10^{17} m^{-3}$), and neutral gas density (approx $3.2 \times 10^{21} m^{-3}$ at 100 mtorr) a first estimate

Table 5.1: Leading destruction (D) and production (P) reactions for H⁻ in the ICPS

Process	Reaction	Rate Coefficients (m ³ s ⁻¹)	Reference
Dissociative attachment (P)	H ₂ + e → H + H ⁻	$2 \times 10^{-15} e^{(-0.01/T_e)} + 2 \times 10^{-14} e^{-10/(10 T_e)}$	[9]
	H ₃ ⁺ + e → H ₂ ⁺ + H ⁻	$2.59 \times 10^{-15} T_e^{-1.27} e^{-6.45/(T_e+0.1)}$	[92][105]
Electron stripping (D)	H ⁻ + e → H + 2e	$1.24 \times 10^{-12} T_e^{0.03} e^{-10.44/T_e}$	[155][105]
Mutual neutralization (D)	H ₃ ⁺ + H ⁻ → 4H	$8.29 \times 10^{-13} (300/T_g)^{0.5}$	[156][105]
Neutral collisional detachment (D)	H ⁻ + H ₂ → H + H ₂ + e	$1.62 \times 10^{-16} T_i^{0.417} e^{-6.47/(T_i+0.132)}$	[136]
	H ⁻ + H → H ₂ + e	$3.81 \times 10^{-15} T_i^{0.28} e^{-3.76/(T_i+0.62)}$	[136]

yields negative ion plasma ratios between 16% for the excited DA cross section, and around 0.2% for the ground state DA cross section [9] [92] which are values consistent with typical values of negative ion production within volume sources and also highlights the strong effect that rovibrational states can have on the negative ion ratio.

This process was extended to a create basic model of the ICPS by solving Equation 5.4 and applying the experimentally measured density and temperature profiles from Chapter 4. The rate coefficients for each process were then calculated and are shown in Table 5.1. The rate coefficients are expressed in Arrhenius form where the coefficient is a function of temperature. The DA cross section for of the H₂ gas was chosen using a vibrational state of v" = 6 from Horáček *et al.*, [9]. All the neutral gas was assumed to be in this state for the model.

Figure 5.2(a) shows the results of the reaction rate calculations along the length of the ICPS at 100 mtorr when the filter is applied. The effect of the reduced electron temperature is seen to reduce the electron stripping rate coefficient by two orders of magnitude through the center of the filter (orange profile). At the same time the dissociative attachment rate coefficient is seen to increase by almost an order of magnitude (blue profile) helping to produce conditions within the filter center ideal for negative ion formation.

The leading cause of negative ion destruction in the ICPS is associative detachment of atomic hydrogen H + H⁻ → H₂ + e. Despite the reaction rate being lower than mutual neutralization, the number density of atomic hydrogen is several orders higher than the positive ions and typically > 10% of the neutral H₂ gas in ICP devices [105] [106]. Additionally, the dielectric Pyrex source tube supports increased lifetimes of atomic hydrogen through a low

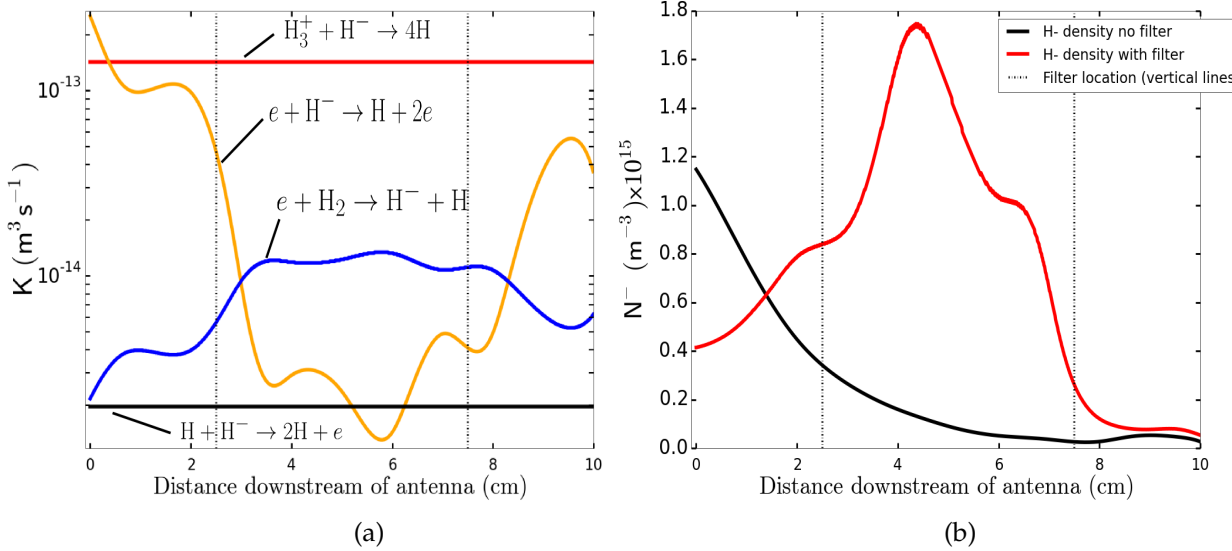


Figure 5.2: Model rate coefficients along the length of the ICPS a) and model results for the negative ion density with and without the filter in b).

surface recombination coefficient of $r_H = 10^{-4}$ for the reaction $\text{H} + \text{H} \rightarrow \text{H}_2$. This atomic recombination coefficient for Pyrex is 2 orders lower than the coefficient for other common source materials such as aluminium and stainless steel [157]. Since the atomic hydrogen fraction is unknown, yet is found to be a key contributor to negative ion losses, measurements of the neutral population using laser induced fluorescence would be desirable in future work.

Figure 5.2(b) shows the model results when the reaction rates from Figure 5.2(a) are combined with the experimental measurements to solve Equation 5.4 for the negative ion density. The model shows good agreement with the negative ion signals measured in Figure 5.1(b) and is able to recreate the profiles for both filtered and unfiltered conditions along the ICPS. Importantly the model is able to capture the trend in the unfiltered case with declining densities from the discharge and the strong density peak through the center for the filtered case. While the model shows an underestimate of the final densities it indicates that the trends in the negative ion profiles shown in Figure 5.1 are explainable by simple first-principle volume production processes.

This model (Fig. 5.2(a)) can be looked at in combination with the results from Chapter 4 to show that the negative ion peak through the center of the filter region is explainable by three combined processes:

- 1) The magnetic field creates a particle trap which locally increases the electron density in the center of the filter (Fig. 4.1) and this provides more electrons for the dissociative attachment processes.
- 2) The particle trap is dominated by cold electrons (Fig. 4.7(b)) which reduces electron stripping losses of H⁻ and enhances the dissociative attachment cross section.
- 3) The filter helps to produce higher rovibrational H₂ temperatures (Fig. 4.13(b)) which increases the dissociative attachment downstream of the discharge under the filter.

5.2 Temporal Variation of H⁻

Experiments were performed at four positions along the source to investigate the behaviour of the negative ions into the afterglow. The technique involved pulsing the laser and plasma interval with a variable time window between 0 μ s and 200 μ s into the afterglow to resolve the fine-scale temporal evolution of the negative ion population into the afterglow (see Fig. 2.23(a) for the experimental setup). The afterglow results will be presented here first in Section 5.2 followed by a discussion of the afterglow dynamics and calculations of total diffusion rates in Section 5.3.

The axial positions at $x = 1$ cm, $x = 5$ cm, $x = 8.5$ cm and $x = 11.5$ cm were chosen for the afterglow experiments where both I_{PD} and I_{DC} were measured simultaneously to provide the negative ion fractions at each time step. Additionally, two types of magnetic field geometry were compared (shown in Figure 5.3 where the transverse filter (right) has been used in the previous chapters and the cusp filter (left) is commonly used in negative ion sources in tandem. The two magnetic field types are measured separately here to isolate their individual effect on the negative ions. The cusp field was made up of 8 magnets which totalled the same volume and same magnetic material mass as the transverse filter but arranged in a different geometry. The radial cusp filter was attached around the source tube in a ring around the tube centered at $x = 5$ cm. The cusp filter used alternating magnetic poles facing inward toward the tube with a small gap between each magnet where the laser beam

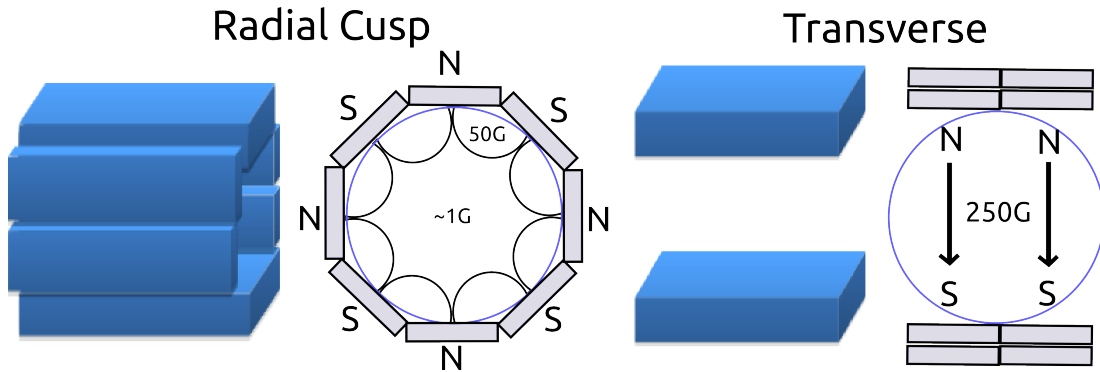


Figure 5.3: Geometry of the two magnetic filters used in this Section. (Left) 'Radial cusp' filter with alternating magnetic pole orientations. (Right) Transverse filter described previously in Figure 2.3. Note that both filters had the same net volume and mass of magnetic materials but were arranged differently. The blue circle represents the source tube orientation.

could pass through from the side. The 3-axis magnetic probe was used (See Section 2.1.2) to measure the magnetic field vector of the radial cusp at different locations. The Hall probe measurements through the central axis of the filter showed relatively uniform magnetic fields inside the filter where only weak anisotropies existed inside the center of the cusp with a z-directed field of 1 Gauss to 3 Gauss and edge cusp fields between 40 G and 60 G. The forward power of the system was kept at constant 250 W throughout the experiments. The pulsed duty cycle was 20% with 20 milliseconds 'on' time and 80 milliseconds 'off' time.

A basic description of the physics occurring in the early afterglow of a plasma discharge is relatively well established [158] [45] and can be described as follows. When the plasma is switched off, the highly mobile electrons begin to exit the system first which establishes the afterglow ambipolar field. As the electron density falls to around 1% of the 'discharge on' levels in the afterglow, the ratio of electric screening (Debye length) to the characteristic length of the system (Λ) becomes unity $\lambda_{De}/\Lambda = 1$. At this point the ambipolar electric field can reach across the source and accelerate the remaining electrons to the walls before it finally collapses leaving behind a cold ion-ion plasma in electronegative gasses. This ion-ion plasma is free to recombine or diffuse in a field-free environment to the walls in the late afterglow. Experimentally the latter of these two processes has been recorded [159] where strong negative ion wall currents have been reported in the post ion-ion plasma afterglow proceeding the collapse of the ambipolar field indicative of H^- destruction primarily by wall diffusion.

In the case of the ICPS, the afterglow processes of mutual neutralization, dissociative attachment, and diffusion are superimposed together and interact in the presence of complex magnetic field geometry. The afterglow results will be shown in the following section (Sec. 5.2) and the discussed with respect to the plasma dynamics will be afterwards in Section 5.3.3.

This section presents the afterglow results for electrons and negative ions at four positions along the source. The colouring follows previous chapters with black profiles indicating data without the filter and the red profiles indicating the transverse filter with the new radial cusp filter is shown as the blue colored profiles. The dotted profiles for each colour indicate the electron current draw (I_{DC}) for each of the filters respectively with the I_{DC} scale shown on the right y-axis for each figure.

5.2.1 x = 1 cm Afterglow Results

Figure 5.4(a) shows the negative ion signals at $x = 1$ cm just in front of the antenna. The profile trend for all three conditions shows an initial increase in negative ions reaching a peak at $50 \mu\text{s}$ of approximately 2.75 mA for both filters and 1 mA for the unfiltered case. The increase in negative ions over this period is consistent with the cooling of hot electrons near the discharge in the early afterglow increasing the dissociative attachment rate [15]. These profiles show a competition between the production and destruction reaction rates over time. The destruction processes seen after $50 \mu\text{s}$ will be shown in Section 5.3.3 to be consistent with the rate for mutual neutralization. All three profiles begin to decay from $50 \mu\text{s}$ to $220 \mu\text{s}$ down to similar levels of around 0.5 mA .

The electron currents (dotted profiles) are seen to decay quickly from the end of the pulse reaching levels below 1% of initial values after $50 \mu\text{s}$. The electron current from the cusp filter is seen to hold a higher current by a few mA during the early afterglow. This is the expected behaviour from the cusp as it is designed to help prevent electron losses to the walls with its curved radial field geometry. The time scales and shapes for these afterglow negative ion profiles are consistent with other negative ion hydrogen sources [151] however it will be shown that there are strong spatial dependencies for electron

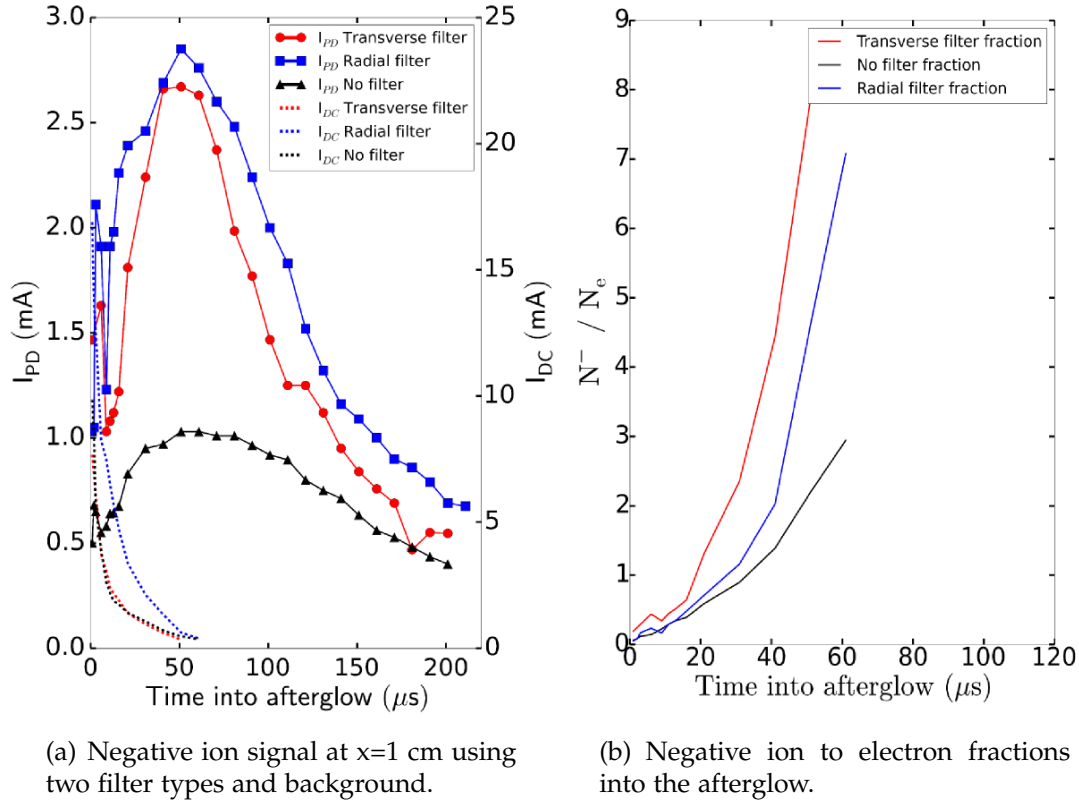


Figure 5.4: Photodetachment current into the afterglow at $x=1$ cm with the negative ion fraction. (red) transverse filter, (blue) cusp filter, (black) no filter.

decay across the plasma source.

Figure 5.4(b) shows the respective negative ion fractions at $x = 1$ cm which grow exponentially into the afterglow due to the simultaneous declining electron current and growing negative ion currents. The negative fractions are seen to begin at similar levels for all three conditions in the early afterglow and increase up to between 3:1 and 8:1 over approximately $60 \mu\text{s}$ with the strongest fractions for the transverse filter.

It is worth noting here that the difference in the time axis between the figures is a result of the electrons having almost completely decayed after $60 \mu\text{s}$ due to their higher diffusion and mobility. The n^-/n_e fractions can only be measured as long as electrons are in the system and the persistence seen here of the ions beyond the electron decay time ($\geq 50 \mu\text{s}$) is indicative of the forma-

tion of an ion-ion afterglow plasma. These ion-ion plasmas are common for pulsed electronegative plasmas [46] [158] [15] and are a major aspect of the chemistry used in industrial plasma processing. The length of time to create conditions for ion-ion plasmas has been shown to relate to both the ambipolar field strength and the discharge power [158] [45].

5.2.2 x = 5 cm Afterglow Results

Figure 5.5(a) presents the negative ion signals immediately under the filter at x = 5 cm and represents the afterglow dynamics of the negative ions inside the center of the filter trap. The negative ion signals for both the cusp filter and the transverse filter cases shows an unexpectedly strong exponential decay profile from the early afterglow with currents ranging from 4.6 mA and 7.7 mA respectively. These negative ion currents represent the highest current measurements seen throughout the source and support the previous experiments from the spatial profiles showing a negative ion peak centered in this region for the transverse filter in Section 5.1.

The x = 5 cm position is characterized by destruction processes in the afterglow as the electrons are already cold (0.2 eV) during the discharge on time and can not be cooled further in the afterglow for dissociative attachment. As a result, no increase in the negative ion signal is seen for either the cusp filter or the transverse filter and so the peak in the negative ion signal under the filter during continuous operation cannot be enhanced into the afterglow. The unfiltered case at x = 5 cm does not show this exponential decay and instead shows a peak forming around 40 μs into the afterglow.

The electron decay profiles are quite steep at x = 5 cm, with the electron current reaching low levels around only 25 μs into the afterglow. In the near afterglow, the electron current for the radial cusp filter is approximately three times higher than for the transverse and unfiltered case. This may suggest that the field geometry of the radial cusp filter affects the initial afterglow electron transport and hence the time scale for the ambipolar field formation in the early afterglow.

The negative ion fractions for the x = 5 cm position are shown on the right (Fig. 5.5(b)). The fractions of the cusp and unfiltered case both range between 0.3:1 at the start of the afterglow with both reaching up to 7:1 after 70 μs

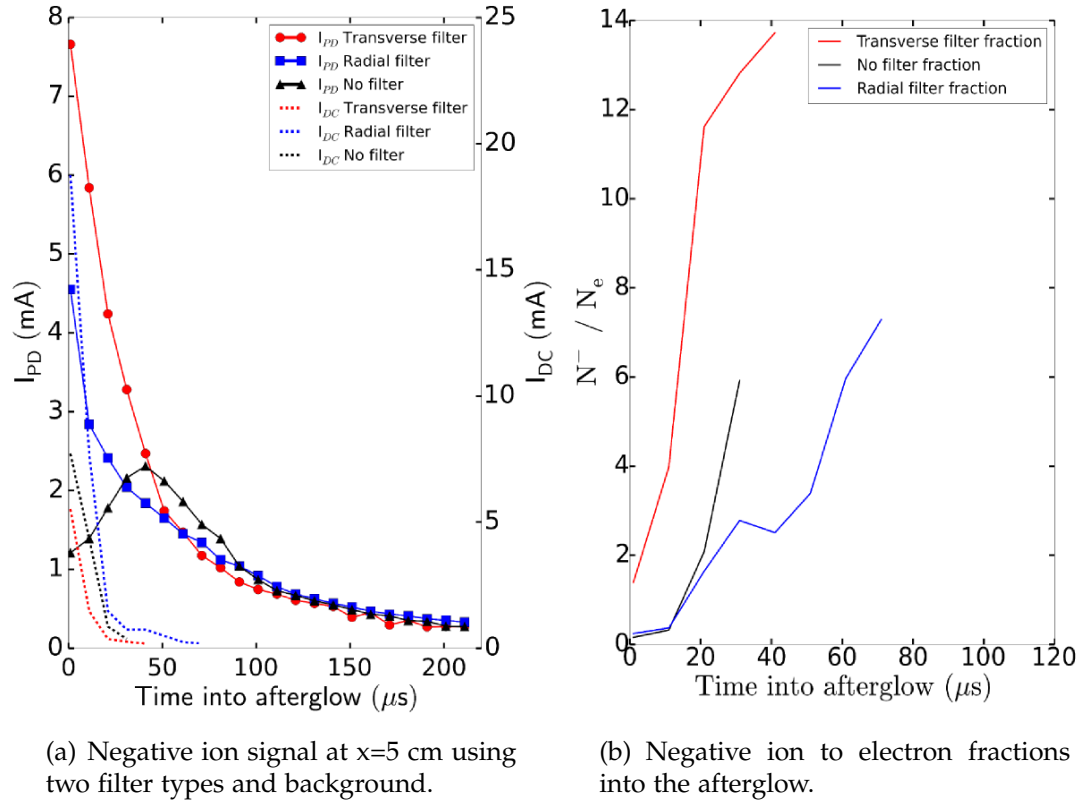


Figure 5.5: Photodetachment current into the afterglow at $x=5$ cm with the negative ion fraction. (red) transverse filter, (blue) cusp filter, (black) no filter.

and $30 \mu\text{s}$ respectively. Despite the fact that destructive processes dominate for the transverse filter, the high initial negative ion density combined with a rapid electron decay means that the negative ion fraction is seen as high as 14:1 which occurs at approximately $40 \mu\text{s}$ into the afterglow. This negative ion fraction was the highest measured in the ICPS.

5.2.3 $x = 8.5$ cm Afterglow Results

Figure 5.6(a) shows the negative ion signals downstream of the filter at $x = 8.5$ cm. The transverse filter shows an increase in current in the first $25 \mu\text{s}$ of the afterglow with the radial filter and unfiltered case both show latent increases in negative ion current with peaks occurring in the later afterglow around $100 \mu\text{s}$ and $130 \mu\text{s}$ respectively. The profiles show the formation of late afterglow

ion-ion plasmas at this location.

The electron decay time varies markedly between the three conditions with the transverse filter measuring a short decay of around 50 μs compared with the radial cusp showing a characteristic high afterglow electron current and decaying on a long time scale of > 100 μs with a high electron current of between 2 mA to 8 mA. This ability of radial cusp magnetic geometries to trap electrons into the afterglow for up to hundreds of microseconds has been shown by other authors [15] using EEPF measurements into the afterglow which indicated that the cusp system can trap electrons over a wide range of energies and time scales. The long decays of the radial filter and the unfiltered case indicate that the ambipolar field collapse is delayed at this downstream location in the absence of a transverse field. These features will be discussed further when discussing the afterglow reaction rates in Section 5.3.3.

The negative ion fractions at $x = 8.5$ cm are shown in Figure 5.6(b) and generally exhibit much lower afterglow fractions than those seen at $x = 5$ cm and $x = 1$ cm. The negative ion fractions in the early afterglow are negligible for the unfiltered case but increase to 0.35:1 after 100 μs . The radial cusp filter fraction grows exponentially to 1.2:1 at 100 μs where the increase in negative ion is seen to peak. The transverse fraction grows from 0.2:1 in the early afterglow up to around 1.6:1 after 40 μs .

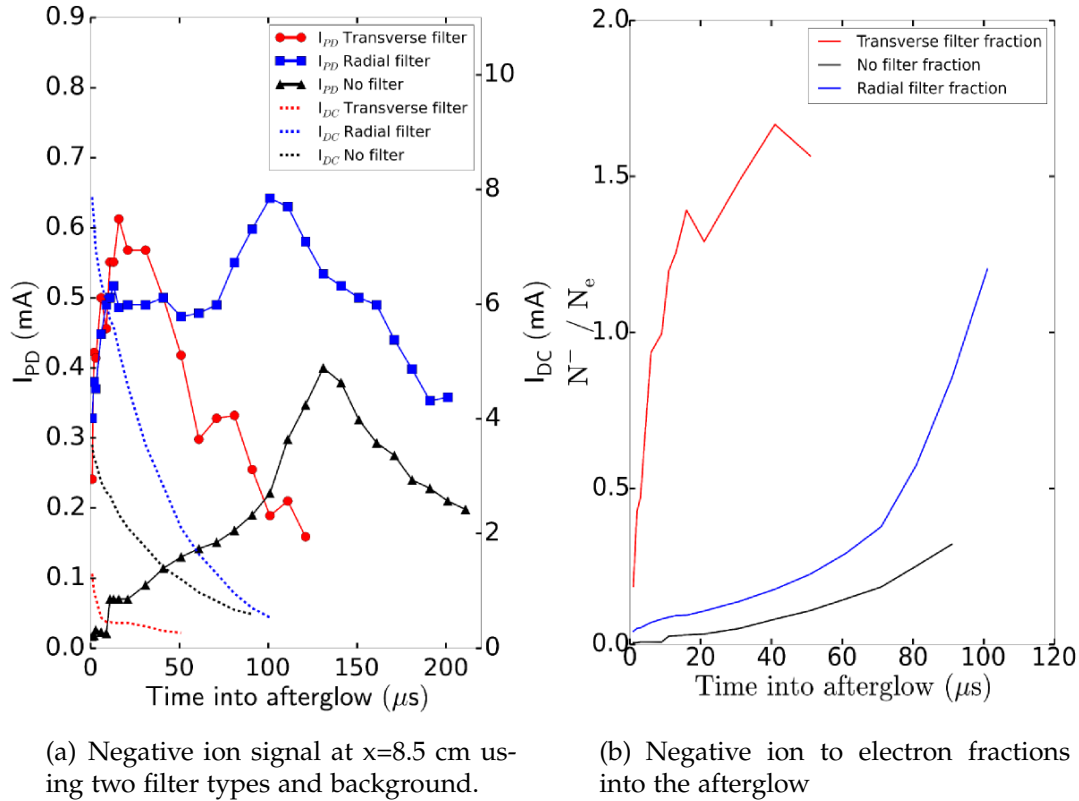


Figure 5.6: Photodetachment current into the afterglow at $x=8.5$ cm with the negative ion fraction. (red) transverse filter, (blue) cusp filter, (black) no filter

5.2.4 $x = 11.5$ cm Afterglow Results

Figure 5.7(a) shows the negative ion signal downstream at $x = 11.5$ cm. For the transverse filter at this position, this axial position lies at the edge of the filter field and has an intersecting non-uniform magnetic field geometry at this location (See Figure 2.3(d)). Additionally, the plasma densities are low in this region at around 10^{15} m^{-3} compared to $3 \times 10^{16} \text{ m}^{-3}$ inside the filter and so there are less electrons available to form negative ions via dissociative attachment.

The profiles for the transverse filter field show a strong increase in the negative ion signal in the early afterglow increasing by a factor of 5 from 0.1 mA up to 0.55 mA in the first 20 μs . This is in addition to a rapidly decaying electron I_{DC} current of only 20 μs . After the peak the signal decays exponentially over 200 μs .

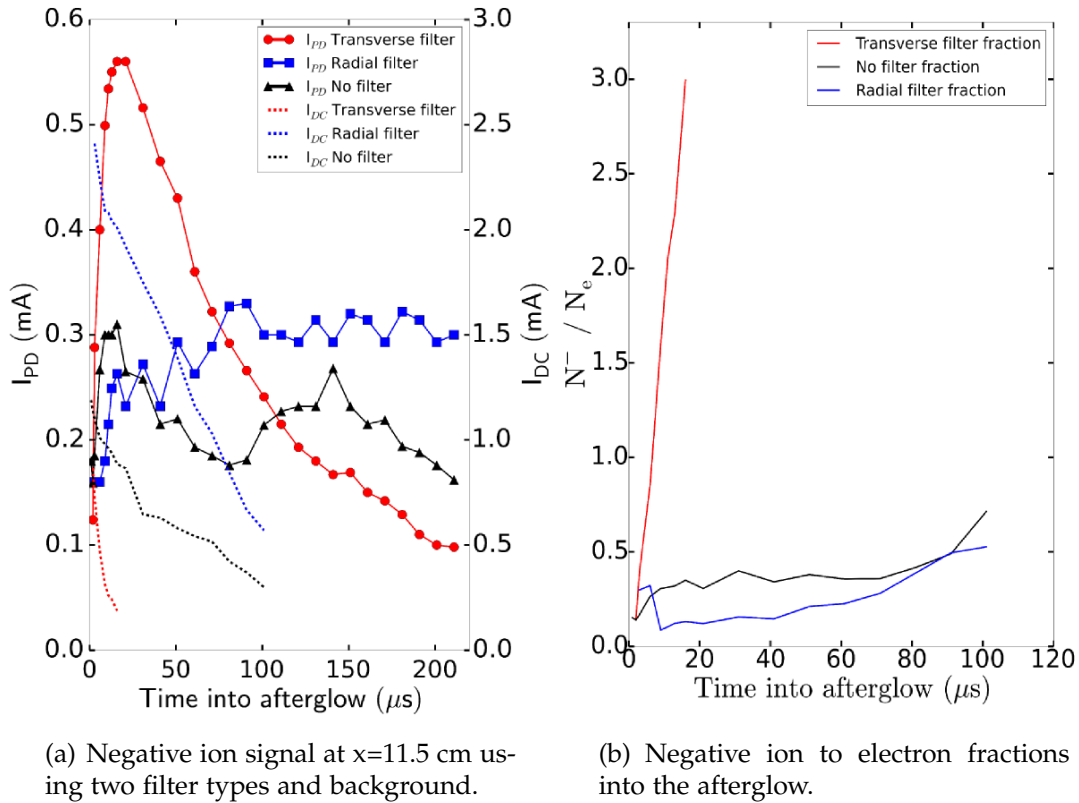


Figure 5.7: Photodetachment current into the afterglow at $x=11.5$ cm with the negative ion fraction. (red) transverse filter, (blue) cusp filter, (black) no filter.

In contrast the radial filter exhibits a steady negative ion current of around 0.3 mA throughout the afterglow phase. Similarly the unfiltered profile extends up to 200 μ s and shows a two-peaked profile, the first in the early afterglow at 10 μ s and the second at 140 μ s.

These steady long decays for the cusp and unfiltered cases correlates with the long electron decay times of 100 μ s and indicates the delayed collapse of the ambipolar field downstream of the discharge when not applying a transverse field. This also indicates the transverse field increases afterglow losses of electrons to the walls which may enhance the breakdown of the ambipolar field.

The negative ion fractions at 11.5 cm are shown in Figure 5.7(b). The radial and unfiltered cases show relatively low fractions which are constant over 100

μs into the afterglow with values ranging from 0.25:1 to 0.5:1. The transverse filter shows a short-live and strong increase in the negative ion fraction up to 3:1 within 10 μs into the afterglow which corresponds to a rapid decline in the electron current.

5.2.5 Concluding Afterglow Remarks

The results from this section shows a wide variety in the spatio-temporal behaviour of negative ions in the ICPS in both the near and far afterglow. Using the transverse filter on the ICPS shows that it produces the strongest negative ion currents and also exhibits the highest negative ion fractions throughout the afterglow. The transverse filter also shows the lowest overall electron residence times meaning that it decreases the time it takes for the ambipolar field to breakdown.

In contrast the radial cusp filter shows intermediate negative ion currents and fractions which shows similarities to the transverse filter at some axial positions ($x = 1 \text{ cm}$ and $x = 5 \text{ cm}$) yet shows similarities to the unfiltered case at the other positions ($x = 8.5 \text{ cm}$ and $x = 11.5 \text{ cm}$). The cusp field supports the longest afterglow electron currents and the longest electron decay times which implies that it helps to maintain the ambipolar field longer into the afterglow.

The unfiltered case shows the lowest negative ion densities into the afterglow and the lowest negative ion fraction across all four of the measurement positions which means both the radial filter and the transverse filter both produce more negative ions across the source than without a filter.

5.3 Reaction Rate Comparisons

Since the afterglow physics are complex and difficult to separate, rate coefficients were calculated from the afterglow data in Section 5.2. The rate coefficients will be used to help determine the dominant mechanisms taking place at different positions within the afterglow. The theory behind this rate coefficient calculation method will be shown first in this section and an ex-

ample of the rate fitting procedure will be shown.

The rate coefficient of a plasma process can be estimated into the afterglow by measuring the change in density over time of the plasma reactants provided that the time scale of the measurement is small with respect to the time scale of the plasma process. An analysis of the afterglow results from Section 5.2 will be made to estimate the mechanism driving the dynamic afterglow processes of production and destruction to asses whether the process is from dissociative attachment, mutual neutralization or from localized diffusion processes within the source.

5.3.1 Ambipolar Diffusion

The ambipolar field and diffusion coefficients play a key role in these processes and they will be briefly considered here with respect to the results as they relate to the later discussion in Section 5.3.3.

The ambipolar diffusion term arises when the flux of positive and negative charges to the walls are equal. From Equation 4.3 the flux of a given negatively charged particle species (either negative ions or electrons) can be written as:

$$\Gamma_- = \mu_- n_- \vec{E} - D_- \nabla n_- \quad (5.5)$$

where the negative subscript refers to the species charge. In quasi-neutral conditions, the fluxes of positive and negative plasma species are equal:

$$\mu_- n_- \vec{E} - D_- \nabla n_- = \mu_+ n_+ \vec{E} + D_+ \nabla n_+ \quad (5.6)$$

Solving Eqn. 5.6 for the electric field (\vec{E}) gives the ambipolar field:

$$\vec{E} = \frac{\nabla n_{+-}}{n_{+-}} \cdot \frac{D_- + D_+}{\mu_- + \mu_+} \approx \frac{D_-}{D_+} \cdot \frac{\nabla n_{+-}}{n_{+-}} \quad (5.7)$$

Substituting the ambipolar electric field back into Eqn. 5.5 gives the total flux:

$$\Gamma = -\frac{\mu_+ D_- + \mu_- D_+}{\mu_+ + \mu_-} \cdot \nabla n \quad (5.8)$$

where the group of fraction constants on the right hand side is referred to as the ambipolar diffusion constant:

$$D_a = \frac{\mu_+ D_- + \mu_- D_+}{\mu_+ + \mu_-} \quad (5.9)$$

Despite the increased diffusion and mobility of the electrons over negative ions, this equation has been shown to hold for negatively charged species up to negative ion fractions of 10:1 $\alpha = n^-/n_e \leq 10$ [160] which is the upper limit of negative ion ratios seen in the ICPS. The ambipolar diffusion constant is similar to the free diffusion constant as it scales the ∇n term for the force balance equation and $\nabla^2 n$ for the particle continuity equation:

$$\frac{\partial n}{\partial t} - D_a \nabla^2 n = \text{production} - \text{loss} \quad (5.10)$$

This particle continuity is especially relevant in afterglow plasmas as the densities of different species change. In the afterglow of a plasma, the generation and loss terms on the right hand side of Eqn. 5.10 can be represented by second order reaction rates of positive and negative species [45] [160]:

$$\frac{\partial n}{\partial t} = D_a \nabla^2 n - k_R n^2 \quad (5.11)$$

Where k_R is the rate coefficient for binary production and loss reactions for positive and negative species (n_+, n_-) which contribute to the reaction into the afterglow. This continuity equation accounts for both the ambipolar diffusion of particles through the $D_a \nabla^2 n$ term, and the binary plasma reactions are accounted for in the $k_R n^2$ term [158]. This equation will be used to fit the negative ion profiles seen in section 5.2 to estimate the dominance of either the diffusion term or the binary reaction term in the ICPS afterglow.

The process of calculating the reaction rates and diffusion terms from the afterglow data will be detailed in the following section.

5.3.2 Total Reaction Rate Fit

The time rate of change in a particle density $[A]$ can be expressed from the standard second order chemistry rate law as a combination of diffusion and chemical reactions:

$$\frac{d[A]}{dt} = D_a \nabla^2 n - k [A]^2 \quad (5.12)$$

with k as the rate constant and $[A]$ as the density of the reactant as a function of time. Note that this $[A]$ is the preferred chemistry notation and is equivalent to the previous $n(t)$ density notation.

Since the density changes are a function of either diffusion or of chemical reactions, the question then arises; are the trends in negative ion afterglow density from Section 5.2 due to movement of H^- particles via diffusion through the source (the $D_a \nabla^2 n$ term) or are the changes in H^- afterglow density from local chemical reactions creating and destroying the negative ions at each location into the afterglow (the $k [A]^2$ term).

As the afterglow data from the previous section (Section 5.2) shows the negative ion density vs time, an expression of the results can be made using Equation 5.12 to show the density $[A]$ as a function of time into the afterglow. The data then has the form of the standard chemistry reaction rate problem. In the absence of diffusion process such as those found in high density gasses and in fluids, $D_a = 0$ and Equation 5.12 can then be separated and integrated:

$$\int_{[A]_0}^{[A]_t} \frac{1}{[A]^2} d[A] = -k \int_0^t 1 dt \quad (5.13)$$

Then:

$$\frac{1}{[A]_t} = -kt + \frac{1}{[A]_0} \quad (5.14)$$

This yields the standard chemistry reaction rate equation which relates the change of density of a reactant $[A]$ over time to a rate constant k and the initial density concentration A_0 . Thus the chemical reaction rate for production and loss of a particle species can be found from plotting the $[A]$ vs time data on an inverse scale and taking the slope of the line to find the reaction rate

coefficient k (eg. Figure 5.8). In plasmas this is a common way of determining binary reaction rate coefficients (eg. [45] [160]).

This approach, however, only works when the chemical diffusion processes is suppressed (i.e $D_a = 0$) such as when operating at higher pressures (> 1 Torr). For the afterglow measurements in this chapter, the pressure is low enough that $D_a \neq 0$ and so measuring the afterglow measurements represent a combination of diffusion and chemical reactions at each location.

For the measurements in this chapter, the diffusion term cannot be ignored from Equation 5.12 and the integration of Equation 5.12 instead becomes:

$$\frac{1}{[A]_t} = \int (D_a \nabla^2 n) dt - k_R t + \frac{1}{[A]_0} \quad (5.15)$$

The second term here is the integral of the density Laplacian and is difficult to obtain directly, however the indirect effect will be to simply modify to the measurement of the chemical reaction rate coefficient which we will add the subscript R for clarity k_R . The diffusion term in Equation 5.15 represents the unknown movement of particles either toward or away from the probe tip and thus contributes an 'effective diffusion rate coefficient' which we can simply define as Δk_D such that Equation 5.15 can be expressed as:

$$\frac{1}{[A]_t} = \Delta k_D - k_R t + \frac{1}{[A]_0} \quad (5.16)$$

The k_D term can be indirectly measured now by assuming that it affects the main production and loss rate chemical rate k_R by a factor ranging from zero (no diffusion) to a high number (diffusion dominated). If there is low diffusion present, then the calculated reaction rates from the afterglow H^- data will match the known dissociative attachment production rate coefficient. Similarly any decreases in the data should then match the known rate of H^- mutual neutralization. However if diffusion dominates, the calculated rate coefficients from the afterglow data will be markedly different to the known chemical reaction rates.

Second order rate coefficients were calculated from the slope of the experimental measurements of a particle density over time when they are plotted on an inverse density scale. The experimentally determined slopes are a combination of the Δk_D and k_R rates and so will be defined as the total rate coeffi-

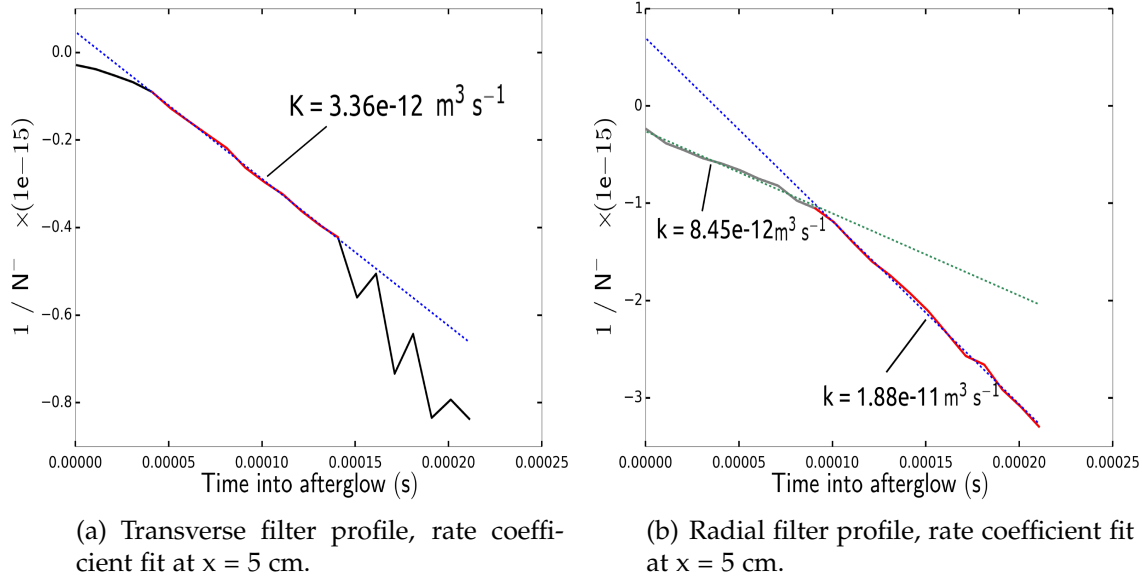


Figure 5.8: Examples of the method used to calculate total rate coefficients k_{TOT} from the afterglow data.

cient k_{TOT} . If the calculated total rate dominated by binary reactions then the Δk_D diffusion term will be zero and the calculated rate coefficient k_{TOT} will equal the known rate coefficient k_R . However if k_{TOT} is markedly higher than the known binary reaction rate coefficients, then the diffusion term Δk_D will be dominant which indicates that the plasma is in a diffusive regime. In this diffusive regime, the negative ion fluxes to the probe are a result of transport from adjacent areas inside the source during the afterglow rather than localized chemical production and destruction of negative ions near the probe tip.

Figure 5.8 shows two examples of the rate coefficient fit from the negative ion signals at $x = 5$ cm in Figure 5.5(a). The profiles represent the exponential negative ion decay profiles for the radial filter and the transverse filter. The rate calculations show the value of k_{TOT} . Since the negative ion density is always decreasing at $x = 5$ cm these slopes are negative and represent the rate coefficients of H^- loss at this location. The radial filter in Figure 5.8(b) shows two separate rate coefficient fits which correspond to two different loss rates occurring into the afterglow.

The following section will present the results of the rate calculations for the negative ion profiles at each of the four positions from Section 5.2.

5.3.3 Reaction Rate Results

Reaction rates were calculated where possible at each of the 4 positions using the negative ion signals shown in Section 5.2. Total reaction rate fits were made for the increasing and decreasing slopes for each profile and compared to the leading rate coefficients for production and destruction.

The results of the rate coefficient fits are discussed below and are summarized in Table 5.2. The table shows the common binary production and destruction rate coefficients (k_R) which are dissociative attachment, mutual neutralization and neutral collisional detachment. These are shown for reference to the calculated rates (k_{TOT}) for each profile to help identify the likely mechanism for the negative ion results.

Note that at the experimental densities, the negative ions have relatively long mean free paths for destruction. For mutual neutralization, the mean free path is ≈ 32 cm, for neutral H stripping of $H^- \approx 2$ cm, and diffusion to the walls ≈ 6 cm with a magnetic field. In the afterglow the ions can travel up to several centimeters in tens of microseconds depending on the density and diffusivity.

5.3.3.1 $x = 1$ cm Total Rates

The rates were first calculated from the $x = 1$ cm profiles in Figure 5.4(a). The rate coefficients were measured for both the $x = 1$ cm transverse profile and the unfiltered profile corresponding to the production (increasing) and destruction (decreasing) slopes.

The total production reaction rate for the transverse filter (Fig. 5.4(a)) (red profile) up to $50 \mu s$ was found to be $2.40 \times 10^{-13} m^3 s^{-1}$ which would correspond to the upper end of the dissociative attachment rate coefficient [9] [161]. The increase in the negative ions into the afterglow at $x = 1$ cm downstream is explainable by dissociative attachment if sufficiently high highly rovibrational H_2 is present. Since the electron temperature is high at this location near the antenna, the reduction in the electron temperature into the

early afterglow allows for increased negative ion production.

The destruction rate on the down slope was calculated at $7.69 \times 10^{-13} \text{ m}^3 \text{ s}^{-1}$. This destruction rate coefficient corresponds closely to the mutual neutralization rate of the $\text{H}^- + \text{H}_3^+$ reaction which has a value of $1.33 \times 10^{-13} \text{ m}^3 \text{ s}^{-1}$. This reaction rate shows that the total rates k_{TOT} is dominated by the binary reaction chemistry term k_R and a suppression of the diffusive term δk_D close to the discharge. This is explainable due to the high plasma densities and higher gas densities near the antenna inhibiting afterglow transport of the negative ions from this location which forces binary destructive events to occur.

The unfiltered negative ion profile (Fig. 5.4(a)) (black profile) shows a similar density peak to the filtered case up to $50 \mu\text{s}$ with a production rate constant of $8.33 \times 10^{-12} \text{ m}^3 \text{ s}^{-1}$ and a destruction rate after $50 \mu\text{s}$ of $3.70 \times 10^{-12} \text{ m}^3 \text{ s}^{-1}$. This shows an increase in negative ion production far greater than the dissociative attachment rate at the start of the afterglow period. This result indicates that without the filter in place the negative ion signal at $x = 1 \text{ cm}$ is dominated by diffusion of negative ions from adjacent areas of the discharge. This is most likely related to the spatial distribution of the DC electric field without the magnetic filter in place which directs negatively charged species inward towards the antenna (see Paunská *et al.*, [147]) and this may also be the reason for the highest negative ion density being closest to the antenna in unfiltered inductive systems (see Figs. 5.1(b) and 5.2(b)).

For the unfiltered profile after $50 \mu\text{s}$ the destruction rate is an order of magnitude higher than the rate expected for the primary destructive process of mutual neutralization. This indicates that the destruction of negative ions via diffusion out of the central region and is consistent with the time period after the breakdown of the ambipolar field rather than by mutual neutralization. This is also consistent with the time-scale of the end of the I_{DC} decay which signals the collapse of the ambipolar field.

5.3.3.2 $x = 5 \text{ cm}$ Total Rates

The afterglow measurements at $x = 5 \text{ cm}$ for the transverse filter are shown in Figure 5.5(a) (red profile). The profiles show strong exponential loss of H^- from the beginning of the afterglow with no increase in the negative ion

Table 5.2: Total rate coefficients for H^- calculated from afterglow data in the ICPS for Production (P) and Destruction (D).

Reaction	k_R Rate Coefficient ($\text{m}^3 \text{ s}^{-1}$)
Dissociative attachment (P)	$\approx 10^{-14} (\mathbf{v''} \gg 0)$
Mutual neutralisation (D)	$\approx 1.2 \times 10^{-13}$
Neutral collisional detachment (D)	$\approx 1.2 \times 10^{-15}$
Axial Position and Filter	k_{TOT} Total Rate Coefficient ($\text{m}^3 \text{ s}^{-1}$)
(1cm) Transverse filter (P)	2.40×10^{-13}
(1cm) Transverse filter (D)	7.69×10^{-13}
(1cm) No filter (P)	8.33×10^{-12}
(1cm) No filter (D)	3.70×10^{-12}
(5cm) Transverse filter (D1)	1.15×10^{-12}
(5cm) Transverse filter (D2)	3.36×10^{-12}
(5cm) Radial filter (D1)	8.45×10^{-12}
(5cm) Radial filter (D2)	1.88×10^{-11}
(5cm) No filter (P)	4.60×10^{-12}
(5cm) No filter (D)	1.89×10^{-11}
(8.5cm) Transverse filter (P)	3.27×10^{-11}
(8.5cm) Transverse filter (D)	1.27×10^{-11}
(8.5cm) No filter (P)	4.44×10^{-12}
(8.5cm) No filter (D)	1.49×10^{-12}
(11.5cm) Transverse filter (P)	6.38×10^{-11}
(11.5cm) Transverse filter (D)	7.04×10^{-12}

$$\Delta k_{TOT} / k_R$$

signal indicating dominance of destructive processes at this location. The transverse filter profile exhibits two exponential decay k_{TOT} rate coefficients, the first from 2 μs to 40 μs and the second from 40 μs onwards. The first rate coefficient was calculated as $1.15 \times 10^{-12} \text{ m}^3 \text{ s}^{-1}$ and the second at $3.36 \times 10^{-12} \text{ m}^3 \text{ s}^{-1}$. The initial decay rate up to 40 μs is similar to the mutual neutralization rate. However from 40 μs to 150 μs , the rate increases to around an order higher than the mutual neutralization coefficient and this indicates a switch from binary reaction losses to diffusive losses as the plasma density drops and allows for diffusion process to begin to dominate. The I_{DC} decay profile shows a rapid breakdown of the ambipolar field and the negative ions, which are semi-magnetized in this region, are quickly lost to the walls along the magnetic field lines. The data is consistent with a high number of negative ions present during the 'discharge on' period which exit the system resulting in a rapid ambipolar breakdown in the early afterglow. This result suggests that the rapid breakdown in the ambipolar field and loss of negative ions could be mitigated against with the use of a strong tandem cusp at this location which could extend the negative ion decay time into the afterglow.

The situation is similar for the radial filter (Fig. 5.5(a)) (blue profile) which also shows two k_{TOT} rate rate coefficients. The first is calculated at $8.45 \times 10^{-12} \text{ m}^3 \text{ s}^{-1}$ and the second at $1.88 \times 10^{-11} \text{ m}^3 \text{ s}^{-1}$. These rates are up to two orders of magnitude higher than the mutual neutralization rate coefficient which indicates strong diffusion processes.

The I_{DC} decay time is slightly longer for the radial filter but the field strength here is seen to be not strong enough to prevent the rapid loss of negative ions from diffusing to the walls in the afterglow. This is most likely due to the relatively weak field at the cusp edge and the long mean free path for the negative ions. If the magnetic field strength of the cusp was strongly increased then the wall diffusive losses could be controlled, however, the cusp cannot prevent ions from diffusion upstream and downstream to adjacent areas of the source. Using a combination of the transverse field and the cusp field here would prevent the ions from exiting upstream and downstream provided that the field is strong enough to semi-magnetize the H^- ion.

The unfiltered negative ion signal at $x = 5 \text{ cm}$ (Fig. 5.5(a)) (black profile) does not show the rapid decline seen for the transverse and radial filters at the onset of the afterglow but rather a peak in current around 50 μs . The rate coefficient for the increase on the left side of the peak was calculated at $4.60 \times 10^{-12} \text{ m}^3 \text{ s}^{-1}$ which is 2 orders higher than the rate for dissociation.

tive attachment. The decay rate on the right hand side was calculated at $1.89 \times 10^{-11} \text{ m}^3 \text{ s}^{-1}$ around two orders higher than the mutual neutralization rate. The timing of the peak is consistent with the I_{DC} ambipolar breakdown and is explainable by diffusive transport of negative ions from adjacent areas driven by ion-ion free diffusion. It should be noted that several of these datasets were taken several times on separate days, especially at the $x = 5 \text{ cm}$ position to verify that the trends were reproducible.

5.3.3.3 $x = 8.5 \text{ cm}$ Total Rates

The afterglow measurements at $x = 8.5 \text{ cm}$ for the transverse filter are shown in Figure (Fig. 5.6(a)) (red profile). The profile shows a strong initial increase in negative ions reaction coefficient of $3.27 \times 10^{-11} \text{ m}^3 \text{ s}^{-1}$ which is three orders of magnitude above the dissociative attachment rate coefficient. While the net density of negative ions from this peak is low, the rate of increase over such a short time frame indicates the peak is from diffusion from neighbouring areas. Since the peak occurs around $25 \mu\text{s}$ the increased influx of negative ions would have to be within only several centimeters of the $x = 8.5 \text{ cm}$ measurement position. The decay slope of the transverse profile after $25 \mu\text{s}$ was measured at $1.27 \times 10^{-11} \text{ m}^3 \text{ s}^{-1}$ which is also indicative of diffusive losses on the I_{DC} decay time scale.

The unfiltered profile at $x = 8.5 \text{ cm}$ (Fig. 5.6(a)) (black profile) shows a delayed increase in the negative ion current at around $125 \mu\text{s}$ with a production rate coefficient of $4.44 \times 10^{-12} \text{ m}^3 \text{ s}^{-1}$ which is high compared to dissociative attachment. The delayed onset of the peak in the unfiltered case coincides with a long I_{DC} electron decay time and hence again correlates with the time scale of the ambipolar breakdown.

Similar to the unfiltered profile, the radial profile at $x = 8.5 \text{ cm}$ shows a delayed peak which coincides with the I_{DC} decay around $100 \mu\text{s}$ into the afterglow.

5.3.3.4 $x = 11.5 \text{ cm}$ Total Rates

The afterglow measurements at $x = 11.5 \text{ cm}$ for the transverse filter are shown in Figure (Fig. 5.7(a)) (red profile). Here at 11.5 cm the transverse filter shows

an early sharp peak in the I_{PD} current before an exponential-like decay. The peak in the signal here has the strongest rate increase seen in the ICPS of $6.38 \times 10^{-11} \text{ m}^3 \text{ s}^{-1}$ which is three orders of magnitude higher than the dissociative attachment coefficient. The exponential decay from $20 \mu\text{s}$ to $220 \mu\text{s}$ has a decay rate of $7.04 \times 10^{-12} \text{ m}^3 \text{ s}^{-1}$ which most likely corresponds to the ion-ion free-diffusion rate as the I_{DC} current draw is seen to disappear after only $20 \mu\text{s}$, again consistent with the location of the negative ion peak.

5.3.3.5 Afterglow Concluding Remarks

These afterglow results present several key overall findings. Firstly, the changes in local negative ion density are found to be mostly diffusion dominated across the ICPS under these power and pressure conditions. Near the antenna, the higher plasma densities and gas pressure are seen to partially inhibit plasma diffusion and so the rate coefficients for production and loss are found to be closer to dissociative attachment and mutual neutralization coefficients at this location. Overall however, these results indicate that the ICPS operating at 250 W at 100 mtorr is well within a diffusion dominated afterglow regime downstream of the discharge.

Several studies which calculated the rate coefficient for mutual neutralization of negative ions in nitrogen plasma mixtures used gas pressures as high as 500 mtorr and atmospheric pressure at plasma densities of at least 10^{16} m^{-3} . These high pressures were found to be required to successfully inhibit the diffusion effect and prevent it from influencing the measurement of the mutual neutralization rate coefficient [162] [158] [163]. Since the measurements here were performed at 100 mtorr using hydrogen gas with a lower collisional cross section than nitrogen, the conclusion of a diffusion dominated afterglow regime is certainly reasonable.

The rate results show that the diffusion time is spatially and temporally sensitive and that the localized diffusive loss coefficient is between one to three orders of magnitude higher than the mutual neutralization rate coefficient (See the $\Delta k_{TOT} / k_R$ ratios in Table 5.2). The localized increases in the ICPS were found to be a combination of dissociative attachment and diffusion from nearby areas of the source. The time scale of the negative ion peaks from diffusive processes often coincided with the disappearance of the I_{DC} electron signal from the afterglow and the collapse of the ambipolar field. This is evi-

dence of a shift from ambipolar confinement to a free-diffusion regime in an ion-ion plasma.

Under the transverse filter at $x = 5$ cm the highest negative ion density is seen, this high density is seen to rapidly decay due to diffusive losses to the walls inside the filter. It was not possible to mitigate these losses with the addition of the radial cusp filter due to the field not being strong enough to prevent H^- losses to the walls. However, it may be possible to maintain this population longer into the afterglow for pulsed plasma applications with the addition of a strong radial cusp filter.

The time scale of the I_{DC} decay profile correlates with the peaks negative ion signals which suggests that the I_{DC} signal from an uncompensated Langmuir probe can be used as a simple and reliable indicator of the the switch between the ambipolar and free diffusion regime in the afterglow for negative ion sources. This time scale is seen to be spatially dependent along the length of the source and could be used as a tool to predict the timing of negative ion peaks into the afterglow with applications toward controlling the pulsed afterglow plasma chemistry.

Conclusions and Future Work

This thesis presented the first measurements from a newly designed inductive system. The aim of this project was to characterize and optimize the ICPS and to investigate new low temperature plasma phenomenon related to the transverse magnetic field. The major findings from the experimental and numerical studies which were presented in Chapters 3-5 will be summarized and discussed which include: (1) Power transfer optimization, (2) Plasma properties across the ICPS, and (3) Negative ion dynamics into the afterglow. The recommendations for future work will then be presented.

6.1 Power Transfer Optimization

The systems power transfer circuit was investigated initially by modelling of the impedance matching network to understand the power transfer efficiency. The impedance matching system and the total power transfer circuit was able to be accurately modelled using a circuit of variable complex resistors. The model was extended to be able to predict optimal circuit components for arbitrary impedance matching circuits which can be used on plasma systems.

Measurements of the power transfer efficiency and plasma resistance were then made comparing argon to hydrogen. The plasma resistance of argon was seen to be approximately 4 times higher than hydrogen. The magnetic filter was seen to increase the plasma resistance by up to a factor of two in argon and up to a factor of three in hydrogen compared to the unfiltered case. This increase in resistivity translated to a gain in power transfer efficiency of 6% in argon and up to 25% for hydrogen. The reason for the difference was found to be that high resistivity plasmas such as argon already have a high

ratio of plasma resistance to matching circuit resistance and hence the gains from increasing the plasma resistance have depreciating returns for increasing the power transfer efficiency.

The location of the magnetic filter with respect to the antenna was found to significantly affect the power transfer efficiency of the source with power efficiencies ranging between 31% and 64% in hydrogen simply by moving the magnetic filter. In argon the effect on power transfer efficiency was lower with the ranging between 91% and 95%, however, during this 4% gain in efficiency the magnetic filter almost doubled the plasma resistivity from 13 Ohms to 26 Ohms. This result indicates that, while improving the plasma resistivity does not yield increased power efficiency for naturally highly resistive species, the magnetic filter can still continue to strongly increase the plasma resistance in both hydrogen and argon regardless of the low power efficiency gains.

The power transfer efficiency was seen to be optimal for hydrogen when the magnetic filter was placed directly in front of the antenna, however when the filter was placed behind the antenna, the H-mode was suppressed to the low efficiency E-mode. In contrast, in argon, the highest efficiency was obtained when the filter was placed 3 cm behind the antenna. The results suggested that both the natural plasma resistance and the plasma skin depth play a role in determining the optimal location of the magnetic field to enhance the power transfer efficiency of the source.

A peak in the power transfer efficiency was seen in argon and hydrogen when the magnetic field strength applied to the source was near 5 to 10 Gauss. This field strength corresponds to an electron cyclotron frequency of 13.56 MHz and 27.12 MHz which matches the driving frequency of the amplifier and its first harmonic. This result suggests that the edges of the magnetic filter can support electron cyclotron resonance heating where increased energy is coupled into the plasma through the electrons. This hypothesis is supported by the EEPF measurements in hydrogen near the antenna which showed very high effective electron temperatures of 12 eV, consistent with ECR wave heating of the electrons near the antenna due to the magnetic field edge geometry.

6.2 Plasma Properties Across the ICPS

Axial measurements were made across the ICPS at 1 cm intervals to measure a variety of plasma conditions. These measurements were also supported by 1d and 3d models which were developed to help explain some interesting experimental results from the magnetic filter.

The hydrogen plasma density measurements revealed the presence of a density peak inside the magnetic filter which occurred over a wide range pressures between 15 mtorr and 150 mtorr. This was not seen across the same pressure range for the argon, however, there was some indirect evidence in the measurements for it beginning to possibly form at low pressure of 2 mtorr. The dependence of the density peak on magnetic field strength revealed that at 50 mtorr pressure, the peak begins to form at a field strength of 120 G but is completely suppressed at 800 G with the maximum measured at 250 G. The peak did not form at any magnetic field strength for 10 mtorr. These measurements also revealed that the high confinement 800 G magnetic filter can be used to control the effective system size by suppressing the diffusion of charged species. At 50 mtorr this resulted in plasma densities which could be generated as high as 10^{17} m^{-3} near the antenna with only 200 W forward power.

Axial EEPF measurements were taken along the length of the source at several pressures which confirmed the presence of the density peak for hydrogen. The magnetic filter was shown to not only cool the electron population to as low as 0.2 eV, but it increased the population of low energy electrons inside the trap and this effect was strongest at 50 mtorr. This result shows that the density peak seen under the filter field consisted of a high density of cold electrons, which is ideal for negative ion formation. The density peak region also exhibited a dome shaped floating potential profile which indicated a slightly ion-rich plasma which suggested the mechanism driving the density peak could be ion driven rather than electron driven. The EEPF measurements showed that the maximum cooling effect in hydrogen occurs at magnetic field strengths of only 40 G and that increasing the magnetic field does not increase cooling above this. The EEPF results in argon showed that the cooling effect from the magnetic filter was much less than for hydrogen and that lower pressures may be required to see the same localized cooling in argon as seen in hydrogen.

Two models were developed to help explain how the magnetic filter affected charged particle transport along the source. A 1d transport model was developed using a fluid approach to investigate the dominant effects of the magnetic filter on diffusion, mobility and drift motions. The model showed that the magnetic filter used with a 250 G filter will heavily suppress streamwise particle transport unless weak electric fields are present to create positive x-directed $E \times B$ streamwise drift velocities. The 1d model also suggested that electric fields could emerge due to electron diamagnetic drift motion upstream of the filter edge and that these drifts may produce lateral electric fields which can drive ions and electrons into the filter to become trapped.

To investigate the 1d model results in a 3d environment, a 1:1 scale model of ICPS was developed which used single seed particle tracking to visualize drift motions and possible transport pathways for the development of the particle trap. The 3d model results showed that individual ions undergo a two step process of first entrainment and then trapping inside the filter. This process was found to occur only under certain semi-magnetized collisional conditions and required weak lateral electric fields to be present upstream of the center of the filter. The 3d model results also produced a criteria of the plasma conditions which can predict the formation of the particle trap in other systems and potentially when using different gasses.

Rotational H₂ temperatures were measured axially along the source using optical emission spectroscopy to determine the effect of the filter on the neutral gas inelastic excitation states. Since the cross section for dissociative attachment to form negative ions is highly sensitive to the rovibrational state of the molecular gas, increases in the rotational gas temperature should help promote localized negative ion formation in the source. The results showed that the transverse filter increased the rotational gas temperature by up to 40% (+150 K) at both 10 mtorr and 75 mtorr. Interestingly this increase in temperature increased with increasing distance from the source which indicates that the mechanism for neutral gas heating is by electron confinement and collisional energy transfer which likely occurs downstream of the discharge over time scales of the gas residence time (milliseconds). This is an important result as it shows that the magnetic enhancement can increase the inelastic gas state and promote negative ion formation downstream of the discharge where negative ion formation can be controlled.

6.3 Negative Ion Dynamics into the Afterglow

Negative ion measurements were performed along the length of the source using photodetachment to create a spatial profile of the negative ion population in the ICPS. The unfiltered negative ion profile showed the highest negative ion concentration close to the antenna with decreasing density further down stream with negative ion densities of approximately 10^{15} m^{-3} . However with the application of the magnetic filter, the negative ion density became strongly localized to the center of the filter with a peak density of approximately 10^{16} m^{-3} which corresponded to a high negative ion fraction of 34% with respect to the electron population. This surprising result was able to be reproduced computationally by developing a simple reaction chemistry model which used known rate coefficients for production and destruction of negative ions and used the experimental data of the densities and electron temperature from ICPS measurements. The fact that this reaction chemistry model was able to reproduce the filtered and unfiltered data means that the negative ion profiles in the ICPS can be totally accounted for by standard volume production mechanisms. These results show that under certain conditions the negative ion density can be improved up to an order of magnitude at a desired location within the source. While these measurements were taken at 100 mtorr, the peak in plasma density has been shown by one other author to also be reproducible at a low pressure [133]. Results from the 3d model in this work suggest that the peak formation at lower pressure is possible due to the presence of the tandem cusp arrangement and that the density peak may be able to be created across a wide range of pressures and powers which may be exploitable for fusion sized NBI systems.

Four positions along the source were chosen to make detailed measurements of the negative ion dynamics into the afterglow. The negative ion population showed strong spatial and temporal sensitivity across the ICPS revealing complex and dynamic process into the afterglow. Near to the discharge, the afterglow measurements showed that the production and loss mechanisms for the negative ions are dominated by the binary reaction processes of dissociative attachment and mutual neutralization whereas further down the source in lower density areas, the negative ion measurements showed diffusion dominated processes into the afterglow. Measurements revealed a switch between ambipolar regimes and free-diffusion regimes which were related to the collapse of the ambipolar field seen in the electron current measurements. The time scales for this regime change were not spatially uniform across the length of the source and were seen to be modified by the presence of mag-

netic fields which suggests that the time frame for this regime switching to occur can be controlled and optimized externally via magnetic enhancement of the source.

6.4 Future Work

The results from this work point to several future avenues which are relevant to research relating to both processing plasmas and for the possible development of a high density volume-only pulsed negative ion source.

- A full treatment of different magnetic field geometries could be used to widen the parameter space of power and pressure for both plasma ignition and also to increase power transfer efficiency.
- A comprehensive model must be developed in order to ascertain the plasma mechanisms responsible for the enhancement of the power transfer efficiency from the magnetic field. I suggest that a hybrid numerical fluid/global model would have to be developed similar to that developed by Yang *et al.*, [118] which can incorporate external 2d or 3d magnetic fields.
- An investigation into using different magnetic geometries to control the afterglow ion free-diffusion regime could yield interesting results for both a future pulsed NBI source and for control over low pressure processing plasma conditions such as afterglow chemistry, etch rates and layer deposition across a target.
- Experiments should be conducted related to the electron cyclotron resonance heating observed at the upstream edge of the filter near the discharge using a variety of external magnetic configurations. These results could be extended to include the majority of the source for the purpose of both maximizing gains in power transfer efficiency and also for increasing plasma homogeneity.
- A series of experiments should be conducted to attempt to reproduce the particle trap using the criteria outlined in Section 4.5.5. The trap

should be tested using a variety of gasses beginning with argon and helium and then using electronegative gasses such as SF₆. Radial measurements of the plasma potential will reveal the presence of lateral electric fields upstream of the filter and quantify their strength necessary for the entrainment and trapping to occur.

- The peak in negative ion density seen inside the particle trap could be extended and validated in future in experiments using sensitive methods such as cavity ring down spectroscopy. Axial measurements of the atomic neutral density could also be measured using laser induced fluorescence to help quantify the distribution of one of the main H⁻ loss mechanisms.
- The results of the 3d particle modelling suggests that density of cold electrons inside the particle trap can certainly be increased via a strong yet localized ring of cusp magnets. The afterglow measurements suggest that the primary losses at this location are wall losses due to magnetization of the H⁻ ions along the transverse field lines and so the cusp field magnets need only be the width of the transverse filter magnets and should be strong enough to redirect ions not just electrons from the walls. Particle transport into the filter at low pressure conditions could also possibly be enhanced by the use of externally pulsed solenoids to control afterglow particle transport.
- Lastly, to test the viability of a caesium-free neutral beam source, a small prototype NBI system should be built to extend the results of this thesis. New source configurations should be tested such as positioning of the filter field directly above an extraction grid while the particle trap has formed. The source could operate under high frequency pulsed power conditions to maximize negative ion currents and minimize electron current during gridded extraction. The role of the cusp filter strength should be investigated to ascertain its effect on afterglow ion diffusion rates and lowering the pressure at which the particle trap can form.

Appendix A

Appendix: Magnetic Field Code

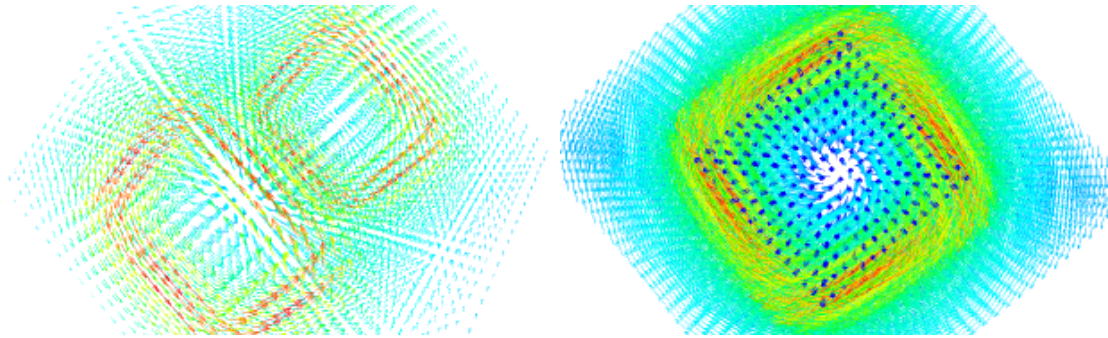
This appendix displays the custom Python code developed for the calculation of the 3d magnetic field profile of the transverse filter using arbitrary magnetic dipole moments in a gridded domain. The code follows the methodology set out previously in Chapter 2 (Eqns. 2.1,2.2) and is restated here for clarity:

$$\vec{A}(x, y, z) = \sum_m \vec{A}(\vec{r}_a) = \sum_m \frac{\vec{M}(\vec{r}_m) \times (\vec{r}_m - \vec{r}_a)}{|\vec{r}_{m-a}|^3} \quad (\text{A.1})$$

Where \vec{A} is the magnetic vector potential field, a is each location of 3d grid to iterate over, m is the position of each permanent magnetic pole, $\vec{M}(\vec{r}_m)$ is the magnetic moment of each magnetic pole. After performing the calculation for each point in space a for each magnetic moment, the vector field \vec{A} is produced and shown in Figure A.1. The curl of this magnetic vector potential field yields the magnetic field vector at each point in space:

$$\vec{B}(x, y, z) = \vec{\nabla} \times \vec{A}(x, y, z) \quad (\text{A.2})$$

The code begins by creating a 3d grid of points and calculating the optimal number of domains to split the x-axis slices into for a parallel computation. The magnetic domains are selected as grid locations where the permanent magnets are located, and the domains outside are set to NaN. These locations are then fed to the 'Worker' function which performs the calculation of \vec{A} at each point in the grid for each magnetic field domain. The worker function is sent slices of the X-Z plane in chunks from the multiprocessing pool. The curl of this new vector field is then taken for the B-field calculation using the 'vec_field_deriv' function. Finally the B-field is generated as a variable and plotted using the *Mayavi* package in Python.



(a) Magnetic vector potential at low resolution of the two magnetic filter blocks.

(b) Magnetic vector potential view from above the top magnet.

Figure A.1: Results from the 3d magnetic vector potential calculation of the filter from two different perspectives using two different grid cube resolutions (0.5 cm and 0.3 cm). Magnetic moment locations are the dark blue cubes in (b).

A.1 Python Code

```

import numpy as np
from mpl_toolkits.mplot3d import Axes3D
import mayavi.mlab
import multiprocessing
import scipy.fftpack as fftpack
import copy
import time

time1 = time.time()

'''----the main grids---'''
resolution = 30j # This is the grid size steps for the grid cubes resolution.

max_threads = multiprocessing.cpu_count() #for parallel calc
max_threads_range = range(max_threads+1)[1:]
int_res = int(str(resolution)[-1])
res_range = range(int_res)
av_slice = int(int_res/max_threads)
remainder = int_res%max_threads
slice_list = []
myslice_list2 = []

'''----computes the chunks for parallel code later on using the resultion and number of cores on the CPU'''
sliced_array = [i for i in np.arange(0, int_res, 1)]

def chunks(slice_array, chunk_size): #used to select sub-slices
    final_slices = []
    #returns successive n-sized chunks from initial array."""
    for i in range(0, len(slice_array), chunk_size):
        final_slices.append(slice_array[i:i + chunk_size])

    return final_slices

myslice_list2 = chunks(sliced_array,max_threads) #filling holes
step_res = .1 / int_res

```



```

        continue
    else:
        r_3 = np.linalg.norm(rm_ra)**3
        zing = cross_prod*(r_3**-1)
        A1_sum = A1_sum + zing

    A_slice[:,i,j,k] = A1_sum

    return (myslice, A_slice)

'''-----MultiProcessing, the pool takes from the myslice_list2 arrays and assigns CPUs to them as they come-----'''
run_on = False
if run_on == True:
    pool = multiprocessing.Pool(processes=max_threads)
    #results = [pool.apply_async(worker, args=(x,) for x in tables]
    results = [pool.apply_async(worker, args=(myslice, A)) for myslice in myslice_list2]
    output = [p.get() for p in results]

for n, chunk in enumerate(output):
    myslice_chunk = chunk[0]
    A_chunk = chunk[1]
    A_final[:,myslice_chunk[0]:myslice_chunk[-1]+1,:,:] = A_chunk[:,myslice_chunk[0]:myslice_chunk[-1]+1,:,:]

'''-----curl of A. converts the magnetic vector potential A array to the magnetic field B---'''
def vec_field_deriv(array,axis): #df(x)/dy = (A[1],0), df(z)/dx = (A[0],2)
    new_array_prime = np.zeros_like(array)
    if axis == 0: # the xaxis is variable, y,z constants, this is A(x)
        for j in range(len(array[1])):
            for k in range(len(array[2])):
                new_array = copy.copy(array[:,j,k])
                new_array_prime[:,j,k] = fftpack.diff(new_array)
    elif axis == 1: # the yaxis is variable, x,z constants, this is A(y)
        for i in range(len(array[0])):
            for k in range(len(array[2])):
                new_array = copy.copy(array[i,:,k])
                new_array_prime[i,:,k] = fftpack.diff(new_array)
    elif axis == 2: # the zaxis is variable, x,y constants, this is A(z)
        for i in range(len(array[0])):
            for j in range(len(array[1])):
                new_array = copy.copy(array[i,j,:])
                new_array_prime[i,j,:] = fftpack.diff(new_array)
    #
    return new_array_prime

'''---the B calc---'''
A = A_final

B = np.array([ vec_field_deriv(A[2],1) - vec_field_deriv(A[1],2),
    vec_field_deriv(A[0],2) - vec_field_deriv(A[2],0),
    vec_field_deriv(A[1],0) - vec_field_deriv(A[0],1)           ])

time2 = time.time(), 'calc time'

'''-----3D Plotting-----'''
plotting = False
seed_map = False
if plotting == True:
    mayavi.mlab.figure(size=(1280,800))

if seed_map == True:

```

```

seed_choice = 'plane'

field = mayavi.mlab.pipeline.vector_field(x,y,z,B[0],B[1],B[2])

magnitude = mayavi.mlab.pipeline.extract_vector_norm(field)

contours = mayavi.mlab.pipeline.iso_surface(magnitude,
#                                              contours=[0.2,0.8,0.5],
                                              transparent=True,
                                              opacity=0.8,
                                              colormap='YlGnBu',
                                              vmin=0, vmax=maxB
                                              )
field_lines1 = mayavi.mlab.pipeline.streamline(contours, seedtype=seed_choice,seed_resolution = 50
,seed_scale = 1,
                                              integration_direction='both',
                                              extent = [0.,1,0,0,-0.05,0.05],
                                              colormap='YlGnBu',
                                              vmin=0, vmax=maxB)

'''plane widget'''
if seed_choice == 'plane':
    field_lines1.seed.widget.point1 = [0, 0, 0]

'''sphere widget'''
if seed_choice == 'sphere':
    field_lines1.seed.widget.enabled = True
    field_lines1.seed.widget.center = [0.05,0,0]

mayavi.mlab.quiver3d(x,y,z,A[0],A[1],A[2],name="Vector potential")#0.0000035
mayavi.mlab.quiver3d(x,y,z,M1,M2,M3,name="Magnetic Moments", mode = 'cube',scale_factor = .0035)#.015
mayavi.mlab.axes(extent = [0.,1,-.05,.05,-.05,.05])
mayavi.mlab.view(azimuth = 270, elevation = 90,distance='auto', focalpoint=[.05,0,0])
mayavi.mlab.show()

```

Appendix: The Plasma Frequency

The plasma frequency is the frequency of propagating electrostatic (Langmuir) waves within the plasma. The plasma frequency is described in many texts but will be derived here for reference as it relates to the hairpin probe diagnostic material in Chapter 2 and the hairpin measurements shown in Chapter 4.

B.1 Plasma Frequency Derivation

Consider a block of uniform charges in which a surface section containing n charges of the charge block is separated by a distance δx . If the surface of charge has unit area and is separated parallel to the block, then the electric flux can be equated to the electric field caused by the separation for a given charge density:

$$\nabla \cdot \vec{E} = E_x = -\frac{\sigma}{\epsilon_0} \quad (\text{B.1})$$

where the charge density per unit area is:

$$\sigma = n_e q dx \quad (\text{B.2})$$

We are interested in the movement of the charged surface in the x-direction as a function of time and so we can equate the force on the charges to the

field:

$$\vec{F} = m_e \frac{d^2 \vec{x}}{dt^2} = q \vec{E}_x = -\frac{n_e q^2}{\epsilon_0} dx \quad (\text{B.3})$$

The equation of force related to the displacement has the form of simple harmonic motion as the force on the particle is a function of the distance to the block:

$$\frac{d^2 \vec{x}}{dt^2} = -\frac{n_e q^2}{m_e \epsilon_0} = -k dx \quad (\text{B.4})$$

where the right hand side weights are the 'spring constant' k of the system:

$$k = \frac{n_e q^2}{m_e \epsilon_0} \quad (\text{B.5})$$

This oscillator equation then has a solution for the displacement of the electron surface at time t :

$$dx_0 \sin(\sqrt{k} t) \quad (\text{B.6})$$

In Eq. B.6 the angular frequency of the oscillating electron surface is \sqrt{k} . This number is called the plasma frequency (ω_{pe}) and is the fundamental time scale of the plasma. This number is important because it represents a frequency boundary below which electromagnetic and electrostatic waves are absorbed and above which waves are allowed to freely propagate within the medium.

Appendix C

Appendix: Molecular Dynamics

C.1 Electronic Term Symbols

Molecular hydrogen (H_2) is the simplest molecular system. It exhibits positive and negative ions, rotational and vibrational levels, electronic excitations and varying electron and nuclear spin states. The molecule is a linear homonuclear diatomic and as such has no permanent electric dipole moment. With the exception of induced time-varying dipole excitations, linear homonuclear diatoms cannot directly emit EM rotational spectra. Instead the rotational levels can be measured during electronic orbital transitions from excited states. The Fulcher band is an electronic transition band which offers information about the rotational states of H_2 and is an attractive option for measurement as it generally exhibits good intensity and lies within the optical spectrum around 600 nm, suiting most instruments. Emission spectra relating to vibrational modes is more difficult to resolve as the fundamental vibrational mode of H_2 begins in the mid infra-red around 2000 nm [164] and so the rotational and vibrational states of H_2 are often measured from electronic transitions.

For electronic excitation molecular term symbols are used to indicate the net molecular state at a glance and are used to describe electronic transitions. The molecular term symbol used can be generalized as follows:

$$^{2S+1}\Lambda_{g/u}^{+/-} \quad (C.1)$$

where S is the total spin of the molecule, Λ is the net angular momentum projected along the internuclear axis, + and - refer to the reflection symmetry given by $(-1)^l$ where l is the orbital angular momentum quantum number, g/u refers to the molecule having either gerade (even) or ungerade (uneven)

net orbital symmetries. The symbol Λ can have integer values which represent net angular momentum quantum states having symbols $\Sigma, \Pi, \Delta, \Phi$ for $\Lambda = 0, 1, 2, 3$ respectively. For each possible orbital, in order of increasing energy, a prefix is assigned shown as (X, B, C, \dots) in upper-case letters for the singlet state, and in lower-case letters to denote a spin changed triplet state. For example the ground state of H_2 can be written $X^1\Sigma_g^+$. Despite its popularity, this notation obfuscates the type of orbitals filled for the excitation states and which principle quantum state they are occupying. For single orbital transitions, an equivalent notation can be used where the principal state and orbital type are shown (eg. $2p$) and the spin change may be inferred from the $2s + 1$ prefix in the molecular term symbol. For example the ground state of H_2 can also be written as $1s^1\Sigma_g^+$ indicating a singlet, gerade state where the two electrons have opposite $\frac{1}{2}$ spins ($2s+1 = 1$), with no net angular momentum and are occupying the lowest $1s$ shell ($\Lambda = 0 = \Sigma$ and $l = 0$, even parity). Similar to historical literature, these notations will be used interchangeably in this work. The opening to the extensive work of Fantz & Wunderlich [100] has more introductory information on the molecular term properties in hydrogen.

C.2 Rotation

In addition to this electronic excitation state term, the rotational quantum number (J) represents the total angular momentum for rotation and is integer quantized ($J = 0, 1, 2, 3, \dots$). Consider two particles of mass m rotating at a distance r around a fixed axis at a particular angular velocity ($r\omega$); the higher this velocity, the higher the energy (rotational temperature) of the gas. For a classical rigid system of rotating bodies around an axis, the moment of inertia (I) for each body is:

$$I_i = mr_i^2 \quad (C.2)$$

With angular momentum (L):

$$L_i = I_i r\omega \quad (C.3)$$

The classical Hamiltonian for these particles is:

$$H_{x,y,z} = \frac{L_1^2}{2I_1} + \frac{L_2^2}{2I_2} + \frac{L_3^2}{2I_3} \quad (\text{C.4})$$

While the angular momentum operators do not commute for 3 variables, the rotation can be mapped onto a 2 dimensional spherical surface allowing the rotation to be then described by only two values with respect to an arbitrary axis. The first value m_J is the magnetic rotational quantum number (denoted as K when reference axis is the molecular axis rather than lab-frame) represents the z-component of the angular momentum vector. The second value J called rotational quantum number represents the total magnitude of the angular momentum vector (Fig. C.1). The possible values of m_J range between $\Delta m_j = \pm 1, \pm 2, \pm 3, \dots \pm J$ with high m_j numbers representing orbital momentum toward the z-axis and $m_j = 0$ represents orbital momentum perpendicular to the z-axis, although the total energy only depends on J .

The eigenvalues (E_J) of this system represent the allowed energy states of rotation and are proportional to J^2 :

$$E_J = \frac{\hbar^2}{2I} J(J+1) \quad , \quad J = 0, 1, 2, 3, \dots \quad (\text{C.5})$$

where \hbar is the reduced Planck constant and J is the sum of the angular net momentum (L) and net spin (S). Equation C.5 can be normalized to term values in units of wavenumber (cm^{-1}) so that the energy states can be read off as spacings between spectral peaks:

$$F(J) = \frac{E_J}{hc} = \tilde{B} J(J+1) \quad , \quad \tilde{B} = \frac{\hbar}{4\pi c I} \quad (\text{C.6})$$

Equation C.6 is assumed to be in the gas phase here where \tilde{B} is called the rotational constant. To find the separation between rotational bands from a given initial rotational state (eg. J), a simple substitution can be made into Equation C.7 of $J \rightarrow J + 1$ and $J \rightarrow J - 1$ and the difference between the two is simply $2\tilde{B}$. This is not only convenient notation for spectroscopic work but also relates the wavenumber of emission lines to molecular separation distances and rotational quantum numbers. Centrifugal distortion of the bond length can reduce Equation C.7 by a distortion factor of $\tilde{D} J^2(J+1)^2$ where $\tilde{D} = \frac{4\tilde{B}}{\omega^2}$, however this energy is typically several orders of magnitude lower

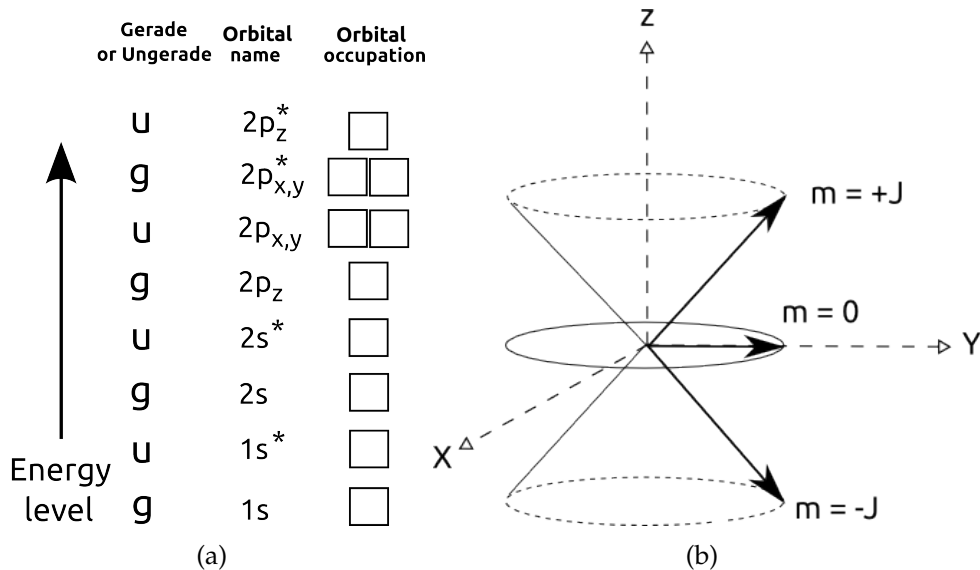


Figure C.1: a) Molecular orbital diagram options for H_2 showing possible electronic transition channels (Fulcher- α state is $2p^3\Sigma_g^+$). The box can be filled with two spin up or down electrons in a variety of bonds, the * represents anti-bonding sub shells. b) Generalized vector schematic of the two rotational numbers m_J and J . Here m_J is the projection of the \vec{J} vector onto an arbitrary z-axis and J is the magnitude of the vector.

that of \tilde{B} and can be neglected for most applications.

Changes in rotational number where $\Delta J = +1$ are called R-branch transitions and $\Delta J = -1$ changes are called P-branch transitions. When the angular momentum of the molecule is greater than zero (i.e. $\Lambda > 0$), then the $\Delta J = 0$ transition is allowed and this is called the Q-branch. The Q-branch is important as it 'preserves' the rotational states during an electronic transition and one particular Q-branch in H_2 is used for measuring neutral gas temperatures. The Fulcher- α band is considered to be a Hund's case type (b) [165] where spin-orbit coupling ($L \cdot S$) is weak. The rotational line strengths depend on the direction of the ΔJ and this dependence is called the Hönl-London (HL) factor. For Hund's case (b) the HL factor for the Q-branch transition is simply:

$$S_{J,J} = \frac{2J+1}{2} \quad (\text{C.7})$$

where $S_{J,J}$ here is the Hönl-London factor for a $\Delta J = 0$ transition with low spin-orbit coupling.

C.3 Vibration

The rotational and vibrational energy states can also be found non-classically by decoupling the wave functions of the electrons from those of the nuclei which allows for separate analysis of each. This process is called the Born-Oppenheimer (BO) approximation and it reasons that the time scales of change for the electrons and nuclei are sufficiently different due to their differing mass such that they may be considered uncoupled from each other. The BO approximation can be used whenever the potential energy surfaces of the molecule have sufficient spacing such that:

$$\psi = (\vec{x}_i, \vec{x}_k) = \psi_e(\vec{x}_i) \psi_{vr}(\vec{x}_k) \quad (\text{C.8})$$

The Shrödinger wave equation for the nuclei can be explicitly separated:

$$\frac{\hbar^2}{2m_n} \frac{\partial \psi(x)}{\partial x^2} + \psi(x)(V(x) - E_{el} - E_{v,J}) = 0 \quad (\text{C.9})$$

where \hbar is the reduced Planck's constant, $V(x)$ is the displacement potential and $E_{v,J}$ is the rovibrational energy of the molecule. The solutions of Eqn. C.9 yields both the rotational solutions (already shown with a classical derivation in Eqn. C.7) and also the vibrational solution. Setting aside the higher order terms, the expression for the vibrating rotor is:

$$G(v) = \omega_e(v + \frac{1}{2}) \quad (\text{C.10})$$

where ω_e is the harmonic wavenumber and v is the vibrational quantum number. The vibrational mode has a distortion factor similar to the rotational mode of $\omega_e \chi_e(v + \frac{1}{2})$ with χ_e being the damping constant. Vibrational modes have energy levels much higher than the rotational levels and vibrational bands can often be seen to have rotational structure superposed on top of them in an emission spectrum. The comparatively slow change in nuclei position relative to the electrons results in vibrational state wave functions overlapping preferentially with those in close proximity when electronic transitions occur. This transition preference is called the Frank-Condon (FC) principle and it is dependent on the current vibrational state and the final electronic orbital transition. The degree of preference for vibrational states transitions to retain their wave function overlap is represented as a multiplicative scaling in the transition probability and are presented in detail for

various transitions in Astashkevich *et al.*, [97] and de Graaf [101] including references therein. For the Fulcher- α band, the values for the FC scaling range from 0.01 to 0.34, favouring neighbouring low-level vibrational transitions.

C.4 Nuclear Spin

The four nuclear spin states of H_2 can be combinations of up (α) and down (β) between the two nuclei $\alpha\alpha, \alpha\beta, \beta\beta, \beta\alpha$ molecular symmetry can be shown as antisymmetric 'ortho' dihydrogen (*a*) or symmetric 'para' dihydrogen (*s*) with either positive (+) or negative parity (−) with respect to the electron wave function through the internuclear axis. The nuclear spin degeneracy can be expressed as $(2I + 1)$ where I is the total nuclear spin. For ortho hydrogen, $I = 1$ with a spin degeneracy of 3, whereas para hydrogen, $I = 0$ with a spin degeneracy of 1. This leads to a 3:1 ratio of ortho to para H_2 and has an effect on electronic transition populations and also relative intensity of transitions for the Fulcher- α emission. Wave function antisymmetry requires that odd numbered rotational numbers only occur for ortho hydrogen and even numbered rotational numbers only occur for para hydrogen and this can be seen in the Fulcher transitions channels shown in Figures 2.20(a) and 2.20(b) and also in the alternating line intensities of the band measurements shown in Figure 2.19.

Bibliography

1. U. Nations, "The united nations on world population in 2300," vol. 30, pp. 181–187, 01 2004. (cited on page 1)
2. J. Byrne, L. Mills, D. Strahan, R. Boyle, B. Collins, K. Stopforth, and L. Becker, "Global trends in renewable energy investment 2015," *Frankfurt School UNEP Collaborating Centre for Climate and Sustainable Energy Finance*, 2015. (cited on page 1)
3. J. J. Conti, P. D. Holtberg, J. Beamon, A. M. Schaal, J. Ayoub, and J. T. Turnure, "Annual energy outlook 2014," *US Energy Information Administration*, 2014. (cited on page 2)
4. R. Highfield, V. Jamieson, N. Calder, and R. Arnoux, "Iter: A brief history of fusion," *New Scientist*, 2009. (cited on page 2)
5. J. Stearns, K. Berkner, and R. Pyle, "Neutral-beam design options," 1976. (cited on page 2)
6. F. W. L, "Production of negative ions and noise in negative ion beams," *Phys. Rev.*, vol. 89, pp. 411–415, Jan 1953. (cited on page 2)
7. J. Dowell and T. Sharp, "Vibrational structure in the dissociative attachment of electrons in hydrogen," *Physical Review*, vol. 167, no. 1, p. 124, 1968. (cited on page 3)
8. M. Allan and S. Wong, "Effect of vibrational and rotational excitation on dissociative attachment in hydrogen," *Physical Review Letters*, vol. 41, no. 26, p. 1791, 1978. (cited on page 3)
9. J. Horáček, M. Čížek, K. Houfek, P. Kolorenč, and W. Domcke, "Dissociative electron attachment and vibrational excitation of H₂ by low-energy electrons: Calculations based on an improved nonlocal resonance model," *Physical Review A*, vol. 70, no. 5, p. 052712, 2004. (cited on pages 3, 124, 153, and 170)
10. J. Hiskes and A. Karo, "Generation of negative ions in tandem high-density hydrogen discharges," *Journal of applied physics*, vol. 56, no. 7, pp. 1927–1938, 1984. (cited on page 3)

11. M. Bacal, "Volume generation of H-ions in plasmas," *Physica Scripta*, vol. 1982, no. T2B, p. 467, 1982. (cited on page 3)
12. M. Bacal, "Volume production of hydrogen negative ions," *Nuclear Instruments and Methods in Physics Research Section B: Beam Interactions with Materials and Atoms*, vol. 37, pp. 28–32, 1989. (cited on pages 3 and 53)
13. M. Bacal, G. Hamilton, A. Bruneteau, H. Doucet, and J. Taillet, "Measurement of h- density in plasma by photodetachment," *Review of Scientific Instruments*, vol. 50, no. 6, pp. 719–721, 1979. (cited on pages 3, 62, and 66)
14. K. Leung, K. Ehlers, and M. Bacal, "Extraction of volume-produced H- ions from a multicusp source," *Review of Scientific Instruments*, vol. 54, no. 1, pp. 56–61, 1983. (cited on page 3)
15. M. Hopkins and W. Graham, "Time-resolved electron energy distribution function measurements in a pulsed magnetic multipole hydrogen discharge," *Journal of applied physics*, vol. 69, no. 6, pp. 3461–3466, 1991. (cited on pages 3, 4, 5, 6, 101, 147, 157, 159, and 161)
16. M. Hanada, N. Akino, Y. Endo, T. Inoue, M. Kawai, M. Kazawa, K. Kikuchi, M. Komata, A. Kojima, K. Mogaki, *et al.*, "Development and design of the negative-ion-based NBI for JT-60 super advanced," *J. Plasma Fusion Res. Ser.*, vol. 9, p. 208, 2010. (cited on page 3)
17. R. Gutser, D. Wunderlich, U. Fantz, *et al.*, "Negative hydrogen ion transport in RF-driven ion sources for ITER NBI," *Plasma Physics and Controlled Fusion*, vol. 51, no. 4, p. 045005, 2009. (cited on pages 3, 5, and 134)
18. "Euro fusion." <https://www.euro-fusion.org>. Accessed: 2018-05-13. (cited on page 4)
19. K. Leung and K. Ehlers, "H- ion formation from a surface conversion type ion source," *Journal of Applied Physics*, vol. 52, no. 6, pp. 3905–3911, 1981. (cited on page 3)
20. M. Bacal and H. J. Doucet, "PMI report number 763," 1976. (cited on page 3)
21. A. Aanesland, J. Bredin, P. Chabert, and V. Godyak, "Electron energy distribution function and plasma parameters across magnetic filters," *Applied Physics Letters*, vol. 100, no. 4, p. 044102, 2012. (cited on pages 4, 89, 90, 96, 100, 101, 115, and 117)

22. A. Aanesland, J. Bredin, and P. Chabert, "A review on ion-ion plasmas created in weakly magnetized electronegative plasmas," *Plasma Sources Science and Technology*, vol. 23, no. 4, p. 044003, 2014. (cited on pages 4, 6, 90, 115, and 117)
23. P. Van Amersfoort, J. Geerlings, L. T. Kwakman, A. Hershcovitch, E. Granneman, and J. Los, "Formation of negative hydrogen ions on a cesiated W (110) surface; the influence of hydrogen implantation," *Journal of applied physics*, vol. 58, no. 9, pp. 3566–3572, 1985. (cited on page 5)
24. M. Bacal, "Negative hydrogen ion production in fusion dedicated ion sources," *Chemical Physics*, vol. 398, pp. 3–6, 2012. (cited on pages 5 and 124)
25. M. Bacal, "Effect of fast positive ions incident on caesiated plasma grid of negative ion source," *Review of Scientific Instruments*, vol. 83, no. 2, p. 02B101, 2012. (cited on page 5)
26. K. Leung, S. Walther, and W. Kunkel, "H- formation in a barium-seeded hydrogen discharge," *Physical review letters*, vol. 62, no. 7, p. 764, 1989. (cited on page 5)
27. B. Heinemann, H. Falter, U. Fantz, P. Franzen, M. Fröschle, R. Gutser, W. Kraus, R. Nocentini, R. Riedl, E. Speth, *et al.*, "Design of the half-size ITER neutral beam source for the test facility elise," *Fusion Engineering and Design*, vol. 84, no. 2-6, pp. 915–922, 2009. (cited on page 5)
28. R. Hemsworth, H. Decamps, J. Graceffa, B. Schunke, M. Tanaka, M. Dremel, A. Tanga, H. De Esch, F. Geli, J. Milnes, *et al.*, "Status of the ITER heating neutral beam system," *Nuclear Fusion*, vol. 49, no. 4, p. 045006, 2009. (cited on page 5)
29. D. P. Moehs, J. Peters, and J. Sherman, "Negative hydrogen ion sources for accelerators," *Plasma Science, IEEE Transactions on*, vol. 33, no. 6, pp. 1786–1798, 2005. (cited on page 5)
30. P. Stockli, M., "Volume and surface enhanced volume negative ion sources..," *Plasma Science, IEEE Transactions on*, vol. 33, no. 6, pp. 1786–1798, 2005. (cited on page 5)
31. D. Riz and J. Paméla, "Modeling of negative ion transport in a plasma source," *Review of scientific instruments*, vol. 69, no. 2, pp. 914–919, 1998. (cited on page 5)

32. J. Peters, "H- ion source activities at DESY," *Review of scientific instruments*, vol. 65, no. 4, pp. 1237–1239, 1994. (cited on page 5)
33. J. Arancibia Monreal, P. Chabert, and V. Godyak, "Reduced electron temperature in a magnetized inductively-coupled plasma with internal coil," *Physics of Plasmas*, vol. 20, no. 10, p. 103504, 2013. (cited on pages 6, 69, 75, 84, 85, 96, 101, and 115)
34. J. Y. Kim, W.-H. Cho, J.-J. Dang, K.-J. Chung, and Y. Hwang, "Electron cyclotron resonance heating by magnetic filter field in a negative hydrogen ion source," *Review of Scientific Instruments*, vol. 87, no. 2, p. 02B117, 2016. (cited on pages 6, 82, and 107)
35. U. Fantz, L. Schiesko, and D. Wunderlich, "Plasma expansion across a transverse magnetic field in a negative hydrogen ion source for fusion," *Plasma Sources Science and Technology*, vol. 23, no. 4, p. 044002, 2014. (cited on pages 6 and 90)
36. M. Thomas, D. Rafalskyi, T. Lafleur, and A. Aanesland, "Experimental investigation of electron transport across a magnetic field barrier in electropositive and electronegative plasmas," *Plasma Sources Science and Technology*, vol. 25, no. 4, p. 045018, 2016. (cited on pages 6 and 90)
37. J. Boeuf, J. Claustre, B. Chaudhury, and G. Fubiani, "Physics of a magnetic filter for negative ion sources. ii. E × B drift through the filter in a real geometry," *Physics of Plasmas*, vol. 19, no. 11, p. 113510, 2012. (cited on pages 6, 90, 128, and 130)
38. J. Boeuf, B. Chaudhury, and L. Garrigues, "Physics of a magnetic filter for negative ion sources. i. collisional transport across the filter in an ideal, 1d filter," *Physics of Plasmas*, vol. 19, no. 11, p. 113509, 2012. (cited on pages 6, 90, and 130)
39. S. Kolev, G. Hagelaar, G. Fubiani, and J. Boeuf, "Physics of a magnetic barrier in low-temperature bounded plasmas: insight from particle-in-cell simulations," *Plasma sources science and technology*, vol. 21, no. 2, p. 025002, 2012. (cited on pages 6 and 90)
40. U. Fantz, C. Hopf, D. Wunderlich, R. Friedl, M. Fröschle, B. Heinemann, W. Kraus, U. Kurutz, R. Riedl, R. Nocentini, *et al.*, "Towards powerful negative ion beams at the test facility ELISE for the ITER and DEMO NBI systems," *Nuclear Fusion*, vol. 57, no. 11, p. 116007, 2017. (cited on page 6)

41. "Grand view research publication." <https://www.grandviewresearch.com/press-release/global-chemical-vapor-deposition-cvd-market>. Accessed: 2018-05-13. (cited on page 7)
42. M. Haverlag, A. Kono, D. Passchier, G. Kroesen, W. Goedheer, and F. De Hoog, "Measurements of negative ion densities in 13.56-MHz RF plasmas of CF₄, C₂F₆, CHF₃, and C₃F₈ using microwave resonance and the photodetachment effect," *Journal of applied physics*, vol. 70, no. 7, pp. 3472–3480, 1991. (cited on page 7)
43. A. Howling, L. Sansonnens, J.-L. Dorier, and C. Hollenstein, "Time-resolved measurements of highly polymerized negative ions in radio frequency silane plasma deposition experiments," *Journal of applied physics*, vol. 75, no. 3, pp. 1340–1353, 1994. (cited on pages 7 and 9)
44. A. Howling, J.-L. Dorier, and C. Hollenstein, "Negative ion mass spectra and particulate formation in radio frequency silane plasma deposition experiments," *Applied physics letters*, vol. 62, no. 12, pp. 1341–1343, 1993. (cited on page 7)
45. D. Smith and M. J. Church, "Binary ion-ion recombination coefficients determined in a flowing afterglow plasma," *International Journal of Mass Spectrometry and Ion Physics*, vol. 19, no. 2, pp. 185–200, 1976. (cited on pages 7, 156, 159, 166, and 168)
46. C. Corr, P. Steen, and W. Graham, "Temporal phenomena in inductively coupled chlorine and argon-chlorine discharges," *Applied Physics Letters*, vol. 86, no. 14, p. 141503, 2005. (cited on pages 7 and 159)
47. M. A. Lieberman and S. Ashida, "Global models of pulse-power-modulated high-density, low-pressure discharges," *Plasma Sources Science and Technology*, vol. 5, no. 2, p. 145, 1996. (cited on pages 7 and 87)
48. R. Dodd, S. You, P. Bryant, and J. Bradley, "Negative ion density measurements in a reactive dc magnetron using the eclipse photodetachment method," *Plasma Sources Science and Technology*, vol. 19, no. 1, p. 015021, 2010. (cited on page 7)
49. J. W. Bradley, R. Dodd, S.-D. You, N. Sirse, and S. K. Karkari, "Resonance hairpin and langmuir probe-assisted laser photodetachment measurements of the negative ion density in a pulsed dc magnetron discharge," *Journal of Vacuum Science & Technology A: Vacuum, Surfaces, and Films*, vol. 29, no. 3, p. 031305, 2011. (cited on page 7)

50. S. Canulescu, J. Whitby, K. Fuhrer, M. Hohl, M. Gonin, T. Horvath, and J. Michler, "Potential analytical applications of negative ions from a pulsed radiofrequency glow discharge in argon," *Journal of Analytical Atomic Spectrometry*, vol. 24, no. 2, pp. 178–180, 2009. (cited on page 7)
51. A. Kono, M. Haverlag, G. Kroesen, and F. De Hoog, "Temporal behavior of the electron and negative ion densities in a pulsed radio-frequency CF₄ plasma," *Journal of applied physics*, vol. 70, no. 6, pp. 2939–2946, 1991. (cited on page 7)
52. "Dc magnetron sputtering system." <https://www.pfonline.com/articles/vacuum-deposition-and-coating-options>. Accessed: 2018-05-13. (cited on page 9)
53. R. P. Chang, C. Chang, and S. Darack, "Hydrogen plasma etching of semiconductors and their oxides," *Journal of Vacuum Science and Technology*, vol. 20, no. 1, pp. 45–50, 1982. (cited on page 8)
54. D. Lundin and K. Sarakinos, "An introduction to thin film processing using high-power impulse magnetron sputtering," *Journal of Materials Research*, vol. 27, no. 5, pp. 780–792, 2012. (cited on page 9)
55. H. Höglberg, L. Tengdelius, M. Samuelsson, F. Eriksson, E. Broitman, J. Lu, J. Jensen, and L. Hultman, "Reactive sputtering of δ-ZrH₂ thin films by high power impulse magnetron sputtering and direct current magnetron sputtering," *Journal of Vacuum Science & Technology A: Vacuum, Surfaces, and Films*, vol. 32, no. 4, p. 041510, 2014. (cited on page 9)
56. D. Fenner, D. Biegelsen, and R. Bringans, "Silicon surface passivation by hydrogen termination: A comparative study of preparation methods," *Journal of Applied Physics*, vol. 66, no. 1, pp. 419–424, 1989. (cited on page 9)
57. V. Tiron, I.-L. Velicu, I. Pana, D. Cristea, B. G. Rusu, P. Dinca, C. Porosnicu, E. Grigore, D. Munteanu, and S. Tascu, "HiPIMS deposition of silicon nitride for solar cell application," *Surface and Coatings Technology*, 2018. (cited on page 9)
58. J. Stark, T. Retschinsky, and A. Schaposchnikoff, "Untersuchungen über den lichtbogen," *Annalen der Physik*, vol. 323, no. 12, pp. 213–251, 1905. (cited on page 27)

59. H. M. Mott-Smith and I. Langmuir, "The theory of collectors in gaseous discharges," *Physical review*, vol. 28, no. 4, p. 727, 1926. (cited on page 27)
60. P. Chabert and N. Braithwaite, *Physics of radio-frequency plasmas*. Cambridge University Press, 2011. (cited on pages 28, 71, 77, 105, and 130)
61. M. J. Druyvesteyn, "Der niedervoltbogen," *Zeitschrift für Physik A Hadrons and Nuclei*, vol. 64, no. 11, pp. 781–798, 1930. (cited on page 30)
62. M. Bacal, "Physics aspects of negative ion sources," *Nuclear Fusion*, vol. 46, no. 6, p. S250, 2006. (cited on pages 31 and 107)
63. M. Bacal and M. Wada, "Negative hydrogen ion production mechanisms," *Applied physics reviews*, vol. 2, no. 2, p. 021305, 2015. (cited on pages 31, 53, and 152)
64. V. Godyak and S. Oks, "Measurement of electron energy distribution in an RF plasma," *Sov. Phys. Tech. Phys.*, vol. 24, no. 7, 1979. (cited on page 33)
65. V. Godyak and V. Demidov, "Probe measurements of electron-energy distributions in plasmas: what can we measure and how can we achieve reliable results?," *Journal of Physics D: Applied Physics*, vol. 44, no. 23, p. 233001, 2011. (cited on pages 33, 69, and 113)
66. V. Godyak, R. Piejak, and B. Alexandrovich, "Measurement of electron energy distribution in low-pressure RF discharges," *Plasma sources science and technology*, vol. 1, no. 1, p. 36, 1992. (cited on pages 33 and 101)
67. M. Tichy, P. Kudrna, J. Behnke, C. Csambal, and S. Klagge, "Langmuir probe diagnostics for medium pressure and magnetised low-temperature plasma," *Le Journal de Physique IV*, vol. 7, no. C4, pp. C4–397, 1997. (cited on page 37)
68. R. Stenzel, "Microwave resonator probe for localized density measurements in weakly magnetized plasmas," *Review of Scientific Instruments*, vol. 47, no. 5, pp. 603–607, 1976. (cited on page 40)
69. R. Piejak, V. Godyak, R. Garner, B. Alexandrovich, and N. Sternberg, "The hairpin resonator: A plasma density measuring technique revisited," *Journal of applied physics*, vol. 95, no. 7, pp. 3785–3791, 2004. (cited on pages 41 and 50)

70. M. A. Lieberman and A. J. Lichtenberg, *Principles of plasma discharges and materials processing*. John Wiley & Sons, 2005. (cited on pages 43, 72, 97, and 127)
71. F. F. Chen, *Introduction to plasma physics*. Springer Science & Business Media, 2012. (cited on page 43)
72. R. Piejak, J. Al-Kuzee, and N. S. J. Braithwaite, "Hairpin resonator probe measurements in RF plasmas," *Plasma Sources Science and Technology*, vol. 14, no. 4, p. 734, 2005. (cited on pages 44 and 50)
73. G. Gogna and S. Karkari, "Microwave resonances of a hairpin probe in a magnetized plasma," *Applied Physics Letters*, vol. 96, no. 15, p. 151503, 2010. (cited on pages 46, 47, and 49)
74. S. Karkari, A. Ellingboe, C. Gaman, I. Swindells, and J. Bradley, "Electron density modulation in an asymmetric bipolar pulsed dc magnetron discharge," *Journal of Applied Physics*, vol. 102, no. 6, p. 063308, 2007. (cited on page 46)
75. L. K. Warne, W. A. Johnson, G. A. Hebner, R. E. Jorgenson, and R. S. Coats, "Model for resonant plasma probe," tech. rep., Sandia National Laboratories, 2007. (cited on page 48)
76. G. S. Gogna, *Study of resonance hairpin probe for electron density measurements in low temperature plasmas*. PhD thesis, Dublin City University. School of Physical Sciences; National Centre for Plasma Science and Technology (NCPST), 2012. (cited on page 48)
77. M. Abdel-Rahman, T. Gans, V. Schulz-von Der Gathen, and H. Döbele, "Space and time resolved rotational state populations and gas temperatures in an inductively coupled hydrogen RF discharge," *Plasma Sources Science and Technology*, vol. 14, no. 1, p. 51, 2005. (cited on pages 51 and 119)
78. Z. Gavare, G. Revalde, and A. Skudra, "Plasma temperature determination of hydrogen containing high-frequency electrodeless lamps by intensity distribution measurements of hydrogen molecular band," *International Journal of Spectroscopy*, vol. 2010, 2010. (cited on page 51)
79. C. M. Samuell and C. S. Corr, "Atomic and molecular hydrogen gas temperatures in a low-pressure helicon plasma," *Plasma Sources Science and Technology*, vol. 24, no. 4, p. 045003, 2015. (cited on page 51)

80. G. L. Majstorović, N. Šišović, and N. Konjević, "Rotational and vibrational temperatures of molecular hydrogen in a hollow cathode glow discharge," *Plasma Sources Science and Technology*, vol. 16, no. 4, p. 750, 2007. (cited on page 51)
81. E. Surrey and B. Crowley, "Spectroscopic measurement of gas temperature in the neutralizer of the jet neutral beam injection system," *Plasma physics and controlled fusion*, vol. 45, no. 7, p. 1209, 2003. (cited on page 51)
82. T. Gans, V. Schulz-von Der Gathen, and H. Döbele, "Time dependence of rotational state populations of excited hydrogen molecules in an RF excited plasma reactor," *Plasma Sources Science and Technology*, vol. 10, no. 1, p. 17, 2001. (cited on pages 51, 54, 55, and 121)
83. T. Gans, M. Osiac, D. O'Connell, V. Kadetov, U. Czarnetzki, T. Schwarz-Selinger, H. Halfmann, and P. Awakowicz, "Characterization of stationary and pulsed inductively coupled RF discharges for plasma sterilization," *Plasma physics and controlled fusion*, vol. 47, no. 5A, p. A353, 2005. (cited on page 51)
84. M. Osiac, T. Schwarz-Selinger, D. O'Connell, B. Heil, Z. L. Petrovic, M. Turner, T. Gans, and U. Czarnetzki, "Plasma boundary sheath in the afterglow of a pulsed inductively coupled RF plasma," *Plasma Sources Science and Technology*, vol. 16, no. 2, p. 355, 2007. (cited on pages 51 and 53)
85. Y. Takama and K. Suzuki, "Experimental studies on nonequilibrium plasma flow in a convergent–divergent magnetic field," *Plasma Sources Science and Technology*, vol. 17, no. 1, p. 015005, 2007. (cited on pages 51 and 52)
86. T. V. Tsankov, K. Toko, and U. Czarnetzki, "Rotational and vibrational temperatures in a hydrogen discharge with a magnetic x-point," *Physics of plasmas*, vol. 19, no. 12, p. 123503, 2012. (cited on pages 51 and 52)
87. S. Briefi, D. Fink, S. Mattei, J. Lettry, and U. Fantz, "Determination of discharge parameters via OES at the Linac4 H- ion source," *Review of Scientific Instruments*, vol. 87, no. 2, p. 02B104, 2016. (cited on page 51)
88. U. Fantz, H. Falter, P. Franzen, D. Wunderlich, M. Berger, A. Lorenz, W. Kraus, P. McNeely, R. Riedl, and E. Speth, "Spectroscopy – a powerful diagnostic tool in source development," *Nuclear fusion*, vol. 46, no. 6, p. S297, 2006. (cited on page 51)

89. O. Leroy, J. Perrin, J. Jolly, M. Péalat, and M. Lefebvre, "Thermal accommodation of a gas on a surface and heat transfer in CVD and PECVD experiments," *Journal of Physics D: Applied Physics*, vol. 30, no. 4, p. 499, 1997. (cited on page 52)
90. T. Shikama, S. Kado, H. Zushi, and S. Tanaka, "Molecular zeeman spectroscopy for H₂ Fulcher- α band spectra as a local measurement of rovibrational structures," *Physics of plasmas*, vol. 14, no. 7, p. 072509, 2007. (cited on page 52)
91. U. Fantz, P. Franzen, W. Kraus, M. Berger, S. Christ-Koch, H. Falter, M. Fröschle, R. Gutser, B. Heinemann, C. Martens, P. McNeely, R. Riedl, E. Speth, A. Stäbler, and D. Wunderlich, "Physical performance analysis and progress of the development of the negative ion RF source for the ITER NBI system," *Nuclear Fusion*, vol. 49, no. 12, p. 125007, 2009. (cited on pages 52 and 90)
92. H. Tawara, Y. Itikawa, H. Nishimura, and M. Yoshino, "Cross sections and related data for electron collisions with hydrogen molecules and molecular ions," *Journal of Physical and Chemical Reference Data*, vol. 19, no. 3, pp. 617–636, 1990. (cited on pages 53, 93, 100, 110, 127, and 153)
93. C. Samuell, *Hydrogen plasmas and their interaction with fusion-relevant materials*. PhD thesis, PhD thesis, 2014. (cited on pages 53 and 91)
94. L. Marques, J. Jolly, and L. Alves, "Capacitively coupled radio-frequency hydrogen discharges: The role of kinetics," *Journal of Applied Physics*, vol. 102, no. 6, p. 063305, 2007. (cited on page 53)
95. B. Xiao, S. Kado, S. Kajita, and D. Yamasaki, "Rovibrational distribution determination of H₂ in low temperature plasmas by Fulcher- α band spectroscopy," *Plasma physics and controlled fusion*, vol. 46, no. 4, p. 653, 2004. (cited on page 54)
96. G. H. M. Spectra and M. Structure, "Spectra of diatomic molecules," 1950. (cited on page 57)
97. S. Astashkevich, M. Käning, E. Käning, N. Kokina, B. Lavrov, A. Ohl, and J. Röpcke, "Radiative characteristics of 3p Σ , Π ; 3d Π - Δ - states of H₂ and determination of gas temperature of low pressure hydrogen containing plasmas," *Journal of Quantitative Spectroscopy and Radiative Transfer*, vol. 56, no. 5, pp. 725–751, 1996. (cited on pages 57, 59, 60, and 196)
98. I. Kovács and L. Nemes, *Rotational structure in the spectra of diatomic molecules*. Hilger London, 1969. (cited on page 57)

99. G. Dieke, "The molecular spectrum of hydrogen and its isotopes," *Journal of Molecular Spectroscopy*, vol. 2, no. 1-6, pp. 494–517, 1958. (cited on page 59)
100. U. Fantz and D. Wunderlich, "Franck–Condon factors, transition probabilities, and radiative lifetimes for hydrogen molecules and their isotopomeres," *Atomic Data and Nuclear Data Tables*, vol. 92, no. 6, pp. 853–973, 2006. (cited on pages 59 and 192)
101. M. J. de Graaf, *A new hydrogen particle source*. PhD thesis, Boek-en Offsetdrukkerij Letru, 1994. (cited on pages 59, 61, and 196)
102. J. Van der Mullen, "Excitation equilibria in plasmas; a classification," *Physics Reports*, vol. 191, no. 2-3, pp. 109–220, 1990. (cited on page 60)
103. R. L. Day, R. J. Anderson, and F. A. Sharpton, "Radiative decay constants of the H₂ Fulcher bands," *The Journal of Chemical Physics*, vol. 69, no. 12, pp. 5518–5520, 1978. (cited on page 60)
104. R. Spindler, "Franck-Condon factors for band systems of molecular hydrogenâ€”II The (C1πu-X1σ+ g, D1πu-X1σ+ g) and (h3σ+ g-c3πu) systems," *Journal of Quantitative Spectroscopy and Radiative Transfer*, vol. 9, no. 5, pp. 627–642, 1969. (cited on page 61)
105. A. Hjartarson, E. Thorsteinsson, and J. Guðmundsson, "Low pressure hydrogen discharges diluted with argon explored using a global model," *Plasma Sources Science and Technology*, vol. 19, no. 6, p. 065008, 2010. (cited on pages 63, 91, 150, and 153)
106. T. Kimura and H. Kasugai, "Properties of inductively coupled RF Ar/H₂ plasmas: Experiment and global model," *Journal of Applied Physics*, vol. 107, no. 8, p. 083308, 2010. (cited on pages 63, 91, and 153)
107. M. Bacal and G. Hamilton, "H- and D- production in plasmas," *Physical Review Letters*, vol. 42, no. 23, p. 1538, 1979. (cited on pages 66, 68, and 150)
108. M. Bacal, "Photodetachment diagnostic techniques for measuring negative ion densities and temperatures in plasmas," *Review of Scientific Instruments*, vol. 71, no. 11, pp. 3981–4006, 2000. (cited on page 66)
109. J. Conway, N. Sirse, S. Karkari, and M. M. Turner, "Using the resonance hairpin probe and pulsed photodetachment technique as a diagnostic for negative ions in oxygen plasma," *Plasma Sources Science and Technology*, vol. 19, no. 6, p. 065002, 2010. (cited on page 66)

110. H.-J. Lee, I.-D. Yang, and K.-W. Whang, "The effects of magnetic fields on a planar inductively coupled argon plasma," *Plasma Sources Science and Technology*, vol. 5, no. 3, p. 383, 1996. (cited on pages 69, 77, 82, and 107)
111. G. Kiuttu, "Calculation of inductive electric fields in pulsed coaxial devices using electric vector potentials," in *Pulsed Power Plasma Science, 2001. PPPS-2001. Digest of Technical Papers*, vol. 2, pp. 1506–1508, IEEE, 2001. (cited on page 72)
112. V. Godyak, "Electrical and plasma parameters of ICP with high coupling efficiency," *Plasma Sources Science and Technology*, vol. 20, no. 2, p. 025004, 2011. (cited on page 75)
113. D. Rauner, S. Briefi, and U. Fantz, "Rf power transfer efficiency of inductively coupled low pressure H₂ and D₂ discharges," *Plasma Sources Science and Technology*, vol. 26, no. 9, p. 095004, 2017. (cited on page 75)
114. B. Singha, A. Sarma, and J. Chutia, "Sheath and plasma parameters in a magnetized plasma system," *Pramana*, vol. 55, no. 5, pp. 899–910, 2000. (cited on page 75)
115. V. Vahedi, M. Lieberman, G. DiPeso, T. Rognlien, and D. Hewett, "Analytic model of power deposition in inductively coupled plasma sources," *Journal of applied physics*, vol. 78, no. 3, pp. 1446–1458, 1995. (cited on page 87)
116. P. Jain, M. Recchia, M. Cavenago, U. Fantz, E. Gaio, W. Kraus, A. Maistrello, and P. Veltri, "Evaluation of power transfer efficiency for a high power inductively coupled radio-frequency hydrogen ion source," *Plasma Physics and Controlled Fusion*, vol. 60, no. 4, p. 045007, 2018. (cited on page 87)
117. M. Cavenago and S. Petrenko, "Models of radiofrequency coupling for negative ion sources," *Review of Scientific Instruments*, vol. 83, no. 2, p. 02B503, 2012. (cited on page 87)
118. W. Yang, H. Li, F. Gao, and Y.-N. Wang, "Hybrid simulations of solenoidal radio-frequency inductively coupled hydrogen discharges at low pressures," *Physics of Plasmas*, vol. 23, no. 12, p. 123517, 2016. (cited on pages 87 and 182)
119. A. Günther-Schulze, "Die wirkung eines transversalen magnetfeldes an der kathode der glimmentladung," *Zeitschrift für Physik*, vol. 24, no. 1, pp. 140–147, 1924. (cited on page 89)

120. L. Beckman, "The influence of a transverse magnetic field on a cylindrical plasma," *Proceedings of the Physical Society*, vol. 61, no. 6, p. 515, 1948. (cited on page 89)
121. S. Sen and R. Gupta, "Variation of discharge current in a transverse magnetic field in a glow discharge," *Journal of Physics D: Applied Physics*, vol. 4, no. 4, p. 510, 1971. (cited on page 89)
122. S. N. Sen and D. C. Jana, "Current voltage characteristics of glow discharge in longitudinal magnetic field," *Journal of the Physical Society of Japan*, vol. 43, no. 5, pp. 1729–1735, 1977. (cited on page 89)
123. H. Amemiya, "Production of electron-free plasma by using a magnetic filter in radio frequency discharge," *Japanese journal of applied physics*, vol. 30, no. 10R, p. 2601, 1991. (cited on page 89)
124. Y. Arnal, J. Pelletier, C. Pomot, B. Petit, and A. Durandet, "Plasma etching in magnetic multipole microwave discharge," *Applied Physics Letters*, vol. 45, no. 2, pp. 132–134, 1984. (cited on page 89)
125. M. Sasao and K. Sato, "Alpha-particle diagnostics with high-energy neutral beams," *Fusion technology*, vol. 10, no. 2, pp. 236–242, 1986. (cited on page 89)
126. R. Middleton, "A survey of negative ion sources for tandem accelerators," *Nuclear Instruments and Methods*, vol. 122, pp. 35–43, 1974. (cited on page 89)
127. M. Bacal, A. Bruneteau, and M. Nachman, "Negative ion production in hydrogen plasmas confined by a multicusp magnetic field," *Journal of applied physics*, vol. 55, no. 1, pp. 15–24, 1984. (cited on page 89)
128. J. Bredin, P. Chabert, and A. Aanesland, "Langmuir probe analysis of highly electronegative plasmas," *Applied Physics Letters*, vol. 102, no. 15, p. 154107, 2013. (cited on pages 89 and 105)
129. I. Djermanov, S. Kolev, S. Lishev, A. Shivarova, and T. Tsankov, "Plasma behaviour affected by a magnetic filter," in *Journal of Physics: Conference Series*, vol. 63, p. 012021, IOP Publishing, 2007. (cited on page 89)
130. M. Hopkins and W. Graham, "Electron energy distribution function measurements in a magnetic multipole plasma," *Journal of Physics D: Applied Physics*, vol. 20, no. 7, p. 838, 1987. (cited on pages 90, 96, 101, and 105)

131. A. Smolyakov, W. Frias, I. Kaganovich, and Y. Raitses, "Sheath-induced instabilities in plasmas with $E \times B$ drift," *Physical review letters*, vol. 111, no. 11, p. 115002, 2013. (cited on page 90)
132. P. Hazarika, M. Chakraborty, B. Das, and M. Bandyopadhyay, "A technique to control cross-field diffusion of plasma across a transverse magnetic field," *Physics of Plasmas*, vol. 23, no. 12, p. 122105, 2016. (cited on page 90)
133. W.-H. Cho, J.-J. Dang, J. Y. Kim, K.-J. Chung, and Y. Hwang, "Optimization of plasma parameters with magnetic filter field and pressure to maximize H- ion density in a negative hydrogen ion source," *Review of Scientific Instruments*, vol. 87, no. 2, p. 02B136, 2016. (cited on pages 90, 93, 94, 108, 139, 150, and 181)
134. A. Phelps, "Collisions of H+, H 2+, H 3+, ArH+, H-, H, and H 2 with Ar and of Ar+ and ArH+ with H 2 for energies from 0.1 eV to 10 keV," *Journal of physical and chemical reference data*, vol. 21, no. 4, pp. 883–897, 1992. (cited on page 93)
135. N. Hayashi, T. Nakashima, and H. Fujita, "Reduction of electron temperature in RF plasma using magnetic filter," *Japanese journal of applied physics*, vol. 38, no. 7S, p. 4301, 1999. (cited on page 94)
136. R. K. Janev, D. Reiter, and U. Samm, *Collision processes in low-temperature hydrogen plasmas*. Forschungszentrum Jülich, Zentralbibliothek, 2003. (cited on pages 95, 110, and 153)
137. K.-J. Chung, B.-K. Jung, Y. An, J.-J. Dang, and Y. Hwang, "Effects of discharge chamber length on the negative ion generation in volume-produced negative hydrogen ion source," *Review of Scientific Instruments*, vol. 85, no. 2, p. 02B119, 2014. (cited on page 97)
138. V. Godyak, R. Piejak, and B. Alexandrovich, "Evolution of the electron-energy-distribution function during RF discharge transition to the high-voltage mode," *Physical review letters*, vol. 68, no. 1, p. 40, 1992. (cited on page 101)
139. M. Hopkins, M. Bacal, and W. Graham, "Enhanced volume production of negative ions in the post discharge of a multicusp hydrogen discharge," *Journal of applied physics*, vol. 70, no. 4, pp. 2009–2014, 1991. (cited on page 101)

140. V. A. Godyak, "Nonequilibrium EEDF in gas discharge plasmas," *IEEE transactions on plasma science*, vol. 34, no. 3, pp. 755–766, 2006. (cited on page 105)
141. S. Samukawa and S. Furuoya, "Time-modulated electron cyclotron resonance plasma discharge for controlling generation of reactive species," *Applied physics letters*, vol. 63, no. 15, pp. 2044–2046, 1993. (cited on page 107)
142. E. Speth, H. Falter, P. Franzen, U. Fantz, M. Bandyopadhyay, S. Christ, A. Encheva, M. Fröschle, D. Holtum, B. Heinemann, *et al.*, "Overview of the RF source development programme at IPP garching," *Nuclear Fusion*, vol. 46, no. 6, p. S220, 2006. (cited on page 107)
143. S. Iordanova, "Spectroscopic temperature measurements in hydrogen inductively-driven plasmas at low pressures," in *Journal of Physics: Conference Series*, vol. 113, p. 012005, IOP Publishing, 2008. (cited on page 121)
144. S. Iordanova and I. Koleva, "Optical emission spectroscopy diagnostics of inductively-driven plasmas in argon gas at low pressures," *Spectrochimica Acta Part B: Atomic Spectroscopy*, vol. 62, no. 4, pp. 344–356, 2007. (cited on page 121)
145. H.-H. Doh and Y. Horiike, "Gas residence time effects on plasma parameters: Comparison between Ar and C₄F₈," *Japanese Journal of Applied Physics*, vol. 40, no. 5R, p. 3419, 2001. (cited on page 123)
146. A. Phelps, "Cross sections and swarm coefficients for H+, H₂+, H₃+, H, H₂, and H- in H₂ for Energies from 0.1 eV to 10 keV," *Journal of Physical and Chemical Reference Data*, vol. 19, no. 3, pp. 653–675, 1990. (cited on page 127)
147. T. Paunská, A. Shivarova, K. Tarnev, and T. Tsankov, "Negative hydrogen ion maintenance in small radius discharges: Two-dimensional modeling," *Physics of Plasmas*, vol. 18, no. 2, p. 023503, 2011. (cited on pages 130, 148, 150, and 171)
148. T. Šimko, V. Martišovitš, J. Bretagne, and G. Gousset, "Computer simulations of H+ and H 3+ transport parameters in hydrogen drift tubes," *Physical Review E*, vol. 56, no. 5, p. 5908, 1997. (cited on page 134)
149. A. Phelps, "Cross sections for collision of electron, positive and negative ions, and neutral atoms and molecules with H₂ and surfaces for mod-

- elling low pressure discharges in H₂," *Personal Notes*, 2011. (cited on page 134)
150. A. Holmes, G. Dammertz, and T. Green, "H- and electron production in a magnetic multipole source," *Review of scientific instruments*, vol. 56, no. 9, pp. 1697–1702, 1985. (cited on page 147)
 151. C. Michaut, M. Bacal, Y. I. Belchenko, J. Auvray, C. Konieczny, and J. Stephan, "Study of pulsed discharge operation of volume H- ion source," *Review of scientific instruments*, vol. 65, no. 4, pp. 1207–1209, 1994. (cited on pages 147 and 157)
 152. U. Fantz, P. Franzen, W. Kraus, M. Berger, S. Christ-Koch, M. Fröschle, R. Gutser, B. Heinemann, C. Martens, P. McNeely, *et al.*, "Negative ion RF sources for ITER NBI: status of the development and recent achievements," *Plasma Physics and Controlled Fusion*, vol. 49, no. 12B, p. B563, 2007. (cited on page 150)
 153. P. Chabert, T. Sheridan, R. Boswell, and J. Perrin, "Electrostatic probe measurement of the negative ion fraction in an sf6 helicon discharge," *Plasma Sources Science and Technology*, vol. 8, no. 4, p. 561, 1999. (cited on page 151)
 154. C. Corr, N. Plihon, and P. Chabert, "Transition from unstable electrostatic confinement to stable magnetic confinement in a helicon reactor operating with ar/ sf 6 gas mixtures," *Journal of applied physics*, vol. 99, no. 10, p. 103302, 2006. (cited on page 151)
 155. B. Peart, D. Walton, and K. Dolder, "Electron detachment from H-ions by electron impact," *Journal of Physics B: Atomic and Molecular Physics*, vol. 3, no. 10, p. 1346, 1970. (cited on page 153)
 156. M. Eerden, M. Van de Sanden, D. Otorbaev, and D. Schram, "Cross section for the mutual neutralization reaction H 2+ + H-, calculated in a multiple-crossing landau-zener approximation," *Physical Review A*, vol. 51, no. 4, p. 3362, 1995. (cited on page 153)
 157. J. Jolly and J.-P. Booth, "Atomic hydrogen densities in capacitively coupled very high-frequency plasmas in H 2: Effect of excitation frequency," *Journal of applied physics*, vol. 97, no. 10, p. 103305, 2005. (cited on page 154)
 158. D. Smith, A. Dean, and N. Adams, "Space charge fields in afterglow plasmas," *Journal of Physics D: Applied Physics*, vol. 7, no. 14, p. 1944, 1974. (cited on pages 156, 159, 166, and 175)

159. W. L. Fite and J. Rutherford, "Negative ions in afterglows in atmospheric gases," *Discussions of the Faraday Society*, vol. 37, pp. 192–202, 1964. (cited on page 156)
160. A. Phelps, "The diffusion of charged particles in collisional plasmas: free and ambipolar diffusion at low and moderate pressures," *Journal of research of the National Institute of Standards and Technology*, vol. 95, no. 4, p. 407, 1990. (cited on pages 166 and 168)
161. J. Horáček, M. Čížek, K. Houfek, P. Kolorenč, and W. Domcke, "Dissociative electron attachment and vibrational excitation of h₂ by low-energy electrons: Calculations based on an improved nonlocal resonance model. ii. vibrational excitation," *Physical Review A*, vol. 73, no. 2, p. 022701, 2006. (cited on page 170)
162. B. H. Mahan and J. C. Person, "Gaseous ion recombination rates," *The Journal of Chemical Physics*, vol. 40, no. 2, pp. 392–401, 1964. (cited on page 175)
163. M. Church and D. Smith, "Ionic recombination of atomic and molecular ions in flowing afterglow plasmas," *Journal of Physics D: Applied Physics*, vol. 11, no. 16, p. 2199, 1978. (cited on page 175)
164. G. D. Dickenson, M. L. Niu, E. J. Salumbides, J. Komasa, K. S. Eikema, K. Pachucki, and W. Ubachs, "Fundamental vibration of molecular hydrogen," *Physical review letters*, vol. 110, no. 19, p. 193601, 2013. (cited on page 191)
165. F. Hund, "Zur deutung einiger erscheinungen in den molekelspektren," *Zeitschrift für Physik A Hadrons and Nuclei*, vol. 36, no. 9, pp. 657–674, 1926. (cited on page 194)